ABSTRACT

Title: METALLIC NANO-PARTICLES AS FUEL ADDITIVES IN AIR-BREATHING COMBUSTION

Gregory Young, Doctor of Philosophy, 2007

Directed By: Associate Professor, Dr. Kenneth H. Yu, Department of Aerospace Engineering

For volume limited propulsion systems, the use of metals as fuel additives offers to increase performance by increasing the volumetric energy stored in the fuel. High-speed airbreathing combustors generally have very short residence times which do not allow for complete combustion of traditional metal particles such as aluminum and boron, which are typically larger than 1 μm. The development of nano-scale metals has opened up the possibility of utilizing metals in high-speed propulsion systems.

This research effort was conducted in order to determine the viability of utilizing metallic nanoparticles as fuels or fuel supplements for high-speed airbreathing applications. The study was broken into two main parts; the first was a fundamental investigation into the combustion behavior of boron nanoparticles in a controlled setting, while the second was a demonstration of the performance potential of the nanoparticles in a realistic airbreathing combustor configuration.

Initially, the combustion behavior of boron nanoparticles was studied in a controlled flame environment to extract basic combustion parameters, such as ignition criterion and burning time as functions of surrounding temperature and oxygen concentration. Ensemble average burning times of boron nanoparticles were obtained for the first time, while the range of ignition time data was extended into a lower temperature range. The burning time results were compared to both diffusion and kinetic limited theories of particle combustion. It was found that the size dependence on particle burning times did not follow either theory. A kinetic limited burning time correlation has been proposed based upon Arrhenius parameters extracted in this study.

Finally, the fundamental combustion behavior of both boron and aluminum nanoparticles was studied extensively in an airbreathing combustor simulating ramjet conditions in an effort to determine the viability of using metallic nanoparticles as fuels or fuel supplements in high-speed airbreathing propulsion system. Experiments were conducted with hydrocarbon only (ethylene), mixtures of ethylene and boron, and mixtures of ethylene and aluminum. The oxidation of the metals was studied through the emission of BO_2 and AlO at wavelengths of 546 nm and 488 nm respectively. Temperature measurements inside the combustor using thermocouples were made in order to determine boundaries in which the addition of boron or aluminum provided a positive thermal output for a variety of equivalence ratios ranging from 0.52 to 0.7, metal loadings ranging from 9.7 to 15.2% by weight, and combustor residence times ranging from 6 to 10.5 milliseconds (combustor inlet velocities of 40 – 70 m/s). Both BO_2 emission data and temperature measurements indicated that a critical temperature exists for sustained combustion of the boron particles. Tests with measured peak temperatures

below 1700 K indicated no benefit of boron addition, while experiments with measured peak temperatures above 1770 K showed a positive thermal contribution from boron addition. All tests using nanoaluminum displayed a noteable positive addition to the thermal output of the system. These results suggest that even when employing nano-sized boron, only a small envelope for complete energetic extraction exists in combustors with short residence times. On the other hand, great hope exists for the use of nanoaluminum in high speed airbreathing combustors.

METALLIC NANOPARTICLES AS FUEL ADDITIVES IN AIRBREATHING COMBUSTION

By

Gregory Young

Dissertation Submitted to the Faculty of the Graduate School of the
University of Maryland, College Park, in partial fulfillment
of the requirements for the degree of
Doctor of Philosophy
2007

Advisory Committee:
Dr. Kenneth Yu
Dr. James Baeder
Dr. Michael Zachariah
Dr. Ashwani Gupta
Dr. Bao Yang

DEDICATION

This work is dedicated to my family without whom I could not have hoped to accomplish anything. By family I include more than just my mother and siblings. I include everyone who has helped me along the way, no need to name names; I think you know who you are. I don't have the words to show my appreciation; all I can say is thanks. I'd specifically like to dedicate this work to my wife Chrissy, who has supported me every step of the way. Thanks.

ACKNOWLEDGMENTS

I would like to express my sincere thanks to all of those who lent their support to me through the course of this research. In particular, I would like to thank Dr. Kenneth Yu, my advisor, for providing guidance and encouragement through the entire effort. I would also like to specifically thank Dr. Michael Zachariah for his input and support throughout. Additionally I would like to express my gratitude towards my remaining committee members, Dr. James Baeder, Dr. Ashwani Gupta, and Dr. Bao Yang.

I am especially grateful to the Naval Surface Warfare Center-Indian Head Division for providing me with the opportunity to conduct this research. Specifically I would like to thank Mr. Gary Prybyla, my supervisor, for his support and patience. In addition I would like to express my thanks to Mr. Kevin Gessner, Mr. Bob Kaczmerak, and Mr. Chris Fawls.

Finally I would like to thank all of the members of the Advance Propulsion Research Lab, who have made the last few years extremely enjoyable. I would specifically like to thank Mr. Rama Balar and Mr. Mike Krasel for all of their time and effort involved in this study. Lastly, I would like to thank Mr. Kyle Sullivan of the Co-Laboratory for Nanoparticle Based Manufacturing and Metrology for his time and effort in support of this research.

TABLE OF CONTENTS

LIST OF FIGURES

LIST OF TABLES

NOMENCLATURE

A	Area
A^*	Critical Area for Choking Flow
B	Spalding Transfer Number
C_c	Cunningham Correction Factor
d_q	Quenching Diameter
dt	Incremental Time
dx	Incremental Axial Distance
Da	Damkohler Number
D	Particle Diameter
D_o	Initial Particle Diameter
E	Charge of an Electron
E	Electrical Field Strength
E_a	Activation Energy
f	Fuel to Air Ratio
F	Thrust
F_D	Drag Force
g	Acceleration due to Gravity
h	Convective Heat Transfer Coefficient
$\bar{h}_i$	Enthalpy of Formation of Species i
H	Combustor Inlet Channel Height
I_{sp}	Specific Impulse

J	Jet Momentum Flux Ratio
J_e	Jet Initial Momentum Flow
L	Lift Force
k	Thermal Conductivity
m	Mass
m_{Al}	Mass of Aluminum
m_f	Final Mass
m_i	Initial Mass
m_{o2}	Mass of Oxygen
$\dot{m}$	Mass Flow Rate
M	Mach Number
MW	Molecular Weight
n	Number of Charges on a Particle
N_i	Number of Moles of Species i
Nu	Nusselt Number
p_{O2}	Partial Pressure of Oxygen
P	Pressure
P_o	Stagnation Pressure
Q_5	Heat Released by Surface Reaction
r	Jet Incremental Radius
R	Jet Radius
R_u	Gas Constant
Re_d	Reynolds Number Based on Sphere Diameter

Sc	Schmidt Number
$S_{particle}$	Characteristic Particle Stopping Time
t	Time
t_b	Burning Time
$t_{b,diff}$	Time Scale for Diffusion Limited Burning
$t_{b,kin}$	Time Scale for Kinetically Limited Burning
t_1	Stage 1 or Ignition Stage of Boron Combustion
t_2	Stage 2 or Full-Fledged Combustion Stage of Boron Combustion
T	Temperature
T_{ave_metal}	Average Measured Temperature for a Given Metallized Test
$T_{ave\_ethylene}$	Average Measured Temperature for a Given Hydrocarbon Only Test
T_g	Gas Temperature
T_o	Stagnation Temperature
T_q	Quenching Temperature
T_{tc}	Thermocouple Temperature Reading
T_∞	Ambient Temperature
$T_{o,\infty}$	Ambient Stagnation Temperature
U	Velocity
U_{ave}	Average Velocity
U_e	Jet Exit Velocity
U_J	Jet Velocity
U_x	Axial Component of Velocity
U_∞	Freestream Velocity

V	Particle Velocity
V_{TE}	Terminal Electrostatic Velocity
w	Width of Pilot Jet Slot
x	Axial Distance
X_{eff}	Effective Oxidizer Concentration
$X_{o,\infty}$	Oxygen Mole Fraction in the Far Field
X_{O2}	Oxygen Mole Fraction
y	Vertical Distance
Y_{CG}	Carrier Gas Mass Fraction
$Y_{o,\infty}$	Oxygen Mass Fraction in the Far Field
Z	Electrical Mobility
α_s	Thermal Diffusivity
β_v	Evaporation Coefficient
ε_{tc}	Thermocouple Emissivity
Δh_r	Lower Heating Value on a Mass Basis
Δm	Change in Mass
η	Thermal Ratio
γ	Ratio of Specific Heats
λ	Mean Free Path
ν	Kinematic Viscosity
ρ	Density
ρ_l	Liquid Phase Density
ρ_J	Jet Gas Density

ρ_p	Particle Density
ρ_s	Solid Phase Density
$\rho\ \Delta h_r$	Lower Heating Value on a Volumetric Basis
ρ_∞	Freestream Gas Density
$\rho\ I_{sp}$	Density Impulse
μ	Fluid Viscosity
μ_s	Fluid Viscosity at Thermocouple Surface
μ_∞	Fluid Viscosity in the Far Field
ξ	Similarity Variable
σ	Boltzman Constant
Φ	Equivelance Ratio

CHAPTER 1

INTRODUCTION

1. Introduction

Airbreathing propulsion systems offer the potential of increasing vehicle range due to the fact that they are considerably more efficient than rockets. For volume limited systems, the use of metals as fuel additives offers to increase performance even further by increasing the volumetric energy stored in the propulsion system. However, traditional metals such as aluminum and boron require longer combustor residence times than hydrocarbons or hydrogen, which are typically used in airbreathing systems. The development of nano-scale metals has opened up the possibility of utilizing metals in high-speed propulsion systems.

The focus of this study was to determine the fundamental ignition and combustion behavior of both boron and aluminum nanoparticles for which very little data exists. Due to the lack of available data, the combustion behavior of boron nanoparticles was first studied in a controlled flame environment to extract basic combustion parameters, such as ignition criterion and burning time.

With an understanding of the fundamental behavior of both boron and aluminum nanoparticles, the next portion of this study was to determine whether or not either material could be considered a viable fuel/fuel supplement in a high speed airbreathing propulsion system. The fundamental combustion behavior of both boron and aluminum

nanoparticles were studied extensively in an airbreathing combustor simulating ramjet conditions.

Chapter 1 provides some basic background and motivation for the study, while Chapter 2 discusses relevant research available in the literature. Chapter 3 describes in detail the experimental approach used in this study. Chapter 4 outlines the basic characterization studies required to meet the goals of the current research. Finally, Chapters 5 and 6 discuss in detail the results of this research.

1.1 Jet Propulsion Classification

Propulsion mechanisms provide a force that moves bodies that are initially at rest, changes a velocity, or overcomes retarding forces when a body is propelled through a medium[1]. Jet propulsion is a means of locomotion whereby a reaction is imparted to a device by the momentum of ejected matter. Two common forms of jet propulsion are rocket propulsion and duct propulsion. Duct propulsion is a class of jet propulsion and includes turbojets and ramjets; these engines are commonly referred to as air breathing engines.

1.2 Airbreathing Propulsion Systems

Airbreathing propulsion systems differ from rockets in that as their name implies they use atmospheric oxygen together with a fuel carried onboard as the propellant system. Rockets carry their oxidizing agent onboard in a variety of ways depending on the type of rocket. By obtaining oxygen from the atmosphere, airbreathing systems are considerably more efficient than rockets. Furthermore, most airbreathing engines are

reusable, not just refurbishable like rockets. An additional feature for space access is short turn around time, with potential cost reduction of 10-100 times per pound payload[2]. However, airbreathing devices are limited to that portion of the atmosphere, where air is dense enough to provide sufficient thrust, typically around 100 km[3]. Figure 1.1 provides a summary of the performance envelope of the different jet propulsion systems[4]. As the figure shows, airbreathing systems have much higher specific impulses (I_{sp}) than rockets. The range that a vehicle can attain is directly proportional to the vehicles I_{sp}, this implies that airbreathing propulsion systems should be the vehicle of choice for long range missions.

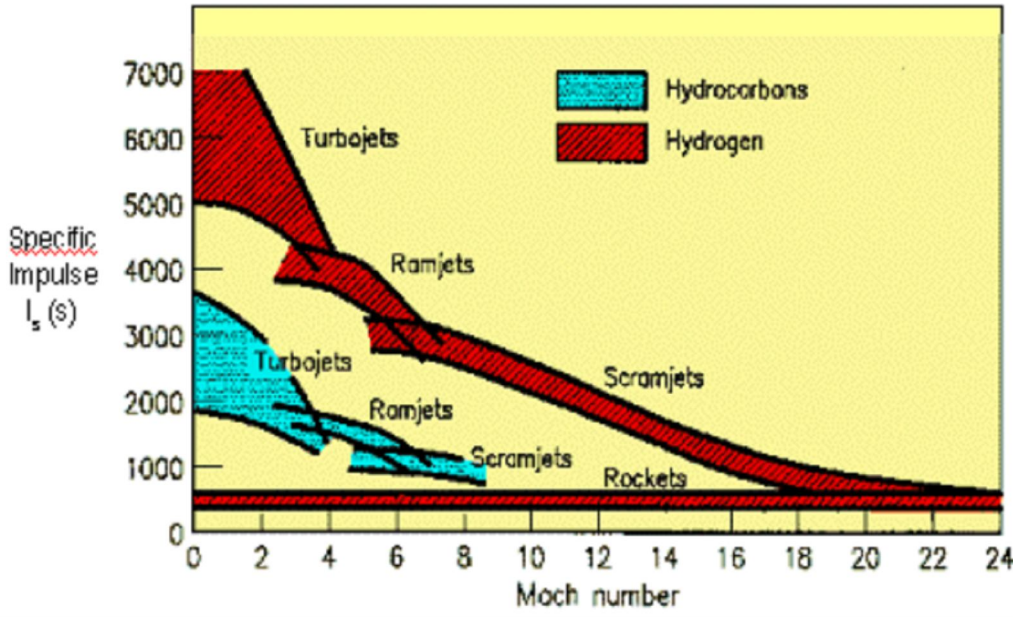

Fig. 1.1 Performance Envelope of Jet Propulsion systems[4]

Airbreathing propulsion systems can be classified into two categories: 1) Engines with rotating machinery, and 2) engines without rotating machinery. Engines with rotating machinery include turboprops, turbojets, and turbofans. Engines without rotating

machinery include ramjets and scramjets. Ramjet performance is the main focus of this thesis. Typically turboprops are limited to speeds of about Mach 0.7, turbofans and turbojets are limited to speeds up to about Mach 3.0, ramjets operate between Mach 2 and 5, while for higher speeds scramjets are employed[3].

1.2.1 Ramjets/Ducted Rockets

Simple in concept, the ramjet uses fixed components to compress and accelerate intake air by ram effect. Ramjets cannot operate from a standing start; they must be accelerated to high speeds by some other form of propulsion due to the fact that they rely on the ram effect for air compression, thus the name ramjet. They have also been called a flying stovepipe due to the absence of rotating parts that characterize turbine engines[2].

The basic ideas behind the operation of a ramjet are fairly straightforward. There are typically four components to the engine, an inlet, diffuser, combustor and an exit nozzle. In most cases, supersonic air enters the inlet and is decelerated through the diffuser. The diffuser is analogous to the compressor of a turbine engine. Compression itself is dependent on velocity and it increases dramatically with flight speed. After the diffuser, the air enters the combustor where it is mixed with injected fuel. The mixture burns in the combustor, quite often with the aid of a flame holding device of some sort. The burning mixture imparts thermal energy to the gas, which expands to high velocity through an exit nozzle at speeds greater than the entering air. This process produces the thrust necessary for ramjet flight.

Although, ramjets are capable of operating at subsonic speeds, they are most suited to supersonic flight due to the higher pressure rise accompanying higher flight

speeds[3]. For speeds above Mach 3, turbine based propulsion systems become impractical. A ramjet engine is one alternative that is especially attractive due to its simplicity in the fact that it has no rotating parts. Generally, ramjets can be broken into three different types: 1) Liquid Fuel, 2) Solid Fuel, 3) Ducted Rockets. The first approach to estimating the performance of a ramjet engine is that of a heat engine or thermal engine closed cycle analysis, often referred to as a Brayton Cycle Analysis[5]. A temperature-entropy diagram of the ideal ramjet is shown in Figure 1.2 to illustrate the cycle. The stations correspond to those given in Figure 1.3. Briefly, the cycle goes as follows. Adiabatic compression from station 0 to station 2, which is accompanied by an increase in static temperature. From station 2 to station 4, there is a constant static pressure heat addition due to the combustion of fuel and air. Finally, from station 4 to station 6 there is an adiabatic expansion through the nozzle to the atmospheric static pressure. This analysis is an idealized case and does not consider any losses or irreversibilities.

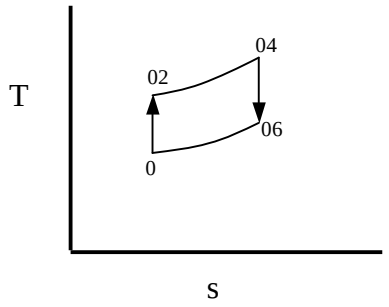

Fig. 1.2 Brayton Cycle Temperature-Entropy Diagram for Ramjet

Figure 1.3[5] shows a schematic diagram of a typical liquid fuel ramjet engine. Supersonic air is decelerated through a diffuser after which it enters the combustion chambers at subsonic speeds. Liquid fuel, usually a hydrocarbon, is injected and combusted with the atmospheric air. Often flame holding devices are employed to encourage flame stabilization. After the combustion chamber the combustion products are accelerated through an exhaust nozzle into the atmosphere to provide thrust. Liquid fuels offer a number of advantages over solid fuels[6].

1) Better specific thrust
2) Higher modulation ratios for liquids because of their incompressibility
3) More compactness and optimization of available space compared to ducted rockets (storage tanks can be made in any shape)

For these reasons, the use liquid fuels proves necessary when the specified missions involve long ranges or when the flight envelope entails considerable altitude and or Mach number variations[6].

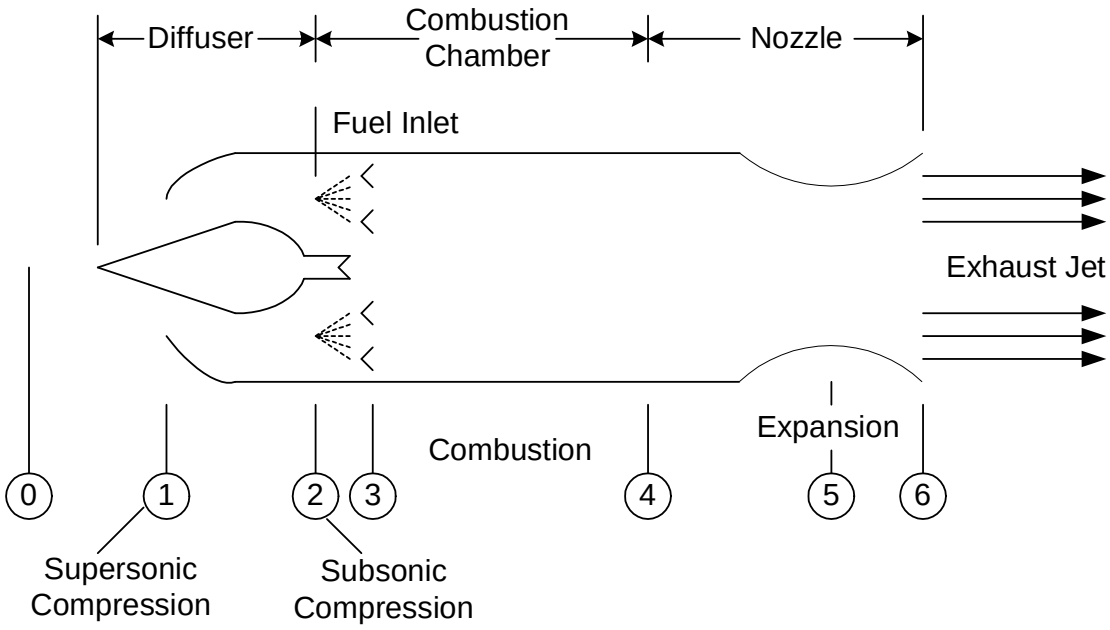

Fig. 1.3 Schematic Diagram of a Liquid Fueled Ramjet[5]

One variant of the LFRJ is the use of slurry, slush, or gelled fuels. Typically solid particles such as aluminum or boron can be added to a liquid hydrocarbon fuel to produce a gel or slurry. These additives are used to increase the energetic output of the fuel. Although the theoretical output of the fuel increases with the addition of these solid particles, a new set of challenges arises. Perhaps the largest challenge comes from the fact that the combustion efficiency in the chamber may significantly decrease because the solid particles require a minimum amount of energy to initiate their combustion and the residence time in the chamber may not permit complete combustion[6].

Solid Fuel Ramjets (SFRJ) have been considered for propulsion devices in missiles since the 1930's[7]. Figure 1.4[3] shows a schematic diagram of a typical solid fueled ramjet. In a SFRJ, the fuel is stored in a solid matrix such as a polybutadiene, polyether, polyester, polyeurethane, polymethilmetacrylate, or plexiglass. There have

been numerous studies incorporating metals into the solid fuel matrix as a means of increasing the energetic content of the fuels[8-11].

Atmospheric air is decelerated and brought into the combustor section upon which it reacts with the solid fuel. The solid fuel pyrolyses and creates a fuel rich diffusion flame near its surface. Fuel regression rates depend primarily on the inlet air temperature and the air mass flux[7]. Often a secondary combustion chamber is employed to achieve complete fuel/air mixing and combustion. After the combustion chamber, just as in the liquid fuel ramjet, the combustion products are accelerated through an exhaust nozzle to the atmosphere to provide thrust. SFRJ's have several major advantaged over LFRJ's.

1. Storage as a solid fuel is more efficient.
2. Storage as a solid fuel is typically safer since there is no possibility of fuel leakage
3. Solid fuel provides insulation to the combustor walls allowing higher temperature operation.

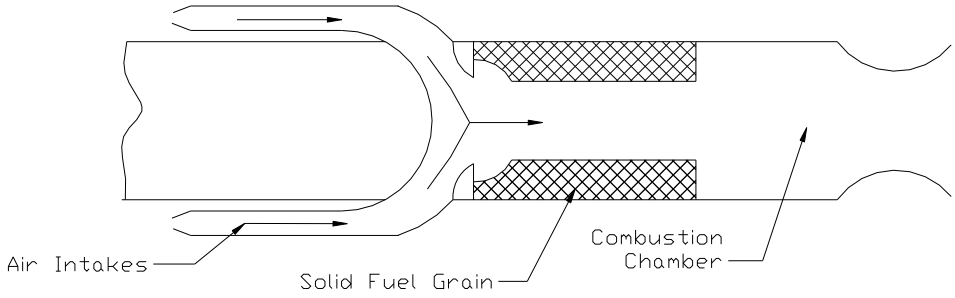

Fig. 1.4 Schematic Diagram of a SFRJ[3]

Ducted rockets or air augmented rockets, differ form SFRJ's in that they burn a fuel rich propellant/gas generator whose products are then combusted with the

atmospheric air. The gas generator provides hot combustible products to the main combustion chamber. This promotes faster and generally more complete combustion, however, since some oxidizer is carried on board in the fuel rich propellant some of the initial benefits of the air breathing system are lost. The principal attribute of a ducted rocket is the simplicity, ruggedness, and handling ease it enjoys by virtue of its solid fuel. In tactical missile applications this factor can weigh heavily and can favor the selection of a ducted rocket even though its performance might be only one-half to two-thirds that of a LFRJ[11]. Figure 1.5[3] shows a schematic of a ducted rocket.

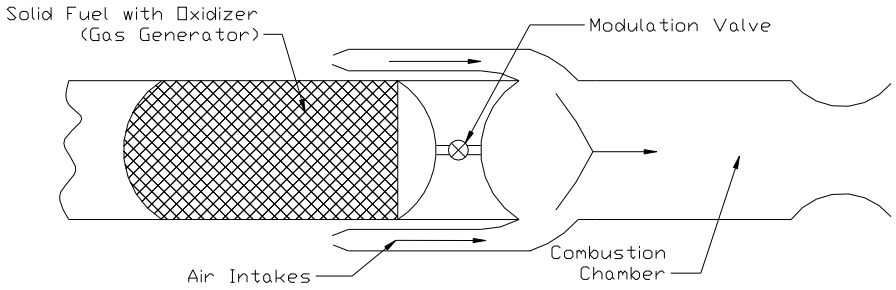

Fig. 1.5 Schematic Diagram of a Ducted Rocket[3]

Ramjets have a number of advantages over other propulsion systems.

1. Simple design (e.g. no moving parts).
2. Higher speed operation than turbojets.
3. Greater efficiency in terms of specific impulse than rockets → generally translates into increased range.

However there are a number of disadvantages with ramjet compared to the other jet propulsion systems.

1. Can not generate static thrust → need a booster system to operate

2. Generally lower thrust to weight than rockets
3. Can only operate in the earth's atmosphere
4. Operation is limited to approximately $2 < \text{Mach} < 5$

1.3 Brief History of Ramjets

Ramjet concepts have been around since the early 1900's[14]. Numerous countries have been involved with their development including the United States, Great Britain, France, Germany, Russia (or USSR for part of ramjet history), China, Israel, and South Africa. Applications range from boost to main propulsion for aircrafts, gun projectiles, missiles, and space launch vehicles. Rene Lorin of France is generally credited with first recognizing the possibility of using ram pressure in a propulsion device, however, Lake of the United States was issued the first patent for a subsonic ramjet cycle device in 1909[2], and Albert Fono of Hungary holds the first patent for the use of a ramjet engine as a means of propulsion for supersonic flight in 1928[3,5]. Although the concept of a ramjet was around much earlier, the onset of World War II brought about the true beginnings of the ramjet, with a peak coming in the 1950's.

In Germany, Trommsdorff led a successful effort that began in 1935 to develop artillery shells powered by multiple-shock, conical-inlet, liquid-fueled ramjets. These shells actually accelerated from Mach 2.9 to 4.2 in trials in the early 1940's[14]. The Germans fielded the first operational ramjet powered missile in the form of the V1 "buzzbomb" powered by a subsonic flight speed pulsejet engine. In 1939 under the direction of Merkulov, Russia successfully flight-tested a tandem boosted ducted rocket using a magnesium/aluminum solid fuel[2]. The first ramjet powered airplane was

designed and tested by Leduc in France, with the first powered flight taking place in April 1949.

Reid (United States) and Marquardt (England) joined the ramjet development effort in the early 1940's in the form of aerial guided projectiles and aircraft performance augmenters, respectively. These efforts continued after World War II and resulted in weapon systems such as the BOMARC (U.S. Air Force), Talos (U.S. Navy), and Bloodhound (United Kingdom). In France a number of operational ramjet missiles (VEGA, CT-41, and SE 4400) were deployed in the last 1950's and 1960's[2]. In the 1990's China and South Africa began ramjet development programs.

1.4 Motivation

While hydrogen is a popular choice for airbreathing propulsion systems particularly scramjets, due to its high gravimetric heating values, there are some major disadvantages with the use of hydrogen.

1. Low density requires large storage tanks. Large tanks suffer large drag penalties.
2. Liquefaction requires the use of cryogenics, which complicates the system and restricts storage capabilities.
3. More hazardous than hydrocarbons.

Naturally, one alternative is the use of hydrocarbons. Although the gravimetric heating value of typical hydrocarbons is less than half that of hydrogen, the volumetric heating value is very comparable. The result is a more compact system capable of greater range. Furthermore, liquefaction and storage of hydrocarbons is quite simple. Hydrocarbons are

typically stored as a liquid, but can also be stored easily as a gel, slurry, or as part of a solid matrix in a fuel rich solid propellant or solid fuel. To further increase the performance of hydrocarbon fuels, it is possible to add metal additives which can increase overall performance and in particular the energy density of a system. Aluminum has been used as an additive in solid propellant rocket motors for many years. In addition, aluminum has been studied as a fuel additive in Solid Fueled Ramjets (SFRJ). Boron has been studied for many years as a fuel and or a fuel supplement because of its high gravimetric and volumetric heating values[8]. Boron has been investigated as a fuel supplement in solid rocket motors, hybrid rocket engines, and SFRJ's. One major issue with previous studies in a traditional ramjet setting, is that all of the studies have been conducted using micron size particles or larger.

Metal additives such as aluminum have been used in solid rocket motors for many years as a means of increasing performance since they have the ability to increase the volumetric heat release of the propellants. However, one downfall in using these additives is that it in many cases incomplete combustion of the additives results in lower than expected performance. Typically this is a result of large agglomerates forming and not fully reacting in the combustor. With these problems evident in rocket motors, the use of metal additives has not been fully realized in air breathing combustors since residence times are typically much smaller. Now with the creation of nanoscale particles, it is expected that combustion times for individual particles will decrease significantly and the potential benefits for air breathing systems may be realized. Olsen[15] provided a summary of micron-sized aluminum particle burn times in various environments. Typical burn times for particles from about 20 μm to 100 μm vary from about three

milliseconds to about thirty milliseconds with a fair amount of scatter attributed to variations in methods, test conditions, data reduction methods, and the use of relatively wide particle size distributions. Parr[16] reported burn times of agglomerated nano-sized aluminum particles of less than 1 millisecond, burning in a steam environment. In addition, Parr found that the ignition temperatures of some types nanoaluminum are significantly decreased compared to micron-sized aluminum. In a series of shock tube measurements, Bazyn[17] also found burn times of nanoscale aluminum to be less than one millisecond in environments of primarily oxygen or carbon dioxide in temperatures ranging from 1200-2200 K and pressures ranging from 4-32 atmospheres. If we consider that typical residence times in a ramjet engine are on the order of milliseconds, it would seem that it would be possible to extract all or most of the energy from these aluminum particles within the engine and maximizing the performance provided that the particles are close to their original size within the combustor. Furthermore, Tepper and Kaledin[18] found that the addition of ALEX particles can act as a combustion accelerant for RP-1 in oxygen when compared to gelled and neat RP-1 in terms of ignition delay.

Traditionally, metals have been considered as additives to solid or gelled fuels, however, Goroshin et. al.[19] point out through a series of thermochemical calculations that powdered metals alone, in particular boron and aluminum, can provide substantial performance increases over hydrocarbon fuels. Palaszewski[20] and Mordosky[21] have demonstrated the ability to gel hydrocarbons with aluminum particles with up to 55% by weight aluminum. Mordosky[21] gelled nanoaluminum with RP-1, and tested it with gaseous oxygen in a rocket engine environment, with some c* efficiencies reported greater than 90%. Furthermore, nano-sized aluminum and boron were investigated as a

fuel supplement in hybrid rocket engines[22] and were proven to significantly increase regression rates of solid fuels. More recently Palaszewski[23] utilized nano-sized aluminum as an additive to gelled hydrocarbons in pulsed detonation engines.

In airbreathing propulsion one of the most important parameters in determining a fuel's potential is the heating value. However for volume limited systems, the heating value per unit volume can become the driving parameter for performance. Table 1.1 shows the lower heating values of RP-1 fuels with and without the addition of aluminum or boron determined from a series of calculations. The lower heating value corresponds to the case where none of the water in the products is assumed to condense. The density of the fuels is also determined from calculations. As Table 1.1 shows, the heating value per unit mass decreases with the addition of aluminum, however, the volumetric heating value increases significantly due to the high density of aluminum compared with that of RP-1.

To illustrate further the benefits of these additives, figures 1.6-1.9 show calculated ideal ramjet specific impulses as a function of Mach number for a variety of additive loadings in RP-1. Specific impulse is an important parameter for all forms of propulsion as it is directly related to the range that a vehicle can attain. The specific impulse of a ramjet is dependent on many parameters such as fuel to air ratio and altitude. In order to simplify the analysis the calculations were based upon ideal ramjet assumptions, and are made considering each air/fuel mixture is in stoichiometric proportions, which may not necessarily be ideal for the given fuel. In addition, the calculations were performed with air properties at an altitude of 10 km (~60,000 ft). While the standard specific impulse (I_{sp}) actually decreases with increasing metal content, the density impulse (ρI_{sp}) increases

significantly with increasing metal content. In the case of boron, the addition of 50% by weight boron to RP-1 yields an improvement of approximately 50% in density impulse. For volume limited systems, such as missiles, this improvement in potential performance is undeniable.

Table 1.1 Lower Heating Values of Various Fuels

Fuel	**Δh_r (kJ/kg)**	**ρ (g/cc)**	**$\rho\Delta h_r$ (MJ/m^3)**
Hydrogen (H_2)	119,971	0.07	8,398
RP-1 (CH_2)	39,688	0.80	31,750
Aluminum	31,643	2.7	85,436
Boron	58,497	2.34	138,762
RP-1/5%Al	39,286	0.829	32,568
RP-1/10%Al	38,883	0.861	33,478
RP-1/20%Al	38,079	0.931	35,452
RP-1/50%Al	35,665	1.234	44,011
RP-1/5%B	40,628	0.827	33,609
RP-1/10%B	41,569	0.856	35,598
RP-1/20%B	43,450	0.921	40,029
RP-1/50%B	49,092	1.192	58,536

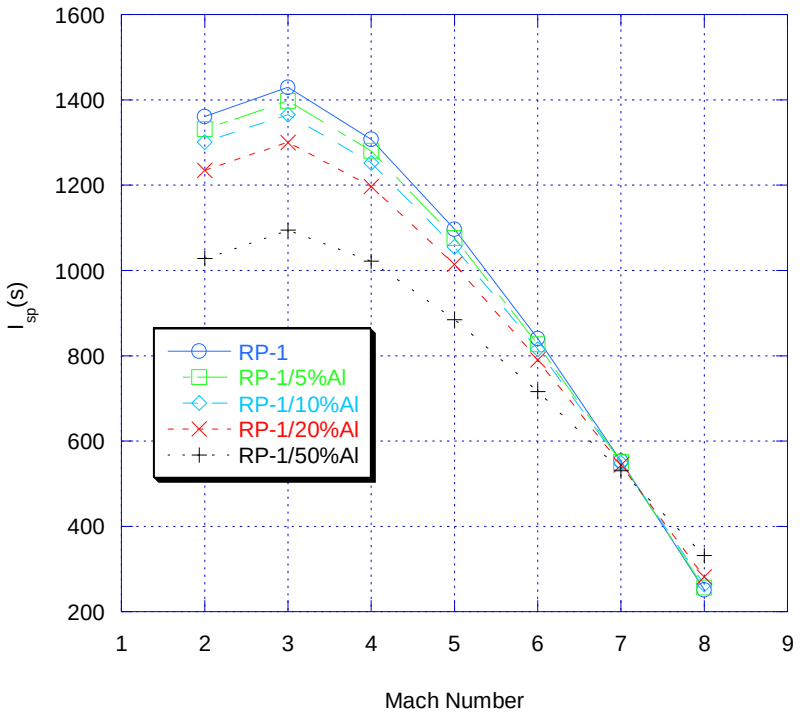

Figure 1.6 I_{sp} of Aluminum Loaded RP-1 Fuels

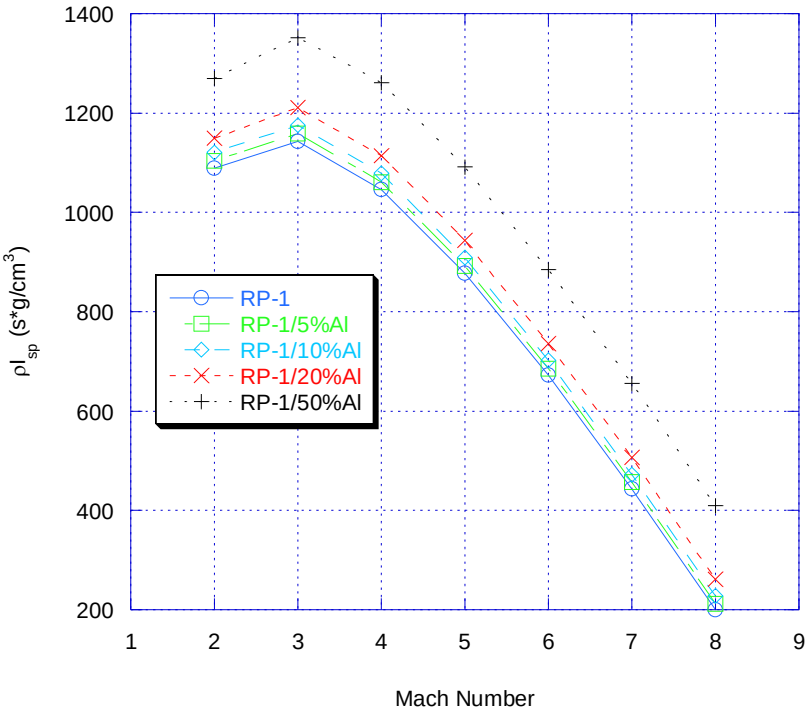

Figure 1.7 ρI_{sp} of Aluminum Loaded RP-1 Fuels

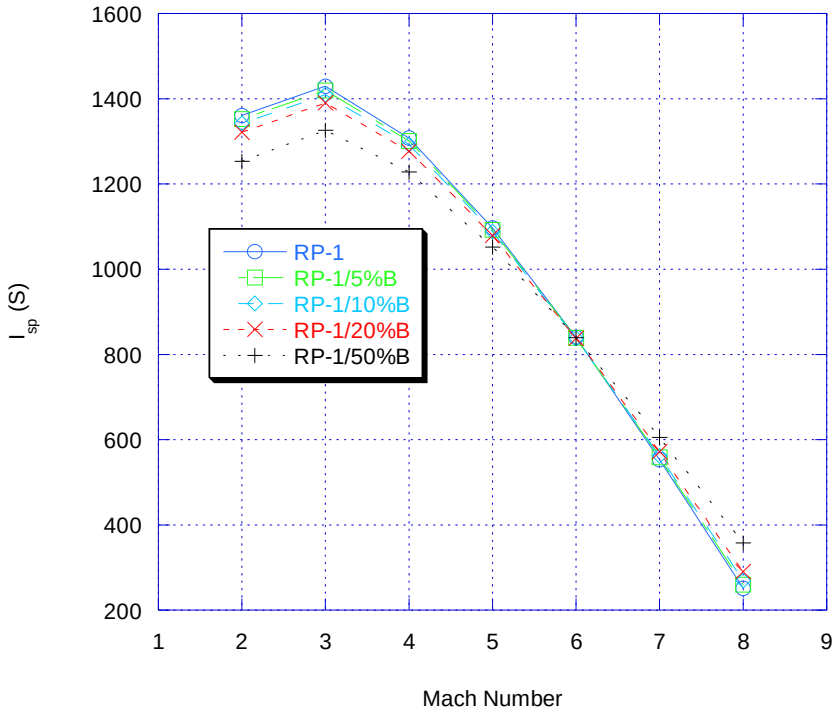

Figure 1.8 I_{sp} of Boron Loaded RP-1 Fuels

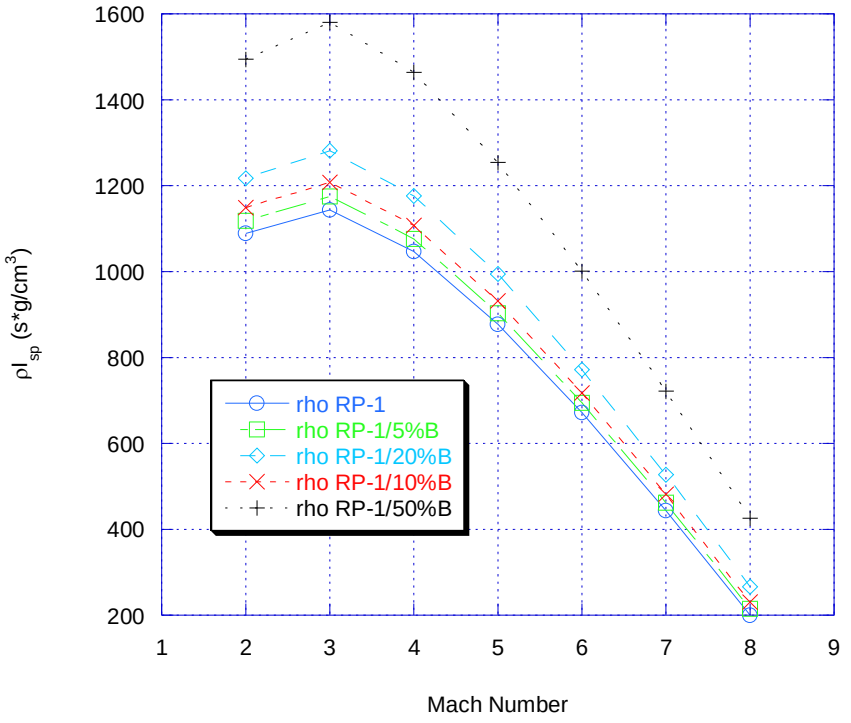

Figure 1.9 ρI_{sp} of Boron Loaded RP-1 Fuels

1.5 Objectives/Goals

The overall goal of this research program was to determine whether metallic nanoparticles could be used as suitable fuels/supplements for airbreathing propulsion systems. Meeting the overall goal was a multi-step process that required completion of a number of sub-tasks or objectives along the way.

The first objective to be met was to develop an experimental approach/technique for evaluating the ignition/combustion characteristics of nanoparticles under various conditions. Once the approach was developed the burning behavior of boron nanoparticles needed to be understood in a controlled flame environment so that fundamental ignition and combustion behavior could be extracted as functions of temperature and gas composition. Parameters such as critical ignition temperature, gas composition, ignition times, and burning times were all to be studied.

Finally, the behavior of both boron and aluminum nanoparticles was to be investigated in a hydrocarbon/air environment simulating ramjet conditions. In order to meet this goal, an airbreathing combustor was to be designed and fabricated in which the performance of metallized fuels could be compared to non-metallized fuels. This also included the design of a simple, reproducible particle injection system.

1.6 Scope

Within this study, the ignition and burning characteristics of boron nanoparticles were studied through both a two-dimensional airbreathing combustor and the post-flame region of a hydrocarbon/air/oxygen flat flame burner. Parameters of interest in this portion of the study include:

1. Minimum temperature and oxygen concentration required for ignition
2. Ignition times as a function of gas temperature and composition
3. Burning times as a function of gas temperature and composition

In addition, the combustion performance of metal nanoparticles laden flows of aluminum and boron were compared directly to a pure hydrocarbon/air analog conditions in order to determine whether or not these particles can be considered as potential fuel additives for high speed airbreathing engines. The metallized fuels are compared directly to analogous ethylene/air tests for fuel performance assessment. A two-dimensional airbreathing combustor was designed and fabricated with optical access for characterization of the combustor under a variety of conditions. The following is a list of parameters under consideration during combustor testing.

1. Combustor inlet velocities ranging from 40 – 70 m/s.
2. Equivalence ratios from 0.5 – 0.7
3. Adiabatic flame temperatures from 1600 K to 2100 K
4. Particle loadings from ~10 – 25% by weight of fuel
5. Nano-sized aluminum versus nano-sized boron particles

1.7 Benefits for commercial applications based upon results of this research

This study assessed the viability of using nanoparticle additives in fuels for airbreathing propulsion systems. The vast majority of studies included in the literature

only consider micron-sized particles as fuel additives. It is quite possible that the use of nanoparticles could allow all or most of the energy to be extracted from the metal additives. This result would be especially encouraging for military applications in which volume limited systems are nearly always utilized.

In addition, this research provided fundamental data on the ignition characteristics nano-sized boron particles in an oxidizing environment containing air/H_2O/CO_2. Burning times were extracted for boron nanoparticles. This data did not previously exist in the literature for boron. Previous studies conducted on nano-sized aluminum showed that nano aluminum behaves differently than traditional micron-sized aluminum particles. For instance, the reactivity of nano-aluminum increases as the particle size decreases. The data shows that nano-aluminum begins to react at lower temperatures than micron sized aluminum. In the case of boron this would be an especially encouraging result given its history of inefficient combustion.

CHAPTER 2

REVIEW OF RELEVANT PREVIOUS STUDIES

2. Review of Relevant Previous Studies

Chapter 2 provides a review of studies relevant to the main theme of the current research.

2.1 Brief Review of Droplet Combustion and the D^2 Law

In many instances of certain metals' combustion regimes, an analogy exists between a metal particle's combustion behavior and that of a liquid droplet, such as a hydrocarbon. If one considers the well known D^2 evaporation law[25] that is commonly used to estimate the diameter of a burning liquid droplet or particle it suggests that:

$$D^2 = D_o^2 - \beta_v t \qquad \text{Eq. 2.1}$$

where: D = particle diameter at time t

D_o = initial particle diameter

β_v = evaporation coefficient

and the evaporation coefficient is defined as:

$$\beta_v = \frac{8\rho_s \alpha_s}{\rho_l} \ln(1 + B) \qquad \text{Eq. 2.2}$$

where ρ_s = solid phase density

α_s = thermal diffusivity of the solid phase

ρ_l = liquid phase density

B = Spalding transfer number

The total burning time, t_b, for the particle is determined by setting the final particle diameter = 0. Therefore the burning time becomes:

$$t_b = \frac{D_o^2}{\beta_v} \qquad \text{Eq. 2.3}$$

Thus, if a similar law could be applied to metal particles, one could easily see how changing the particle size by 1 order of magnitude would decrease burning times by two orders of magnitude, making nanoparticles very attractive when short combustor residence times apply.

2.2 Metal Particle Combustion

In Chapter 1, the great potential of using of metals in propulsion systems was demonstrated in terms of specific impulse and density impulse. Metals possess desirable combustion characteristics such as high heats of combustion or energy release and good physical properties such as density[26,27]. For example the relatively high densities of metals increase the performance of solid propellants and fuels, which, in turn increases the performance of a propulsion system for the same volumetric capacity. Metals were first added to solid propellants in the 1950's when it was found that the addition of aluminum particles substantially increased propellant performance[26,28,29]. Around the same time period, metals were being considered for fuels in ramjets[30]. Aluminum, boron, magnesium, zirconium, and beryllium have all been considered as fuels or fuel additives.

Aluminum is perhaps the most widely used metal as an additive in propellants and fuels. Boron provides the highest energy per unit volume of all elements. However, the inability to extract all of its available energy in reasonable time frames has limited the use

of boron in propellants and fuels. Although beryllium is second to boron in terms of energy per unit volume, the use of beryllium has not been seriously considered due to its extreme toxicity[7]. Even though magnesium and zirconium have each been considered, as Figure 2.1 shows, they both have lower heats of combustion than aluminum in terms of both mass and volume. Therefore, between the difficulty in fully combusting boron in reasonable combustor residence times, beryllium's toxicity, and energetic considerations, it is easy to see why aluminum has been the most widely used metal in fuels and propellants.

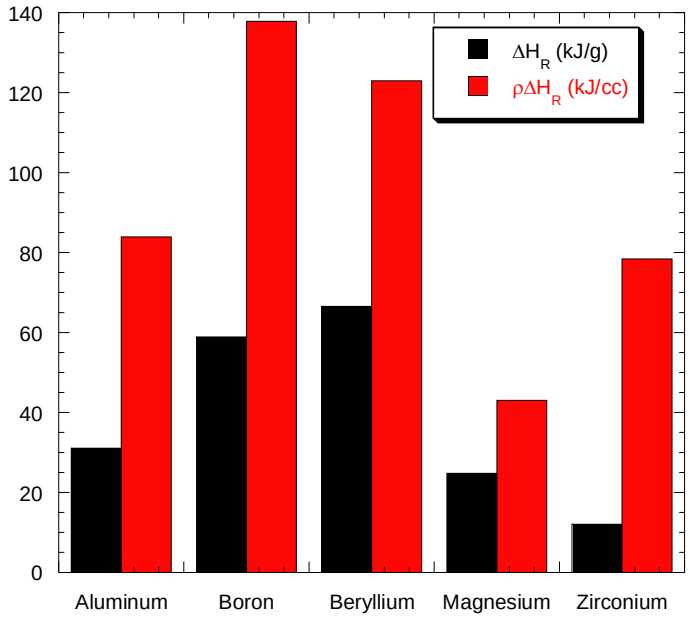

Fig. 2.1 Comparison of Heats of Combustion of Selected Metals

The combustion of metals in oxygen is typically classified by the way the metal is first oxidized to its smallest oxide[31]. This process can either occur with the metal and oxidizer in the gas phase (vapor-phase reaction) or with the metal as a condensed phase (heterogeneous reaction)[31]. Heterogeneous reactions occur at the interface of two

different substances for different phases such as gas-solid or gas liquid interfaces[31]. The determination of which metals burn in a heterogeneous combustion mode can be made by evaluating the thermodynamic and physical properties of the metal and its oxide. A unique feature of metal burning in oxygen is that the flame temperature developed is a specific known value – the vaporization-dissociation or volatization temperature of the metal oxide product[29]. This can be attributed to the physical fact that the heat of vaporization-dissociation or decomposition of the metal oxide formed is greater than the heat available to raise the condensed state oxide above its boiling point. For a metal to burn in the vapor phase the oxide volatization temperatures must be greater than the temperature of the metal boiling point; this is known as Glassman's Criterion[29].

Yetter and Dryer[31] summarize the criteria for determining metal combustion classification as follows:

1) Does the available energy exceed the energy required to heat and volatize the final metal oxide?
2) Does the available energy exceed the energy required to heat and vaporize the metal itself? With sufficient energy the combination of a volatile product and a volatile metal indicates that the metal will burn much like a hydrocarbon droplet.
3) Intersolubility of the metal and its product is also relevant to combustion behavior – for volatile metals, certain solubility combinations are known to lead to disruption and breakup of the original particle. For nonvolatile metals, purely condensed phase combustion may result.

Despite all of the particle combustion studies throughout the literature, studies of single nano-sized particle combustion are limited. There is no data in the literature on single particle nano-sized boron. Most of the studies involving nanoparticles utilize bulk sample techniques, which will be described in subsequent sections.

2.2.1 Aluminum Combustion Fundamentals

Aluminum is of great interest for propulsion applications and has been the subject of many studies since it was first discovered that the addition of aluminum increased the performance of solid propellants. According to Glassman's Criterion[29], aluminum will burn in the vapor phase since its boiling point (2791 K) is lower than the oxide volitization temperature (4000 K). As shown in figure 2.2, Price provides an excellent description of the fundamental processes in aluminum droplet combustion[27]. In this particular portrayal, Price describes the process of an aluminum droplet combusting in a mildly convective flow. Unless the particles undergo some special processing, all aluminum particles start out with an impervious oxide (Al_2O_3) layer around the solid aluminum core, which covers the entire exterior surface of the particle. This oxide layer is typically between 2 to 5 nm. Ignition of the particle is thought to occur when the oxide layer is broken down to expose pure aluminum and the oxidative reactions are vigorous enough to induce a progressive temperature rise. The breakdown of the particle oxide can occur in two ways. The first way is due to the fact that the melting temperature of aluminum oxide (2327 K) is much higher than that of pure aluminum (930 K). As the particle is heated, the molten aluminum expands and creates thermal stresses inside the oxide shell, which could damage the shell exposing pure molten aluminum to the

oxidizing species. The other possibility is that the oxide layer undergoes melting itself, which would require much higher temperatures for ignition.

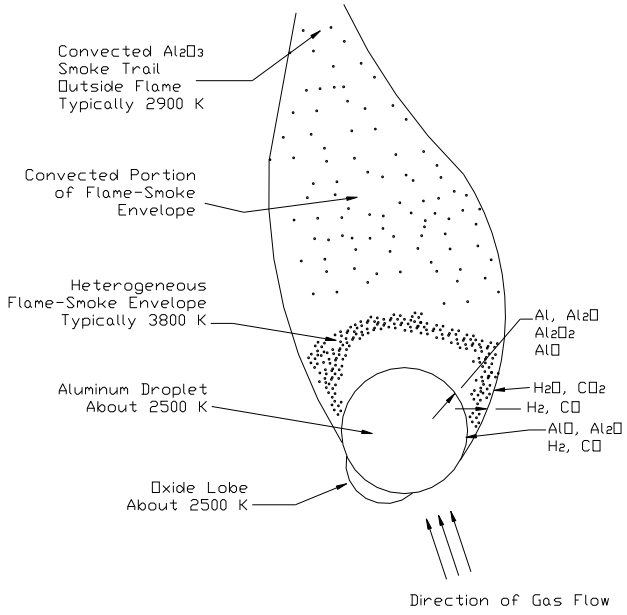

Fig. 2.2 Schematic of an Aluminum Droplet Burning in a Mildly Convective Flow[27]

According to Price[27], following ignition the particle temperature is at approximately 2500 K, with a residue of molten "retracted" oxide on the surface and a detached flame envelope. The temperature is constrained by the oxide melting point and the aluminum boiling point. Because the oxide melting temperature, 2327 K, is higher than the melting temperature of aluminum, 930 K, the aluminum is assumed to be fully melted upon ignition.

The physical processes associated with the various stages of aluminum particle combustion are depicted in figure 2.3[32]. As Price[27] points out, the aluminum particles have a characteristic oxide coating that must be melted or cracked before the particle can ignite. Although the global oxidation reaction of aluminum produces alumina, Al_2O_3,

many suboxides such as AlO, AlO_2, Al_2O_2 exist in the flame zone, with AlO as the most prominent[28]. The condensation of alumina at its estimated boiling point, ~3800 K, sets the approximate temperature of the oxide cloud because Al_2O_3(l) condenses directly from the association of suboxides and the idealized gaseous form, Al_2O_3(g), immediately dissociates back into AlO and O_2[33] as shown in figures 2.2[27] and 2.4[28]. Thermochemical calculations support the concept of a limiting or constant temperature[29].

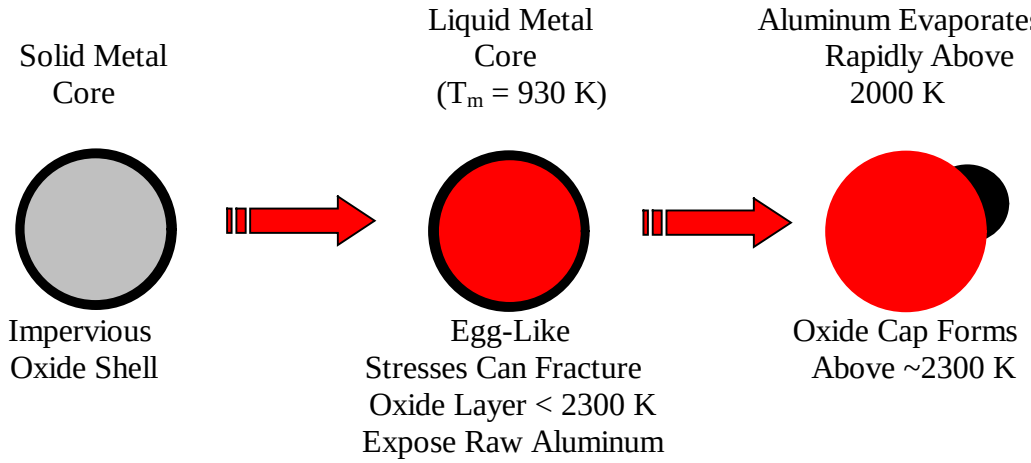

Fig. 2.3 Physical Stages of Aluminum Particle Ignition and Combustion[32]

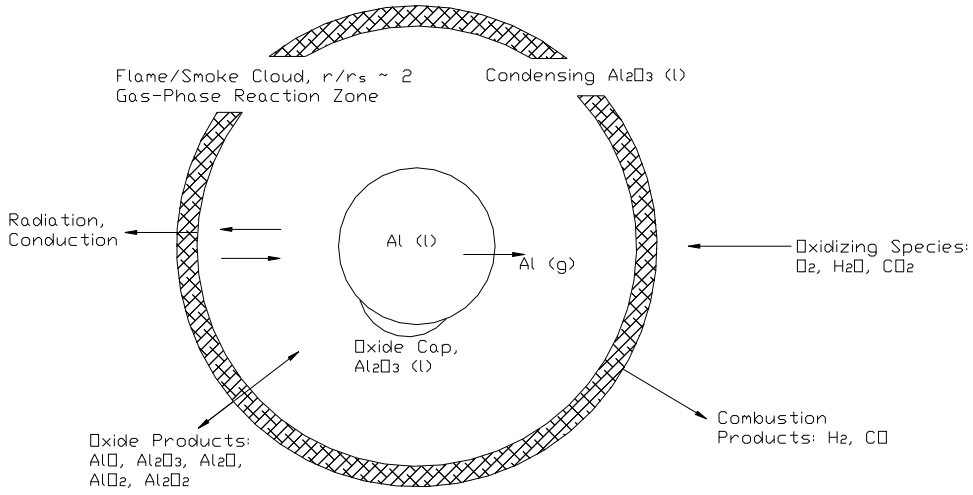

Fig. 2.4 Schematic of Aluminum Particle Combustion by Melcher[28]

The temperature of the system remains constant at the boiling temperature of aluminum oxide because enthalpy changes in the total system are absorbed in the condensation of the aluminum suboxides or in the decomposition of the liquid aluminum oxide[31]. As the particle is heated to the melting temperature of aluminum the solid aluminum begins to change phase, which results in the particle becoming egg-like. At the same time, the oxide shell restricts the molten aluminum from being exposed to the hot environment. If the particle is heated slowly, the oxide shell will grow in thickness around the pure aluminum core[32]. As the temperature of the oxide layer increases beyond 2300 K, the molten aluminum oxide coalesces and forms a pool commonly known as an "oxide lobe". This exposes the pure aluminum, which can now readily evaporate and is available for reaction with the surrounding environment. Even though the boiling point of aluminum is 2767 K, Beckstead[32] suggests that aluminum readily evaporates above 2000 K. Above 2767 K, the molten particle material will boil violently and begin to fragment. Studies have shown that the residuals from quenching aluminum particles form hollow spheres[34]. The flame zone is characterized as homogeneous since the reactions are aluminum vapor and gaseous oxygen. The actual aluminum/oxygen flame zone is characterized by a luminous detached flame of approximately 3800 K, which is expected since the saturation temperature of Al_2O_3 is about 3800 K. Since the aluminum oxide decomposition process is endothermic, the flame temperature is not affected.

2.2.1.1 Aluminum – Single Particle Measurements

There have been numerous studies involving the combustion of a single aluminum particle, nearly all of which dealt with micron-sized or larger particles. Most

of the studies have sought to identify burn times and or ignition temperatures of single particles. In general, there is a significant amount of scatter in the published data. Beckstead attributes this scatter to the different techniques used to obtain the data and the lack of a standard definition for the burning time[34]. By and large, there were only a few types of experiments conducted; 1) propellant ignited particles, 2) gas burner ignited particles, 3) laser ignited particles, and 4) shock tube ignited particles. Parameters of interest include oxidizer types/concentrations, pressure, and ambient temperature.

Friedman and Macek[35,36] and Macek[37] provide some of the first reported burning time data for aluminum particles. Burning times and ignition delays were deduced from particle streak images. They used propane or carbon monoxide flat flame burners to ignite particles ranging from 15-70 μm. In these experiments the effect of fuel did not play a large role in burning times. However, testing in both burners produced a fine oxide smoke and porous or hollow spheres, which were more numerous in the propane flame which contained water in the products as a potential oxidizer. In addition they noted that the particles would fragment and combust vigorously in oxygen rich environments. Friedman and Macek concluded that in their experiments, ignition of the aluminum particles only occurred at temperatures corresponding to the melting of the oxide layer (2300 K).

There were many other experiments similar to those of Friedman and Macek's including studies by Davis[38], Drew[39], Turns[40], Olsen[15], and Foelsche[41] just to name a few. Davis[38] used a carbon monoxide flame to ignite particles that ranged from 53 to 66 μm. From a set of images, Davis found that the particle's flame front was several diameters larger than the particles themselves, which was evidence of vapor-phase combustion. In

addition, Davis witnessed a fine trail of smoke in the particles wake, which was determined to be alumina, further evidence of gas-phase oxidation. Davis also determined that particle fragmentation increased for any oxygen concentration over 32% by volume, and concluded that the ambient oxygen concentration was more important to particle combustion rate than the ambient temperature.

Turns[40] created slurry droplets with diameters ranging from 500 to 1100 μm by adding aluminum powder to JP-10 jet fuel. The droplets were suspended on silicon carbide fibers and then suddenly exposed to the hot exhaust gases of carbon monoxide or methane flames. Using high-speed cinematography, Turns observed that the vapor-phase flame front was smaller with the methane flame, which included vapor phase water in its products, when compared to the 'dry' environment of the carbon monoxide flame. Furthermore, Turns also witnessed the fragmentation of particles in the 'wet' environment.

Olsen[15] used a carbon monoxide/hydrogen/oxygen diffusion flame to ignite particles ranging from 40 to 80 μm. A photomultiplier tube was used to record the combustion event. During some experiments, Olsen interrupted combustion and quenched the particles for examination using Scanning Electron Microscopy (SEM) and X-Ray analysis. He found that the oxidizer concentrations in his study, H_2O, CO_2, and O_2, played a large role in the burning time of the particle. Olsen suggests that if one considers the particle burning rate to follow the famous D^2-law, that the burning rate exponent changes during the combustion event, likely starting at 2 during ignition and decreasing towards burnout. The decreasing burning rate is due to the increasing fraction of aluminum oxide covering the molten aluminum.

Foelsche[41] used photodiodes to measure the burning time of a small cloud of aluminum powder (~22 μm) inside a combustion bomb with the pressure ranging from 38 to 145 atm, at 2630 K. The combustion bomb used nitrogen diluted premixed H_2/O_2 mixtures to create a high-pressure, constant volume environment in 20% excess oxygen concentration. Foelsche[41] monitored the emission of AlO, a gas-phase intermediate in aluminum oxidation as a means of monitoring the burning time. Since Al_2O_3 was not expected to dissociate much at 2630 K, once all of the aluminum was consumed, the source of AlO(g) was also consumed. The data obtained showed a trend of decreasing burning times with increasing ambient pressure. Foelsche found that for the 22 μm particles that the burning time as a function of pressure could be expressed by a power law with an exponent of –0.55.

Bucher[42,43] used a 150 W laser to ignite aluminum particles (230 μm) in pure N_2O, pure CO_2, and in mixtures of O_2, N_2, Ar, and He. In-situ temperature and species distributions around individual burning particles were made using planar laser-induced fluorescence. The study found that the flame diameter around a particle decreased with varying environment gas mixture in the following order: O_2/Ar, O_2/N_2, CO_2, and N_2O. AlO was found to be an intermediate species in the combustion reaction while for the first time the presence of aluminum-oxy-nitrides was established. The measurements confirmed the idea that the aluminum oxide's boiling point limits the flame temperature.

Olsen[15] summarizes the majority of the available data on aluminum single particle experiments at atmospheric pressure. Typical burn times range from about 2 to 30 milliseconds for particles ranging from 10 – 100 μm. Aluminum combustion can be though of in much the same way as a hydrocarbon fuel droplet. With that in mind, most

of the studies on aluminum combustion have attempted to correlate the particle burning times with the "D^2 Law". Beckstead[34] provides an excellent summary of the studies on aluminum combustion in which he attempts to correlate a significant portion of the data available in literature. He proposes the following correlation for burning times of single particles:

$$t_b = \frac{aD^n}{X_{eff} P^{0.1} T_o^{0.2}} \qquad \text{Eq. 2.4}$$

where the pressure is given in atmospheres, temperature in Kelvin, diameter in μm, time in milliseconds, and X_{eff} is an effective oxidizer concentration. X_{eff} takes into account the effects of concentration of carbon dioxide, water vapor, and oxygen:

$$X_{eff} = C_{O_2} + 0.6C_{H_2O} + 0.22C_{CO_2} \qquad \text{Eq. 2.5}$$

a and n are constants with the following possible values:

a = 0.0244 for n = 1.5 or

a = 0.00735 for n = 1.8

Using this correlation figure 2.5 is obtained for a single particle burning in a 2000 K, 1 atmosphere environment of air. The data in the figure has been extrapolated far below the range of diameter from which the correlation came from. This was done only as an exercise to provide an estimate for burning time of particles on the nano-scale. If the correlation is extrapolated into the nanometer regime, the correlation gives burning times on the order of microseconds for a 100 nm particle.

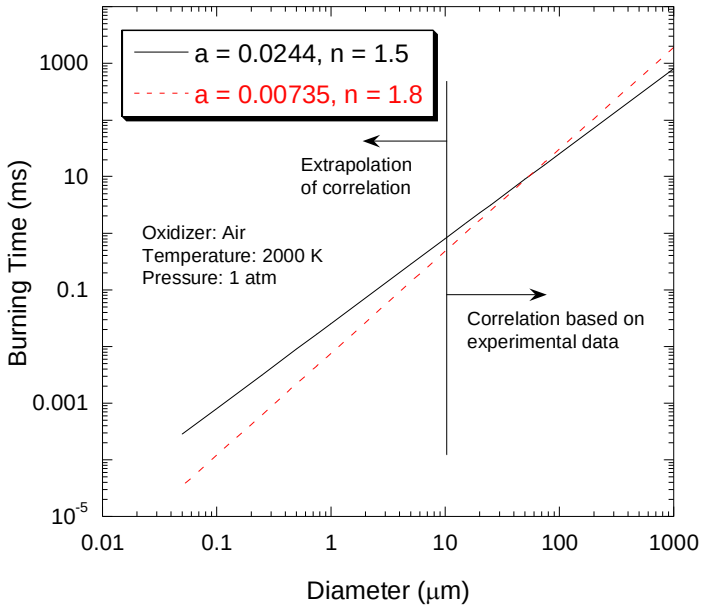

Fig. 2.5 Burning Times of Single Particles Using Beckstead's[34] Correlation

2.2.2 Boron Combustion Fundamentals

Nearly all of the studies involving boron combustion in current literature have been performed with micron-sized particles. Boron has been studied for many years because of its theoretically high energetic potential as demonstrated in figure 2.1. However, in most cases the theoretical performance output of boron-based fuels has not been met. The two major reasons why overall propulsion system performance may be reduced when using boron are; 1) the ignition of boron particles is significantly delayed due to the presence of an oxide layer on the particle surface, and 2) the energy release during the combustion process of boron particles in hydrogen containing gases is significantly lowered due to the formation of HBO_2[44].

Ulas and Kuo[44] claim that the combustion of boron particles is defined by a two-stage process. The first stage of boron combustion was considered as the removal of the

oxide layer. This oxide removal process is a slow, kinetic and/or diffusion controlled process, which constitutes a significant portion of the overall burning time of the particle. After removal of the oxide layer, the second stage begins with the actual combustion of the pure boron material. The full energy release of boron occurs when the final products condense to $B_2O_3(l)$, which is thermodynamically favored below 2400 K[44]. In hydrogen containing environments, the formation of HBO_2 severely inhibits boron combustion. The conversion of $HBO_2(g)$ to $B_2O_3(l)$ in an oxygen and hydrogen atmosphere is slow; thereby reducing the rate of energy release. Figure 2.6, adopted from Beckstead[45], shows the basic physical processes for boron ignition and combustion. Similar to aluminum, the boron particle has a thin oxide layer, which surrounds a pure boron core. The boron oxide shell however, melts at a much lower temperature (722 K) than alumina. According to Glassman's criterion[29], since B_2O_3 has a volatization temperature of 2340 K, and boron's boiling temperature is 4139 K, boron will not burn in the vapor phase.

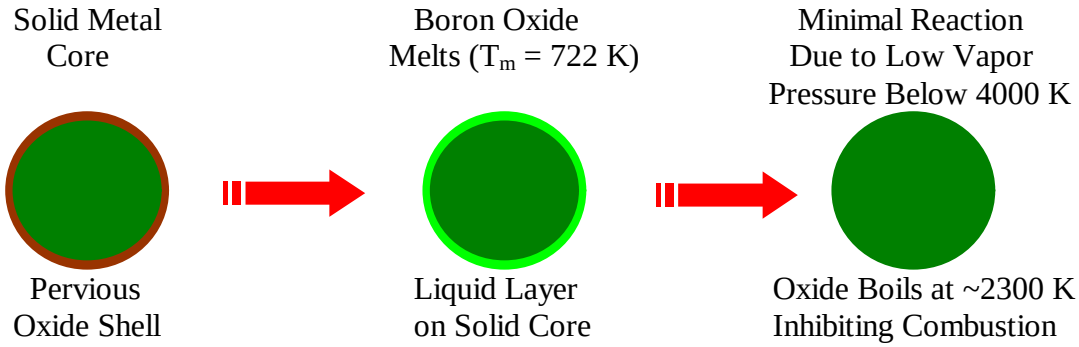

Fig. 2.6 Physical Stages in Boron Ignition and Combustion[45]

As the temperature of the particle rises, the oxide shell melts and forms a liquid layer on the surface; during this time some of the oxide vapor begins to diffuse into the gas phase. The combination of the liquid and vapor phase oxide layer forms a significant

diffusive barrier between the oxidizing environment and the pure boron core, which inhibits oxidation of the pure boron. This stage of combustion is diffusion limited since the diffusion rates are slow compared to the kinetic rates. As the particle is heated further to ~2300 K the oxide layer becomes completely vaporized and the boron begins to melt. The low vapor pressure of boron at this temperature prevents the particle from evaporating below its boiling point. Now the oxidizer can more easily diffuse to the surface than before because the oxide layer is entirely in the vapor phase. This may reduce the oxidizer diffusion time to less than that of the kinetic reaction time, shifting the burning rate limiting mechanism from the diffusion regime into the kinetic regime depending on the environment and particle size.

Because of the potential for a shift in the controlling mechanism once ignition is complete and full-fledged combustion is achieved, each regime may also establish its own distinct physical processes. The diffusion-limited regime tends to create pronounced species and thermal spatial gradients at the surface of the particle, in the oxide layer, and in the oxidizing environment surrounding the particle[50]. The species gradients promote reactant diffusion towards the surface and product diffusion away from the surface, while the thermal gradients encourage heat transfer from the flame zone towards the particle.

After the initial stage of combustion, the boron particles may end up in a kinetically controlled regime. In this case, the spatial species and thermal gradients become less influential on the burning rate. Now, the controlling mechanism is the reaction rate to the individual heterogeneous kinetic reactions at the particle surface. The primary overall surface reaction occurring at this point is:

$$2B_{(l)} + O_{2(g)} \rightarrow B_2O_{2(g)} - 110 \text{ kcal/mole}$$

A large majority of the surface reactions follow one of two paths to the overall reaction depending on the water content in the oxidizing environment. These are shown in figure 2.7[45].

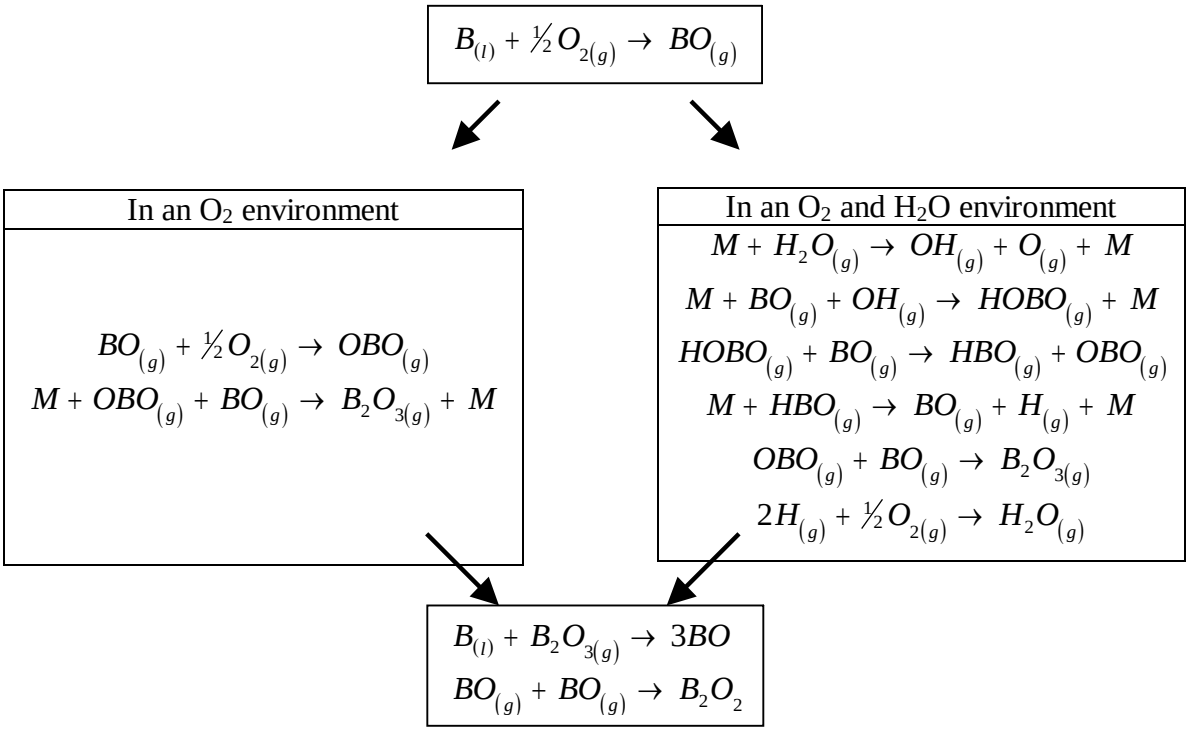

Fig. 2.7 Elementary Heterogeneous Reactions Associated with Boron Particle Oxidation

One way to determine the dominate regime during the particle combustion is through the Damkohler number, which is defined as the ratio of the diffusion burn time to the kinetic burn time[46].

$$Da = \frac{t_{b,diff}}{t_{b,kin}} = \frac{M_B k P d_o X_{o_2,\infty}}{4\rho D \ln\left(1 + iY_{o,\infty}\right)} \qquad \text{Eq. 2.6}$$

where M_B is the molecular weight of boron, k is the thermal conductivity, P is the pressure, do is the initial diameter of the particle, X_{O2} is the ambient mole fraction of

oxygen, ρ is the density of boron, D is the diffusivity Y_{O2} is the ambient mass fraction of oxygen. The Damkohler number compares the controlling rate mechanisms and offers insight into there dependency. For example, large particles combusted at high pressures (Da > 1) will tend to be diffusion rate limited, while small particles at lower pressures (Da < 1) will be kinetically dominated.

2.2.2.1 Boron - Single Particle Experiments

A number of studies have been conducted on single boron particles[46-51]. Macek[47-49] provides some of the first single particle combustion measurements for boron. Similar to their aluminum particle experiments, Macek[47] examined single particle combustion of crystalline boron powder ranging from roughly 35-45 μm in the products of carbon monoxide or propane and oxygen flames. Macek found ignition temperatures to be consistently in the rage of 1850-2000 K and goes on to describe a two-stage combustion process. During the first stage the particle ignites and burns brightly for a short period of time, then becomes extinguished, and finally reignites to burn to completion in the second stage. During the second stage, the particle burns brighter and longer. In addition they studied this two-stage phenomenon spectroscopically and found that both BO and BO_2 were present in both stages. They also found that boron particles required four times as much time to complete their combustion than similar sized aluminum particles in similar environments. Macek[47] also observed that the burning times decreased with increases in ambient gas temperature and oxygen mole fraction. Finally they observed that particle burning times decreased in the presence of water vapor.

In another experiment, Macek[48] investigates the effect of pressure and oxidizer on the burning time of 75 μm crystalline boron particles at 2000 K. The particles were ignited by laser ignition. In this study they found that the burning time of a particle in air and in an oxygen/argon environment decreased from about 45 milliseconds to about 20 milliseconds when the pressure was increased from 1 to 35 atmospheres. In pure oxygen they deduced burn times of only 6.8 milliseconds. Finally, Macek[48] found that in a pure carbon dioxide environment and an oxygen depleted environment of 7% O_2 and 93% N_2 that a steady state combustion is never achieved. Furthermore, the particles could only be brought to a burning regime by an external energy heat flux, and that the burning regime could only be maintained for a brief period before the particle extinguished.

Yeh and Kuo[46], provide a very detailed summary of boron particle combustion testing up to 1996. In addition, they conducted a series of experiments of 2-3 μm amorphous boron powder and 3 μm crystalline boron particles in the post flame region of a flat flame burner. Similar to Macek[47], they found that the particles burned in two-stages. In addition, Yeh and Kuo[46] found through environmental scanning electron microscope (ESEM) images that at elevated temperatures the diffusion of dissolved boron into molten B_2O_3(l) dominates the diffusion of gaseous O_2 through the B_2O_3(l) layer. Dissolution of solid boron into the boron oxide layer caused liquification of boron particles at relatively low temperatures (940 ^oC). X-ray diffraction analysis showed that the surface characteristics of boron particles changed from a crystalline to an amorphous structure after heating to 940 ^oC, meaning that the B_2O_3(l) layer lost its identity at elevated temperatures. Finally, Yeh and Kuo constructed a theoretical model in which they demonstrated that the product of the pressure and particle diameter determined

which burning regime that the particles were under during the second stage of combustion. For example, for Pd << 75 atm-μm, the second stage was dominated by chemical kinetics, for Pd ~ 75 atm-μm, both diffusion and kinetics play large roles, and finally for Pd >> 75 atm-μm, the second stage combustion was dominated mainly by the diffusion of oxygen.

Ulas[44] performed studies on 1 μm amorphous and 3 μm crystalline boron particles in the exhaust of a flat flame burner, similar to the aluminum studies discussed earlier. The flat flame burner combusted mixtures of methane, oxygen, nitrogen trifluoride, and nitrogen. Ulas monitored particle streaks and deduced burning times. He found that in the presence of fluorine, boron does not exhibit the two-stage burning phenomenon observed in non-fluorinated environments. In addition, the presence of hydrofluoric acid (HF) increased the overall burning time of the particles, while atomic fluorine reduced burning times significantly compared to non-fluorinated environments.

Foelsche et. al[51] examined the effects of pressure (30-150 atm.), temperature (2440-2830 K), and excess O_2 concentrations on the burning properties of 24 μm boron crystalline particles in a constant volume combustion bomb using $H_2/O_2/N_2$ mixtures to create the environement. In this study, they found that particle ignition delays were reduced with increased pressure, decreased particle size, and increased temperature. As an example, they found that the ignition delay could be correlated to a power law with an exponent of –0.5. In addition Foelsche examined the effects of two proposed ignition enhancing agents and found that neither CO_2 nor HF reduced ignition delay, and that HF actually increased the ignition delay. Burn times were measured by monitoring the emission of BO_2 which is a reactive intermediary gas-phase species formed through

particle ignition and combustion. According to gas phase modeling studies conducted by Yetter[52], $BO_2(g)$ gets converted to $B_2O_3(g)$ or $HBO_2(g)$ products quickly depending on how much water vapor is present. Therefore, once the source of B/B_2O_3 was consumed, then so was the source of $BO_2(g)$ as well. The BO_2 spectrum is readily observable during both the ignition and combustion stages[53].

2.3 Metal Combustion in Air breathing Engines

As was demonstrated in Chapter 1, metal additives can potentially provide great benefits for air breathing propulsion systems. The benefits arise mainly in the form of energy density for volume limited systems. Pure metals or the addition of metals to more conventional fuels generally increase the energy density of a fuel over non-metallized fuels. For that reason, there have been numerous studies incorporating them into fuels mainly for solid fuel ramjet or ducted rocket applications. Metals have been considered as fuels or additives to fuels in air breathing propulsion systems since the 1930's when the then Soviet Union successfully flight-tested a tandem boosted ducted rocket using a magnesium/aluminum solid fuel[2].

Magnesium, aluminum, boron, and combinations of each have been considered most often for airbreathing engines. For reasons described earlier aluminum and boron have received the most attention. However, magnesium has drawn interest despite the fact that it cannot match the theoretical output of aluminum and boron because it is known to ignite at low temperature and to burn well even at low pressure and low air/propellant ratio[54].

In the 1950's[30] NACA performed a research program utilizing aluminum as the sole fuel. They tested a two inch diameter ramjet engine using both powdered aluminum and wire aluminum as the fuel source and measured combustion efficiencies of about 75% over a wide range of fuel/air ratios at relatively low combustor inlet velocity of 35 m/s (115 ft/s).

Schadow and others[55-57] experimented with boron-based fuels in ducted rocket applications with boron loadings up to 55% by weight. Typical particle sizes ranged form sub-micron to 3 μm. In some cases[55] the experiments were conducted with the boron in a fuel rich solid propellant matrix and in others, the boron was introduced to the combustor in particle form by a carrier gas[56,57]. In these experiments relatively high combustion efficiencies (greater than 90%) were only achieved when local gas temperatures exceeded 2000 K. In fact, Schadow[57] suggests that a minimum temperature of 2300 K is required for very efficient combustion of boron particle laden flows. This temperature corresponds to the melting temperature of boron and the boiling temperature of boron oxide.

Gany et. al[58,59] have examined the combustion characteristics of boron-based solid fuels in a typical SFRJ setting. Gany[58] suggests that part of the problem in achieving efficient combustion of boron in a SFRJ setting can be attributed to the manner in which the material is ejected from the condensed fuel surface to the gas flow. More specifically, the ejection is often irregular with large fragments of uncontrollable dimensions and velocities entering the gas flow. Furthermore, the gas flowfield in SFRJ's is typically characterized by non-uniformities of temperature and species concentrations, which hamper the ignition, and sustained combustion of boron particles

within the combustor. As a means of promoting more efficient ignition and combustion Gany proposes the use of bypass air[58,59] and possibly the use of other additives such as titanium[58]. By including an additive such as titanium, Gany[58] suggests that one can take advantage of the exothermic reaction between titanium and boron to enhance particle preignition rates leading to shorter ignition delays.

More recently, Gany[60] provided a detailed account of the difficulties in achieving efficient boron combustion and their implications in air breathing engines. There are a number of contradictory necessities to achieve efficient combustion. For instance, high temperatures are required for ignition and sustained combustion of boron. However, as Gany points out, the most energetic output of boron combustion occurs when the final product is B_2O_3(l), yet at high temperatures above about 2300 K (the boiling point of B_2O_3) combustion would yield gaseous B_2O_3 whose heat of formation is about 1/3 that of liquid phase B_2O_3. Furthermore, combustion in hydrogen containing environment ultimately leads to the formation of HBO_2(g) whose heat of formation is about 60 times less than B_2O_3(l). Conversion of HBO_2(g) to B_2O_3(l) is very slow, so in combustors with relatively short residence times, formation of B_2O_3(l) is unlikely to occur. Gany[60] calls this phenomenon an “energy trap”.

2.4 Nanoparticle Work

The majority of work to date on nanoparticles has involved testing of bulk samples. A few burning time measurements of nano aluminum have been made[16,17], but the measurements do not guarantee single particles and are more likely agglomerates. Son[61] studied the combustion of nano aluminum in air. In one experiment, Son used a

combustion chamber made of Plexiglas, to combust a "pile" of aluminum at atmospheric pressure in air, nitrogen, nitrogen and argon mixtures, argon and oxygen mixtures, and pure oxygen environments. In another experiment, he studied the ignition requirements of nano aluminum using a laser. He found that the nanoaluminum was much easier to ignite than micron-sized aluminum, and that it readily self deflagrated in air. In addition, the nano aluminum exhibited a two-stage burning phenomenon in air. Son determined the first stage to be surface burning and the second stage to be a bulk reaction. They also found that when burned in air, nano aluminum reacts with oxygen and nitrogen to form oxides, nitrides, and aluminum oxynitrides. Finally, Son found that it was possible to burn the nano aluminum in a nitrogen/argon environment where aluminum nitrides are formed.

Parr[16] studied the ignition delay, burning times, and ignition temperatures of several different types of particles including nanoaluminum in the post flame region of a hydrogen-oxygen-argon Hencken Burner, such that the oxidizing environment was water vapor alone. They estimate that the nanoaluminum agglomerates to about 2 μm as it is introduced into the test section. Their results show that the ambient temperature has a pronounced effect on the burning time and ignition delay. However, of interest is that below about 10 μm the ignition temperature decreases with decreasing particle size, where as "normal" micron sized aluminum generally ignites near 2200 K. In fact, the lowest ignition temperature measured was only 1075 K. Although the nanoaluminum was somewhat agglomerated, typical burning times were less than 1 millisecond at ~2000K, which is significantly lower than burning times of micron sized aluminum, yet

much longer than one could extrapolate from the D^2 type dependence implying that kinetic limited burning is beginning to dominate over diffusion limited burning.

Bazyn[17] investigated reaction times and temperatures of nanoaluminum particles burning in the reflected shock region of a shock tube. He deduced burning times by monitoring the broadband emission of light because under most conditions molecular emission of AlO was not observed. They found that reactions of aluminum occurred at temperatures as low as 1200 K, and that burning times were on the order of tenths of milliseconds.

Park et. al. [24] provides the only true single particle oxidation data of nanoaluminum available in the literature today. In this study, Park oxidized aluminum particles that were either created in situ by a DC arc discharge or laser ablation, or were obtained commercially in an aerosol flow reactor in temperatures up to 1100 ^{o}C. They size selected particles with a Differential Mobility Analyzer (DMA), to send a monodisperse aerosol through the reactor and monitored changes in the particle with a Single Particle Mass Spectrometer (SPMS). Park found that the reactivity of the aluminum particles was enhanced as the particle size decreased. They also found that the reaction rates of single particles were much different than those measured by bulk techniques such as thermal gravimetric analysis (TGA) and that they were consistent with an oxide diffusion controlled rate limiting step.

2.4.1 Nanoparticles in Propulsion

A number of studies have been conducted on utilizing nanoparticles in propulsion systems[21-23,62]. Mordosky[21] studied the potential of nano aluminum for gel propellant

rocket engines. The nano aluminum was gelled with RP-1 and combusted with gaseous oxygen. The purpose of the study was to demonstrate a system similar to a liquid rocket engine, but with a high energy density fuel for greater performance in volume limited systems. In addition, Mordosky[21] suggests that by gelling a propellant one can increase the safety of the vehicle since the possibility of leakage would be negated. Mordosky, incorporated the nano aluminum in the fuel in quantities up to 55% by weight. Some measurements of c* (characteristic exhaust velocity) efficiencies of greater than 90% were made. Furthermore, the c* efficiencies were typically higher than those achieved by Palaszewski[20] using micron sized aluminum. This suggests great promise for the use of nano aluminum in gelled propellants.

Risha[22] investigated the effects of several different types of nano particles on the fuel regression rate in a hybrid rocket engine. The nano particles studied include several different types of aluminum, boron, and boron carbide. He created numerous fuels with varying amount of nano particles added to a hydroxyl terminated polybutadiene (HTPB) solid matrix and compared regression rates as well as c* efficiencies of the fuels to the baseline fuel which was just plain HTPB. Risha found that the majority of the fuels tested with nano particles exhibited an increase in the linear regression rate of the fuel compared to the plain HTPB fuel. This is a very important outcome since one of the major downfalls of the hybrid rocket motor is the typically low regression rate of the fuels. He attributed the increase in regression rate to the increased energy release of the particle near the surface of the fuel. In nearly all of the cases, the measured c* efficiencies were comparable to the baseline HTPB fuel, with boron and boron carbide typically showing the lowest efficiencies.

Palaszewski[23] investigated the potential of nano aluminum gelled with JP-8 as a fuel for a pulse detonation engine. Metal loadings between about 5 and 25% by weight were studied. Palaszewski demonstrated combustion without the addition of oxygen with loadings between 12 and 18% by weight. Again, this is an important finding because by creating a more volumetric energetic fuel, one can improve the performance of systems that are volume limited.

In a set of strand-burning studies, Mench[62] investigated the effects of nano aluminum on the burning rates of solid propellants. The study essentially looked at two identical solid propellants with 18% by weight aluminum: one with micron-sized aluminum, and the other with 50% of the micron aluminum (i.e. 9% by weight of the overall formulation) replaced by nano aluminum. The study found that addition of the nano aluminum increased the burning rate of the propellant by 100%. Increasing the burning rate of a solid propellant can increase the thrust of a rocket motor, allow for a more compact design, or allow the grain design to be optimized in such a way as to improve the mass fraction.

2.4.2 Advantages and Disadvantages of Nano-Sized Particles

In combustion applications, the ignition and burning times of single particles is directly related to the initial particle size. The smaller the particle, the faster the entire particle can heat up and for some metals reach its vaporization temperature. This allows the metal vapors to react more readily with the surrounding oxidizer. Some specific examples of the benefits of nano particles for propulsion related applications include:

1) Shortened ignition delay

2) Significantly decreased burning times
3) They can provide greater flexibility in terms of designing new fuels or propellants
4) Can serve as a gelling agent, minimizing inert or low energy ingredients
5) Increased burning rates and regression rates can improve thrust, and mass fraction

Despite the apparent benefits of nanoparticles for propulsion systems, they do possess some undesirable characteristics. For example, most aluminum or boron nanoparticles have an oxide layer. Although the oxide layer is generally only a few nanometers, as the particles get smaller, the oxide layer begins to occupy a larger fraction of the volume of the particle. This in effect removes some of the available energy from the particle.

2.5 Laminar Jets Exhausting into a Quiescent Atmosphere

As part of this study, a laminar jet is used to inject nanoparticles into the post flame region of a flat flame burner. The details of the particular experiment is discussed in subsequent chapters. However, a brief review is provided here to describe the behavior of a laminar jet as it exhausts into a quiescent atmosphere. In particular, the centerline axial component of velocity is of interest. A simple analysis is provided by Turns[63] of a nonreacting-laminar jet of fluid flowing into a quiescent atmosphere. In this analysis the following assumptions are made[63]:

1) The velocity profile is uniform at the jet exit

2) Close to the jet exit there exists a region called the potential core. Within the potential core, the effects of viscous shear and diffusion have yet to be felt
3) The molecular weights of the jet and the atmosphere are equal, leading to constant density
4) Species molecular transport is by simple binary diffusion governed by Fick's Law
5) Schmidt number, $Sc \equiv \frac{\nu}{D}$, is unity. Implies that momentum and species diffusivities are constant and equal
6) Only radial diffusion of momentum and species is important, axial diffusion is neglected

Throughout the flowfield, the initial jet momentum is conserved. As the jet exhausts into the atmosphere, some of its momentum is transferred to the atmosphere. Therefore, the jet velocity decreases and the atmosphere is entrained into the jet as it proceeds downstream. This can be represented by an integral form of momentum conservation:

$$2\pi \int \rho(r,x) u_x^2(r,x) r dr = \rho_e u_e^2 \pi R^2 \qquad \text{Eq. 2.7}$$

Where R is the jet radius, r_e, and u_e refer to the jet exit density and velocity respectively. Similarly, the carrier gas concentration field is governed by the same processes as the velocity field, namely convection and diffusion and the mass of the fluid exhausting from the jet is conserved:

$$2\pi\int \rho(r,x)u_x(r,x)Y_{CG}(r,x)rdr = \rho_e u_e \pi R^2 Y_{CG,e} \qquad \text{Eq. 2.8}$$

Y_{CG} refers to the mass fraction of the carrier gas. The governing equations for this problem come from the boundary-layer equations, of mass, axial momentum, and species conservation:

$$\frac{\partial u_x}{\partial x} + \frac{1}{r}\frac{\partial(ru_r)}{\partial r} = 0 \qquad \text{Eq. 2.9}$$

$$u_x \frac{\partial u_x}{\partial x} + u_r \frac{\partial u_x}{\partial r} = \frac{\nu}{r}\frac{\partial}{\partial r}\left(r\frac{\partial u_x}{\partial r}\right) \qquad \text{Eq. 2.10}$$

$$u_x \frac{\partial Y_{CG}}{\partial x} + u_r \frac{\partial Y_{CG}}{\partial r} = D\frac{1}{r}\frac{\partial}{\partial r}\left(r\frac{\partial Y_{CG}}{\partial r}\right) \qquad \text{Eq. 2.11}$$

The boundary conditions for this problem are as follows:

$$u_r(0,x) = 0 \qquad \text{Eq. 2.12}$$

$$\frac{\partial u_x}{\partial r}(0,x) = 0 \qquad \text{Eq. 2.13}$$

$$\frac{\partial Y_{CG}}{\partial r}(0,x) = 0 \qquad \text{Eq. 2.14}$$

$$u_x(\infty,x) = 0 \qquad \text{Eq. 2.15}$$

$$Y_{CG}(\infty,x) = 0 \qquad \text{Eq. 2.16}$$

$$u_x(r \le R,0) = u_e \qquad \text{Eq. 2.17}$$

$$u_x(r > R,0) = 0 \qquad \text{Eq. 2.18}$$

$$Y_{CG}(r \le R,0) = Y_{CG,e} = 1 \qquad \text{Eq. 2.19}$$

$$Y_{CG}(r > R,0) = 0 \qquad \text{Eq. 2.20}$$

The velocity field can be obtained by assuming the profiles to be similar. In this case, this implies that the radial distribution of $u_x(r,x)$, when normalized by the local centerline velocity $u_x(0, x)$, is a universal function that depends only on the similarity variable r/x. The solution for the axial component of velocity is given by Schlicting[64]:

$$u_x = \frac{3}{8\pi}\frac{J_e}{\mu x}\left[1+\frac{\xi^2}{4}\right]^{-2} \qquad \text{Eq. 2.21}$$

where J_e is the jet initial momentum flow,

$$J_e = \rho_e u_e^2 \pi R^2 \qquad \text{Eq. 2.22}$$

and ξ contains the similarity variable r/x,

$$\xi = \left(\frac{3\rho_e J_e}{16\pi}\right)^{1/2}\frac{1}{\mu}\frac{r}{x} \qquad \text{Eq. 2.23}$$

By substituting Eq. 2.22 and 2.23 into 2.21, the centerline axial component of velocity is obtained.

$$u_{x,CL} = \frac{3}{8}\frac{u_e^2 R^2}{\nu x} \qquad \text{Eq. 2.24}$$

CHAPTER 3

EXPERIMENTAL APPROACH

3. Experimental Approach

Chapter 3 discusses the details of the experiments utilized to meet the goals of this study. There were two major experiments conducted, a flat flame burning experiment and an airbreathing combustor experiment, each of which had its own goals and challenges to be met. Within the two main experiments there were several sub-experiments to be conducted.

3.1 Flat Flame Burning Experiment

A series of experiments were conducted in order to determine critical parameters with regards to the ignition of the particles as well as their reaction times. Only SB99 Boron nanoparticles (described later) were examined in this portion of the study. To date there have been several studies investigating these parameters in nano-aluminum[16,17].

For this set of experiments a commercially available Mckenna Flat Flame burner using a methane/oxygen/air mixture was utilized. The burner is designed to provide a stable laminar premixed flat flame for long durations. It is water-cooled and constructed primarily of stainless steel. During burner operation, the cooling water was run at approximately 0.8 liters per minute. Figure 3.1 is a schematic diagram of the burner, while Figure 3.2 is a photograph of the burner on the test stand. The stainless steel sintered plug model was used in this study.

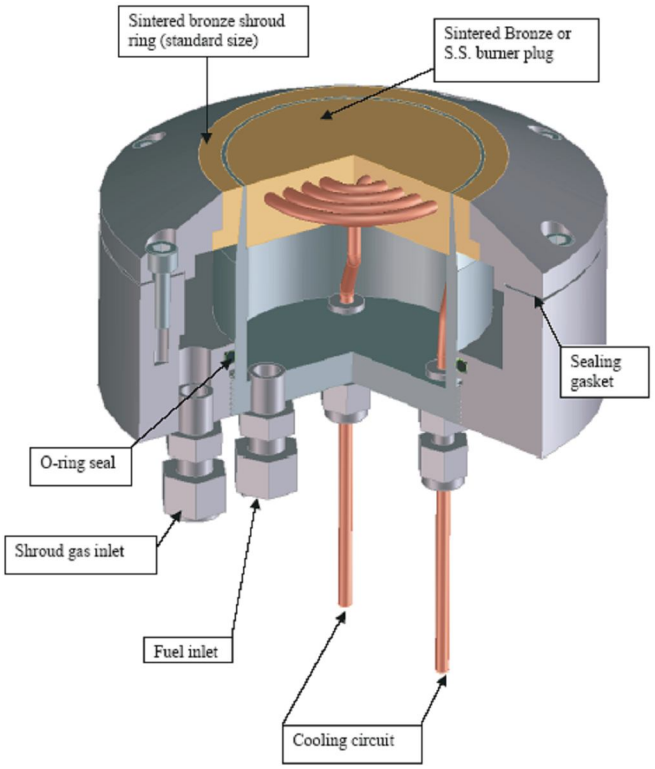

Fig. 3.1 Schematic Diagram of McKenna Flat Flame Burner

At the time of testing, the boron nanoparticles were placed in distilled water to form a solution with a fixed concentration of 1% by weight. Typically. 25 ml of distilled water and 25 mg of boron was used in the experiments. Ideally, one would like to match the total number of particles in the solution to the total number of droplets that are produced by the atomizer, such that each droplet would statistically contain only one particle. However, once nanoparticles are aerosolized, the signature of particle combustion is no longer visible to the human eye, and diagnostic signal levels become too low. Therefore, in order to achieve a reasonable signal to noise ratio, the mass

concentration of particles was held constant for all experiments rather than the particle number concentration.

The solution was subjected to a sonicating-atomizer to create an aerosol using air as the carrier gas with a flow rate ranging from approximately 0.61 to 1.15 liters per minute. Figure 3.3 is a schematic diagram of the components of the sonicating atomizer. A photograph of the actual components is included in Appendix A. The carrier gas was regulated by a rotameter and the flow comes into the atomizer via tygon tubing from the side and leaves as an aerosol through the top. The main body and the two end caps of the atomizer are made of plexi-glass. The end cap located at the top of the atomizer was solid plex-glass with a hole in the center that had a tube attached, which served as the exit for the aerosol flow. A stainless steel cylinder was placed on top of the atomizer to ensure that it stays closed and sealed. The end cap at the bottom of the atomizer had a large hole cut out of it and utilized a thin film to seal the bottom portion of the atomizer. The entire atomizer with the solution was placed into the base of a standard commercial humidifier. The humidifier unit was then turned on and set to approximately ¾ of the maximum power. The humidifier causes the film to vibrate quickly, which created a mist of the solution that was carried away by the carrier gas in the form of an aerosol.

Prior to injection in the post-flame region of the flat flame burner, the aerosol passed through 3 silica-gel dryers placed in series to remove all of the water content from the particles. The aerosol was then injected into the post-flame region of the flat flame burner via a stainless steel tube with an inner diameter of 1 mm that was located 5 mm above the burner surface. The tube was placed at the very edge of the burner such that

the particles would traverse the full diameter of the burner. Figure 3.4 is a schematic diagram of the test set up.

In the vast majority of previous studies using flat flame burners[35,36,46,47] the particles were injected in the direction of the burner flow and the particles were assumed to be traveling at the flame velocity. In this study, the particles are injected perpendicular to the direction of the flow. This allows for adjustment of the particle velocity to allow for increased resolution of events happening in a short duration. By increasing the particle velocity, the events occur over a larger spatial duration, thereby increasing the resolution.

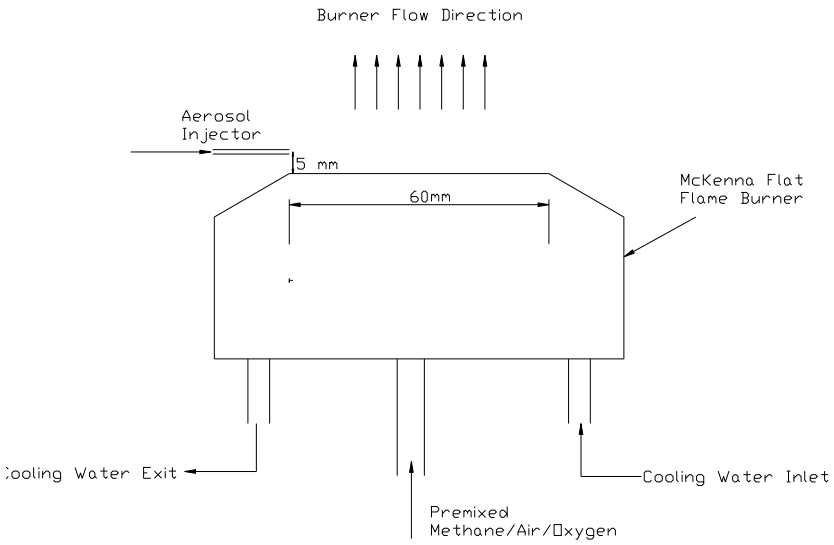

Fig. 3.2 Flat Flame Burning Test Configuration

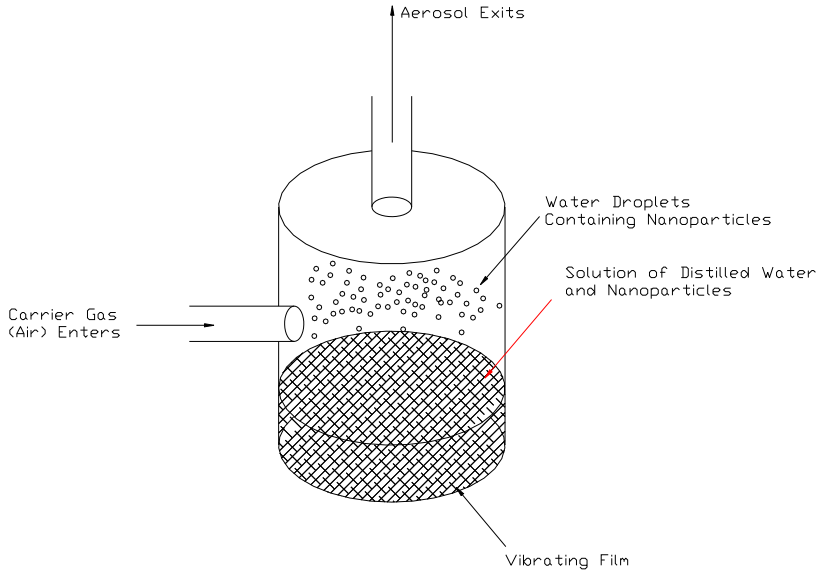

Fig. 3.3 Schematic Diagram of Sonicating Atomizer

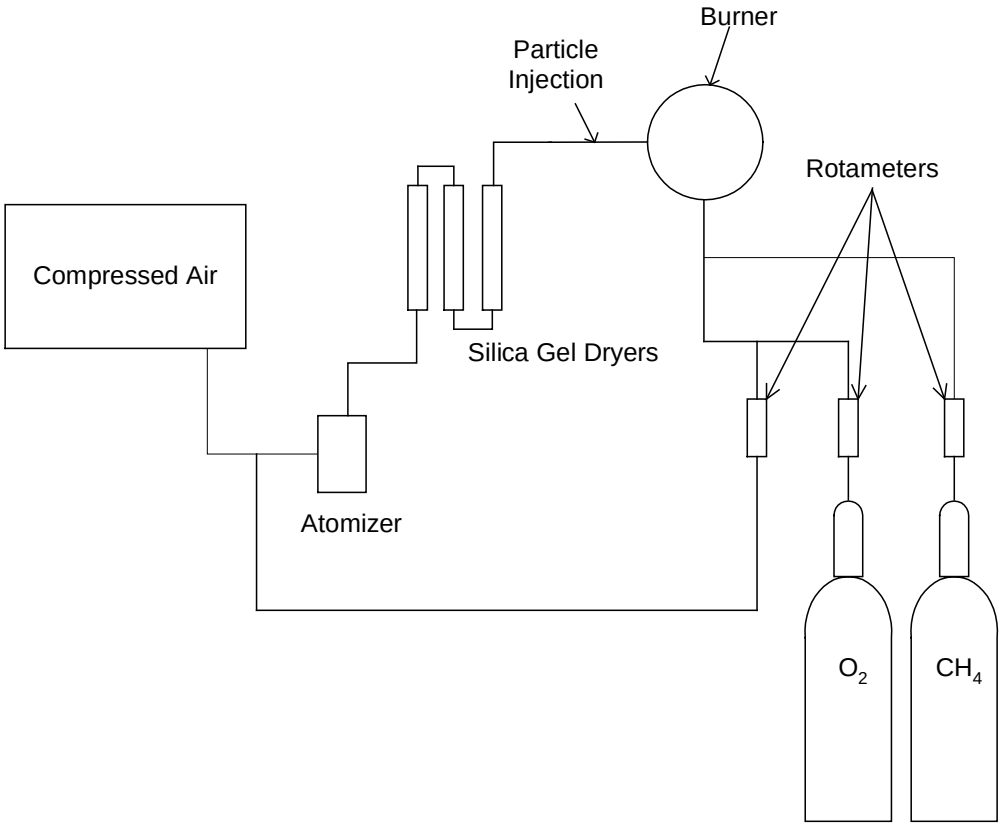

Fig. 3.4 Schematic Diagram of the Flat Flame Burning Experiment

3.1.1 Flow Controls for Flat Flame Burning Experiment

In order to obtain meaningful data, the flame characteristics need to be understood in great detail. As was mentioned, in this study the flat flame burner was operated on a mixture of oxygen, air, and methane. All gas flows were controlled through the use of high precision rotameters. All rotameters were calibrated for the gas being used by utilizing a calibrating gillabrator. Figure 3.5 is an example of the calibrations obtained for the rotameters. As the figure shows the gas flow rates behavior linearly with respect to the settings of the rotameter. The calibrations for the other gases can be found in Appendix C.

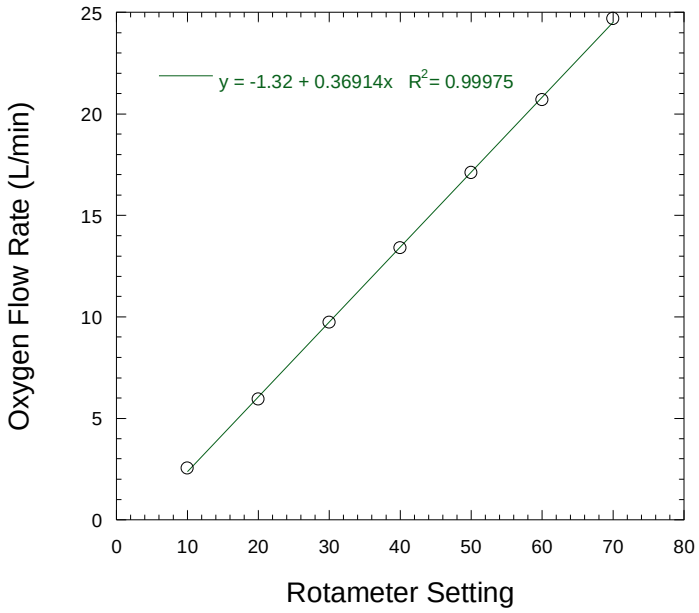

Fig. 3.5 Example of Rotameter Calibration

3.1.2 Particle Image Velocimetry (PIV)

Since the particles were injected perpendicular to the burner flow direction, the velocity of the particles must be measured in order to ensure that a reasonable measurement of ignition delay and burning times could be made. Particle Image

Velocimetry (PIV) was employed in order to resolve the particle velocity at a number of conditions. The basic principle of PIV is to record the light scattered by tracer particles that are a part of the flow or that have been added to the flow. A typical PIV set up includes a high-powered laser and a digital camera. The laser and camera are synchronized such that as the laser is pulsed, the camera collects an image. There are also generally some optic components, which convert the laser beam into a laser sheet. The camera is placed perpendicular to the plane of the laser sheet. The laser sheet is pulsed, switched on and off very quickly, twice at a know interval. The light from the laser sheet is scattered by the particles and collected by the camera as two separate images. The first image collected shows the initial position of the seeding particles, and the second image shows their final positions. The images are broken into interrogation regions from which displacement vectors may be determined through a correlation technique. With the knowledge of the laser pulse interval, the displacement vector can be converted into a velocity vector.

PIV has many advantages over other velocity measurement techniques. For the most part, as long as the seed particles are properly chosen[65] the technique is virtually non-intrusive. It is important to choose appropriate seed particles such that they:

1) Are sufficiently small that they "follow" the flow correctly
2) Are large enough that they provide reasonable scattering signals

To determine if the particles are small enough, one needs to take into consideration the Stokes Number, which will be discussed later.

The fact that PIV is virtually non-intrusive with appropriate seed particles alone is a large advantage over other measurements such as pitot tubes or hotwires. Furthermore,

since the laser provides a sheet, velocity measurements are obtained for an entire plane rather than just point measurements.

A total of 3 different injection velocities were measured corresponding to three different volumetric flow rates controlled by a rotameter. All measurements were made in "cold flow", i.e. non-reacting over a wide range of crossflows, and momentum flux ratios. For this experiment, an Nd:YAG Laser operating at wavelength of 532 nm was synchronized with an Intensified Charge Coupled Device (ICCD) camera. The PIV system used in this study was from LaVision. In some cases PIV can be sensitive to the correlaion technique used during the processing procedure. During this study, for all cases, the standard PIV sum of correlation technique was used to process the data. Figure 3.6 is a schematic diagram of the PIV setup.

In order to conduct the PIV experiments in a simple manner that required the least modification to the test rig, the sonicating-atomizer was utilized with no particles placed in solution. Only 25 ml of distilled water was placed into the atomizer, and the silica gel dryers were removed from the injection lines. The water droplets created by the atomizer were then used as the seed particles for the PIV experiments. An important parameter to consider when using seed particles in any light scattering technique is the Stokes Number which provides a measure of how well the particles follow the flow. The Stokes Number is the ratio of the characteristic particle stopping time or distance to the characteristic fluid time or distance. The characteristic particle stopping distance is given by:

$$S_{particle} = \frac{\rho_p D^2 U}{18\mu} \qquad \text{Eq. 3.1}$$

where μ is the viscosity of the fluid, ρ_p is the seed particle density, U is the velocity of the fluid, and D is the seed particle diameter. The characteristic fluid time in this case is

scaled with the jet core length. In this case the jet core length was taken to be six times the diameter of the injection tube. The average seed particle diameter (water droplets) created by the sonicating atomizer is 5 μm.

The water droplet size was determined by placing a known mass of salt in a known mass of water. The atomizer was then turned on to begin spraying the water droplets assuming that the mass concentration of salt in a droplet was the same as the total mixture. The aerosol was then passed through a series of silica-gel dryers as shown in figure 3.4 to "dry off" the particles. At this point, the aerosol only contained the salt particles. The aerosol was then passed through a Differential Mobility Analyzer (DMA) to determine the size of the salt particle. Since the size of the salt particle was now known, and the mass fraction of salt in the water was known, solving for D_{water} in the following set of equations leads you to the size of the water droplet.

$$m_{salt} = \rho_{salt} * V_{salt} = \rho_{salt} * \frac{\pi D_{salt}^3}{6} \qquad \text{Eq. 3.2}$$

$$m_{water} = \rho_{water} \frac{\pi D_{water}^3}{6} - \rho_{salt} \frac{\pi D_{salt}^3}{6} \qquad \text{Eq. 3.3}$$

Given these parameters the Stokes Number in these experiments ranged from 0.16-0.31. Since the Stokes Number was less than unity, the water droplets did in fact follow the gaseous flow sufficiently for the PIV measurements.

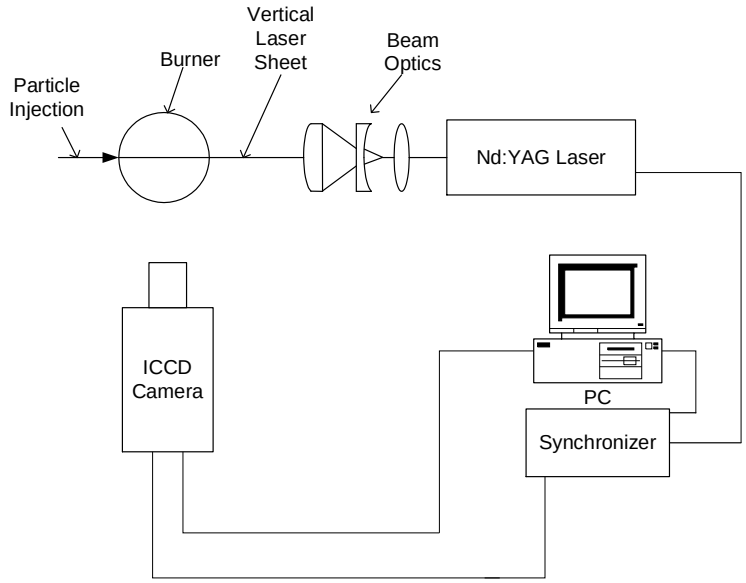

Fig. 3.6 Schematic Diagram of PIV Experiment

3.1.3 Temperature Measurements

In order to know the temperature of the environment the particles were exposed to B-type (Pt-6%Rh/Pt-30%Rh) thermocouples with bead sizes of approximately 200 μm were used for the measuring the temperature. B-type thermocouples are suitable for oxidizing or inert environments and have a range of 0 – 1700 ^{o}C. The typical error associated with a measurement is 0.5% above 800 ^{o}C. The time constant associated with an exposed thermocouple of 200 μm is approximately 0.2 seconds. The time constant is defined as the time required to reach 63.2% of an instantaneous temperature change.

A thermocouple was placed on a "slide" that was marked at 10 mm, 30 mm, and 50 mm axially from the injection location, at a location of 5 mm above the burner surface. The thermocouples were placed in the center of the burner as shown in figure 3.7, which is a schematic diagram of the thermocouple measurement configuration. A detailed photograph of the configuration can be found in Appendix A.

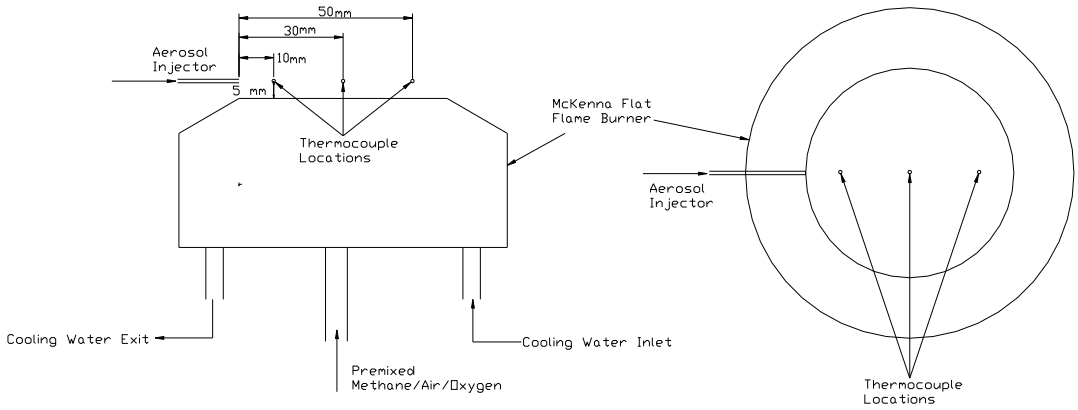

Figure 3.7 Flat Flame Burner Thermocouple Configurations

Since the thermocouples were subjected to very high temperatures, all measurements were corrected for radiation primarily based upon the recommendations of Shaddix[66]. The effects of conduction through the wire and catalysis were neglected. In addition, the temperature readings of interest were taken at what was considered to be a "steady-state". With these assumptions the energy equation for the system reduces to a balance of convection and radiation given by equation 3.2, which can be solved for the gas temperature in equation 3.3.

$$h\left(T_g - T_{tc}\right) = \varepsilon_{tc}\sigma\left(T_{tc}^4 - T_\infty^4\right) \qquad \text{Eq. 3.2}$$

$$T_g = T_{tc} + \frac{\varepsilon_{tc}\sigma\left(T_{tc}^4 - T_\infty^4\right)}{h} \qquad \text{Eq. 3.3}$$

where T_g, T_{tc}, T_∞, ε, and σ are the gas temperature, thermocouple surface temperature, ambient temperature, the thermocouple emissivity, and the Stefan Boltzman constant

respectively. *h*, the convective heat transfer coefficient was determined from an empirical Nusselt number correlation given by Whitaker[67]. The correlation was obtained for a sphere with a Prandtl Number range of $0.71 < Pr < 380$, and Reynolds number range of $3.5 < Re < 76{,}000$ where the Reynolds number is the standard Reynolds number for a sphere. All gas properties are taken at T_g, except for μ_s which is the gas viscosity taken at the thermocouple surface temperature. Since T_g is unknown, this requires an iterative procedure. Gas properties for air were used at the temperatures of interest and were taken from Incropera and Dewitt[68]. For some properties, such as the thermal conductivity of air, *k*, the data from Incropera and Dewitt[68] was plotted and a curve fit was applied to the data and used for data reduction in order to expedite data reduction. Figure 3.8 is an example of such a curve fit.

$$h = \frac{Nuk}{d} \qquad \text{Eq. 3.4}$$

$$Nu = 2 + \left(0.4\,\mathrm{Re}_d^{1/2} + 0.06\,\mathrm{Re}_d^{2/3}\right)\mathrm{Pr}^{0.4}\left(\frac{\mu_\infty}{\mu_s}\right) \qquad \text{Eq. 3.5}$$

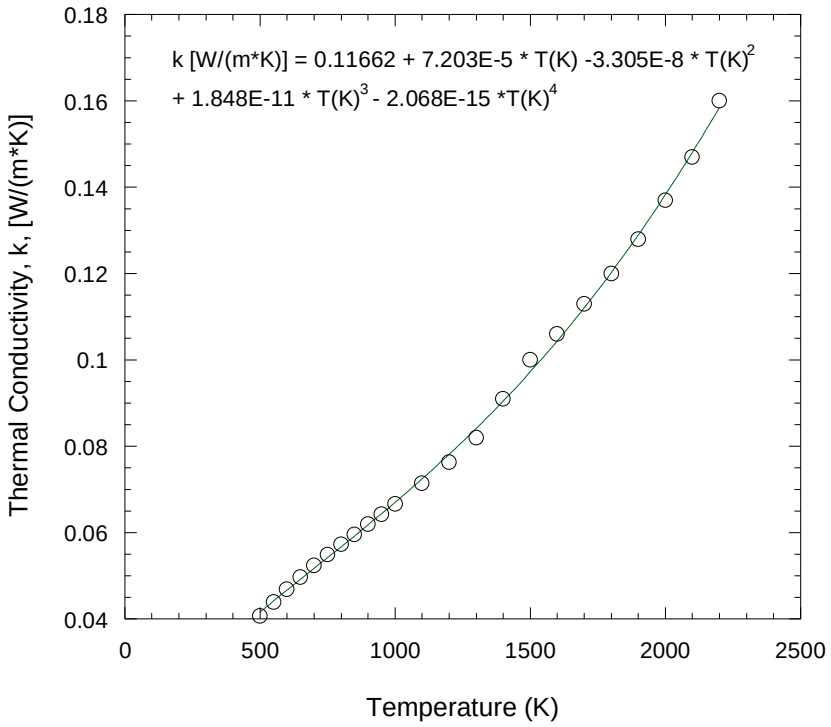

Fig. 3.8 Curve Fit for Air Thermal Conductivity

3.1.4 Chemiluminescence for Flat Flame Burning Experiments

There are a number of sources of optical radiation that are emitted from a flame or combustion system that can be used to study specific combustion characteristics of a given system. The source most directly connected to the combustion reactions, however, is chemiluminescence[69]. Chemiluminescence appears when a certain chemical reaction in a chain of reactions mainly produces some molecules in an electronically excited level[70]. These molecules undergo transitions from higher to lower energy states that result in fluorescent emissions at specific frequencies depending on the molecule that has been excited. Such excited molecules or atoms have radiative lives on the order from 10^{-8} to 10^{-6} seconds[69]. The intensity of the resulting emissions is proportional to the production

rate of the excited state species. For this reason chemiluminescence has been used as a rough measure of reaction time and heat release rate previously[69].

Chemiluminescent images can be obtained at visual wavelengths with standard optics using an appropriate narrow band interference filter to isolate the wavelength of interest. Should the wavelength of interest be outside of the visible range, special lenses may be required. In the boron nanoparticle flat flame burner experiments BO_2 chemiluminescence was monitored by utilizing a narrow bandpass filter centered at 546 ± 2 nm and an Intensified Charge Coupled Device (ICCD) camera. The bandpass filter has a 10 nm full width half maximum value.

The BO_2 molecule is a reactive intermediary gas-phase species formed throughout boron particle ignition and combustion[51]. According to Spalding[72], the BO_2 spectrum is readily observable during both the combustion and ignition stages of boron combustion. Gas phase modeling studies conducted by Yetter[52] indicate that $BO_2(g)$ gets converted to $B_2O_3(g)$ or $HBO_2(g)$ products quickly depending on the amount of water vapor present. Therefore, once the source of B/B_2O_3 was consumed, then so was the source of $BO_2(g)$ as well[51]. As a result, monitoring the emission of the BO_2 molecule was a reasonable approach towards measuring the reaction/burning time of boron.

3.2 Airbreathing Combustor Experiments

After determining the fundamental ignition and combustion behavior of the nanoparticles in the flat flame burner experiments, the next set of experiments in this study provided a demonstration of the ability or inability to extract the energy from metallized nanoparticles within reasonable residence times and realistic combustor

conditions (reactant/product species). A combustor simulating a ramjet engine was designed and fabricated for this purpose. The combustor utilized in this study was located on the reacting test stand at the Advanced Propulsion Research Laboratory at the University of Maryland.

3.2.1 Overall Design Strategy

The overall goals of this research effort were described earlier, with a large component based on a demonstration of the use of metallic nanoparticles in an airbreathing combustor, under realistic combustor conditions, namely residence time. With this in mind, the overall design strategy for this portion of the study was to design and test a combustor capable of providing a wide array of diagnostic capability. Specifically, the combustor needed to provide optical access so that any number of optical or a variety of laser diagnostics could be employed. In addition, the combustor needed to be capable of providing a means of using other diagnostics such as probes should they be desired. All testing conducted in this study was with the combustor operating in a ramjet-simulating mode. As will be discussed, the combustor provided means of operating in other modes such as a ducted rocket configuration. Finally, this study called for a simple, yet reproducible means of delivering the particles into the combustor, which will be discussed in detail in a subsequent section. All design drawings not presented here are included in Appendix A.

3.2.2 Flow Facilities

The airflow for the combustor experiments was provided by an Atlas Copco Compressor that can provide up to 358 cubic feet per minute at delivery pressures up to 150 psig. The compressor delivers clean dry air through a series of filters and dryers to the laboratory supply lines. The air is then delivered to an individual test rig by a 2 inch diameter steel pipe.

3.2.3 Particle Delivery System Design

The particles were introduced into the combustor via a reverse cyclone seeder similar to the technique used by Glass[73]. The seeder consists of three main parts, the main body, and two end caps. One of the two end caps contained a port in which high pressure stainless steel tubing was attached to the seeder as a means of exhaust for the particle laden flow.

The main body of the seeder was constructed from 304 Stainless Steel. The inner diameter of the main body was 6.35 cm (2.5 in). The overall length of the main body was 20.3 cm (8.0 in), although 2.54 cm (1 in.) on each side was left for insertion of the end caps. The seeder was sealed with O-rings at the main body and end cap interfaces. A stainless steel tube was welded to the outside of the main body near the top of the seeder. This was the location of the gas entrance into the seeder. The tube was welded such that the carrier gas enters the seeder tangentially with respect to the walls and promotes circulation within the seeder. Similarly stainless steel tubing was used for the exhausting particle laden flow. The seeder was designed to be intentionally heavy

walled in the event that the combustor experienced flashback into the seeder. A schematic diagram of the seeder is provided in figure 3.9.

The stainless steel exhaust tubing was located in the center and extended down into the seeder 4 inches (10.16 cm). As the gas entered the top of the seeder it was forced down towards the bottom of the seeder where the particles were loaded. Before the gas left the seeder it formed a "cyclone" which entrained the particles into the gas flow. A particle-laden flow was established and could be delivered to the combustor for testing. Of the available volume, the length available for the particles was 15.24 cm (6 in), however the seeder was never more than about 1/3 full of particles. A photograph of the seeder components can be found in Appendix A.

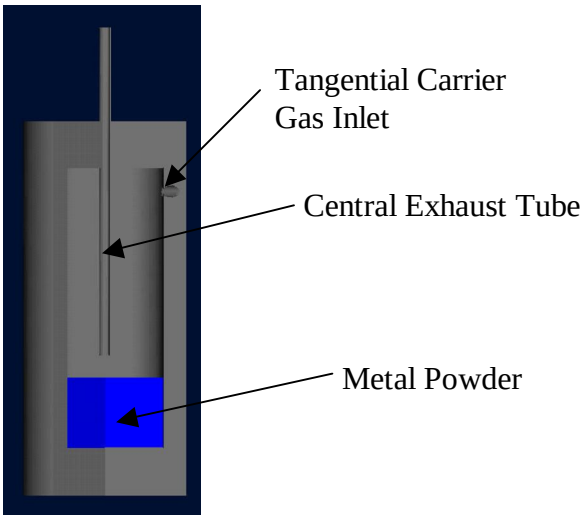

Fig. 3.9 Schematic Diagram of Reverse Cyclone Seeder

A fuel was chosen as the carrier gas since the metallic particles are also fuels. This was done in order to limit the chance of flashback once the combustor was in operation. An inert gas could have been selected, however by using a fuel, which is the

same as the main fuel in the combustor, the combustor is still operating on air and fuel alone with no diluents.

For actual combustor testing an O'Keefe Choke Orifice (0.120 inches, 0.305 cm) with a small portion (0.75 inch, 1.91 cm) of stainless steel tubing welded onto the end was used to connect the seeder to the combustor. The particle-laden flow was not choked at this point, this configuration was simply used as a simple means of connecting the seeder to the combustor. In addition the tubing ended at the center of the combustor, meaning the particles were injected at the center of the combustor and could mix freely. In early testing without the tubing, the particle-laden flow was unable to substantially penetrate the main airflow of the combustor. The tubing therefore provided a means of obtaining meaningful data in combustor testing. A photograph of the modified orifice can be found in Appendix A.

3.2.4 Pilot Flame - Design

The main combustor was ignited by a separate ethylene/oxygen pilot flame. The pilot flame contains two main components, a combustor constructed from 303 Stainless Steel and an exhaust nozzle constructed from graphite. Figure 3.10 is a photograph of the two components together. The nozzle was constructed of graphite as a separate piece so that multiple pilot flame injection schemes could be employed if so desired. For instance the shape of the pilot injection could be changed very easily and at very little cost. A schematic diagram of the nozzle used in this study is included in figure 3.11.

The pilot flame combustor was heavy weight and contained an initial channel and a rearward-facing step that served as the primary mixing and combustion zone prior to

exhausting into the main combustor. The details can be seen in figure 3.12 (all units are in inches unless otherwise noted). The pilot flame was ignited by a standard reusable automotive spark plug, and had four ports available for injection of fuel(s) and oxidizer(s). It was designed this way should the need arise for the entire airbreathing combustor to be utilized in a ducted rocket mode rather than a traditional ramjet. For all testing in this study a nozzle with a slot shape was chosen. The slot was 0.125 inches in width and 0.418 inches in length. The pilot flame was designed to thread directly into the main combustor components at the aft end. The exit nozzle then mated flush with the surface of the main combustor wall. In addition a separate aft end enclosure was designed and fabricated in the event that any testing would need to be conducted on just the pilot flame.

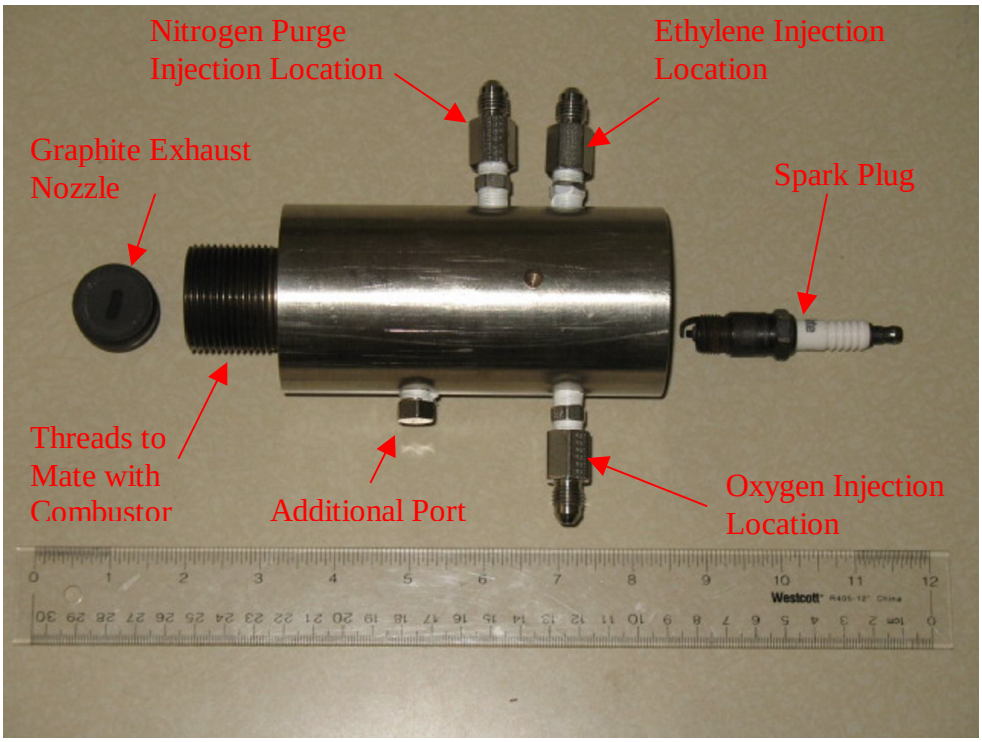

Fig. 3.10 Pilot Flame Components

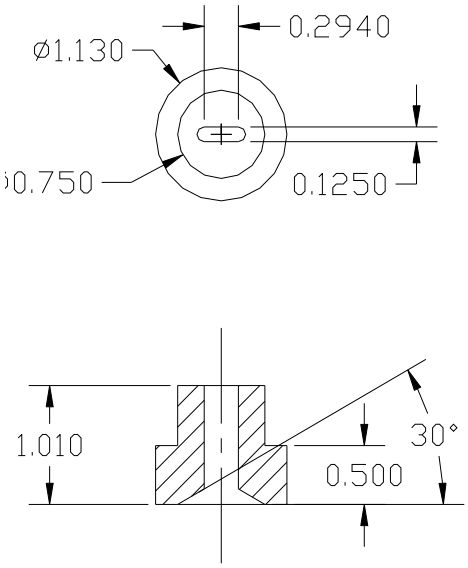

Fig. 3.11 Schematic Diagram of Pilot Flame Nozzle

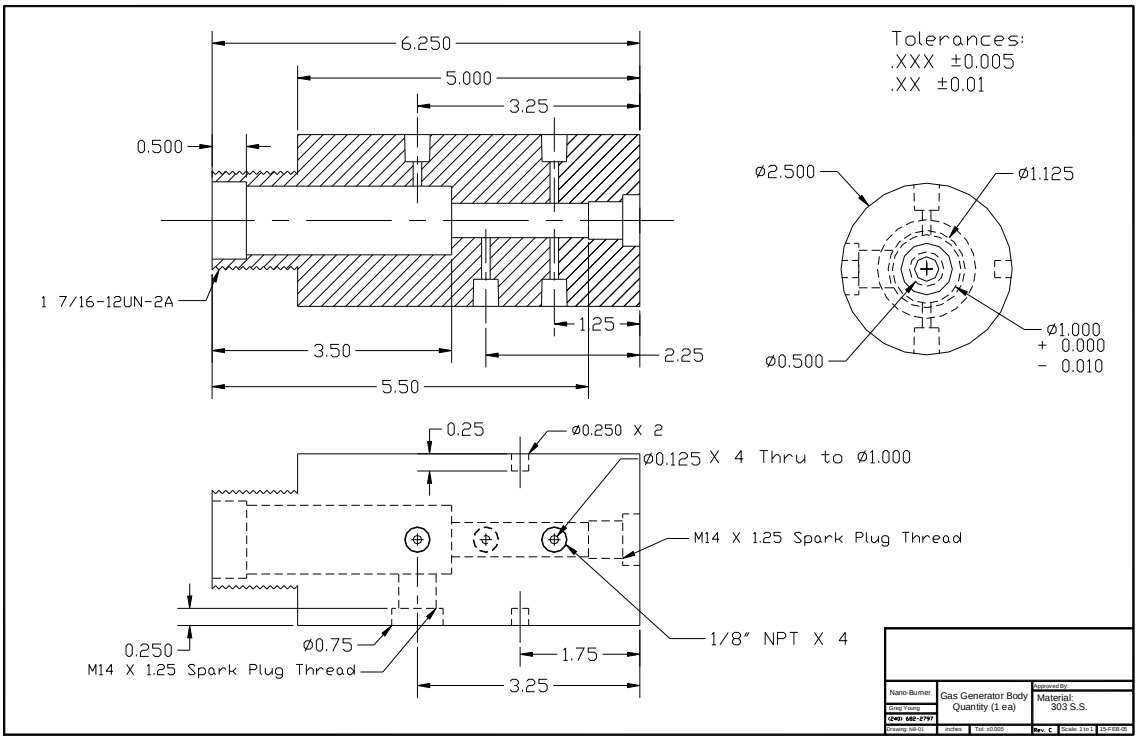

Fig. 3.12 Schematic Diagram of Pilot Flame Combustor

As was mentioned earlier, the pilot flame operated on a mixture of ethylene and oxygen which was spark initiated, through a standard automotive spark plug. In all main combustor testing, the pilot flame conditions were held constant in order to minimize the amount of variables affecting the nanoparticle laden flow combustion. The pilot flame combustor had 6 total ports, 4 for gas flows and 2 for the spark plug depending on test selection. For all of the tests in this study, the spark plug port at the head end of the pilot flame was used. In addition to the oxygen and ethylene, nitrogen was used at the conclusion of each test as a purge gas in order to quench any remaining combustibles and to help cool the system.

3.2.5 Main Combustor Design

An ethylene/oxygen pilot flame was used to ignite the main combustor, which contained air and fuel with or without the addition of aluminum or boron powder. The pilot flame was described in the previous section. Prior to reaching the combustor, the airflow is choked by an orifice with a diameter of 1.00 cm (0.395 in) to ensure a steady mass flow rate for testing. A Wilkerson Regulator controlled the flow and the static pressure upstream of the choke point was recorded with a Setra Model 206 Static Pressure Transducer. The powder was injected approximately 4.3 cm (1.7 in) upstream of the pilot flame. The powder was introduced through a particle seeder (described earlier) using gaseous ethylene as the carrier gas. In addition, ethylene was injected 2.1m (7ft) upstream of the combustor such that it was essentially premixed. During typical combustor testing between 40-60% of the fuel by mass was premixed depending on the

test condition. Lastly, an injection port for additional fuel was added just downstream of the step should the desire to investigate the effects of injection location arise.

The primary combustor in the experiments was two-dimensional with a rearward-facing step. The combustor was constructed entirely from 303 stainless steel. The combustor had a width of 4.45 cm (1.75 in) and prior to the step, a height, H, of 3.81 cm (1.5 in). The step, which was one half of a channel height, was located two channel heights downstream of the pilot flame. The combustor was designed to provide optical access via quartz windows from three sides. Figure 3.13 provides a schematic diagram of the combustor set up.

All gas flows besides the air came from pressurized bottle sources and were choked with O'Keefe orifices and the static pressures upstream of the choke points were recorded by Setra Model 206 Static Pressure transducers. The gas flows were carefully controlled by a Lab View Virtual Interface (VI), which controlled a series of solenoid valves, which dictated the timing of the test according to the user's specifications. This control allowed for repeatable and consistent testing. Following each test, the pilot flame was purged with gaseous nitrogen (N_2), to quench any residual fuels left in the pilot flame combustor. The VI also recorded the static pressure settings of the gas flows as well as the thermocouple data obtained for each test for post processing. The typical duration of a combustor test was three to four seconds.

At the exit plane of the combustor (41.3 cm (16.25 in) from the pilot flame location) there were four ports, which were used in this study to provide access for thermocouple measurements. Two different tops were designed and fabricated, one, which had a slot for a quartz window for optical access and the other with an array of

ports, which could be used for any number of diagnostics. In this study only the top with the quartz window was utilized. High temperature rubber gasket was used to seal most surfaces. In some cases O-rings were used instead of the gasket in order to maintain a gas seal.

Because the air delivery system (described earlier) delivered air from a round pipe, a special adapter was designed to convert the flow from a round pipe to a rectangular cross section. Within this adapter, a honeycomb was placed and used as a flow straightener. The adapter is made up of two components plus the honeycomb, which can be seen in a photograph in Appendix A. Figure 3.14 is a photograph of the assembled combustor on the test stand. All design drawings are supplied in Appendix A.

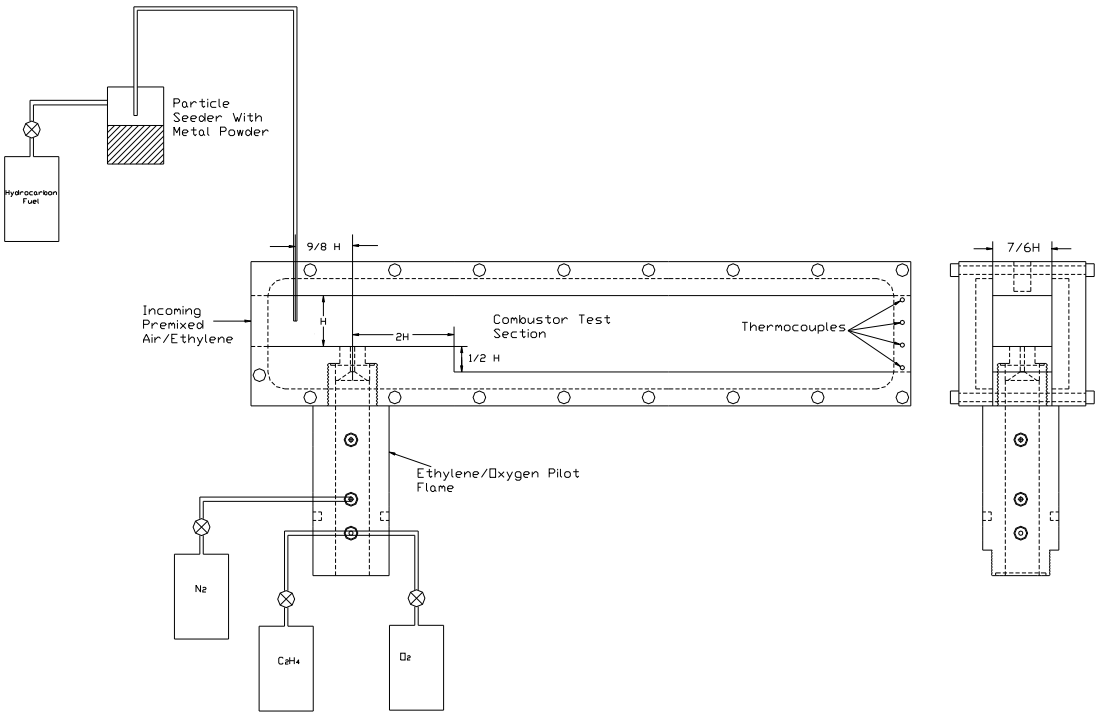

Fig. 3.13 Schematic Diagram of Combustor Set Up

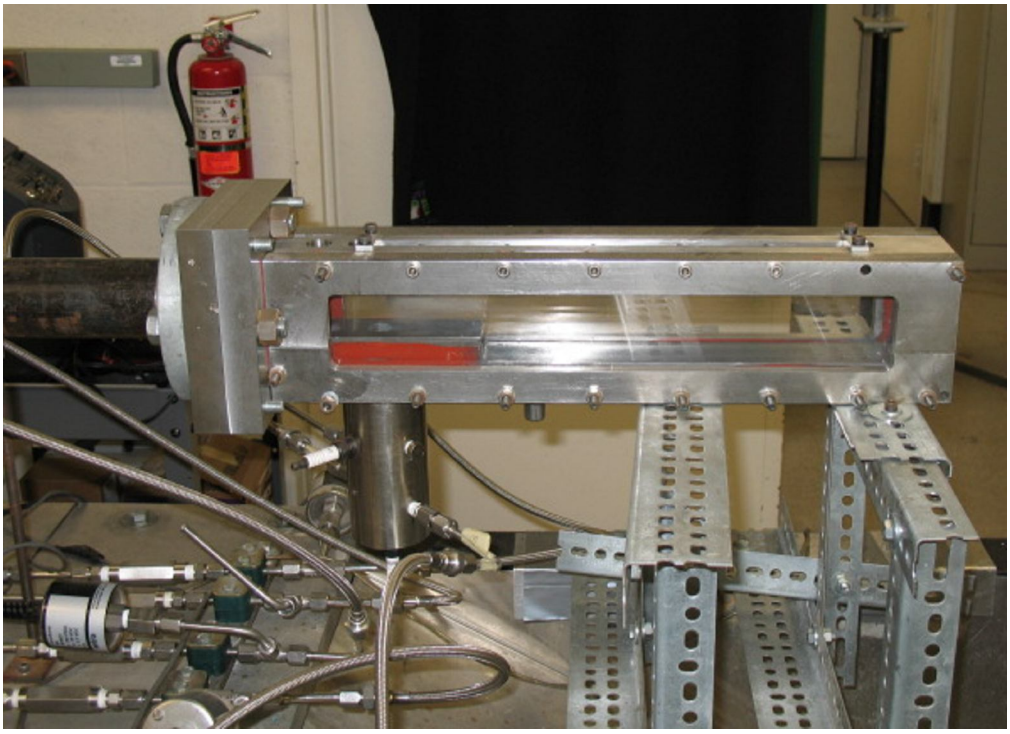

Fig. 3.14 Assembled Combustor on Test Stand

3.3 Combustor Diagnostics

As was previously mentioned the combustor was designed such that many different diagnostics could be applied to it very easily. It was optically accessible through quartz windows from three sides so that any number of laser diagnostics can be relatively easy to apply. In addition there was an array of ports at the exit plane of the combustor, which can be used in a variety of ways for any sort of probe measurement. Similarly, a second "top" portion of the combustor was designed and fabricated with an array of ports for probe measurements. The subsequent sections outline the diagnostics applied to this study, however, the combustor has far greater capabilities depending on the goal of a particular study.

3.3.1 Flow Control for Airbreathing Combustor

Aside from the main airflow, all of the gases were supplied by high-pressure bottles. The flow rates for each individual gas were controlled through the use of a combination of regulators, Setra Model 206 Static Pressure Transducers, and O'Keefe High Presicions Choke Orifices.

Regulators were connected to the gas bottles and the gases were transported to the test section by high-pressure stainless steel tubing. A solenoid valve controlled by a Lab View VI was placed in each gas line for accurate sequencing during testing. After the solenoid valve a check valve was placed in each line for safety purposes. The Setra Pressure Transducers were placed after the check valves just prior to injection into the combustor system. Finally the O'Keefe choke orifices were placed right at the combustor injection points. The Lab View VI also recorded the static pressure in the gas lines

during combustor testing. With the knowledge of the orifice dimensions, and the static pressures, mass flow rates were obtained for a given test through isentropic flow relationships.

3.3.2 Mie Scattering

Mie scattering can be used as a tool for flow visualization in many applications. In general a laser is used to create a beam or planar sheet in given area of interest. The light from the laser is scattered by seed particles, and the scattered light is collected, usually by a camera, in order to provide information about the flow field. Mie scattering differs from other techniques such as Raleigh scattering in that larger seed particles are employed. This results in much higher light scattering intensities, which increases the signal to noise ratio and eliminates the need for a light intensifier in the receiving optics. As a result, the implementation of this technique is easier and the cost is lower[74].

A series of Planar Mie Scattering experiments were conducted during this study in order to ensure that the dispersion of the particles was uniform. An Nd:Yag laser operating at about 12 hz and 532 nm wavelength was synchronized with a FASTCAM-Ultima1024 model 16K high speed camera high speed camera to capture the images. The laser sheet was passed through the window that was located on the top of the combustor with the aid of an "optical arm". The images were then recorded looking directly through the window located on the side of the combustor, such that the laser sheet and camera were perpendicular to each other.

The Mie Scattering experiments were conducted in the fully reacting flow using ALEX nanoaluminum particles as the scattering source. Since the images were taken in a

reacting flow, a narrow bandpass filter centered at 532 ± 2 nm was used to filter out all of the excess radiation coming from the reacting flow. The filter only allowed light with wavelengths near 532 nm to be viewed by the camera, such that it minimized the excess radiation from the reacting flow, and the main source of light captured was the laser light being scattered by the particles in the flow field. Figure 3.15 is a schematic diagram of the Mie Scattering experiment.

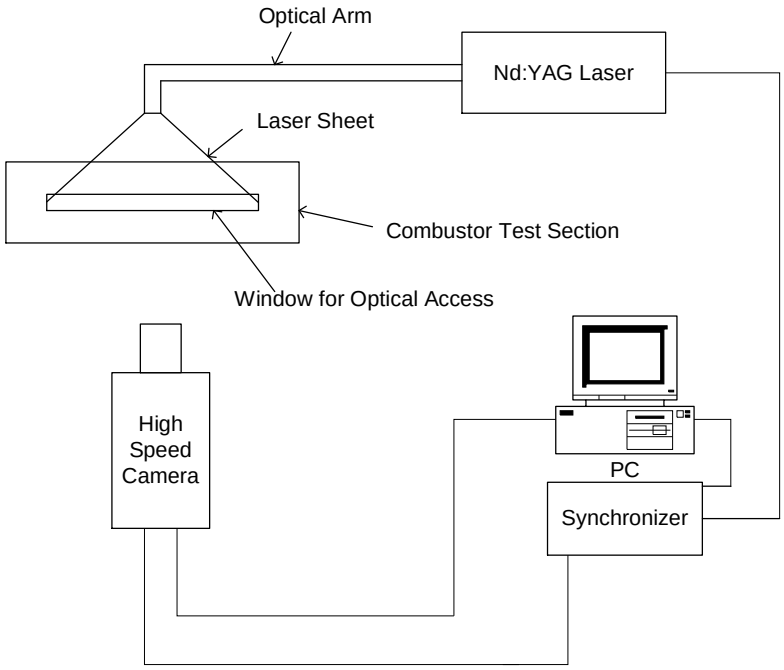

Fig. 3.15 Schematic Diagram of Combustor Mie Scattering Experiment

3.3.3 Chemiluminescence

In the airbreathing combustor portion of this study, the oxidation of the particles was studied through the natural chemiluminescence of selected particle oxides, AlO and BO_2 for aluminum and boron respectively. AlO is a known gas phase intermediate in the oxidation of aluminum[43]. The BO_2 molecule is a reactive intermediary gas-phase species

formed throughout boron particle ignition and combustion[51]. In both cases images were captured using a Cooke Dicam Pro Intensified CCD camera (ICCD) with the appropriate narrowband interference filters in place. The camera was placed so that it was imaging through the side windows, similar to the position of the high speed camera in the Mie Scattering experiment.

The filters were centered at 488 ± 2 nm for AlO and 546 ± 2 nm for BO_2. Both filters had full width half maximum values of 10 nm. Since the primary fuel was a hydrocarbon (Ethylene), the potential for hydrocarbon emission overlapping the BO_2 band existed. In particular, C_2 exhibits several bands in the vicinity of the filter. However, according to Gaydon[75], the C_2 bands near 546 nm are characterized as weak or very weak.

Based upon information from Gaydon[75], there are three possible AlO bands that could be detected with the 488 nm filter. He showed that the band at 484.23 nm has very strong emission characteristics, the band at 486.64 nm has strong characteristics, and the band at 488.88 nm has medium strength emission characteristics. In the wavelengths allowed by the 488 nm band pass filter there were some bands of emission due to hydrocarbon combustion as well. In particular, C_2*, CH*, and CO_2 exhibit bands that overlap the filter. However, Gaydon[75] lists the C_2* and CH* emission as either weak or very weak near 488 nm.

3.3.4 Temperature Measurements

Temperature measurements were made at the exit plane of the airbreathing combustor using a combination of 1000 μm K-type (Chromel/Alumel) and 200 μm B-

type (Pt-6%Rh/Pt-30%Rh) thermocouples. The B-type thermocouples were described in section 3.1.3. K-type thermocouples are suitable for use in clean oxidizing and inert environments, and have a temperature range of –200 – 1250 ^{o}C. The typical error associated with a K-type thermocouple temperature measurement is the larger of 2.2 ^{o}C or 0.75%.

Starting from the bottom of the combustor, the first thermocouple was located at 0.318 cm (1/8 in) and they were spaced 1.693 cm (2/3 in) apart. The K-type thermocouples were placed near the combustor walls, and two B-type thermocouples were located in the bulk flow of the combustor.

The temperature measurements were used to provide combustor temperature profiles and also to provide a means of comparing the thermal output of the different fuels. Once again the thermocouple temperature measurements were corrected for radiation losses using the procedure described in section 3.1.3.

CHAPTER 4

BASIC CHARACTERIZATION STUDIES

4. Basic Characterization Studies

Within this study there were a number of intermediate steps that needed to be taken. First was to understand some of the basic properties of the materials under investigation. Next, since a new experiment was developed (flat flame burning with horizontal particle injection), some basic characterization of the individual components of the experiment was required. Finally, with a newly designed combustor, its behavior under well-defined conditions needed to be understood. This chapter discusses these basic characterization studies that needed to take place prior to obtaining the results that were the main focus of the study. It is broken into three main sections, particle characterization, flat flame burner experiment characterization, and airbreathing combustor characterization.

4.1 Particle Characterization

This study focuses on two different types of nanoparticles. The first is designated as 50 nm ALEX and was purchased from the Argonide Corporation. ALEX is a trade name for aluminum particles formed from the explosion of aluminum wires[76]. The second particles type to be investigated was SB99. SB99 is a boron nanoparticle that was supplied by the Naval Surface Warfare Center – Indian Head Division who purchased the

material from the SB Boron Corporation. The technique used for manufacturing the particles is unknown to the author.

4.1.1 Thermal Gravimetric Analysis (TGA)

A Thermal Gravimetric Analysis was performed to investigate the reactivity of the nanoparticles involved in this study. TGA is a thermal analysis technique used to measure changes in the mass of a sample as a function of temperature and/or time[77]. This technique is commonly used to determine a samples' inorganic material content, degradation temperatures, moisture, etc. In short, to perform a TGA analysis, a sample was tared in a sample pan attached to an ultra-senistive microbalance apparatus inside of a high temperature furnace[77]. The temperature of the furnace was gradually increased at a specified rate. Simultaneously, the mass addition or loss was continually monitored until the desired upper temperature limit was achieved. The environments are commonly argon, helium, nitrogen, air, or even pure oxygen.

4.1.1.1 Determination of Particle Active Content by TGA

The amount of mass gained due to the oxidation process of the particles was found by performing a TGA analysis in a 50/50 oxygen/argon environment. This allows one to deduce the active content of particle. Active content is defined as the amount of pure material in a given particle. This analysis assumes that the samples undergo complete oxidation; therefore the mass added to the sample during oxidation is exclusively a result of oxygen reacting with the particles. The stoichiometric ratio and the amount of oxygen gained during oxidation was used to determine the amount of

active content in the particles. The mass of the oxygen due to oxidation can be expressed as:

$$m_{ox} = \Delta m = m_f - m_i$$

where

m_i: initial mass of the sample

m_f: final mass of the sample

For the complete oxidation of aluminum in an oxygen environment, the stoichiometric equation can be written as:

$$4Al + 3O_2 \rightarrow 2Al_2O_3$$

therefore,

moles of Al = 4/3 moles of O_2

Converting moles of aluminum and moles of oxygen to their respective masses, we get

$$\frac{m_{Al}}{MW_{Al}} = \frac{4}{3}\frac{m_{O_2}}{MW_{O_2}}$$

Finally rearranging and solving for the mass of aluminum we obtain:

$$m_{Al} = \frac{4}{3}\frac{MW_{Al}}{MW_{O_2}} m_{O_2}$$

Calculating the mass of aluminum based on the mass of oxygen due to full oxidation, we have

$$m_{Al} = 1.124 m_{O_2}$$

As an example, using the results obtained from the 50 nm ALEX particles, the percentage mass increase, ζ_i, due to full oxidation of aluminum is 81.95% determined by subtracting the baseline value from the peak value as shown in Figure 4.1.

Figure 4.2 shows the mass gain plot for the SB99 material. The slight dip below 100-weight% in the low temperature regime is due to the evaporation of moisture that was collected in the powder. A similar analysis to the one performed for the ALEX particles reveals that the SB99 material was 72.2% pure boron. The remaining volume of each material was assumed to be the metal oxides Al_2O_3 and B_2O_3 for each material.

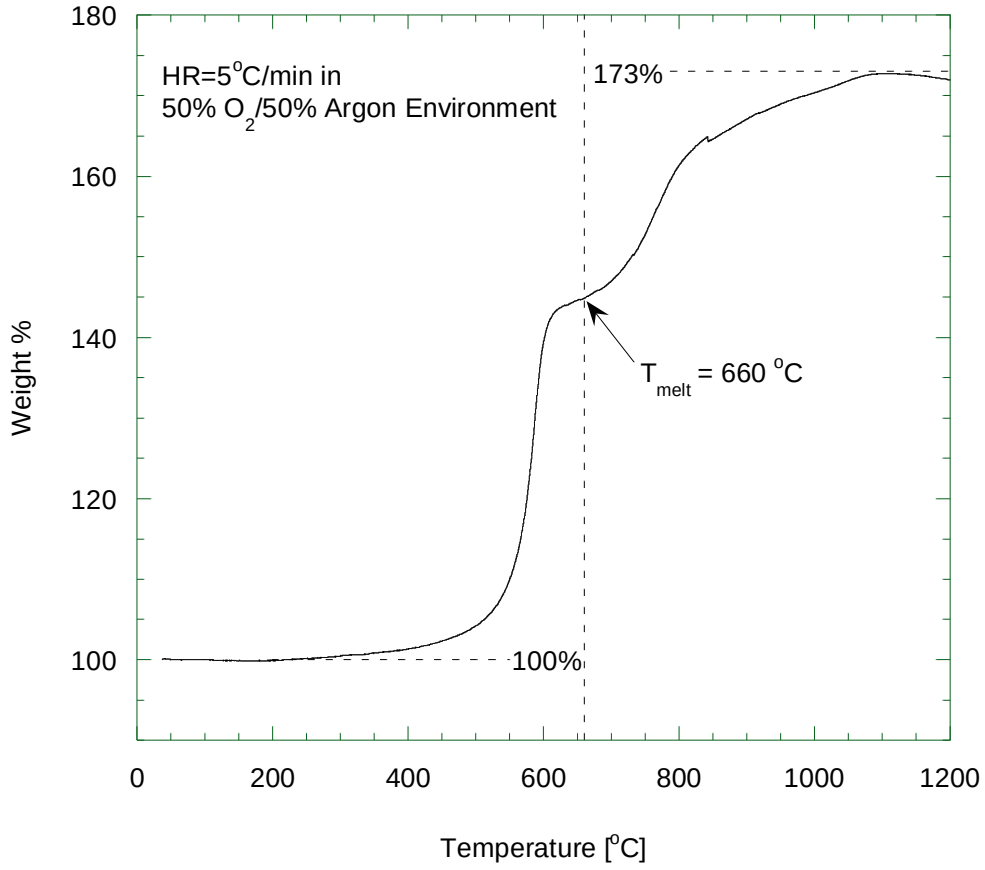

Fig. 4.1 TGA of 50nm ALEX

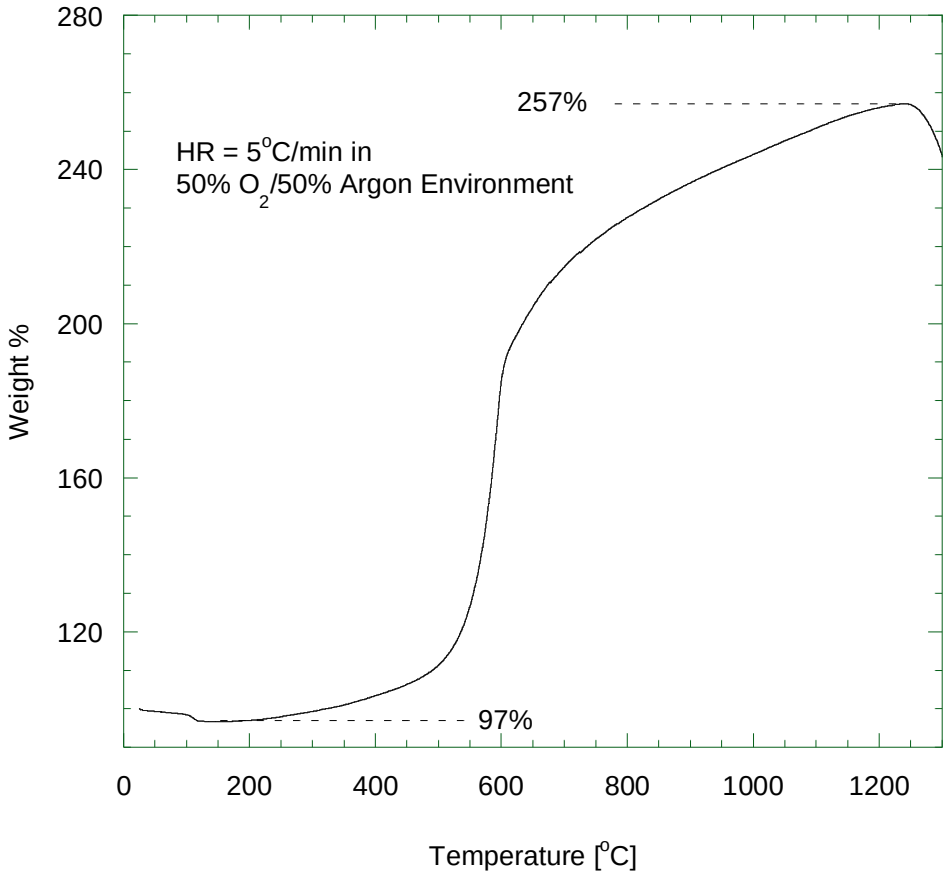

Fig. 4.2 TGA of SB99

4.1.2 Scanning Electron Microscope Imaging (SEM)

Two major uses of a Scanning Electron Microscope (SEM) are to produce high-resolution images and to provide a visual record of the surface of sub-micron materials[78]. The resolution of a typical SEM is about 0.01 μm[79]. Its great depth of field and the accurate rendition of surface features make the SEM well suited to particle sizing and morphology studies[79]. However, when imaging with an SEM, one needs to take precautions against the build up of electric charge on the sample surface, which can deflect the electron beam and cause distortion of the image. Generally this is accomplished by applying a very thin coating of gold or carbon.

Figures 4.3 and 4.4 are SEM Images of the ALEX and SB99 particles respectively. In order to achieve an image with reasonable resolution, the particles were coated with a 60/40 gold/palladium coating. The coating was necessary to eliminate charging of the particles since the materials were conducting. The coating adds approximately 7.5 nm radially to the particles. The images show that both sets of particles are highly spherical in nature.

The manufacturer specifies the ALEX particles as 50 nm, but Figure 4.3 shows that although there were some ALEX particles that were approximately 50 nm in size, the overall size distribution was quite wide with some particles close 200 nm.

Figure 4.4 shows that the SB99 particles were highly agglomerated, but majority of the primary particles were near 50 nm in diameter or less. Reference 80 suggests that the average particle size of the SB99 particles is 62 nm. The images also show that both particle types suffer from some agglomeration. That is, the particles were stuck together to create larger particles. This is important because this is the likely condition that the particles enter the airbreathing combustor and not in their primary particle size.

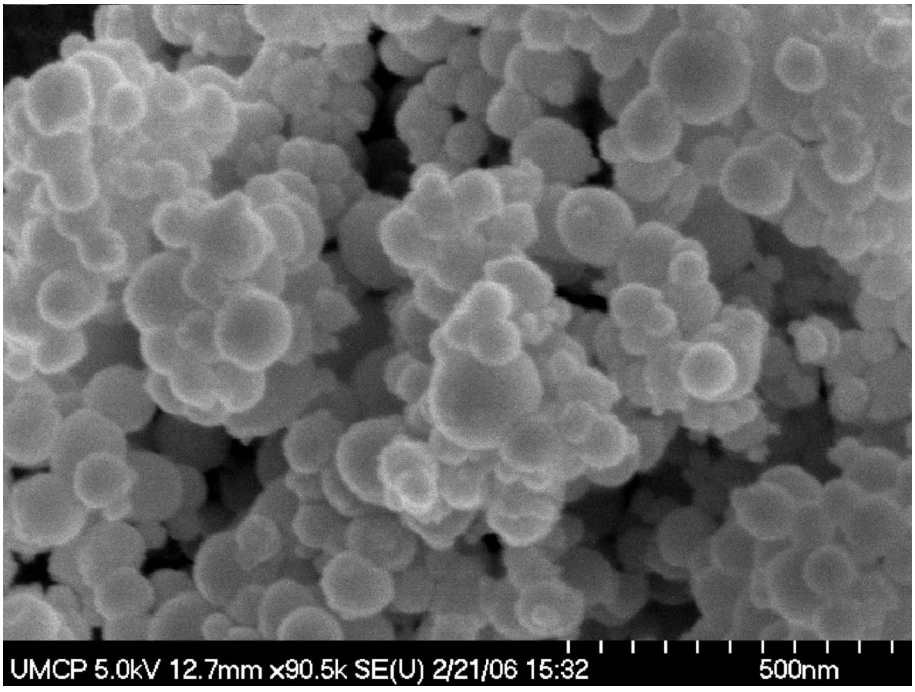

Fig. 4.3 SEM of "50 nm" ALEX

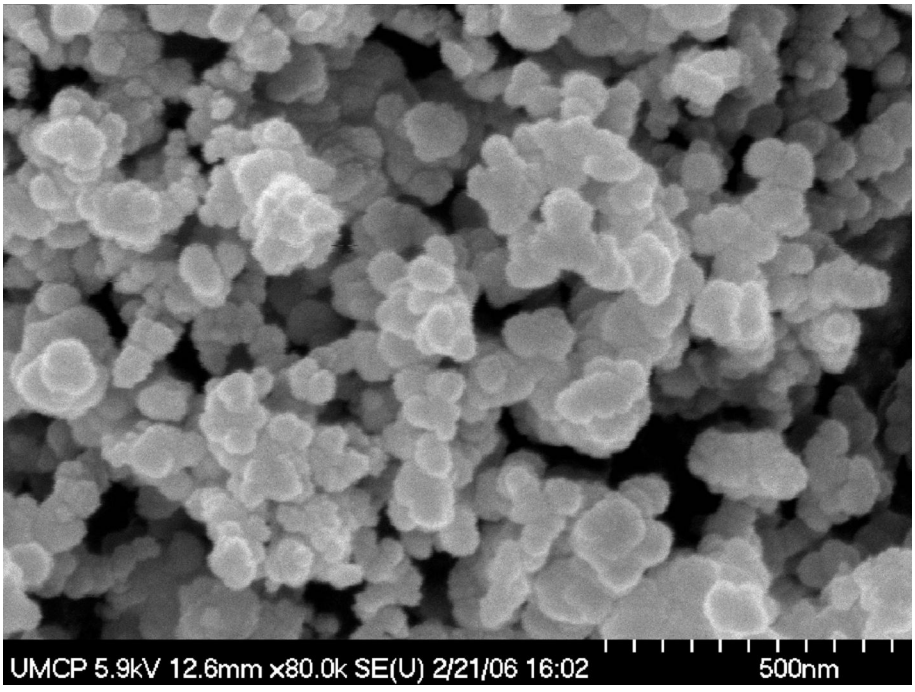

Fig. 4.4 SEM of SB99 Boron Particles

4.2. Flat Flame Burner and Aerosol Injection Characterization

The next portion of this study involved characterizing the McKenna Flat Flame Burner at specified test conditions and the aerosol injection system for the particle ignition and burn time experiments.

4.2.1 Velocity Measurements

A total of 3 different injection velocities were measured corresponding to three different volumetric flow rates controlled by a rotameter. All measurements were made in "cold flow", i.e. non-reacting over a wide range of crossflows, and momentum flux ratios. The goal of the experiment was to cover the range of momentum flux ratios that would be covered in reacting flow, such that the force acting on the jet by the crossflow would be similar. The definition of momentum flux ratio is given by equation 4.1.

$$J = \frac{\sqrt{\rho_J U_j^2}}{\sqrt{\rho_\infty U_\infty^2}} \qquad \text{Eq. 4.1}$$

where the ρ and U represent density and velocity respectively, and the subscripts j and ∞ represent the jet and crossflow respectively.

Table 4.1 provides a summary of the PIV test conditions. As the table indicates, for all of the injection conditions, the jet remained below the critical Reynolds Number (2300) for transition to turbulence, indicating that at the jet exit the flow was laminar for all test conditions. The Reynolds number was based on the injection tube inner diameter (1 mm). The volumetric flow rates were specified by rotameters for all gases, and the average velocities are based upon the results of the one dimensional continuity equation, based on the cross-sectional area of the injection tube. The details of the test set up are provided in Chapter 3.

Table 4.1 Cold Flow PIV Experiment Test Matrix

Burner (Crossflow) Properties		**Jet Properties**			
Volumetric Flow Rate (L/min)	Average Velocity (m/s)	Volumetric Flow Rate (L/min)	Average Velocity (m/s)	Reynolds Number	Momentum Flux Ratio
2.60	0.0153	0.61, 0.84, 1.15	12.89, 17.93, 24.30	811, 1128, 1529	842, 1171, 1587
6.63	0.0391	0.61, 0.84, 1.15	12.89, 17.93, 24.30	811, 1128, 1529	330, 458, 621
10.67	0.0629	0.61, 0.84, 1.15	12.89, 17.93, 24.30	811, 1128, 1529	205, 285, 386
14.71	0.0867	0.61, 0.84, 1.15	12.89, 17.93, 24.30	811, 1128, 1529	149, 207, 280
18.74	0.1105	0.61, 0.84, 1.15	12.89, 17.93, 24.30	811, 1128, 1529	117, 162, 220
22.78	0.1343	0.61, 0.84, 1.15	12.89, 17.93, 24.30	811, 1128, 1529	96, 134, 181
26.82	0.1581	0.61, 0.84, 1.15	12.89, 17.93, 24.30	811, 1128, 1529	82, 113, 154
30.85	0.1819	0.61, 0.84, 1.15	12.89, 17.93, 24.30	811, 1128, 1529	71, 99, 134
34.89	0.2057	0.61, 0.84, 1.15	12.89, 17.93, 24.30	811, 1128, 1529	63, 87, 118
38.93	0.2295	0.61, 0.84, 1.15	12.89, 17.93, 24.30	811, 1128, 1529	56, 78, 106
42.96	0.2533	0.61, 0.84, 1.15	12.89, 17.93, 24.30	811, 1128, 1529	51, 71, 96
47.00	0.2771	0.61, 0.84, 1.15	12.89, 17.93, 24.30	811, 1128, 1529	47, 65, 88

Figure 4.5 is an example of an image pair collected during an experiment. From a total of 50 image pairs collected for a given experiment, velocity vectors were obtained and an example can be seen in Figure 4.6. The image in Figure 4.6 corresponds to the case of highest crossflow (47 L/min) and the intermediate injection flow rate (0.84 L/min). Contours of the axial-component of velocity are given for all three injection flow rates at the highest crossflow condition in figures 4.7-4.9. Qualitative comparison of figures 4.7-4.9 shows that as the injection flow rate is decreased the jet is displaced more by the crossflow as would be expected.

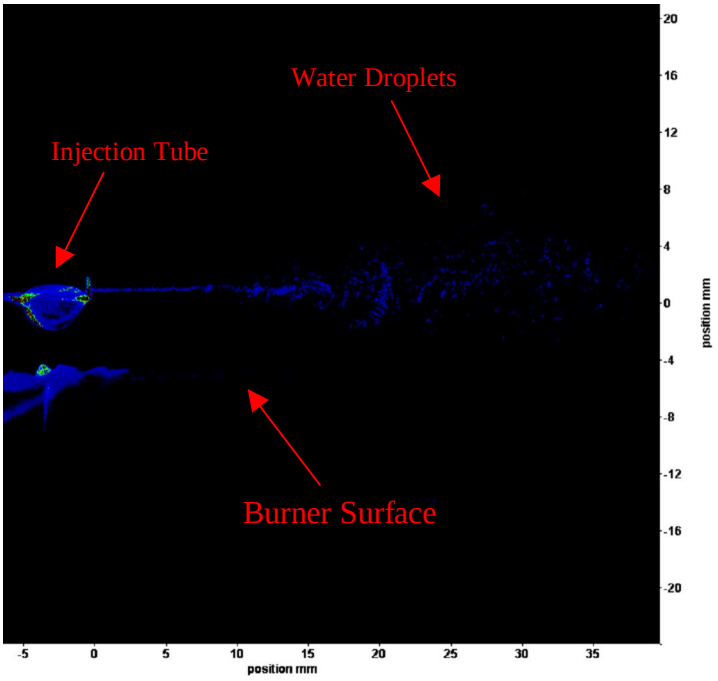

Fig. 4.5 Example of Image Pair

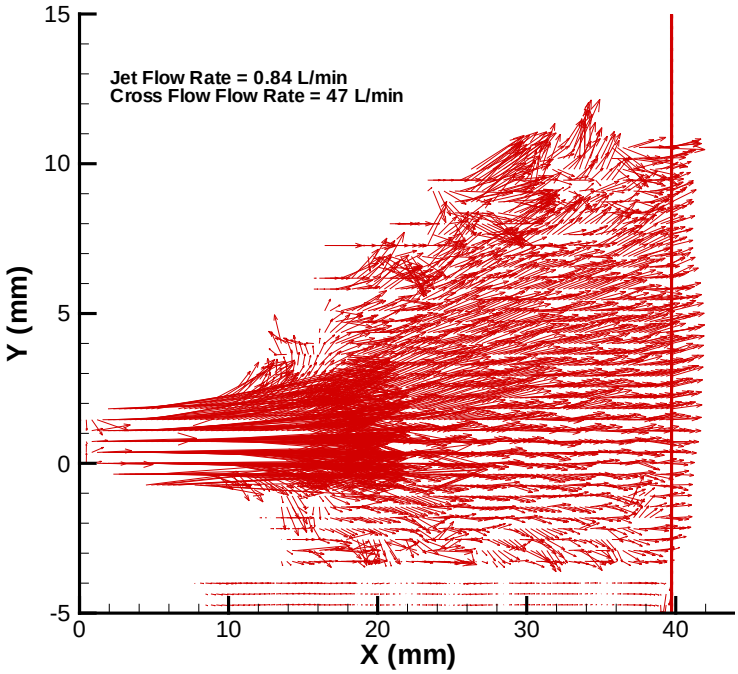

Fig. 4.6 Velocity Vectors Obtained from PIV Experiments

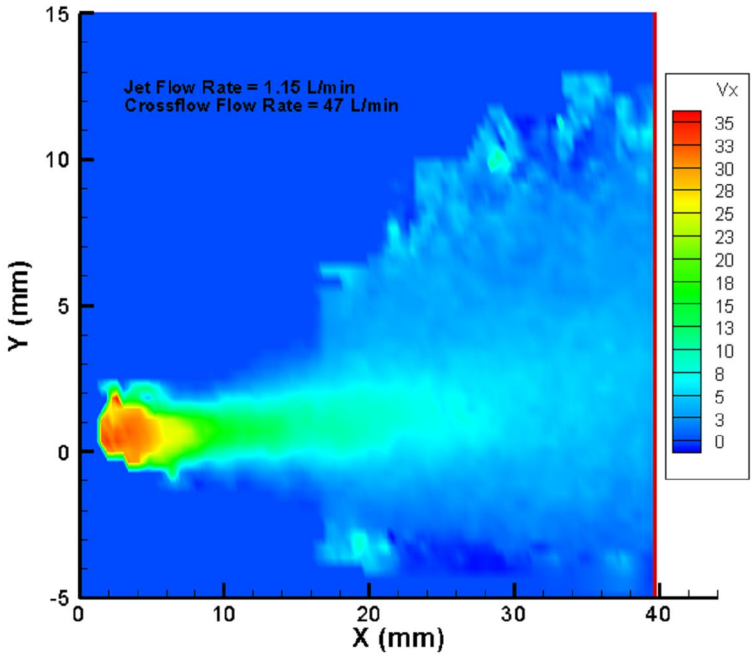

Fig. 4.7 Axial-Component of Velocity Contour for Highest Injection Flow Rate and Crossflow

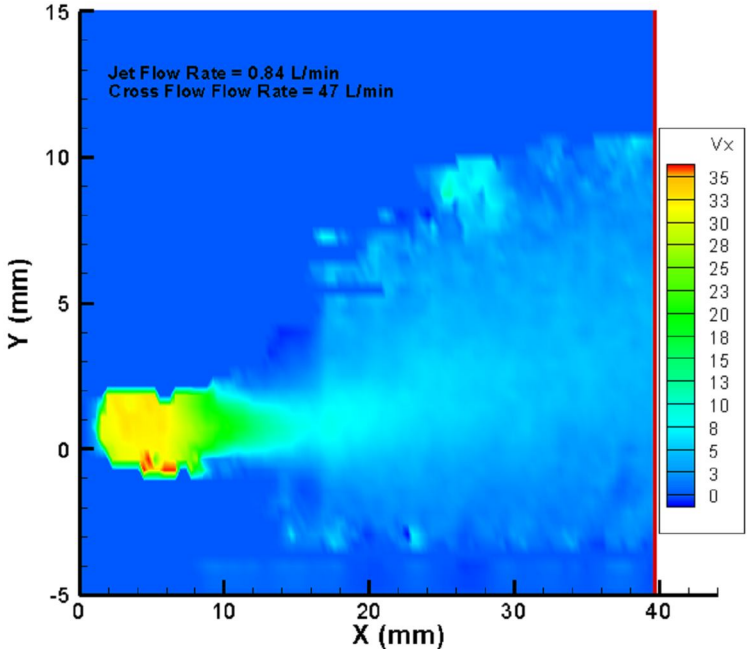

Fig. 4.8 Axial-Component of Velocity Contour for Intermediate Injection Flow Rate and Highest Crossflow

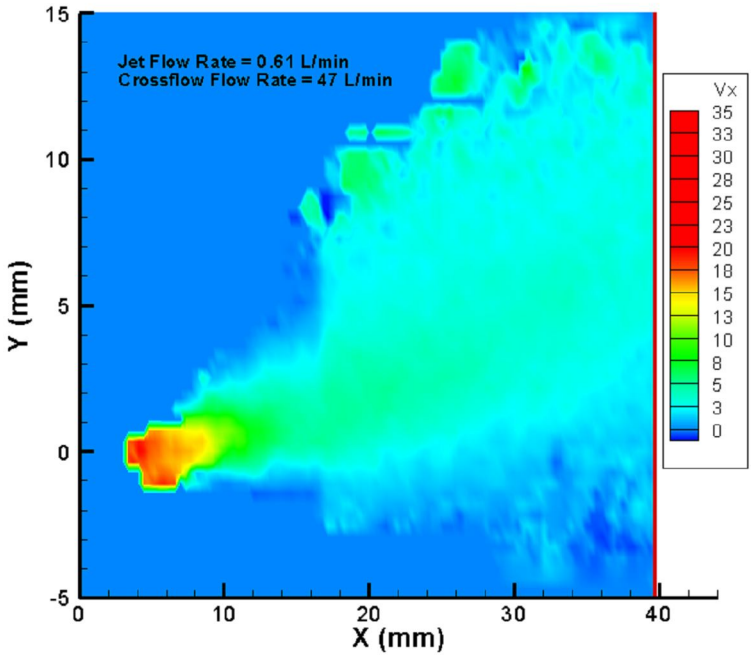

Fig. 4.9 Axial-Component of Velocity Contour for Lowest Injection Flow Rate and Highest Crossflow

Using the commercially available Tecplot computer software, the centerline axial-component of velocities were extracted for use in determining the burning times and ignition delays of the boron nanoparticles. Figure 4.10 shows a collection of a wide range of the data taken in the intermediate jet flow rate case. The numbers in the legend correspond to increasing crossflow, for instance 1a was the lowest crossflow condition (2.60 L/min), and 12a was the highest crossflow condition (47 L/min). As figure 4.10 indicates, the axial-component of the centerline velocity was not greatly influenced by the crossflow over the test conditions. For the actual testing of the boron nanoparticles in the reacting flow, the intermediate injection flow rate was selected.

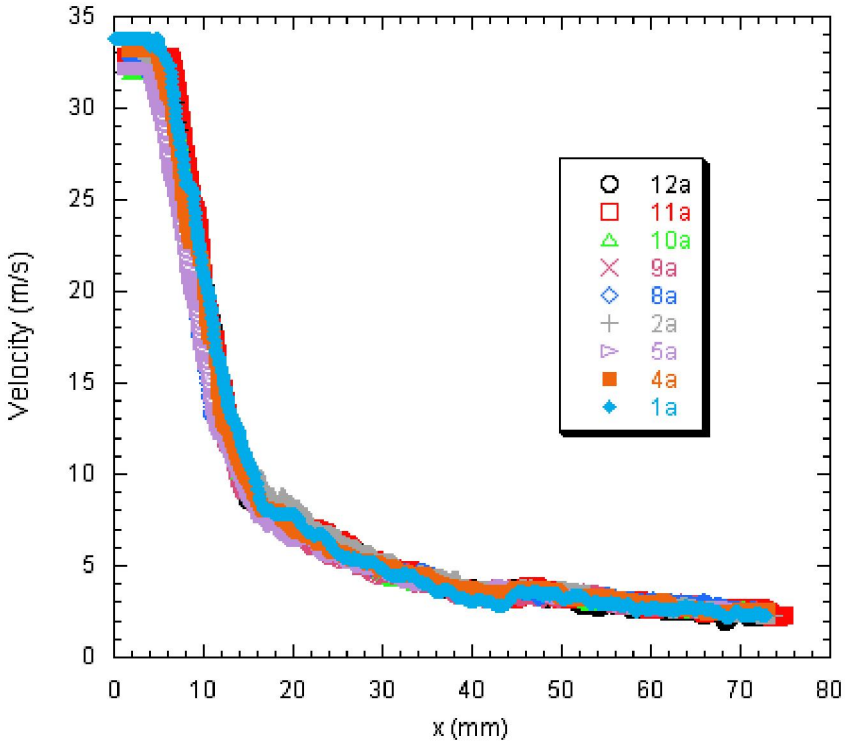

Fig. 4.10 Axial-Component of Centerline Velocity for Intermediate Injection Flow Rate and Several Crossflows

As figure 4.10 shows, for a given injection velocity, the axial-component of the centerline velocity was relatively unaffected by the change in crossflow. Applying the analysis described in Section 2.6 of this thesis of a nonreacting-laminar jet of fluid flowing into a quiescent atmosphere can reasonably explain the results of the PIV experiments.

In this study, the jet actually exhausted into a crossflow, however, a correlation (Eq. 4.2) similar to that of equation 2.24 still represented the data well after a spatial duration of approximately 6 mm, particularly for the two higher injection flow rates.

$$u_{x,CL}(m/s) = \left[a * u_e^2\right] * x^b \qquad \text{Eq. 4.2}$$

In this case the terms involving viscosity and the tube radius have been combined into a single constant, *a*. u_e represents the average of the maximum velocities measured for each crossflow for a given injection flow rate. *a*, and *b* where solved for by applying a curve fit in the form of equation 4.2 in the commercially available computer software Kaleidagraph, the results of which can be seen in figures 4.11-4.13. The red line in the plots is the curve fit itself, which follows the data extremely well, especially for the two higher injection flow rate conditions. In general, the value of the exponent *b*, is in good agreement with the theory of a laminar jet exhausting into a quiescent atmosphere at these levels of crossflow. The exponent, b, ranges from -0.82 to -1.12 compared to –1 which is dictated by theory. Finally since measurements very close to the injection source were not very reliable, the maximum velocity was taken to represent the core centerline velocity up until it reached six millimeters at which point the correlation represents the velocity well. Therefore, when using the measurements to determine burning time and ignition time data, a piecewise function for velocity is used which is given in figures 4.11-4.13. During all of the particle testing, the intermediate jet flow rate was selected (0.84 L/m), therefore the velocity was represented by equation 4.3.

$$\begin{aligned} 0 \le x \le 6mm &\rightarrow u_{x,cl} = 32.79 m/s \\ x > 6mm &\rightarrow u_{x,cl} = \left[0.208(32.79)^2\right] x^{-1.11} \end{aligned} \qquad \text{Eq. 4.3}$$

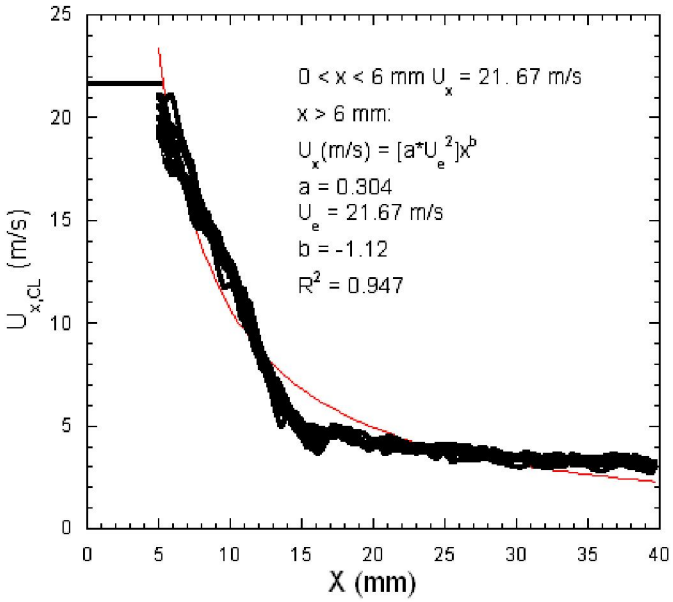

Fig. 4.11 Centerline Axial-Component of Velocity of Lowest Jet Flow Rate (0.61 L/m)

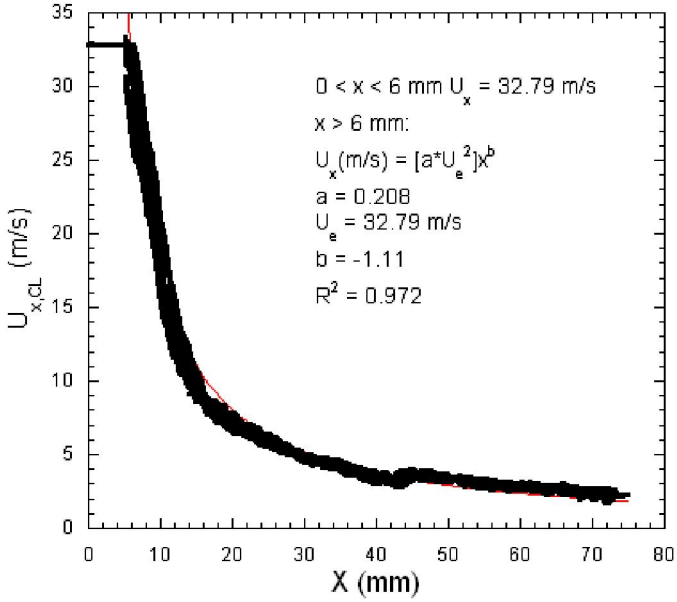

Fig. 4.12 Centerline Axial-Component of Velocity of Intermediate Jet Flow Rate (0.84 L/m)

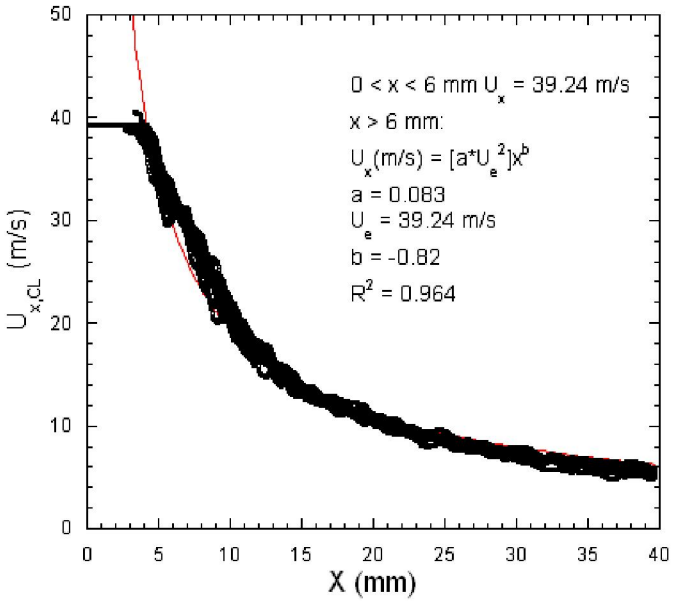

Fig. 4.13 Centerline Axial-Component of Velocity of Highest Jet Flow Rate (1.15 L/m)

With an expression for the particle velocity now known, and the spatial locations (x_1 (start of burning) and x_2 (end of burning)) of the particle burning obtained from the ICCD camera chemiluminescence images, the ignition and burning times were calculated using the following procedure.

$$t_b = t(x_2) - t(x_1) \qquad \text{Eq. 4.4}$$

where t_b was the burning time, t_1 and t_2 were the times associated with reaching the spatial locations x_1 and x_2. The times, t_1 and t_2 are determined utilizing the correlation developed and shown in equation 4.3.

As an example, the location where t_2 took place, i.e. x_2, was found by a technique described in Chapter 5. Since x_2 was now known, and the velocity at a given spatial

location was known from figure 4.12 the time it for the particles to reach x_2 was determined by:

$$t_i = \sum_{i}^{i} t_{i-1} + dt_i \qquad \text{Eq. 4.5}$$

where the subscript *i* refers to a specific location and the subscript *i*-1 refers to its nearest neighbor for which spatial velocity data was available. The incremental time dt_i was found by:

$$dt_i = \frac{dx_i}{U_{ave_i}} \qquad \text{Eq. 4.6}$$

where dx_i is the incremental spatial resolution of the velocity data and $U_{ave,i}$ was determined by:

$$U_{ave_i} = \frac{U_i + U_{i-1}}{2} \qquad \text{Eq. 4.7}$$

where once again, the subscripts *i* and *i*-1 refer to the particular data point (*1* or *2*) and its nearest neighbor for which spatial velocity data was available.

4.2.2 Temperature Measurements

As was outlined in Chapter 3, temperature measurements of the flat flame burner were taken using a 200 μm B-type thermocouple at three locations. After correction for radiation loss, the average of the three measurements was taken and used for data analysis purposes. Table 4.2 gives the test matrix for the flat flame burner experiments as well as the results of the temperature measurements. As the table indicates the measured temperatures are well below the adiabatic flame temperatures at all conditions. This was mainly due to heat loss to the burner through the cooling water. In fact other

researchers[81,82] have demonstrated that the burner is relatively insensitive to equivalence ratio. Instead temperature is driven more by fuel flow rate (i.e. thermal output).

Table 4.2: Flat Flame Burner Test Matrix

Test Condition	Volumetric Flow Rates (L/min)			Product Mole Fractions				Average Burner Temperature (K)
	O_2	Air	CH_4	O_2	H_2O	CO_2	N_2	
1	16.8	30.2	5.8	0.200	0.234	0.117	0.450	1684
2	21.0	29.8	7.3	0.200	0.266	0.133	0.400	1808
3	24.8	27.5	8.7	0.200	0.300	0.150	0.350	1854
5	28.6	24.5	10.1	0.200	0.234	0.117	0.450	1637
6	23.2	30.2	5.6	0.300	0.200	0.100	0.400	1630
7	28.9	29.8	7.3	0.300	0.233	0.117	0.350	1797
8	33.2	26.8	8.8	0.300	0.267	0.133	0.300	1872
9	19.2	24.9	4.6	0.300	0.200	0.100	0.400	1578
10	14.0	26.5	5.8	0.150	0.267	0.133	0.450	1718
11	17.7	33.4	7.3	0.150	0.267	0.133	0.450	1814
13	11.0	20.7	4.5	0.150	0.267	0.134	0.449	1596
14	8.5	28.9	4.5	0.100	0.233	0.117	0.550	1614
15	11.0	28.3	5.6	0.100	0.267	0.134	0.499	1712
16	13.7	35.3	6.9	0.100	0.267	0.134	0.499	1791

4.2.3 Particle Size Measurements

Although the primary particle size of the nanosized boron used in the flat flame burner experiments was near 50 nm, agglomeration of the particles was inevitable even with the sonicating atomizer. In order to understand the size distribution of the agglomerated particles two separate measurements were taken and described in the subsequent sections.

4.2.3.1 TEM

A Transmission Electron Microscope (TEM) was used as a visual aid to understand the agglomerate size. The limit of resolution for a typical TEM is less than

0.001 μm[79]. In a TEM electrons are generated by thermoioninc emission from a heated tungsten filament and are focused by magnetic lenses. Particles in the electron beam absorb and scatter electrons to produce a two-dimensional silhouette image. Samples must be deposited on a special grid for imaging. Typically the grids are 200 mesh electrodeposited screen with a thin film of carbon or Parlodion (1-4% nitrocellulose in amyl acetate covering the screen openings[79]. The film is sufficiently thin compared to the particles such that it causes only slight attenuation of the electron beam, whereas the samples (particles) scatter and absorb the electron beam significantly to form a high contrast image.

A small section of tubing was attached to the end of the aerosol injection system, which led to a TEM grid. The aerosol was allowed to flow for several minutes to ensure sufficient coverage of the grid. Once samples were applied to the grid, images using the TEM were taken and can be seen in Figures 4.14 and 4.15. The images show that the particles are in fact large non-spherical agglomerates of small primary particles. The agglomerates in the images are near 200 nm in size.

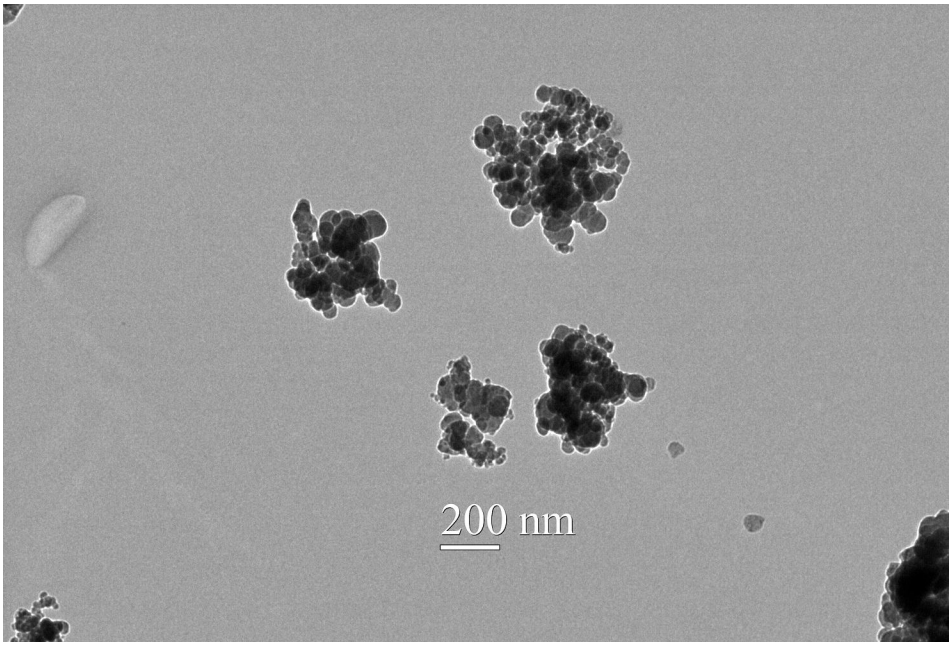

Fig. 4.14 TEM Image of Aerosolized SB99

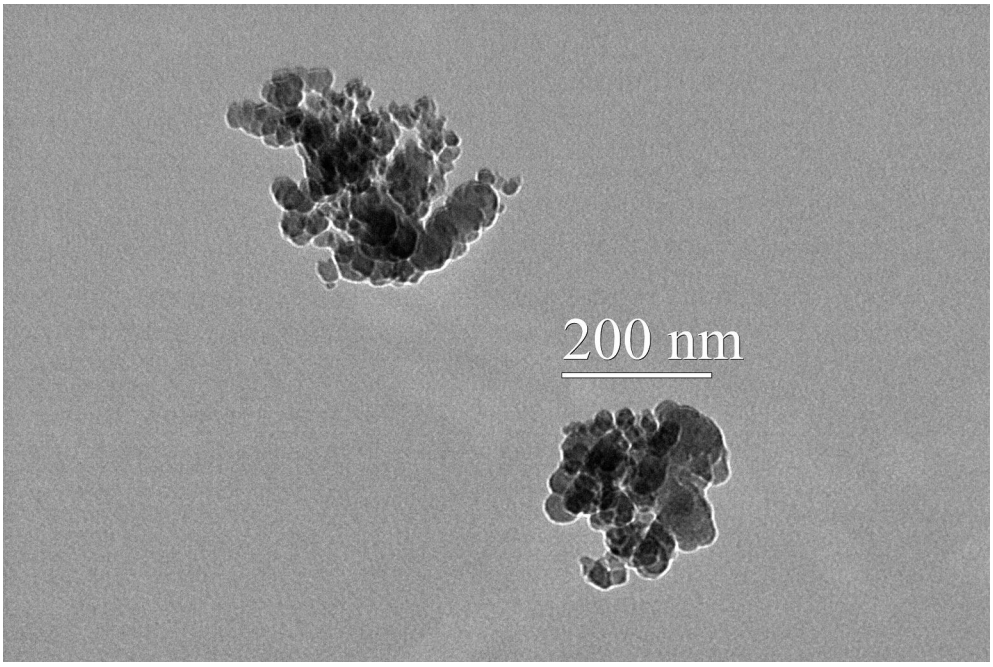

Fig. 4.15 Close-up TEM Image of Aerosolized SB99

4.2.3.2 DMA

As a second and more quantitative measure of agglomerate size a Differential Mobility Analyzer (DMA) was employed. DMA's are commonly used to measure

particle size distribution with high resolution in the submicrometer range[79]. Figure 4.16 is a schematic diagram of a typical DMA set up. The DMA takes advantage of certain properties of a charged particle. Essentially when a charged particle is placed in an electric field it is acted on by a force, F_E. The force on the particles results in the particles traveling at the terminal electrostatic velocity, V_{TE}. For particles in the Stokes region, V_{TE} is obtained by equating (Eq. 4.8) the electrostatic force to the Stokes Drag (Eq. 4.9) and solving for the velocity (Eq. 4.11).

$$neE = \frac{3\pi\mu Vd}{C_c} \qquad \text{Eq. 4.8}$$

$$F_D = \frac{3\pi\mu Vd}{C_c} \qquad \text{Eq. 4.9}$$

where μ is the fluid viscosity, V is the velocity of the particle, d is the particle diameter, n is the total number of elementary units of charge on the particle, e is the charge of an electron, E is the electric field strength, and C_c is the Cunningham Correction factor given by:

$$C_c = 1 + \frac{2.52\lambda}{d} \qquad \text{Eq. 4.10}$$

where λ is the mean free path.

$$V_{TE} = \frac{neEC_c}{3\pi\mu d} \qquad \text{Eq. 4.11}$$

One can relate a particles ability to move in an electric field in terms of the particle's electrical mobility, Z, the velocity of the particle with a charge ne in an electric field of unit strength. Electrical mobility is defined by:

$$Z = \frac{V_{TE}}{E} = \frac{neC_c}{3\pi\mu d} \qquad \text{Eq. 4.12}$$

In a DMA, an aerosol is passed through a neutralizer to the Boltzmann equilibrium charge distribution before entering the electrostatic classifier section. A laminar flow of clean air is surrounded by a thin annular layer of aerosol as the two fluids travel axially between the central rod and the coaxial tube. The voltage is controlled on the central rod, and the tube is grounded. Near the bottom of the central rod is a gap that allows a small airflow to leave the classifier and exit through a central tube. Only particles with a narrow range of mobilities can enter the gap. Particles with larger mobilities reach the central rod before entering the gap, while those with lower mobilities go beyond the gap and are filtered out. Therefore, the exiting aerosol is nearly monodisperse. By adjusting the input voltage over a wide range and connecting the DMA to a Condensation Nuclei Counter (CNC) a size distribution can be obtained for a given aerosol.

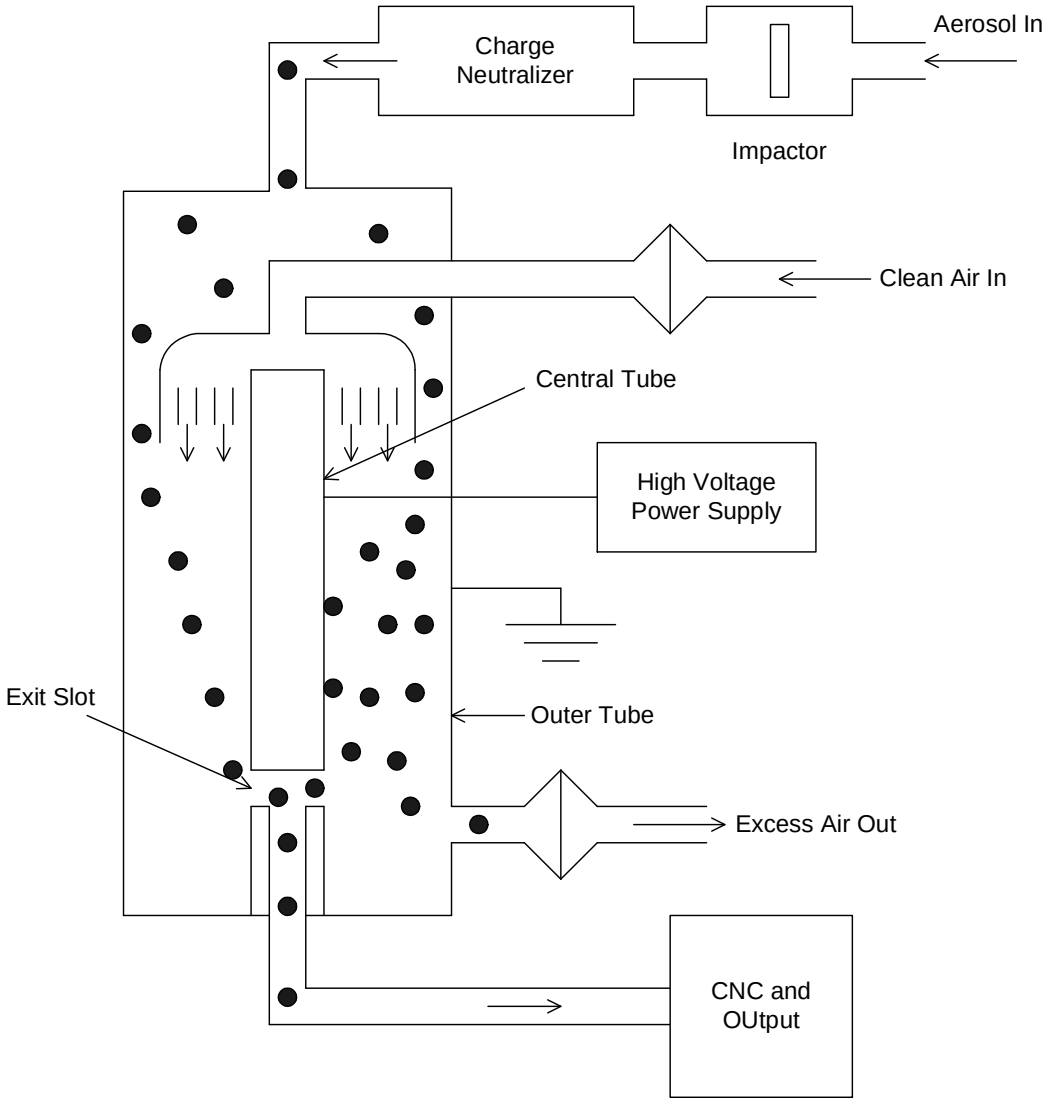

Fig. 4.16 Schematic Diagram of a Typical DMA Set Up[77]

Similar to the TEM sampling a tube was attached to the end of the aerosol injection system and the aerosol was sent to a DMA for analysis. Figure 4.17 shows the size distribution given by the DMA in terms of a mobility diameter. The mobility diameter is defined as the diameter of a sphere with the same friction coefficicent as an agglomerate under similar dynamic conditions[83]. As figure 4.17 shows, the size

distribution is fairly wide, ranging from about 20 nm to about 400 nm with a mean of 200 nm.

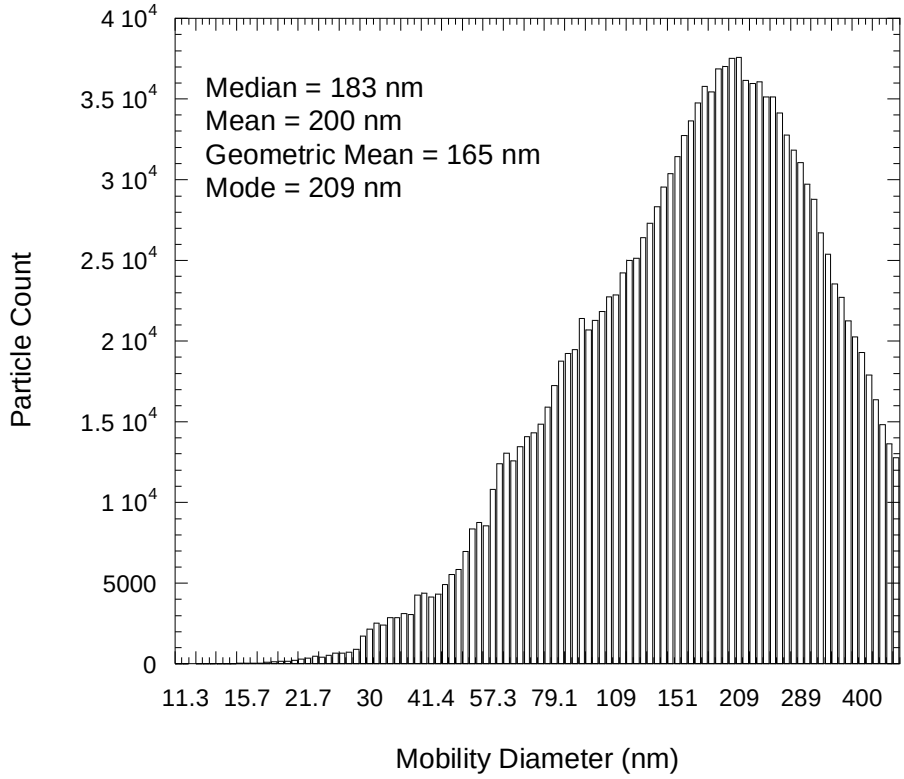

Fig. 4.17 Agglomerate Size Distribution by DMA

4.3 Airbreathing Combustor Characterization

Prior to combustor operation with metallized fuels, a number of experiments were conducted to understand the operation of individual components as well as how the combustor behaved with a standard baseline fuel. The subsequent sections outline these experiments.

4.3.1 Gas Flow Calculation

In section 3.3.1, the details of how the gas flows were controlled were outlined. Since the static pressure data was recorded for all of the gas flows, an accurate estimate of mass flow rates for each individual experiment was possible. For each experiment, the data from the last second of combustor operation was averaged to give the static pressure used in flow rate calculations. In all cases, the measured static pressure was always sufficient to achieve a choked flow condition. Depending on the gas, this is roughly at least twice atmospheric pressure. All gas mass flow rates were calculated from equation 4.13.

$$\dot{m} = \frac{p_o A^*}{\sqrt{RT_o}} \sqrt{\gamma} \left(\frac{2}{\gamma + 1} \right)^{(\gamma+1)/2(\gamma-1)} \qquad \text{Eq. 4.13}$$

Where, p_o, A^*, R, T_o, and γ refer to the stagnation pressure, the throat area of the orifice, the gas constant, the stagnation temperature, and the ratio of specific heats respectively.

4.3.2 Particle Seeder Characterization

In order to determine the mass flow rate of particles a series of experiments were under taken to characterize the particle seeder. Initially, 3M Glass Bubbles, with an average size of 50 μm were used for debugging the system. The carrier gas used in all of the experiments was ethylene and was controlled by a LabView Virtual Interface (VI), a solenoid valve, and Setra Model 206 Static Pressure Transducer, and an O'Keefe choked flow orifice (0.040 inches, 0.102 cm).

After a carrier gas flow rate was selected, tests were run for different lengths of times and the particles were captured in a large bag and weighed on a high precision scale

between each test. In addition, the amount of particles remaining in the seeder was also weighed as a second measurement. The amount of particles placed into the seeder prior to testing was measured and kept constant to within ±0.03 grams because it was found that the seeding rate was very sensitive to the initial amount of particles in the seeder. Specifically, the seeding rate was very sensitive to the distance between the central exhaust tube and the particle interface. In the cases of the aluminum and boron testing, 25 grams of material was put into the seeder for testing. Typically, three tests per time duration were conducted in order to determine the repeatability of the seeder. After debugging, tests proceeded with ALEX/SB99 particles.

Figure 4.18 shows the results from four different test series; the error bars in the figure represent the measurement error for a particular test. The standard deviation for a particular duration ranges from about 0.03 grams to 0.14 grams. As figure 4.18 shows, for the duration of these tests, the total mass collected varies linearly with time. It was not expected that the linear trend would continue for long durations. In fact it was found that after some time the seeding rate approaches zero. During combustor testing, the slope of these lines was used as the mass flow rate of ALEX/SB99 particles. Following each combustor test, the particles remaining in the seeder were weighed to ensure that the total amount used was consistent with the characterization testing. Finally, the seeder was completely cleaned out between each test in order to ensure that each test was occurring under the same conditions.

In addition, since there was a significant amount of free volume in the particle seeder several experiments were conducted in order to determine the amount of time for the seeder to achieve a steady state gas flow rate. In this experiment, a Setra Model 206

Static Pressure transducer was placed just downstream of the seeder to determine when the gas flow after the seeder could be considered constant. An aluminum rod occupying approximately the same volume as the metallic nanoparticles was placed inside the seeder to simulate the real test condition free volume. Figure 4.19 shows the pressure traces of the gas flows during a combustor test for several of the gases used in the test as well as the pilot flame. Comparing the green line (downstream) to the purple line (upstream) it can be seen that after approximately 1.5 seconds the gas reached a steady state for this particular test condition. At 1.0 seconds, the gas reached about 75% of its steady state pressure.

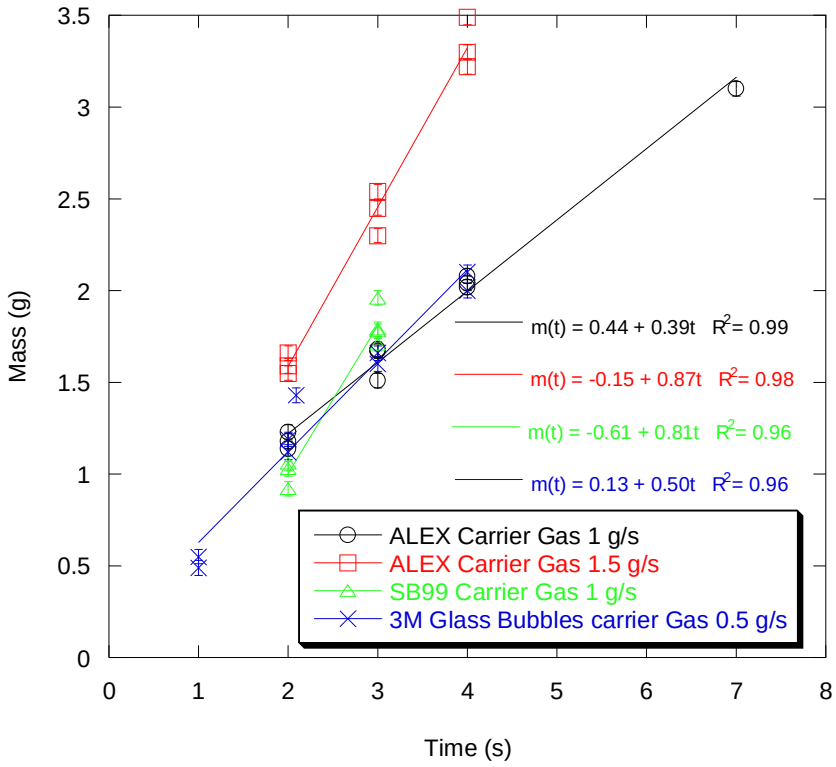

Fig. 4.18 Summary of Seeder Calibration Testing

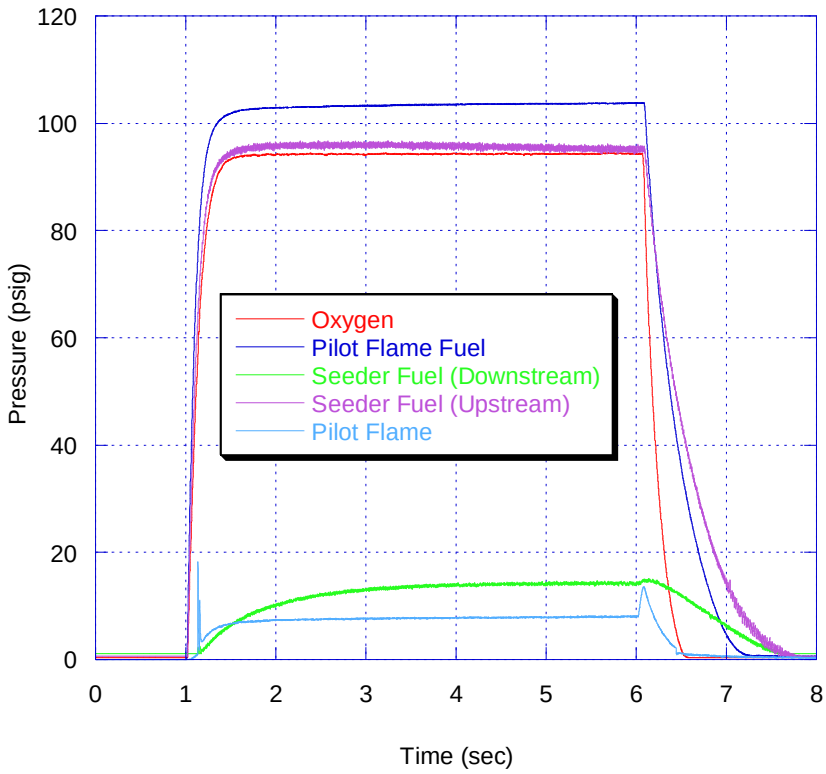

Fig. 4.19 Seeder Carrier Gas Filling Time

4.3.3 Pilot Flame Plume Measurements

As was mentioned earlier, the pilot flame operated on a mixture of ethylene and oxygen which was spark initiated, through a standard automotive spark plug. In all main combustor testing, the pilot flame conditions were held constant. In addition to the oxygen and ethylene, nitrogen was used at the conclusion of each test as a purge gas in order to quench any remaining combustibles and to help cool the system. In fact the small spike seen at the end of the test (light blue line seen in Figure 4.19) was a result of the purge gas turning on to conclude the test. Similarly the spike at the beginning of the test (t = ~1 second) was a result of the ignition of the flammable mixture.

Under normal operating conditions, the pilot flame operated in a steady manner at 4 psig. Table 4.3 provided a summary of the pilot flame test conditions as calculated using the NASA CEA 2000 Chemical Equilibrium computer code[84] based upon a measured combustor operating pressure. The exit temperature, and density were calculated based upon an isentropic flow assumption and the following equations considering that the exit pressure was atmospheric. The velocity was calculated by the one dimensional continuity equation.

$$\frac{P_2}{P_1} = \left(\frac{T_2}{T_1}\right)^{\frac{\gamma}{\gamma-1}} \qquad \text{Eq. 4.14}$$

$$\frac{P_2}{P_1} = \left(\frac{\rho_2}{\rho_1}\right)^{\gamma} \qquad \text{Eq. 4.15}$$

Table 4.3 Pilot Flame Operating Conditions (Calculated)

Measured Pressure (psig)	4
Adiabatic Flame Temperature (K)	3213
Gas Temperature (K) at Exit	3137
Equivalence Ratio Φ	1.07
Gas Exit Velocity (m/s)	800
Gas Density (kg/m^3) at Exit	$8.84*10^{-2}$
Specific Heat Ratio γ	1.11
Mole Fractions at Exit	
CO	0.25466
CO_2	0.13798
H	0.06121
H_2	0.06209
H_2O	0.25524
O	0.05329
OH	0.08937
O_2	0.08613

In addition to the parameters described above the pilot flame plume and crossflow interaction was studied to understand the effects of the crossflow on the plume penetration. A schematic diagram of the basic jet in a crossflow problem is provided in figure 4.20. Basically, as a jet exhausts into a crossflow, the jet trajectory gets deflected

as a result of the force of the crossflow hitting it. Therefore, as the crossflow is increased the jet penetration depth decreases.

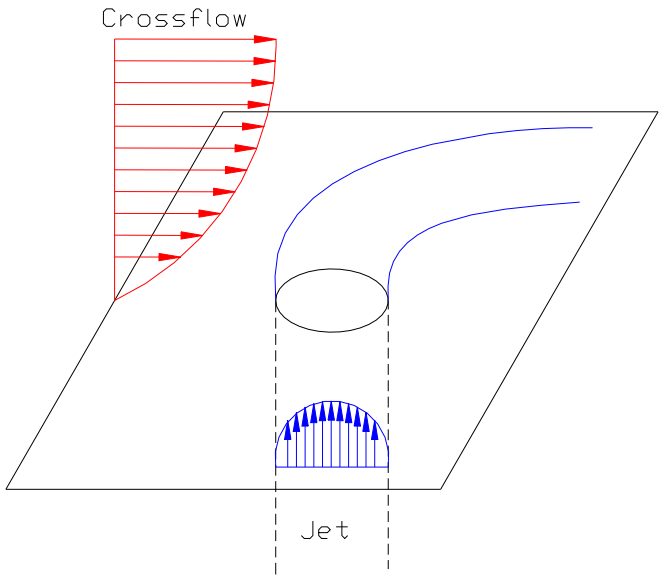

Fig. 4.20 Schematic Diagram of Jet in Crossflow Problem

Unfiltered images were taken with the use of an Intensified Charge Coupled Device (ICCD) Camera of the pilot flame operating in the combustor under airflow conditions selected for fulfilling the main goals of this study without any additional fuel to determine the penetration characteristics of the pilot flame. Figures 4.21-4.23 show light intensity contours of the three crossflows considered. In this case, the crossflow velocity, or combustor inlet velocity is calculated by the one dimensional continuity equation. As would be expected and is clear from the images, the penetration distance (y-axis) decreases from about 2 cm at 40 m/s to about 1.5 cm at 70 m/s.

From these contours the outer boundary was extracted using the commercially available computer software Tecplot to give the profile of the plume jets as seen in Figure 4.24. This figure is a direct comparison of the outer boundaries of the different

conditions and also shows the decreasing penetration depth with increasing crossflow. In this case, the jet exit was considered the origin for both the *x* and *y* locations.

Of primary importance in jet-crossflow interaction is the momentum flux ratio, which was given in equation 4.1, and can be considered the principal controlling parameter in determining the jet penetration[85]. Keffer and Baines[86] found that the penetration profile data obtained from a subsonic jet in crossflow collapsed to a single curve in the near injector region when the coordinate axis were scaled by the momentum flux ratio, *J*. After these profiles were collected, a correlation (Eq. 4.16) based upon the findings of Keffer and Baines[86] for the penetration of the plume jet was developed as a function of the momentum flux ratio, *J*, and physical dimensions such as the *x* and *y* locations of the jet, and the width of the slot, *w*. The results of this correlation can be seen in Figure 4.25, which shows that the data does in fact collapse to a single curve within experimental error.

$$\frac{y}{wJ} = a\left(\frac{x}{wJ}\right)^{n} \qquad \text{Eq. 4.16}$$

For crossflow ratios ranging from 3.06 to 5.36, the exponent, *n*, is 0.224.

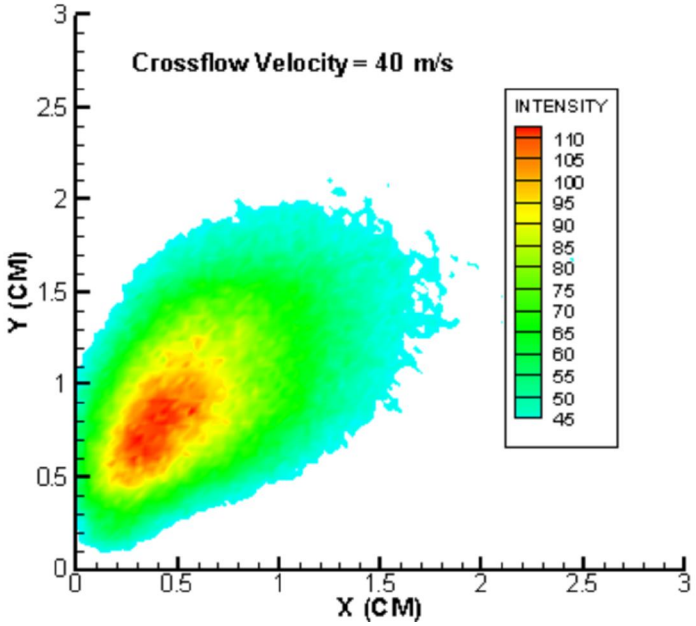

Fig. 4.21 Intensity Contour of Plume Jet for Crossflow of 40 m/s

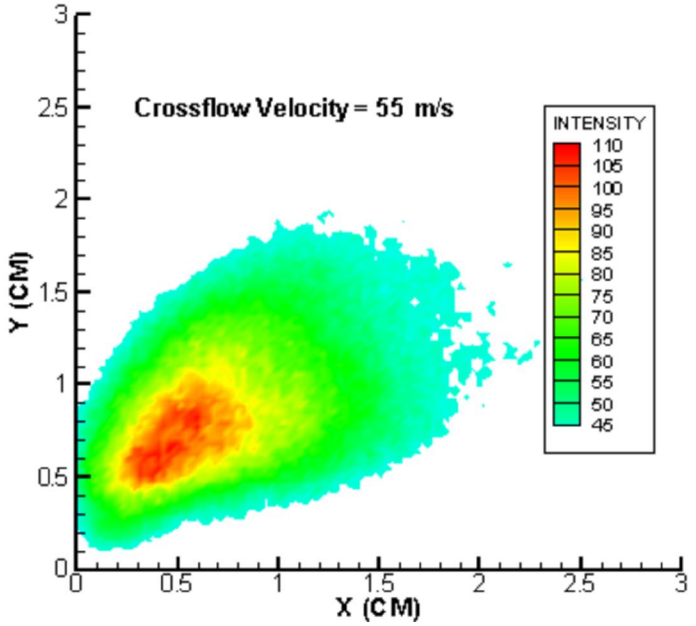

Fig. 4.22 Intensity Contour of Plume Jet for Crossflow of 55 m/s

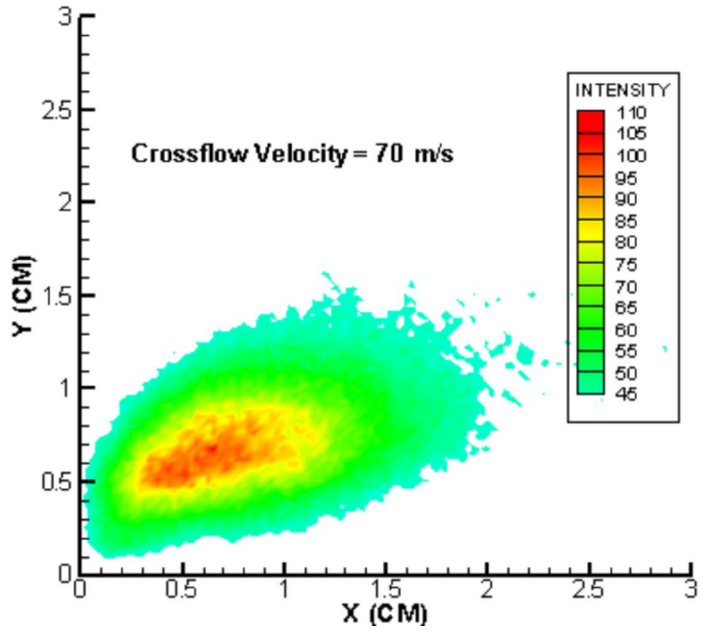

Fig. 4.23 Intensity Contour of Plume Jet for Crossflow of 70 m/s

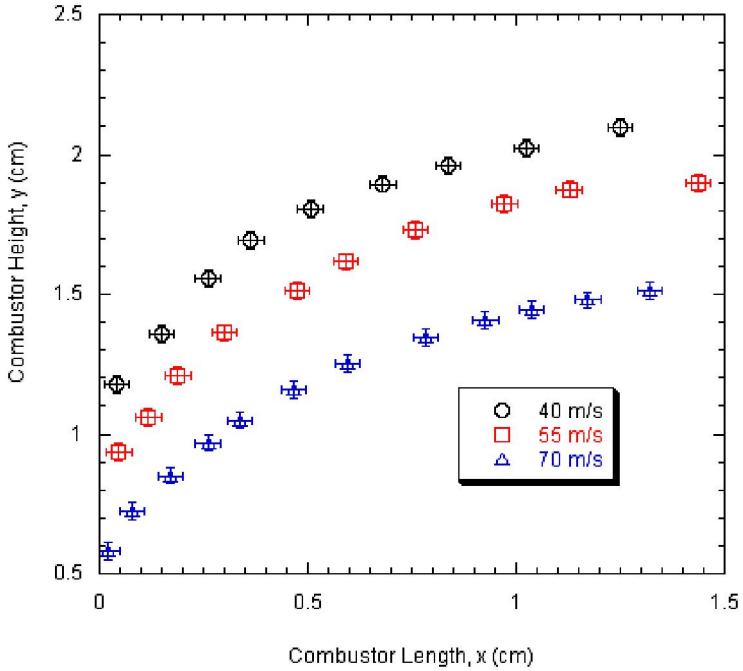

Fig. 4.24 Outer Jet Boundary Profiles for Selected Crossflows

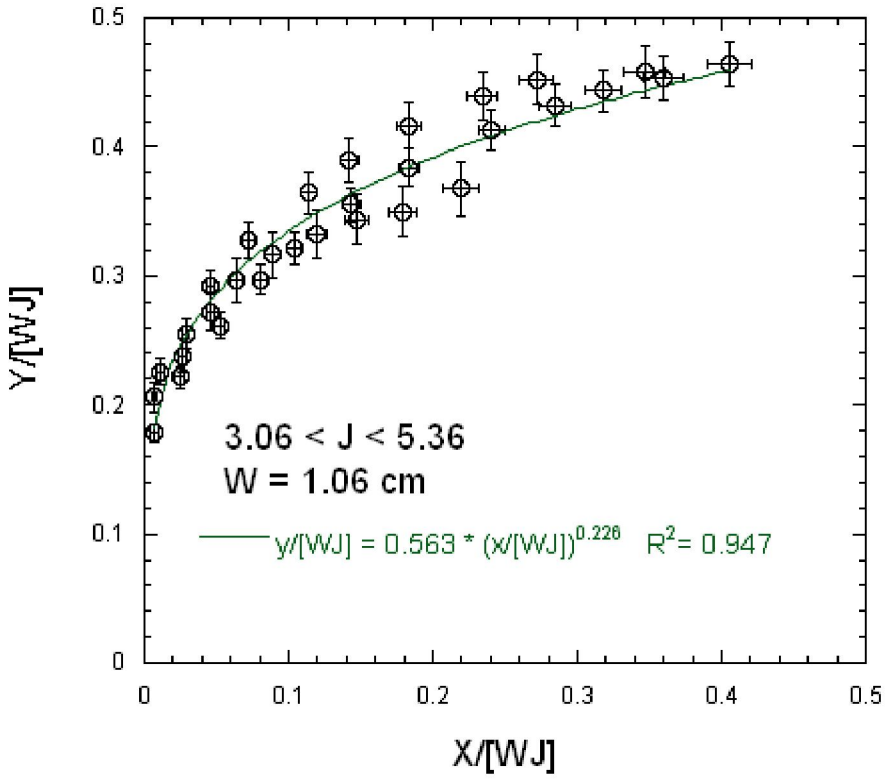

Fig. 4.25 Determination of Jet Penetration Correlation

4.3.4 Blowoff Limits

For the three crossflows selected a series of experiments were conducted to determine the blowoff limits for this combustor. These tests were conducted by premixing ethylene far upstream (2.1 m) of the combustor and conducting experiments in which the pilot flame was turned off to see whether or not the mixture could sustain its own combustion. Typically during an experiment, a flame was established at the location of the pilot flame (see figure 4.26), but in order to determine the blowoff limits of the combustor the pilot flame was turned off. Blowoff is a condition in which a stable and self-sustaining flame is not occurring. Blowoff can occur if a flammable mixture is too fuel lean, or if the gas velocity is well above flame speeds. One resolution to blowoff in high-speed flows is the use of a flame holding device. A flame holding device typically

creates an area of low speed flow where a flame can attach and sustain itself from. In the case of this study, the rearward facing step provides a low speed recirculation zone in which a flammable mixture can potentially sustain itself under appropriates conditions.

In this study, if the equivalence ratio was high enough (yet still fuel lean), the flame would anchor itself at the base of the rearward facing step as shown in figure 4.27. These images were taken with a video recorder with no filtering applied. The flame was considered sustained if it stayed anchored at the base of the step for a period of at least 4 seconds.

Figure 4.28 shows the results of these experiments. As would be expected, as the combustor inlet velocity was increased, the amount of fuel necessary in order to achieve an anchored flame was increased. The equivelance ratio increase from about 0.58 at a velocity of 25 m/s to approximately 0.68 at a velocity of 70 m/s.

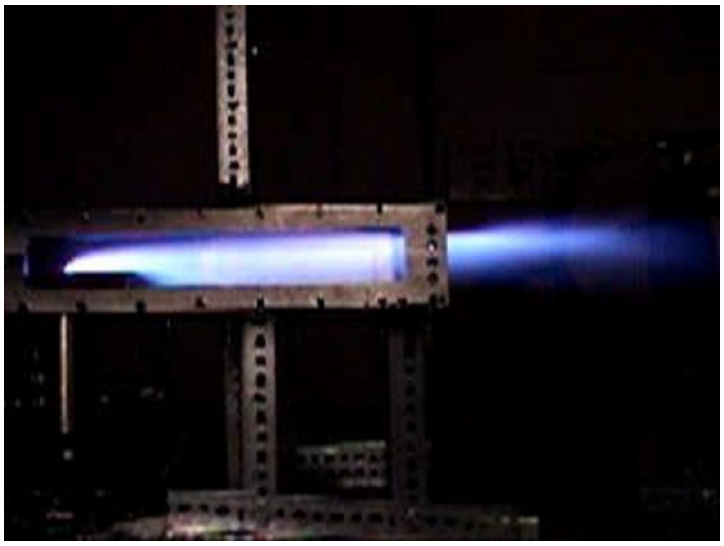

Fig. 4.26 Normal Combustor Operation with Pilot Flame On

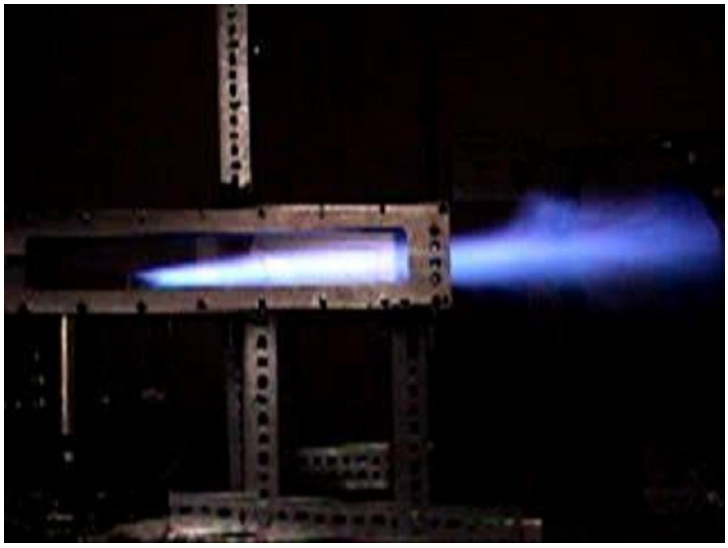

Fig. 4.27 Example of Flame Anchoring at Rearward Facing Step

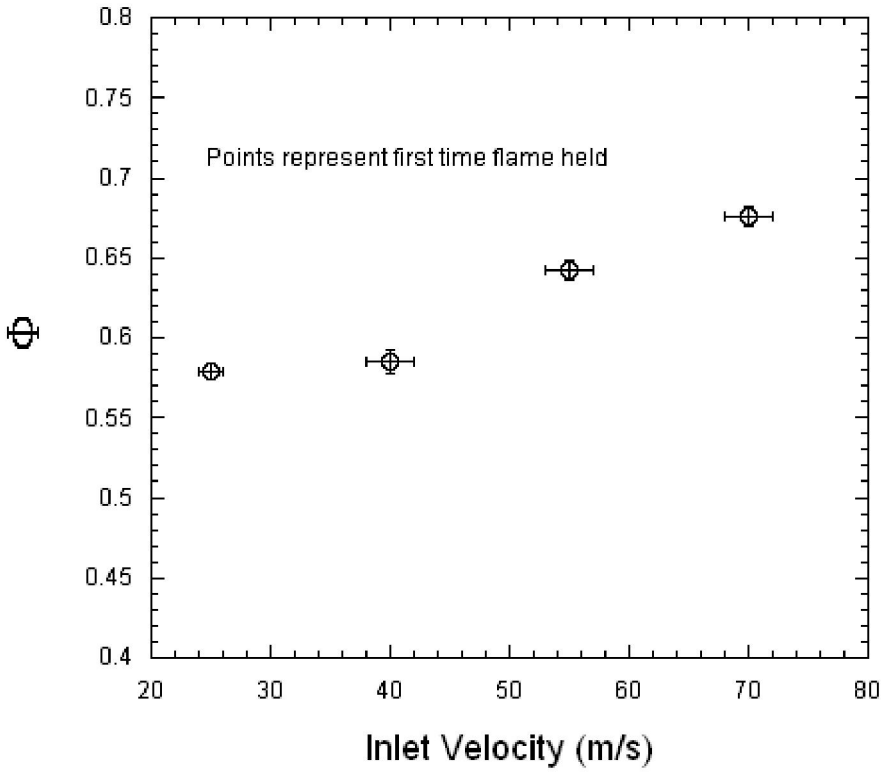

Fig. 4.28 Blowoff Limits

CHAPTER 5

FLAT FLAME BURNER RESULTS AND ANALYSIS

5. Flat Flame Burner Results and Analysis

This Chapter outlines and discusses the results of the flat flame burner experiments for which measurements of ignition and burning times of boron nanoparticles were made. In addition, a brief discussion on recent relevant studies conducted by other researchers is given.

5.1 Brief Discussion of Boron Combustion Physics

Chapter 2 provides a detail discussion of the physics of boron combustion. However a brief summary is provided here to identify some key parameters to be investigated in this study. Early studies on boron particle combustion by Macek[47-49] describe a two-stage combustion process. The first stage, sometimes termed the ignition stage, is associated with particle burning while the particle is still coated with an oxide layer. As the particle heats up to above the B_2O_3 boiling point and the oxide layer is completely removed by evaporation, the second stage of boron combustion begins. Since pure boron has relatively high melting and boiling temperatures, 2350 K and 4139 K respectively, the initial reactions in the consumption of the boron particle involve heterogeneous reactions between the gas phase oxidizer and solid or liquid phase boron. The second stage is essentially the full-fledged combustion of the bare boron particle.

According to Yeh and Kuo[46], the burning time of a boron particle can be described by the following:

$$t_b = t_{b,dif} + t_{b,kin} \qquad \text{Eq. 5.1}$$

where $t_{b,dif}$ and $t_{b,kin}$ refer to the combustion time due to species diffusion and the combustion time due to chemical kinetic mechanisms respectively. They are defined by:

$$t_{b,dif} = \frac{\rho_B d_0^2}{8\rho D \ln\left(1 + iY_{O_2,\infty}\right)} \qquad \text{Eq. 5.2}$$

and,

$$t_{b,kin} = \frac{\rho_B d_0}{2M_B kPX_{O_2,\infty}} \qquad \text{Eq. 5.3}$$

where ρ_B, d_o, ρ, D, $Y_{O2,\infty}$, M_B, k, P, $X_{O2,\infty}$ refer to boron density, the initial diameter of the particle, the gas density, the gas diffusivity, oxygen mass fraction in the freestream, molecular weight of boron, a kinetic rate constant, pressure, and oxygen mole fraction in the freestream respectively. It can be seen from these two equations that the diffusion-controlled combustion is consistent with the D^2-*law* (particle diameter), while the kinetic regime is consistent with a D^1-*law*. In order to determine which mechanism is dominant one can inspect the Damkholer number (Da) for surface reactions, which is defined as a ratio between the diffusion and kinetic time scales:

$$Da = \frac{t_{b,dif}}{t_{b,kin}} = \frac{M_B kPd_0 X_{O_2,\infty}}{4\rho D \ln(1 + iY_{O_2,\infty})} \qquad \text{Eq. 5.4}$$

After substitution of parameters Yeh and Kuo[46] determined that the Damkholer number reduces to:

$$Da = \frac{Pd_0}{75} \qquad \text{Eq. 5.5}$$

where P is in atmospheres and d_0 is in μm. When Da is much larger than unity, the diffusion time scale is much longer than the kinetic time scale. Consequently, the burning time of a particle should follow a D^2-*law*. Conversely, if Da is much less than unity, the combustion is controlled by kinetics, or the D^1-*law*. In the present study involving nanoparticles combustion time scales dependent on a D^1-*law* would be expected because Da is only about 0.003.

5.1.1 Ignition and Combustion Data for SB99 Nano-boron

When the boron particles were subjected to environments with high enough temperatures and oxidizer concentration, a two-stage phenomenon was observed. After a duration where there was no visible event, a yellow/orange emission zone appeared after which a sharp transition to a white glow zone appeared. This is consistent with the observed behavior in the works of Li and Williams[87]. Li and Williams[87] concluded that the yellow zone was the ignition stage, sometimes referred to as stage 1 combustion, concluding with the complete removal of the oxide layer, while the white glow zone was the clean combustion stage of burning, often referred to as stage 2 combustion. From this point forward, time scales associated with the ignition stage (stage 1) will be designated t_1, while time scales associated with stage 2 combustion will be designated as t_2.

During this study, all of the test conditions resulted in at least the beginning of the ignition stage. However, not all of the test conditions provided a suitable environment to reach and complete stage 2 combustion. All of the experiments that had oxygen mole fractions (X_{O2}) greater than or equal to 0.2 reached and completed stage 2 combustion. For the experiments with X_{O2} equal to 0.15, stage 2 combustion was reached for all tests,

however at the lowest temperature condition, stage 2 was not completed within the burner environment. At X_{O2} equal to 0.1, only the highest temperature test resulted in achieving stage 2 of boron combustion. Table 5.1 provides a summary of the results for the ignition and combustion of the SB99 particles.

Table 5.1 Summary of SB99 Ignition and Combustion Results

Test Condition	Product Mole Fractions				Average Burner Temperature (K)	Stage 1 Reached	Stage 2 Reached	Stage 2 Completed
	O_2	H_2O	CO_2	N_2				
1	0.200	0.234	0.117	0.450	1684	yes	yes	yes
2	0.200	0.266	0.133	0.400	1808	yes	yes	yes
3	0.200	0.300	0.150	0.350	1854	yes	yes	yes
5	0.200	0.234	0.117	0.450	1637	yes	yes	yes
6	0.300	0.200	0.100	0.400	1630	yes	yes	yes
7	0.300	0.233	0.117	0.350	1797	yes	yes	yes
8	0.300	0.267	0.133	0.300	1872	yes	yes	yes
9	0.300	0.200	0.100	0.400	1578	yes	yes	yes
10	0.150	0.267	0.133	0.450	1718	yes	yes	yes
11	0.150	0.267	0.133	0.450	1814	yes	yes	yes
13	0.150	0.267	0.134	0.449	1596	yes	yes	no
14	0.100	0.233	0.117	0.550	1614	yes	no	no
15	0.100	0.267	0.134	0.499	1712	yes	no	no
16	0.100	0.267	0.134	0.499	1791	yes	yes	yes

Figure 5.1 is an example of the two-stage phenomenon. This is an inverted "instantaneous" image of visible wavelengths emission taken with an ICCD camera at an exposure time of 150 μs. Typically 50 images per test condition were taken and averaged together during image processing. Upon filtering with a 546 nm (which corresponds to a band of BO_2 emission) narrowband filter, the yellow ignition zone is no longer visible in the images as seen in figure 5.2. BO_2 is known to be prevalent during both the ignition and full-fledged combustion stages of boron combustion[72]. The fact that it was not observed here does not mean that it is non-existent, but rather that for the camera settings used in the experiment (namely exposure time) that the intensity was not significant

enough to detect. This result is actually beneficial as it provides a clear boundary for the ignition and full-fledged combustion stages.

For the purposes of image processing, a background image is taken and averaged together with 50 similar images, and then "subtracted" from the original averaged image. The background image is taken with no particles injected into the post flame region of the burner, but with the carrier gas still flowing. Figure 5.3 is an example of a background image. During image processing, an averaged version of figure 5.3 would be subtracted from an averaged version of figure 5.1 and the result is then processed for further analysis.

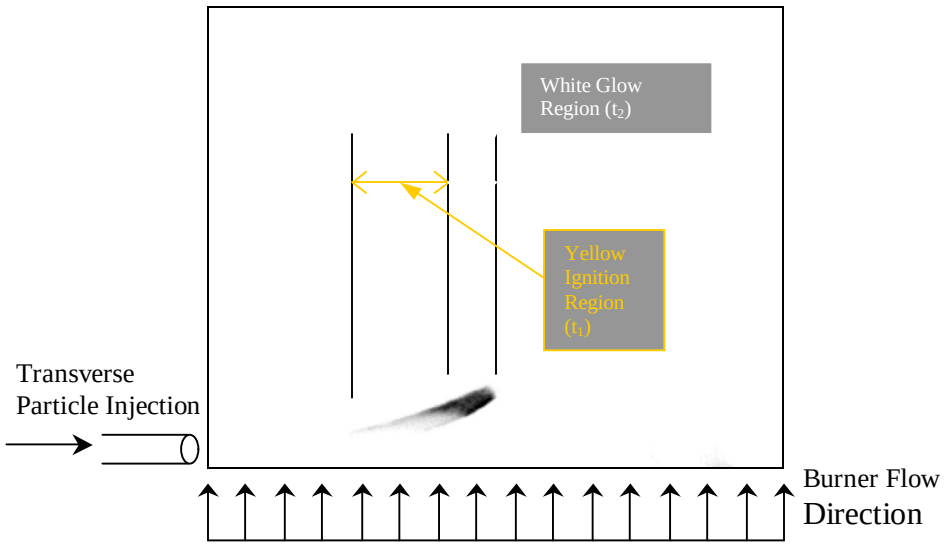

Fig. 5.1 Image of Two-Stage Phenomenon in Nano-Boron Combustion (X_{O2} = 0.3, T = 1797 K)

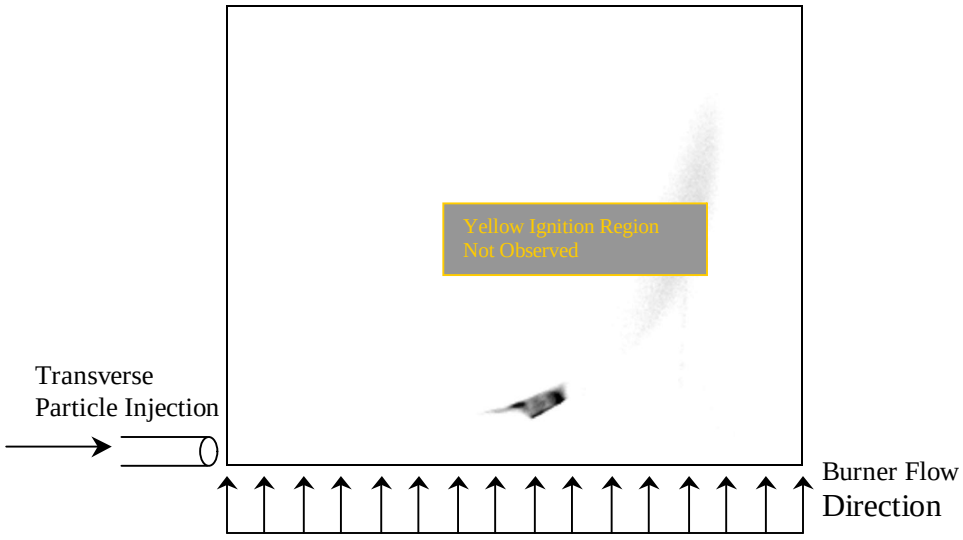

Fig.5.2 Filtered Image in Nano-boron Combustion (X_{O2} = 0.3, T = 1797 K)

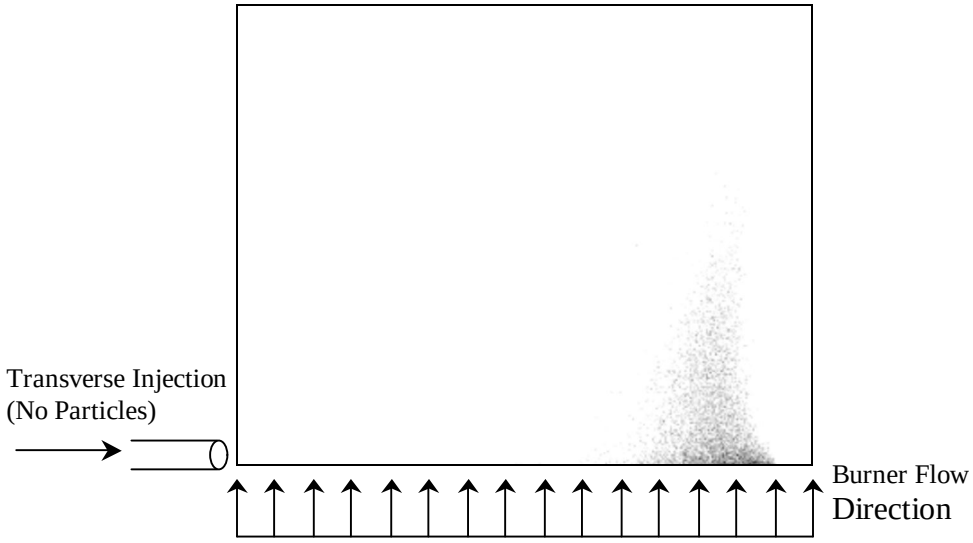

Fig. 5.3 Typical Background Image (no particles, X_{O2} = 0.3, T = 1797 K)

Figures 5.4-5.7 are BO_2 intensity contours plotted for all of the different test conditions. These contours were created by subtracting the filtered averaged images with images taken for a given test condition with no particles flowing as a background

subtraction as was previously mentioned. These images represent second stage boron combustion (bright white zone).

In all cases the scale of the color bar represents intensity, which has arbitrary units. For each oxygen mole fraction test condition the camera exposure time was held constant, along with the looping and binning settings of the camera. However, the intensity levels between the different oxygen mole fraction conditions cannot be compared directly because the camera exposure was different in each case. Table 5.2 provides a summary of the camera settings for the experiments to obtain the filtered images.

Figure 5.4 shows the contours for all of the tests conducted having an oxygen mole fraction of 0.3. It is clear from the figure that as the temperature is increased, the location of the BO_2 emission is shifted closer to the origin (X = 0). This is a clear indication of faster ignition, which would be expected in higher temperature environments. In addition, it is evident that the higher temperature test conditions exhibit higher peak intensity levels. In the case of $X_{O2} = 0.3$ all of the test conditions attempted resulted in and completion of second stage boron combustion.

Table 5.2 Camera Settings for Filtered Experiments

X_{O2}	Exposure (ms)	Binning	Gain (%)	Loops
0.1	2.0	4 x 4	10	2
0.15	1.55	4 x 4	10	2
0.2	1.35	4 x 4	10	2
0.3	1.2	4 x 4	10	2

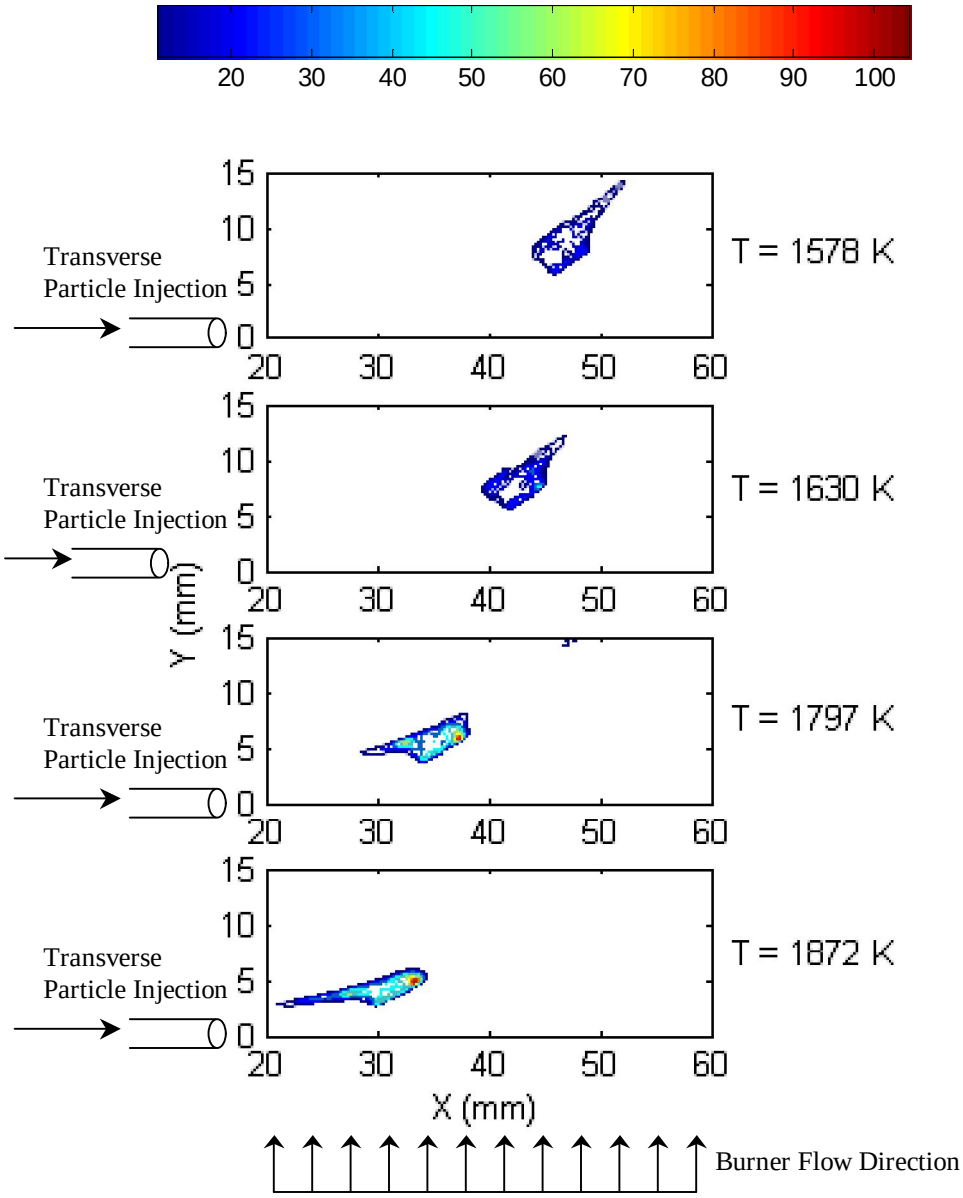

Fig. 5.4 Intensity Contours for X_{O2} = 0.3

Figure 5.5 is a summary of the second stage combustion for the test conditions with an oxidizer mole fraction of 0.2. Once again, as one would expect as the temperature is increased, the ignition location shifts toward the origin, and the higher

temperature tests clearly exhibit higher peak intensities. In addition all of the test conditions with $X_{O2} = 0.2$ resulted in and completion of t_2 combustion.

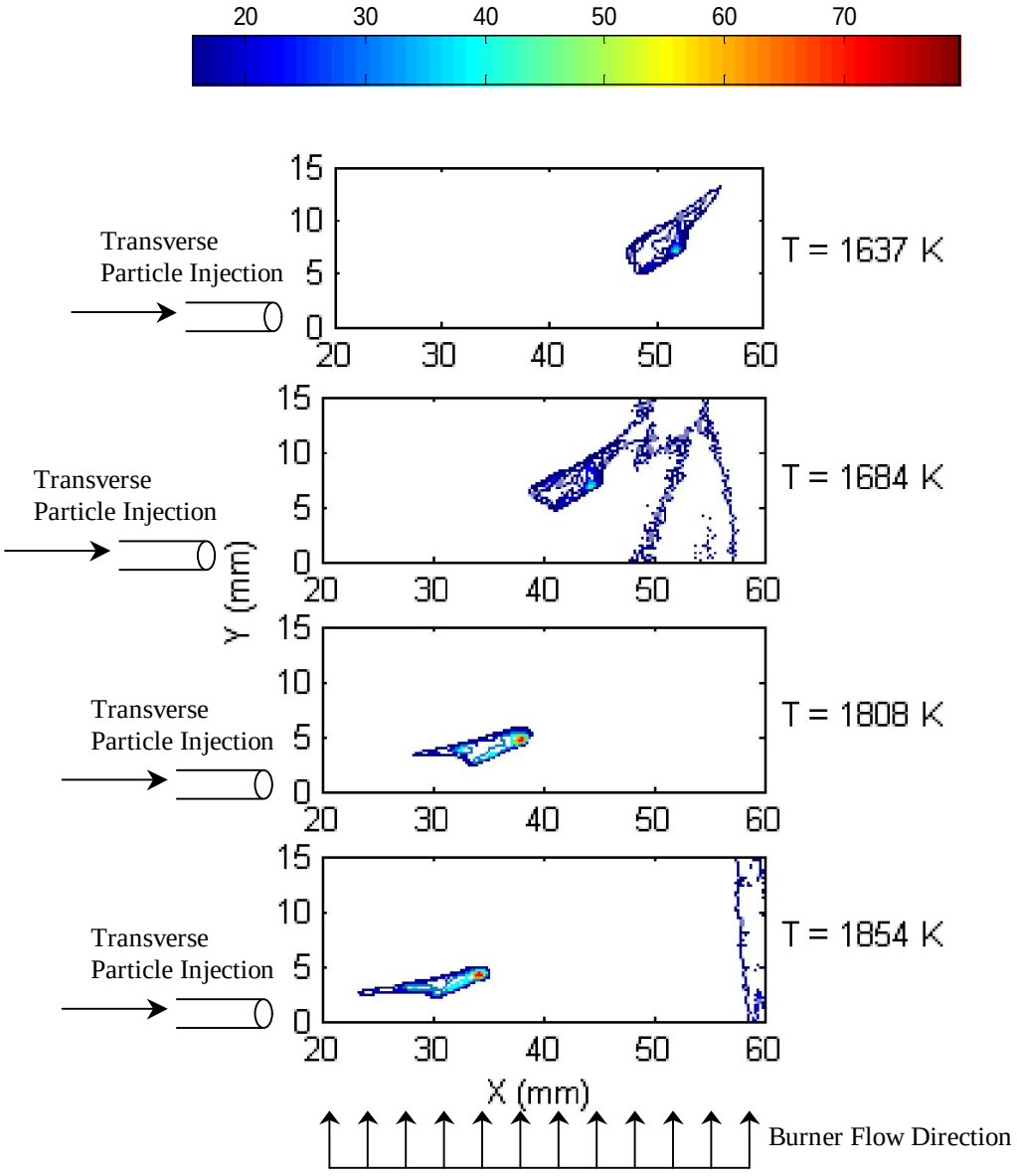

Fig. 5.5 Intensity Contours for $X_{O2} = 0.2$

For the $X_{O2} = 0.15$ conditions, all of the experiments resulted in second stage combustion. However, at the lowest temperature condition, although second stage

combustion started, the particles left the post flame region prior to completion of combustion. Figure 5.6 shows the results of the X_{O2} = 0.15 condition for the filtered images for all of the test conditions in which stage 2 combustion was completed. Unlike the previous test conditions, after the bright white zone there appears to be some BO_2 intensity still being detected as shown in the contours. The intensity levels following the white zone are much lower than within the white zone. It is possible that these are simply a result of residual oxides[15].

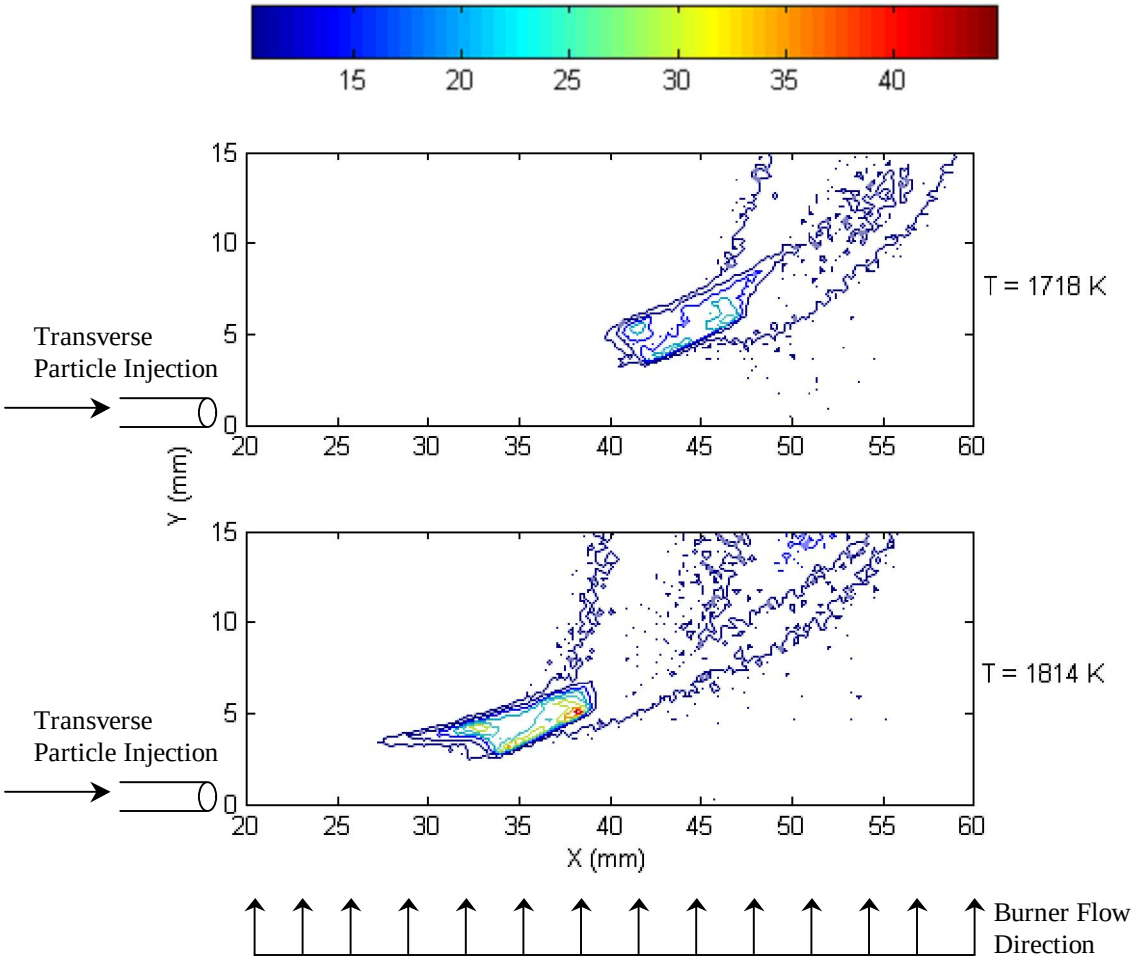

Fig. 5.6 Intensity Contours for X_{O2} = 0.15

Finally, for the X_{O2} = 0.1 test conditions, figure 5.7 shows the contour of the only test condition which clearly achieved stage two burning. At temperatures of 1712 K and 1614 K, stage two combustion was not achieved in this experiment, where as for all of the other oxygen mole fraction conditions at temperatures as low as 1578 K stage two burning was achieved. This indicates that temperature and oxygen mole fraction play an important role in the ignition stages of boron combustion.

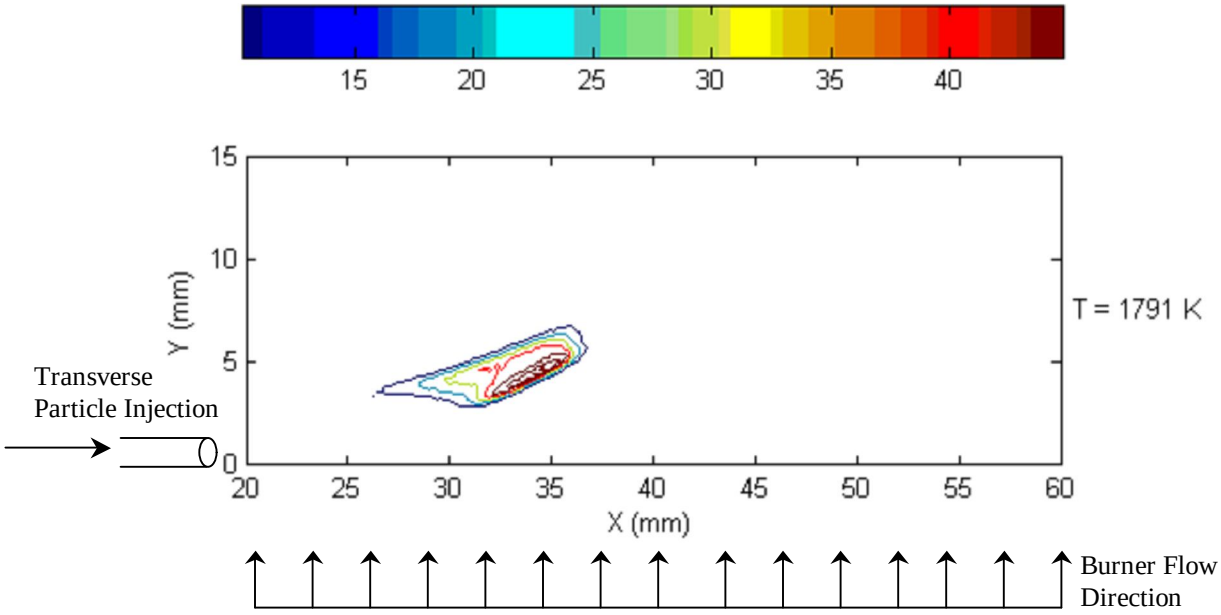

Fig. 5.7 Intensity Contour for X_{O2} = 0.1

In order to be certain that what was being detected was BO_2, a series of experiments were conducted in which a different band pass filter, centered at 532 nm, replaced the 546 nm filter. BO_2 does not have any known bands that emit near 532 nm. Figure 5.8 shows a comparison of intensity levels when changing the filter from 546 nm to 532 nm. In this case the camera settings for exposure, binning, and gain were set identically. It is clear from figure 5.8 that the image collected with the 546 nm filter has

a higher overall intensity than the image collected with the 532 nm filter. In fact the image collected with the 546 nm filter has a total intensity that is 53% higher than the image collected with the 532 nm filter. This indicates that clearly is being detected in levels beyond what ordinary black body radiation would produce. It should be noted that the filters have a 10 nm full width half maximum value, meaning that they would have some overlap, therefore even without black body radiation, some level of emission could still be expected with the 532 nm filter.

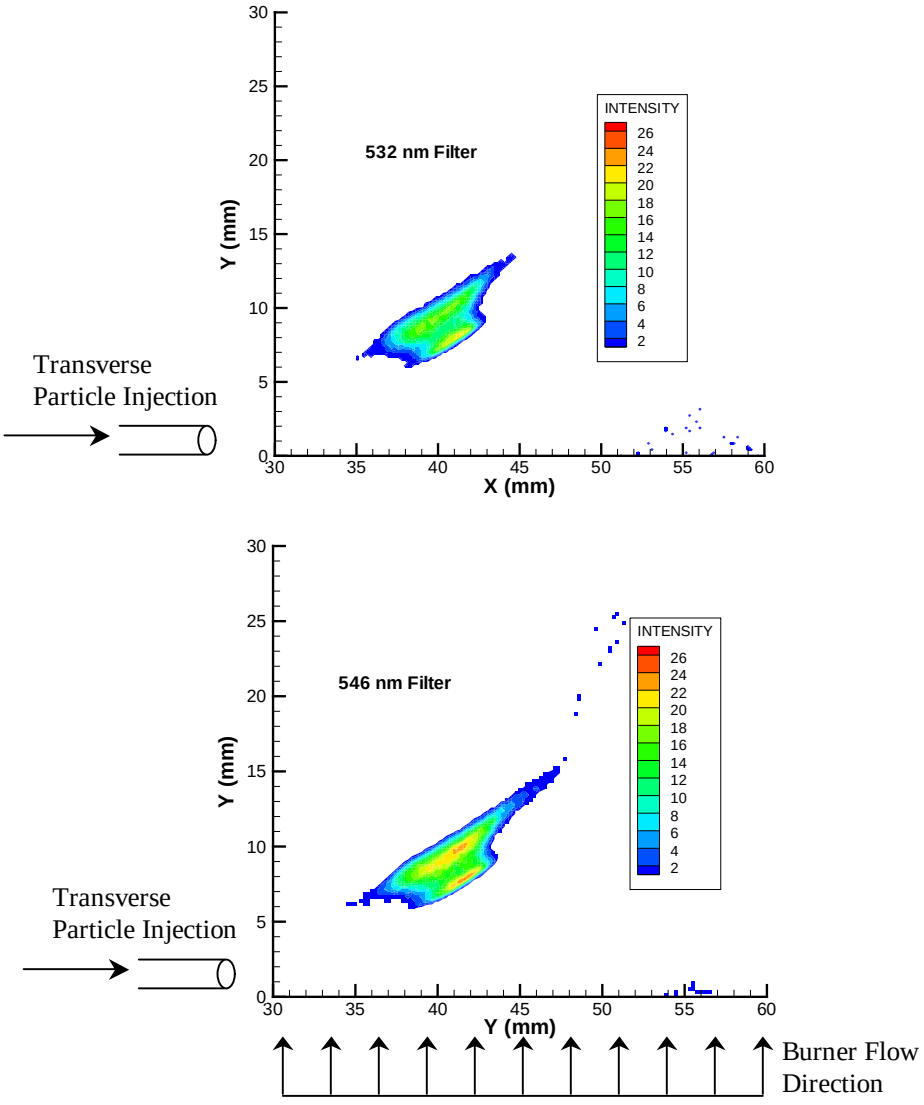

Fig. 5.8 Intensity Contours using Different Filters (X_{O2} = 0.3, T = 1630 K)

Figure 5.9 shows the one-dimensional (i.e. columns of the gray-scale image have been summed) intensity profiles that were obtained from figure 5.8. In this figure, both profiles have been normalized by the maximum value attained in the image collected with the 546 nm filter. Again, clearly the image collected with the 546 nm exhibits higher intensity levels. In fact, the peak intensity levels are about 25% higher, with integrated intensity levels more than 50% higher than the images collected with the 532 nm filter.

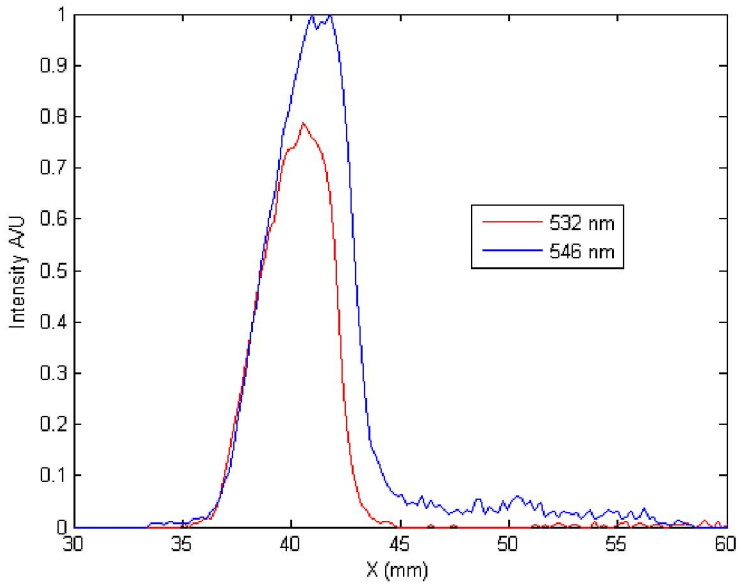

Fig. 5.9 Normalized Intensity Profile Using Different Filters

During data reduction for all of these test conditions, the second-stage or t_2 burning time (filtered images) was determined first. Once the spatial locations of the second-stage combustion were determined the starting location of the second-stage combustion was designated as the ending of stage 1 combustion. However, the results of the ignition stage or first stage of boron combustion, with timescale designated as t_1, is presented first.

In order to determine the spatial locations of the boundaries for second-stage of combustion and the ending of first stage of combustion, the problem was converted to a one-dimensional problem. This was accomplished by summing the intensity in the y-direction and plotting it versus the x-dimension of distance. One reason to conduct the analysis this way is that the shape of the second stage combustion as seen in Figures 5.4-5.7 is not necessarily consistent from test condition to test condition. By making the analysis one dimensional, a systematic approach that did not depend on the "shape" of the combustion was attained.

With a 1D intensity profile, and velocity measurements described in Chapter 4, the ignition delay, ignition time, and burn time were obtained. Generally in this type of problem there are three methods that have been used by other researchers to determine burn time[15]. They include a constant intensity cutoff method, percent peak height method, and a percent total area method.

Since area based methods provide the most unambiguous determination of burn time[88], an area-based method was adopted in this study. In this case the burning time is defined as occupying 95% of the area of the original profile. Unfortunately as Beckstead[34] pointed out, there is no accepted standard area fraction for determining burning times. For the present study, the 95% area rule was adopted to ensure that any estimate of burning time would be relatively conservative. Figure 5.10 is an example of the 1D intensity profile for determining the burning time. In this case the blue line represents the original profile, while the red line represents 95% of the total area, and therefore the burning time.

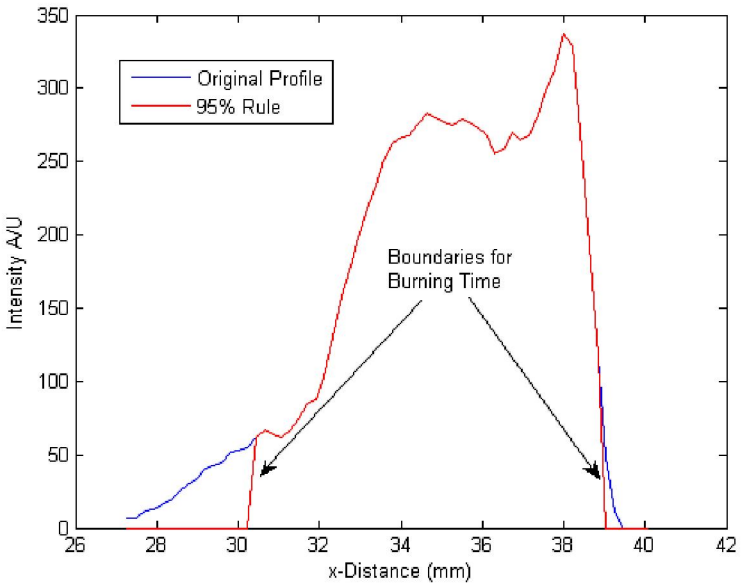

Fig. 5.10 Example of t_2 Burn Time Determination (X_{O2} = 0.2, T = 1808 K)

5.1.2 Ignition Stage, t_1 Results

The starting location for the first stage or ignition stage was determined by examining the averaged unfiltered images. The time scales associated with the first stage of boron combustion have been designated as t_1. The starting point was selected by locating the first sign of light emission in the images, while the ending point was determined from analysis of the filtered images as described above. Figure 5.11 shows the results of the ignition stage, burning times for all of the test conditions that reached and completed second stage combustion. The data shows that for these conditions, the ignition stage is relatively insensitive to oxygen mole fraction, within experimental error. t_1 times range from about 5 milliseconds at the lower temperature levels all the way down to about 1.5 milliseconds at the higher temperature conditions. The ignition stage time is reduced by a factor of about 1/3 over a temperature range of about 200 K.

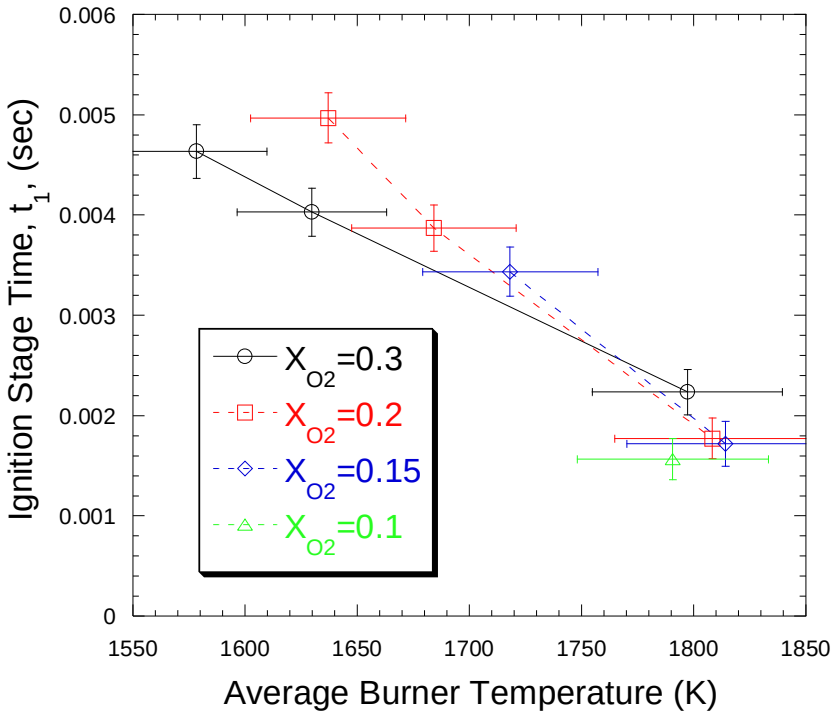

Fig. 5.11 t_1 Burning Times for SB99 Boron

The ignition data obtained in this study is compared directly to the data obtained in the study by Yeh and Kuo[46] for 2-3 μm boron particles in figure 5.12. The Yeh and Kuo[46] study was similar to this one in nature in that they investigated the burning times of larger boron particles in the post flame region of a flat flame burner. Interestingly the data for which there is an overlap in burner temperature is quite comparable, suggesting that the boron nanoparticles do not necessarily behave significantly different that the larger micron-sized particles during the ignition stage. Another interesting note when comparing the data is that the ignition stage appears to become less sensitive to temperature as the temperature exceeds approximately 1750 K.

It is important to note that although the data from the two different studies are being compared, that great care should be taken when interpreting the results. First, the

same exact methods or criteria may not have been used in quantifying the burning time data or even the temperature data for that matter. Beckstead[34] considers this the largest source of data scatter when comparing all of the particle burning experiments conducted by different researchers. Second, the test conditions between the two studies are not necessarily identical, although in each study, the results of the ignition stage studies appear to be relatively insensitive to the product gas species. Finally, another important distinction between this study and all others is that this study obtains ensemble averages of the burning times for a size distribution of agglomerated particles. This could potentially lead to slight biases in the burning and ignition times, whereas in the other studies "single" particles were analyzed. At any rate, the results of this study suggest that there is not a significant difference in the ignition stage of boron combustion between agglomerates of nanoparticles (with mean "particle" sizes of 200 nm), and larger 2-3 μm sized particles, at least where temperature ranges are similar.

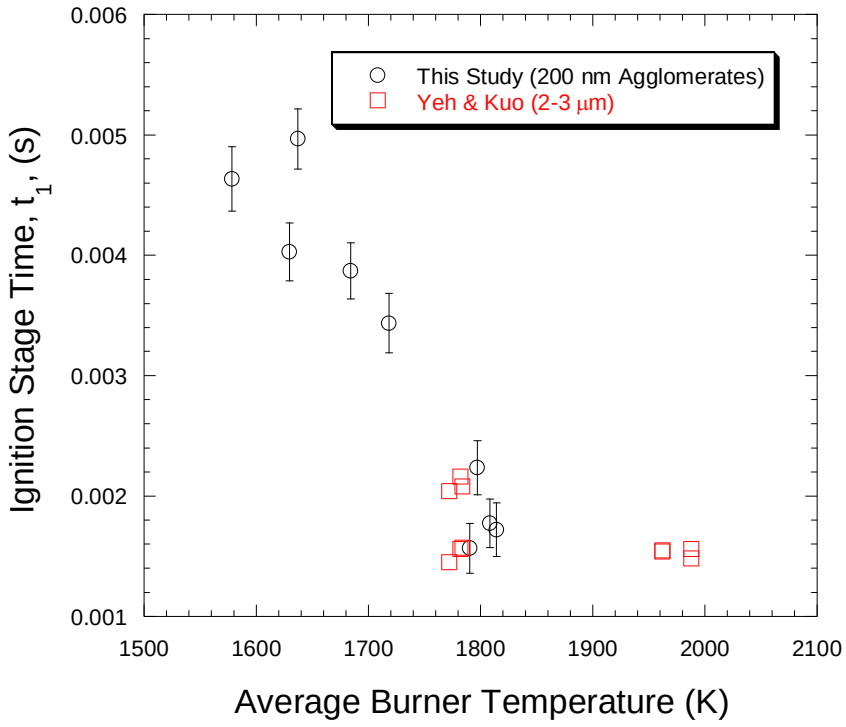

Fig. 5.12 Comparison of Ignition Time, t_1, with Other Data

Since the ignition time, or t_1, was primarily dependent on temperature, an analysis was performed to develop an analytical expression for the particle ignition time. Table 5.3 provides the values of the variables used in this analysis. The analysis assumed that the lumped capacitance assumption was appropriate, in other words, the temperature of the particle is spatially uniform at an instant during a transient process. In order to verify the validity of the lumped capacitance method, the Biot number, *Bi*, should be analyzed. The Biot number provides a measure of the temperature drop across a solid relative to the temperature difference between the surface and fluid. If $Bi << 1$, the resistance to conduction within the solid is much less than the resistance to convection across the fluid boundary layer, therefore, the assumption of a uniform temperature distribution is valid[68].

Table 5.3 Properties Used in Analytical Analysis of Ignition Time

Boron Thermal Conductivity, k, W/[m*K]	27.6
Particle Diameter, D_p, nm	200
Thermal Conductivity of Freestream (air @ 1700 K), k_∞, W/[m*K]	0.113
Convective Heat Transfer Coefficient, h_∞, W/[m^2*K]	1,130,000

The Biot number is defined as:

$$Bi = \frac{h_\infty L_c}{k} \qquad \text{Eq. 5.6}$$

where, h_∞ is the convective heat transfer coefficient, k is the thermal conductivity of the particle, and L_c is the characteristic length defined as:

$$L_c = \frac{V}{A_s} \qquad \text{Eq. 5.7}$$

where V refers to the particle volume, and A_s refers to the particle surface area. The convective heat transfer coefficient can be determined from the definition of the Nusselt number:

$$Nu_D = \frac{h_\infty D_p}{k_\infty} \qquad \text{Eq. 5.8}$$

where D_p is the particle diameter and k_∞ is the freestream thermal conductivity. For laminar flow, i.e., as the Reynolds number approaches zero, the Nusselt number approaches a value of 2 as equation 3.5 would suggest. Substituting in the appropriate parameters yields a typical Biot number of 0.005, substantiating the assumption of lumped capacitance. Since the lumped capacitance method was valid for this analysis, an

energy balance on the particle could be applied. Figure 5.13 is a schematic diagram showing the details of the energy balance.

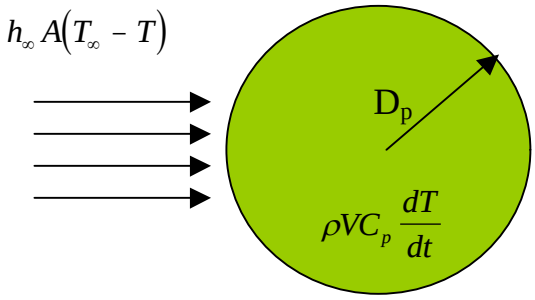

Fig. 5.13 Schematic Diagram of Energy Balance

The energy balance for the particle is given by:

$$\dot{E}_{st} = \dot{E}_{in} - \dot{E}_{out} + \dot{E}_{gen} \qquad \text{Eq. 5.9}$$

where, $\dot{E}$ refers to the rate of change of energy, and the subscripts *st*, *in*, *out*, and *gen* refer to stored, in, out, and generated respectively. In this analysis chemical reactions have been neglected, therefore the rate of energy generated is negligible. Similarly, radiation losses have been neglected; therefore the rate of energy leaving the system is also negligible. With those simplifications, the energy balance reduces to only the storage term and a convective term as a energy input:

$$\dot{E}_{st} = \dot{E}_{in} \Rightarrow \rho_p VC_p \frac{dT}{dt} = h_\infty A_s (T - T_\infty) \qquad \text{Eq. 5.10}$$

Introducing the temperature difference, $\theta = T - T_\infty$, where $\frac{d\theta}{dt} = \frac{dT}{dt}$ and substituting into equation 5.10 we get:

$$\frac{\rho_p VC_p}{h_\infty A_s} \frac{d\theta}{dt} = \theta \qquad \text{Eq. 5.11}$$

Separating variables and integrating from the initial condition, $t = 0$ and $T = T_i$, we obtain:

$$\frac{\rho_p V C_p}{h_\infty A_s}\int_{\theta_i}^{\theta}\frac{d\theta}{\theta} = \int_o^t dt \qquad \text{Eq. 5.12}$$

Evaluating the integral and substituting in the variables results in the solution for the ignition time of the particles:

$$t = \frac{\rho_p D_p C_p}{6h_\infty}\ln\left(\frac{T_{initial} - T_\infty}{T_c - T_\infty}\right) \qquad \text{Eq. 5.13}$$

From this analytical solution a correlation was developed for the ignition times for the two highest oxygen mole fraction conditions, X_{O2} = 0.2, 0.3, in which the constants were lumped together into one "time constant", τ_c, and T_c is the critical temperature to complete ignition in the burner. Figure 5.14 shows the results of the correlation. Critical temperatures were 1610 K and 1550 K for X_{O2} = 0.2, 0.3 respectively.

$$t = \tau_c \ln\left(\frac{T_{initial} - T_\infty}{T_c - T_\infty}\right) \qquad \text{Eq. 5.14}$$

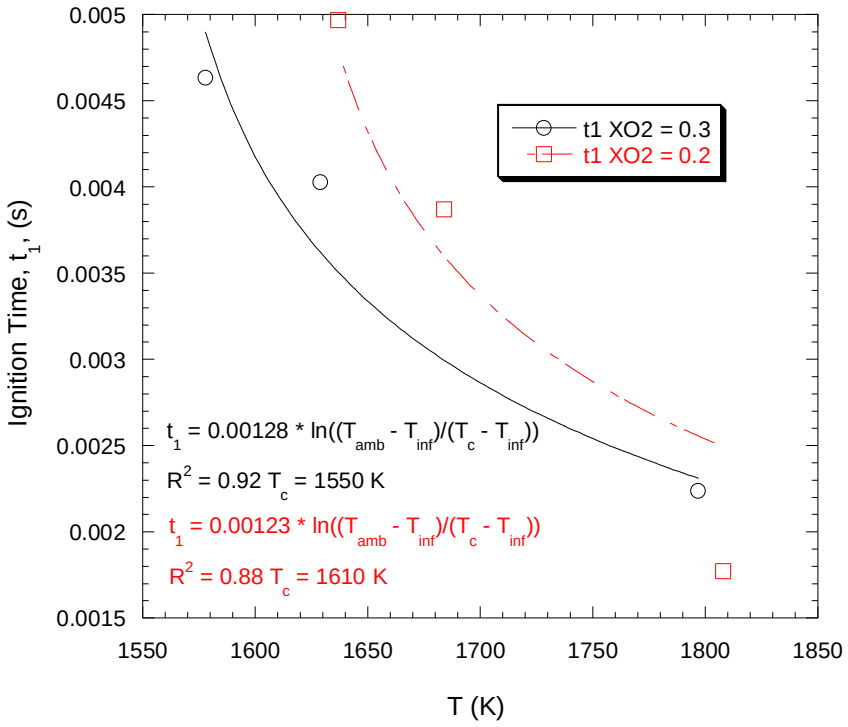

Fig. 5.14 Ignition Time Correlation

5.1.3 Second Stage/Full-Fledged Combustion, t_2 Burning Time Results

A summary of the second stage combustion times corresponding to the white glow zone described earlier is provided in figure 5.15. Typical burning times range from about 3 milliseconds down to about 1.5 milliseconds. Oxygen mole fraction, X_{O2}, had a clear effect on the burning time particularly at the lower range of the temperatures examined in this study. For example the burning time at a temperature of about 1625 K was approximately 50% longer for $X_{O2} = 0.2$ than for $X_{O2} = 0.3$. As the temperature was increased, the effect of X_{O2} was less pronounced although there was still a significant difference between the two highest oxygen mole fractions, 0.2 and 0.3. For $X_{O2} \leq 0.2$ there was no clear effect of oxygen mole fraction on the second stage burning time. However, the effect of temperature became more pronounced at low X_{O2}. In the case of

X_{O2} = 0.15 at the lowest temperature condition second stage combustion was not completed before the flow left the burner area. For X_{O2} = 0.1, second stage combustion was not even reached at all but the highest temperature condition.

These are important results to consider for airbreathing propulsion systems whose lone oxidizer was air, which has an oxygen mole fraction of 0.21. In most practical systems, if a metal were to be used as part of the fuel it would be stored in either a solid hydrocarbon matrix, or in a hydrocarbon gel or slurry. In a best-case scenario with nanoparticles, the total fuel could possibly be comprised of about 50% by weight of the metal. Since the burning times of the hydrocarbon would be much shorter than that of the boron in the fuel, the boron would be left to combust in an environment that only has whatever oxygen content was leftover from the hydrocarbon combustion, i.e. less than X_{O2} = 0.21. Therefore, the hydrocarbon combustion must provide an environment that has a temperature between 1712 K and 1790 K if X_{O2} = 0.1 just to ensure that second stage combustion could take place.

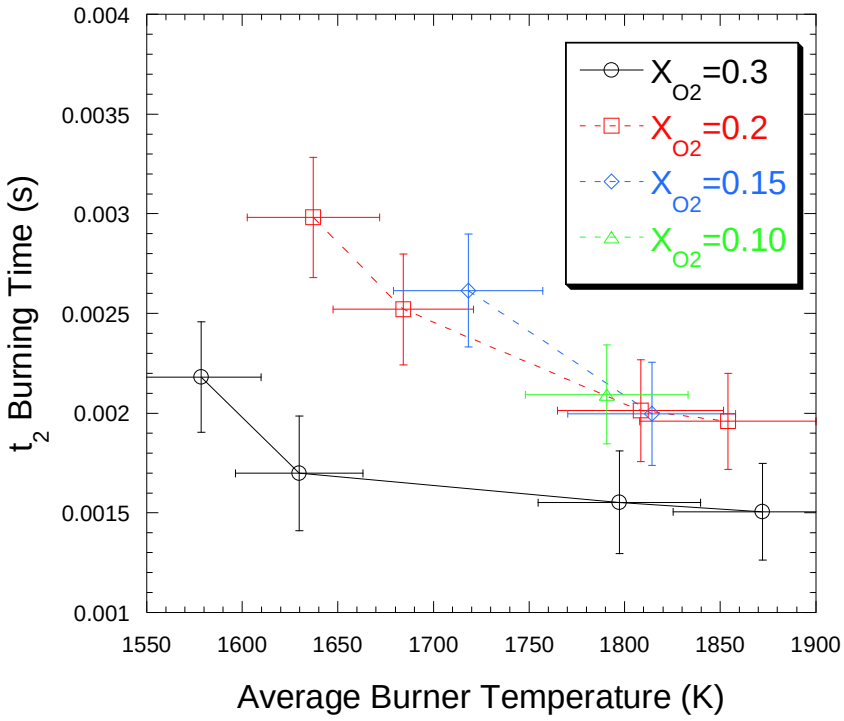

Fig. 5.15 t_2 Burning Times for SB99 B

Figure 5.16 shows the total burning time, t_1 + t_2, for the SB99 particles. The effect of oxygen mole fraction was clear at the lower temperature conditions, which comes directly from the fact that at the lower temperatures the t_2 burning exhibits significant differences in burning time when comparing the X_{O2} quantities. At the lower temperatures, the ignition stage was significantly longer than the full-fledged combustion stage. Therefore the total burning times at the lower temperatures was dominated by the ignition stage. As the temperature was increased, the ignition stage and full-fledged combustion stage became quite comparable.

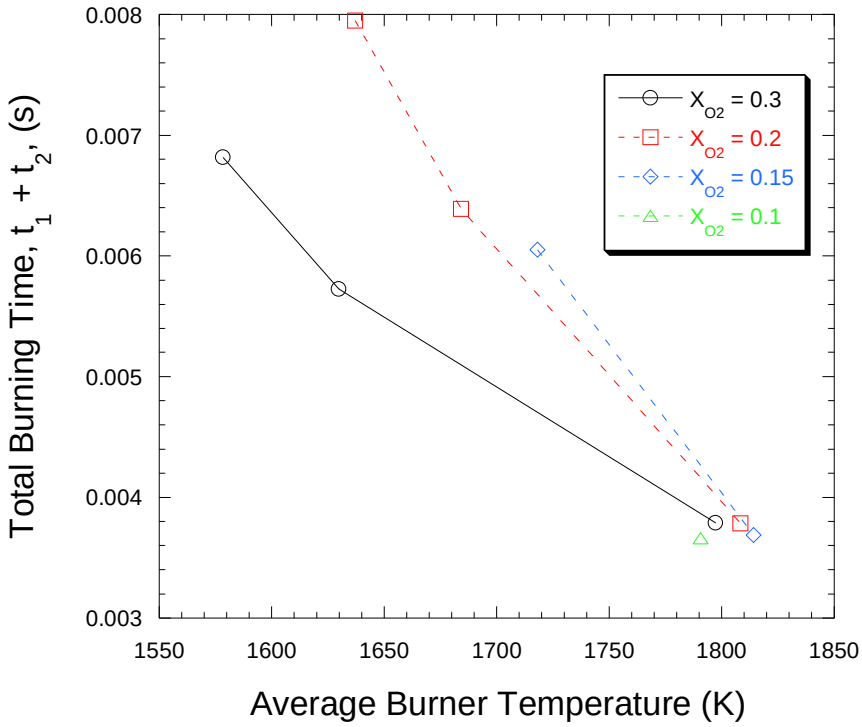

Fig. 5.16 Total Burning Times (t_1+t_2) for SB99 B

Figure 5.17 is a comparison of the full-fledged combustion data collected in this study with data collected in other studies. The data collected by Macek[47,49] used particles ranging from about 30 μm to 100 μm. The data from Li and Williams[87] came from 7 and 10 μm boron particles, while the data from Yeh and Kuo[46] came from particles that were 2-3 μm. The data collected in this study was plotted considering its mean mobility diameter, 200 nm.

Rather than plot just the burning time versus particle size, the product of burning time and oxygen mole fraction (X_{O2}*t_2) was plotted against particle size. These coordinates were chosen since both the chemical reaction time, $t_{b,kin}$, and the diffusion time, $t_{b,diff}$, in equation 5.1 are inversely proportional to X_{O2}, therefore the product of X_{O2}*t_2 is approximately independent of X_{O2}, and should only be dependent on particle

size and pressure[87]. From figure 5.17 it can be seen that the burning time of the largest particles studied by Macek[47,49] are dependent on the particle diameter by a factor of approximately 2, which would be consistent with diffusion limited burning, or the D^2-*law*. The intermediate sized particles studied by Li and Williams[87], and Yeh and Kuo[46] have burning times that approach the kinetic limited regime where the burning time follows a D^1-*law*. As the size of the particles continue to decrease into the nanoparticle range, the particle size dependence continues to decrease, to well below unity ($t_b \sim D^{0.22}$), beyond what traditional theories have explained. Even if the maximum size particle were considered rather than the mean size, i.e. 400 nm instead of 200 nm, the size dependence only reaches $t_2 \sim D^{0.31}$, still well below anything that traditional theory can explain. This result certainly brings into question any benefit achieved from using boron nanoparticles in comparison to micron-sized particles for airbreathing applications. If the burning times are comparable and the nanoparticles suffer from the active content issues described in Chapter 4, then the benefits are likely to be very minimal compared to the downfalls.

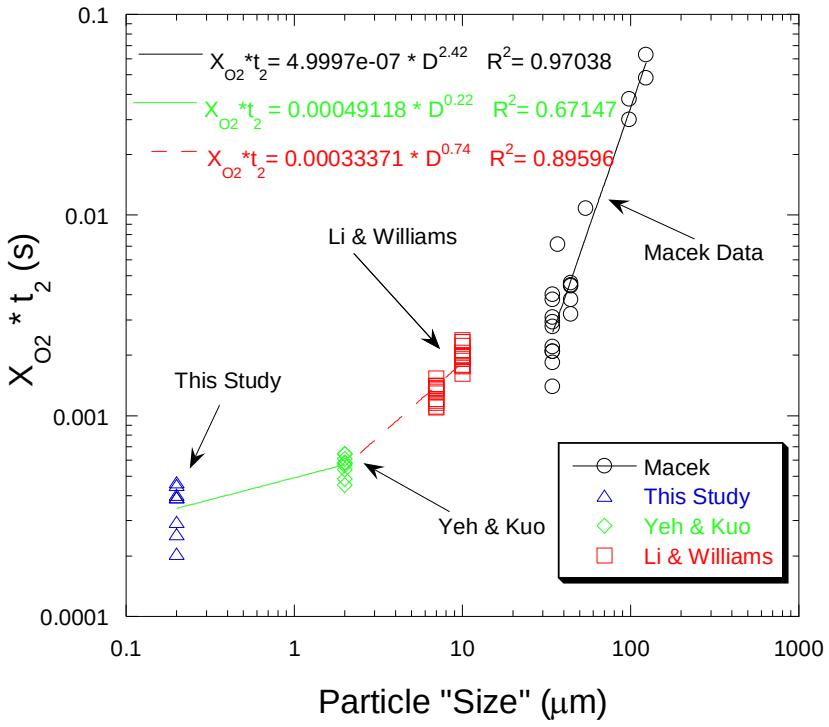

Fig. 5.17 t_2 Burning Time Comparison to Larger Particles

Svante Arrhenius (1859-1927) stated that only those molecules which possess energy greater than a certain amount E_a, the activation energy, will react[29], and these high-energy, active molecules lead to products. The so-called Arrhenius law (Eq. 5.15) to calculate chemical reaction rates was named for Svante Arrhenius.

$$k = A\exp\left(\frac{-E_a}{R_u T}\right) \qquad \text{Eq. 5.15}$$

where A is assumed to include the effect of the collision terms, the steric factor associated with the orientation of the colliding molecules, and the mild temperature dependence of the preexponential factor[25]. R_u is the universal gas constant, and T is the temperature. A form of this Arrhenius law was applied to the data collected in this study for the full

fledged combustion regime of the boron particles. In this case the Arrhenius law took the form of equation 5.16.

$$\frac{1}{X_{O_2} t_2} = A \exp\left(\frac{-E_a}{R_u T}\right) \qquad \text{Eq. 5.16}$$

The results of applying the modified form of the Arrhenius law can be seen in figure 5.18. The data collected by Yeh and Kuo[46] is also included for comparison. In this case, only the data collected for X_{O2} = 0.2 and 0.3 so that the conditions could be most comparable to the Yeh and Kuo[46] data. In this range, the activation energies between the two studies, and two very different particle sizes, are comparable considering experimental error and data scatter. This is in great contrast to similar data for nanoaluminum. Park[24] found that the activation energy of aluminum significantly decreases with decreasing particle size.

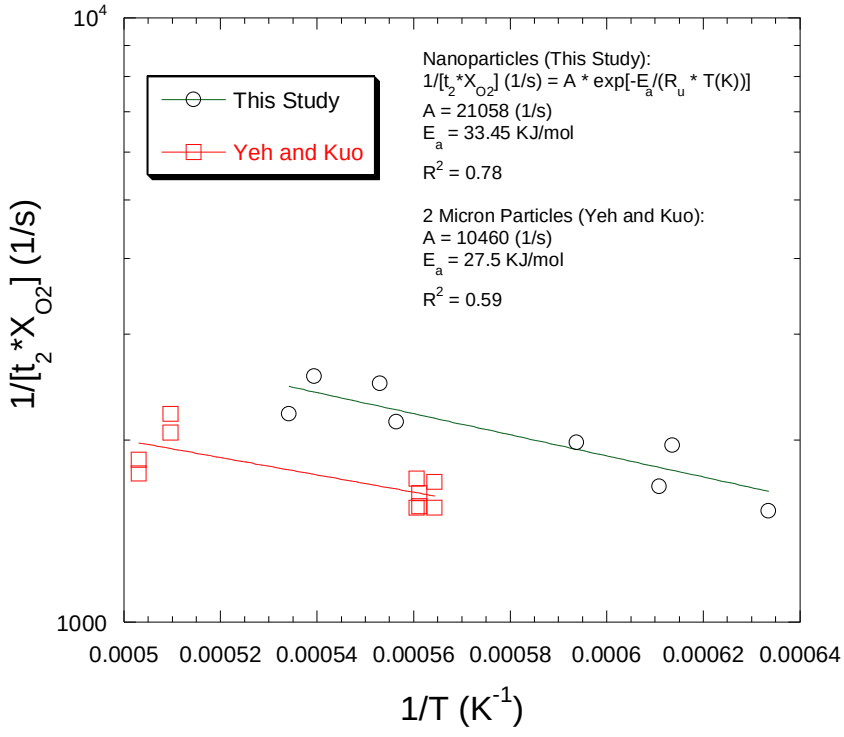

Fig. 5.18 Arrhenius Burning Rate Law for t_2

Since the Damkholer analysis suggests that the burning of these boron nanoparticles should be kinetically controlled, a burning time correlation based on a kinetically controlled system was determined[89] using the Arrhenius parameters obtained above.

$$t_2 = \frac{aD^n}{X_{O_2} A \exp\left(\frac{-E_a}{R_u T}\right)} \qquad \text{Eq. 5.17}$$

The correlation takes the activation energy determined for the nanoparticles in this study, and ranges from the nanoparticle data collected in this study up through the data collected by Yeh and Kuo[46] and can be seen in figure 5.19. This correlation reduces some of the scatter seen in the correlations developed earlier. With the Arrhenius parameters included, the size dependence decreases even further to $t_b \sim D^{0.14}$. Therefore, only a small benefit in burning time was obtained when going from 2-3 μm down into the nanometer range for boron.

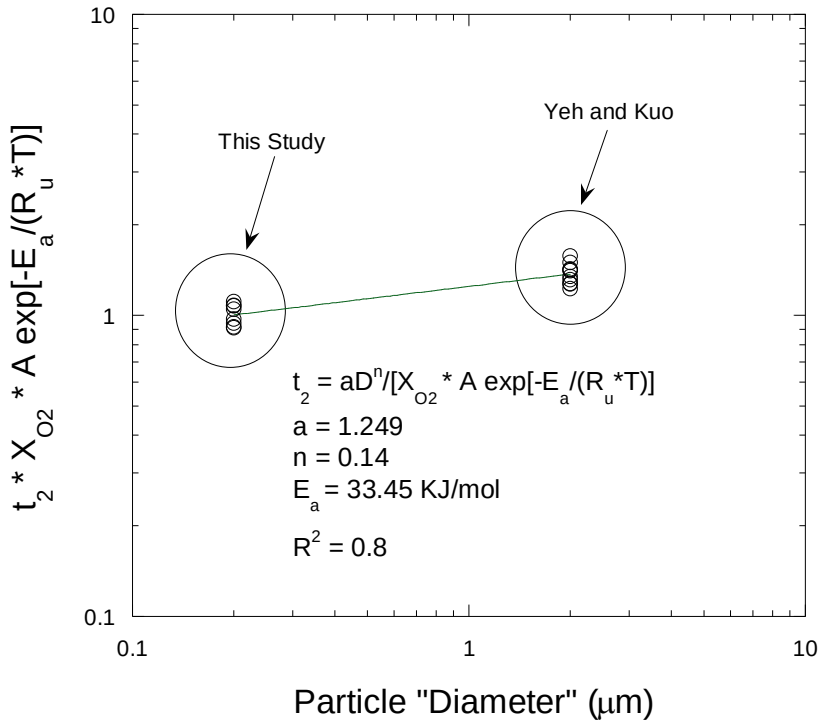

Fig. 5.19 t_2 Burning Time Correlation

5.2 Studies on Nanoaluminum Combustion

As was discussed in detail in Chapter 2, a number of other researchers have studied nanoaluminum in great detail. Bazyn[17] made estimates of burning times for nanoaluminum at high temperatures and pressures in a shock tube. Parr[16] estimated the ignition temperatures, and ensemble average burning times similar to this study of nanoaluminum in a hydrogen/oxygen/diluent Henken burner. Parr's[16] studies revealed that the ignition temperature of some types of nanoaluminum was much lower than that of traditional micron sized aluminum. In fact he found ignition temperatures less than 1100 K for several types of nanoaluminum including ALEX. Parr[16] also demonstrated a larger dependence of burning time on temperature for nanoaluminum which had not previously been established for micron-sized particles. Ordinarily aluminum particle

combustion times are only weakly dependent on temperature once ignition is achieved, as Beckstead's correlation[34] suggests $t_b \sim T^{-0.2}$. This is due to the fact that the larger aluminum particles establish their own temperature field by burning with a detached diffusion flame whose temperature is predetermined by the vaporization-dissociation temperature of the aluminum oxide[85]. Therefore, the surrounding gas temperatures do not play a large role in the particle burning time of micron-sized aluminum.

As a basis for comparison between the burning times of boron and aluminum nanoparticles, at a temperature of about 1600 K, Parr[16] found that aluminum nanoparticles had burning times between roughly 0.8 and 1 millisecond and at 1800 K the measured burning times ranged from about 0.7 to 0.9 milliseconds. In this study at similar temperatures the t_2 burning times of the boron nanoparticles ranged from about 1.7 to 3 milliseconds at roughly 1600 K and 1.5 to 2 milliseconds at about 1800 K. In general the boron nanoparticles had burning times that were 2 to 3 times longer than the aluminum nanoparticles. It should be noted that the environments in the two studies were quite different. In Parr's[16] study, the nanoaluminum was subjected to water vapor as its only oxidizer, whereas in this study the boron was subjected to oxygen, water vapor, and carbon dioxide. As Beckstead's correlation[34] points out, oxygen is a better oxidizer for aluminum than water vapor, therefore in similar environments it would be expected that the burning times of aluminum and boron nanoparticles would be separated by more than a factor of two or three. As was previously mentioned for larger particles boron has burning times that are roughly four times that of aluminum in similar environments.

In a separate study, Huang[89] correlated the data obtained by Parr[16] in a similar form as equation 5.17, which can be seen in equation 5.18.

$$t_b = \frac{D^{0.3}}{X_{eff} * C \exp\left(\frac{-E_b}{RT}\right)} \qquad \text{Eq. 5.18}$$

where D is in cm, X_{eff} is the same as given by Beckstead's correlation[34], $C = 5.5 * 10^{-4}$, and $E_b = 73.6$ kJ/mol. Interestingly, upon doing so, Huang[88] found that the burning time dependence on particle size was only $t_b \sim D^{0.3}$ once again showing that the burning time is only weakly dependent on particle size in the nanoparticle regime. However, nanoaluminum still has other advantages over micron-sized aluminum, such as the greatly reduced ignition temperatures. Therefore in an airbreathing propulsion system where the aluminum would be carried in a solid matrix, gel, or slurry, one would not need nearly as much heat supplied for ignition of the aluminum compared to boron. That provides a several advantages:

1) The aluminum can be a larger percentage of the fuel (increasing density impulse)
2) The combustor performance would be less sensitive to off design conditions. The combustor could operate in a very fuel lean condition and still provide enough heat to ignite and combust the aluminum.

5.3 Implications on High-Speed Airbreathing Combustors

As was established in section 5.1.3 and 5.2, the burning times of both boron and aluminum nanoparticles are only weakly dependent on the initial particle size. This would tend to imply that there might not be a large benefit in employing them as fuels or fuel supplements. However, any reduction in burning time certainly improves the ability to extract the available energy of a particle in a time sensitive environment such as a ramjet or scramjet combustor.

For boron, the total burning time data for realistic airbreathing conditions (i.e. X_{O2} < 0.2 for a traditional ramjet or scramjet) shown in figure 5.14 shows that the shortest total burn times measured were about 4 milliseconds at about 1800 K. Equation 5.3, which describes the burning time for the kinetically dominated regime implies that an increase in pressure will reduce the burning times. For the time durations that the particles were exposed to the flat flame burner products, below about 1700 K (for X_{O2} = 0.1) stage 2 combustion was never achieved. If the particles had been subjected for longer durations it is possible that they could have completed the ignition stage. However, there was no indication in this study that the nano boron would have fully ignited (reached stage 2) at a lower temperature than what other researchers[47, 90, 91] have observed in micron-sized particles. Boron ignition has been observed to occur from 1500-1900 K depending on the type of test and its conditions.

For aluminum, the studies of Parr[16] and Bazyn[17] indicated burning times in the 100's of μs which certainly suggests the possibility of complete combustion of a particle with a high-speed combustor. Perhaps of greater importance was that Parr[16] determined that the ignition temperature for some types of nanoaluminum is lower than traditional micron-sized particles. This could allow the combustor to operate at fuel lean conditions (lower temperatures) yet still provide efficient combustion, which could help reduce the thermal protection requirements, improve specific impulse, and improve density impulse by allowing more of the fuel to be made up of metal.

Unlike boron combustion, H_2O and CO_2 are reasonably effective oxidizers for aluminum. H_2O in particular can inhibit boron combustion, but according to Beckstead[34] is about 60% as effective of an oxidizer as O_2. This is an important since the metals are

essentially burning in the products of hydrocarbon combustion, even though the O_2 concentration is decreasing, H_2O and CO_2 still contribute significantly to the combustion of the aluminum particles.

CHAPTER 6

AIRBREATHING COMBUSTOR RESULTS

6. Airbreathing Combustor Experiments

One of the major goals of this study was to determine whether or not the great potential of metallized fuels can be realized under realistic combustor conditions. In particular, can all of the available energy of a metallized fuel be extracted in the short residence times typical of a high speed airbreathing combustor. Chapter 6 discusses the results of this portion of the study.

6.1 Test Conditions

Once the combustor was designed, fabricated, and some basic characterization studies were conducted, testing under more realistic operating conditions commenced. Initially, ethylene (C_2H_4), a hydrocarbon was used as the sole fuel in order to create a baseline for fuel evaluation. Following the baseline testing, testing started with metallized fuels. The metallized fuels were mixtures of gaseous ethylene with either aluminum or boron added in as a particle laden flow.

Figure 6.1 is a series of images recorded with a Sony Video Recorder showing the combustor operating with and without the addition of aluminum or boron nanoparticles. The ethylene only tests were characterized by the visible blue light as seen in the figure, the tests with aluminum addition appeared white in color, and the tests with boron appeared green or yellowish in color. No filtering was applied in obtaining these images.

Table 6.1 provides a summary of all of the test conditions. The test conditions given are nominal values and all data reduction was conducted on a test-by-test basis, in which the conditions could vary slightly from the given conditions. A total of 20 different types of test were conducted. Test conditions designated by a numeral were ethylene only tests. Conditions designated with a numeral followed by a letter "a" or "b" represent aluminized or boron loaded tests respectively. Tests with the same numeral designation have identical ethylene mass flow rates, such that the only difference between the two is the addition of the metal nanopowders.

The combustor inlet velocity was calculated from a one dimensional mass flow rate calculation knowing the flow area, ambient pressure and the temperature. The metal mass flow rates came from the particle seeder calibration and represent the total mass flow rate of the particles. However, the weight percentages given represents the amount of pure metal powder (i.e. the active content) material in the fuel. The metal oxides were lumped into the fuel for the purpose of the calculations. The adiabatic flame temperatures were calculated with the NASA CEA 2000[84] chemical equilibrium code. The flame temperature calculations take into account the active content of the particles and assumed that the remain particle material was the metal oxide. The equivalence ratio also included both the fuel and oxidizer contributions from the pilot flame.

Table 6.2 shows some of the flow parameters of interest for the different inlet velocities. The Reynolds number was calculated based upon flat plat assumptions, where the average velocity was calculated by the one dimensional continuity equation, the length scale was taken as the distance between the flow straightener and the center of the pilot flame. The upper limit for laminar flow on a smooth flat plate is 3×10^6, therefore

under these assumptions the flow remained laminar up until the pilot flame location. The residence time was calculated using the average velocity and the difference in the axial location of the pilot flame and the thermocouples.

Finally, table 6.3 shows the mole fractions of the main oxidizing species that occur as a result of the gaseous ethylene combustion. Essentially the mole fractions shown are for the test conditions designated by a numeral only. This is shown since the time-scale for the gaseous hydrocarbon combustion is much smaller than that of the metals; therefore, the metals were considered to be burning in the product species of the ethylene combustion.

Table 6.1 Summary of Combustor Test Conditions

Test Condition	Inlet Velocity (m/s)	$\dot{m}_{Metal}$ (g/s)	Wt % Metal	Weight % Premixed C_2H_4	Overall Φ	Adiabatic Flame Temperature (K)
1, 1b	40 ± 1	0, 0.8	0, 12.7 ± 0.6	60, 49	0.64, 0.69	1960, 2090
2, 2b	40 ± 1	0, 0.8	0, 15.2 ± 0.8	49, 38	0.50, 0.57	1685, 1850
3, 3b	55 ± 2	0, 0.8	0, 12.7 ± 0.6	59, 49	0.48, 0.52	1596, 1712
4, 4b	55 ± 2	0, 0.8	0, 9.7 ± 0.5	70, 61	0.64, 0.69	1946, 2065
5, 5b	70 ± 2	0, 0.8	0, 9.7 ± 0.5	70, 60	0.51, 0.54	1660, 1746
6, 6a	40 ± 1	0, 0.39	0, 7.4 ± 0.4	62, 57	0.69, 0.70	2056, 2120
7, 7a	55 ± 2	0, 0.39	0, 7.2 ± 0.4	62, 57	0.51, 0.52	1680, 1744
8, 8a	55 ± 2	0, 0.87	0, 14.8 ± 0.7	48, 40	0.50, 0.52	1645, 1771
9, 9a	55 ± 2	0, 0.87	0, 11.4 ± 0.6	62, 54	0.69, 0.70	2031, 2120
10, 10a	70 ± 2	0, 0.87	0, 11.5 ± 0.6	62, 54	0.54, 0.56	1740, 1825

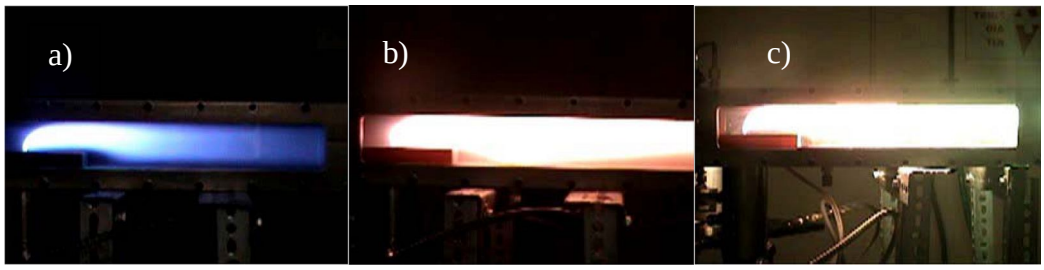

Fig. 6.1 Combustor Operating in Traditional Ramjet Mode with a) Gaseous Ethylene as Fuel b) Gaseous Ethylene with 50 nm Aluminum Particles and c) Gaseous Ethylene with Boron Particles

Table 6.2 Flow Conditions

Inlet Velocity (m/s)	Inlet Reynolds Number, Re	Residence Time (s)
40	64,168	0.0103
55	88,232	0.0075
70	112,295	0.0059

Table 6.3 Mole Fractions of Oxidizing Product Species

Test Condition	X_{O2}	X_{H2O}	X_{CO2}
1	0.075	0.091	0.091
2	0.107	0.072	0.072
3	0.110	0.068	0.068
4	0.074	0.089	0.090
5	0.104	0.073	0.073
6	0.064	0.097	0.098
7	0.103	0.072	0.072
8	0.105	0.071	0.071
9	0.063	0.095	0.096
10	0.095	0.075	0.076

6.1.1 Mie Scattering Results

Planar Mie Scattering was employed to determine the particle dispersion patterns. The test configuration and specific diagnostics were described in Chapter 3. The images were recorded looking directly through the window located on the side of the combustor, such that the laser sheet, which was passed through the top of the combustor, and camera

were perpendicular to each other. Figure 6.2 shows an example of typical instantaneous Mie Scattering Images. These images were taken for test condition 6a.

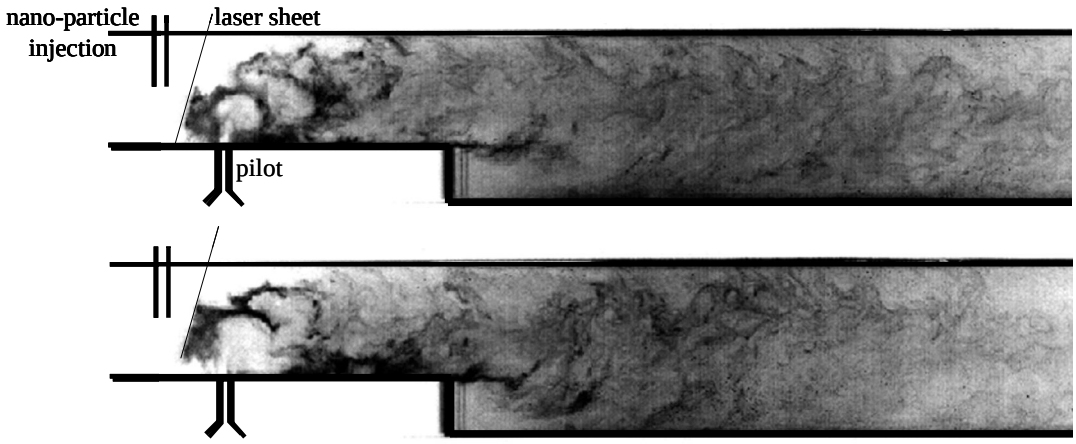

Fig. 6.2 Typical Instantaneous Mie Scattering Images (Inlet Velocity = 40 m/s, wt% Al = 7.4, Φ = 0.7, T_{ad} = 2120 K)

The images show that in the vicinity of the pilot flame the intensity levels fluctuate. This was due to particles being entrained into the pilot jet. Further downstream the scattering intensity appeared to become more uniform. Figure 6.3 illustrates the average intensity contour from all of the images collected from one test. Downstream of the step, the contour shows a fairly uniform scattering intensity, suggesting fairly uniform particle dispersion although the lower portion of the combustor appeared to have a slightly greater intensity.

In order to investigate this further, figure 6.4 shows the average intensity profile from the averaged image at axial positions of 10, 15, and 20 cm for test condition 6a. The spikes near the bottom and top of the combustor were due to reflections from the surfaces of the test rig and should be ignored when interpreting the profiles. At the 10 cm

axial location there was a relatively large spike between the 1 and 2 cm combustor height positions. The spike was associated with the combustor step. Up until the 10 cm axial position, there was a relatively large concentration of particles in the approximate height of the step. A little further downstream (15 and 20 cm) the particles appear to be mixing more thoroughly into the combustor. Inspection of figure 6.4 at the downstream locations indicated that the average intensity was relatively constant up to about the 3 cm vertical location point. At that point the average intensity slowly decreased as the vertical location was increased towards the top portion of the combustor. Near the top of the combustor the average intensity was about 70% of the "constant intensity" region. This indicates that at these axial locations, the majority of the ALEX particles were in the bottom portion of the combustor, which would suggest that for these axial locations the equivalence ratio was not entirely uniform throughout the combustor, although the trend suggests that it was becoming more uniform.

Figure 6.5 is the average intensity profile from the averaged image at axial positions of 10, 15, and 20 cm for test condition 7a. Again there was a large spike at the 10 cm axial location between the 1 and 2 cm vertical locations that was associated with the rearward facing step. At the other axial locations, the intensity was relatively constant through the majority of the combustor, however, the bottom portion of the combustor did tend to exhibit higher intensity levels.

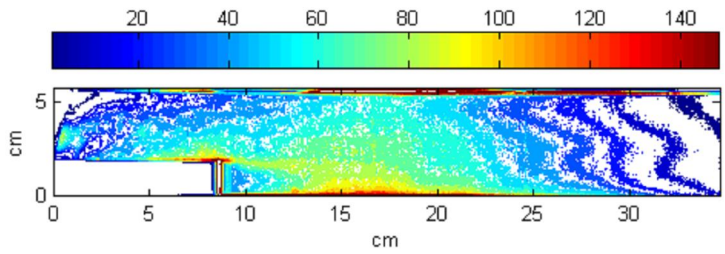

Fig. 6.3 Average Intensity Contour of Mie Scattering Images (Inlet Velocity = 40 m/s, wt% Al = 7.4, Φ = 0.7, T_{ad} = 2120 K)

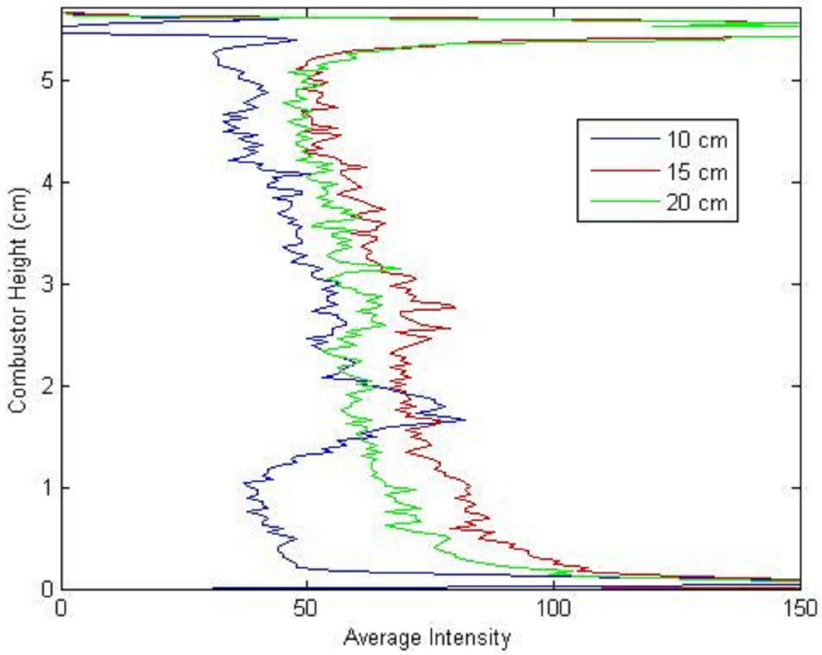

Fig. 6.4 Average Intensity at Axial Locations (Inlet Velocity = 40 m/s, wt% Al = 7.4, Φ = 0.7, T_{ad} = 2120 K)

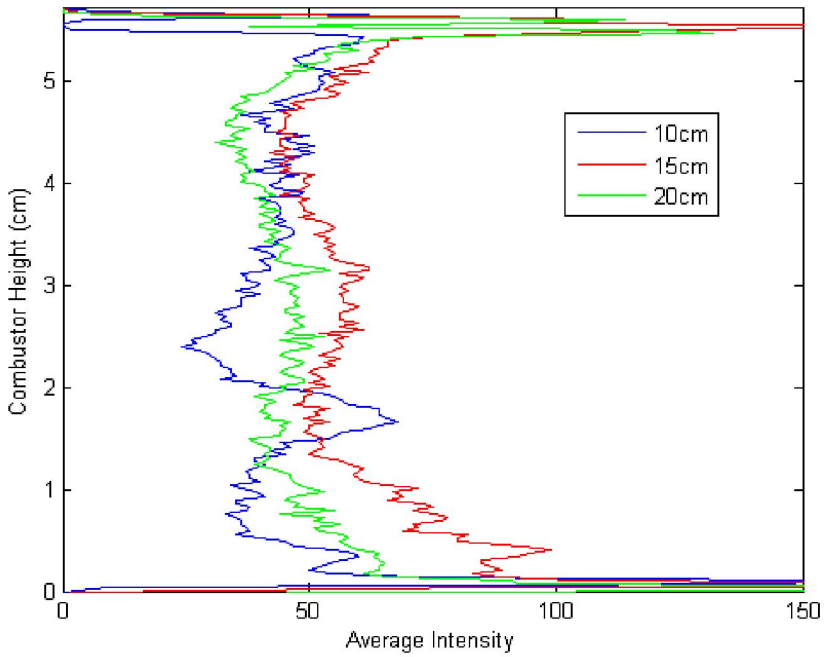

Fig. 6.5 Average Intensity at Axial Locations (Inlet Velocity = 55 m/s, wt% Al = 7.2, Φ = 0.52, T_{ad} = 1744 K)

6.1.2 Chemiluminescence Results

6.1.2.1 AlO Emission

AlO is a known gas phase intermediate in aluminum oxidation[42,43]. Figure 6.6 is series of examples of typical instantaneous images that were obtained with an ICCD camera and a narrow-band interference filter, centered at 488±2 nm. A camera shutter speed of 5 μs and a framing rate of 12 Hz was used to capture the images. The instantaneous images show some fluctuation but qualitatively show that the most intense regions of AlO emission do not extend much beyond the combustor step.

In the wavelengths allowed by the band pass filter there were some bands of emission due to hydrocarbon combustion. In particular, C_2*, CH*, and CO_2 exhibit bands that overlap the filter. However, a series of ethylene/air only tests were conducted

with this filter in place, and the emission due to hydrocarbons was minimal which can be seen in figure 6.7. Testing showed that peak background emission of the hydrocarbon only tests was less than $1/20^{th}$ of the peak emission of the aluminized flows.

Figure 6.7 is a series of AlO intensity contours for all of the aluminized tests obtained by averaging together the images collected in a test. Typically, the images collected in the first second of the test are not used to allow the particle seeder to approach a steady state condition. Therefore in the case of the aluminum testing, in which a typical experiment was four seconds in duration, a total of 36 images were averaged to create the contours. It is clear from the figure that the majority of AlO emission took place within the first 15 cm of the combustor for all conditions. However, there is a clear trend of decreasing axial distance of AlO emission with decreasing combustor inlet velocity.

Comparing the tests with similar inlet velocities and aluminum flow rates (8a and 9a), we see that the test with a higher flame temperature (9a) exhibits higher overall intensities (see figure 6.7). Although the majority of the AlO emission takes place within the first 15 cm of the combustor, the highest temperature tests (6a and 9a) did exhibit some significant emission much further downstream. This could be a result of larger agglomerates igniting and or combusting further downstream compared to the smaller agglomerations, or as Olsen pointed out residual oxides/suboxides[15].

In order to make an estimate for the ignition delay, the intensity was plotted along the length of the combustor starting from the pilot flame (figure 6.8) at a combustor height of 3.75 cm and then converted to time (figure 6.9), by considering the combustor inlet velocity. The ignition delay was estimated by taking the first instance when the

intensity reached half of its maximum value. The delay was virtually identical in all of the tests of a given additive. For aluminum the delay was consistently between 0.3 to 0.4 milliseconds. Typical uncertainty in this measurement is 0.1 millisecond.

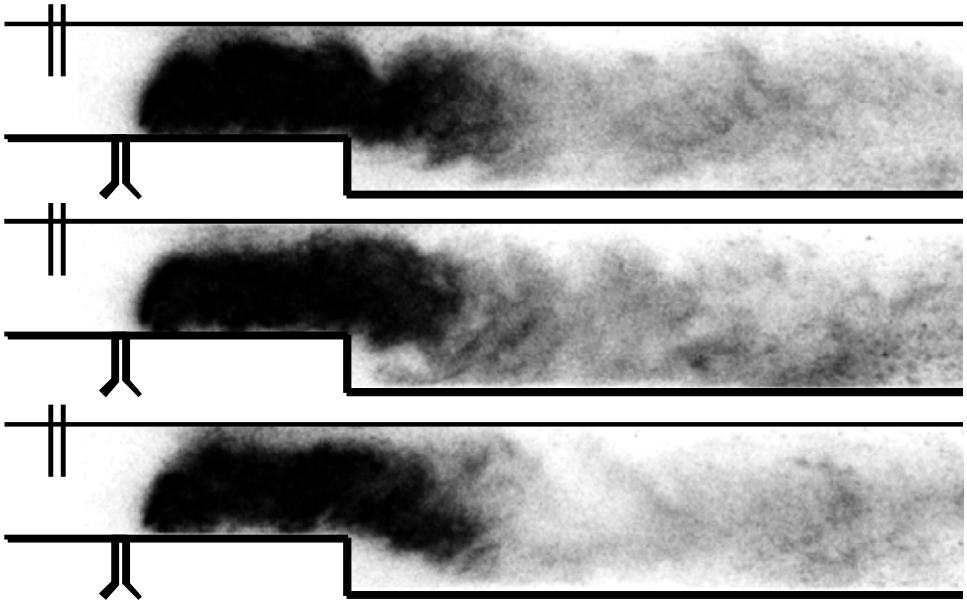

Fig. 6.6 Instantaneous AlO Chemiluminescence Images

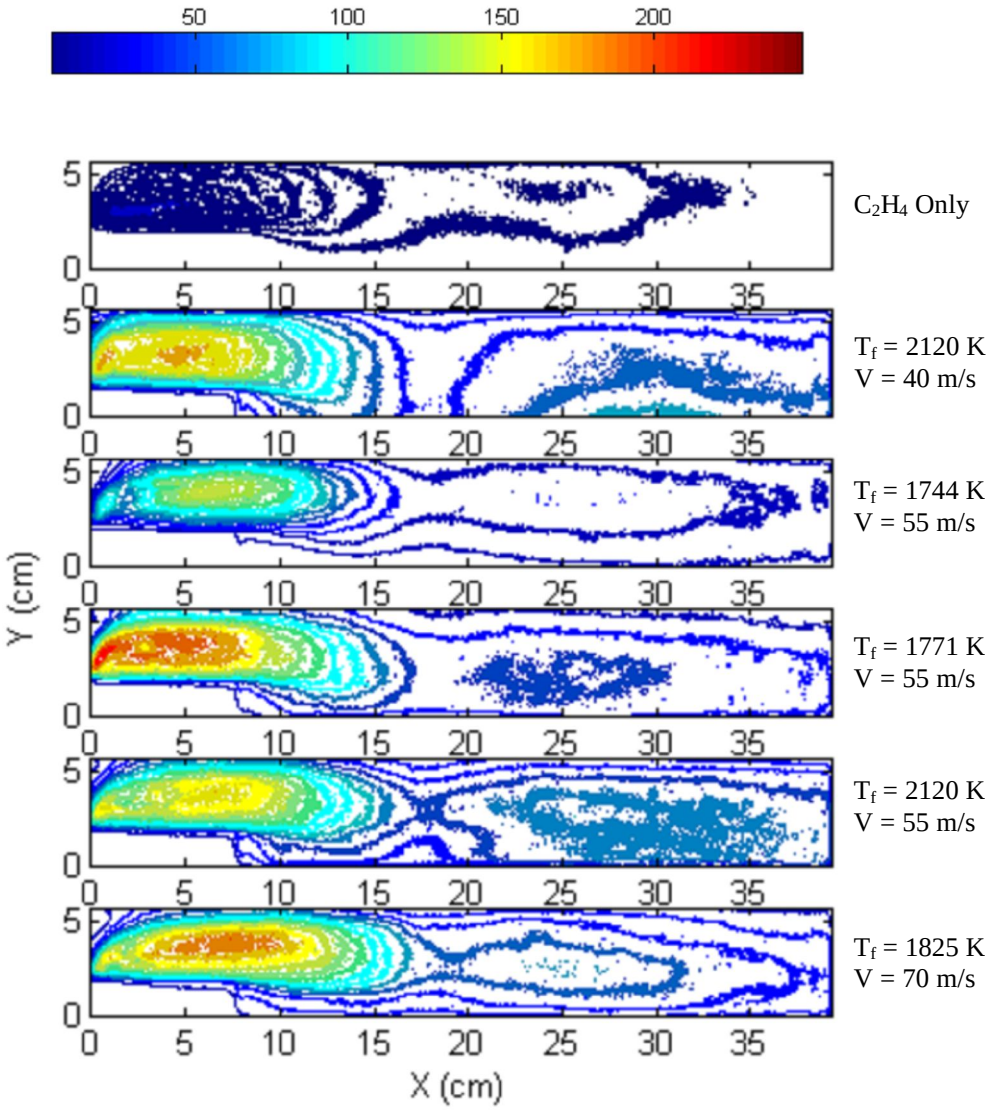

Fig. 6.7 AlO Chemiluminescence Contours (C_2H_4 only, 6a, 7a, 8a, 9a, 10a)

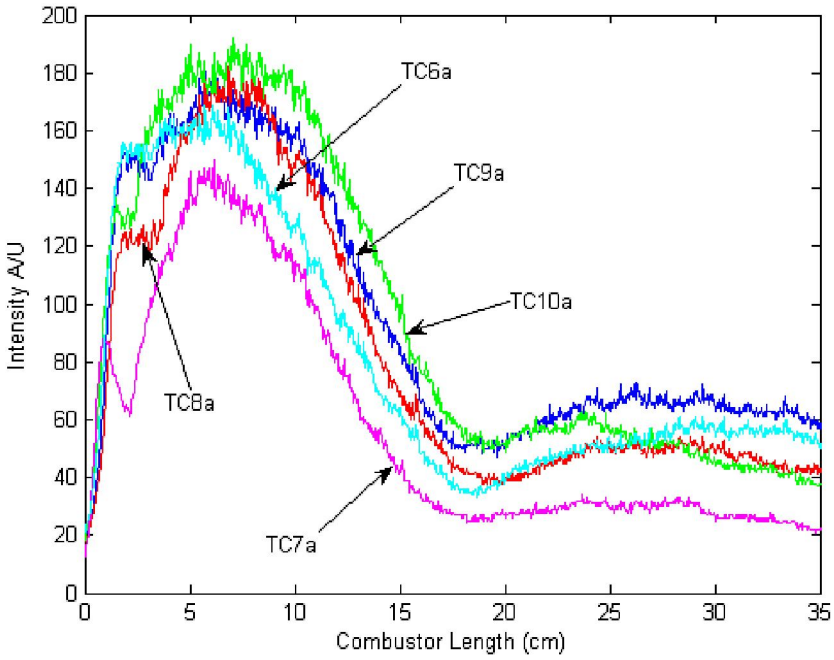

Fig. 6.8 AlO Intensity Profiles Versus Combustor Length

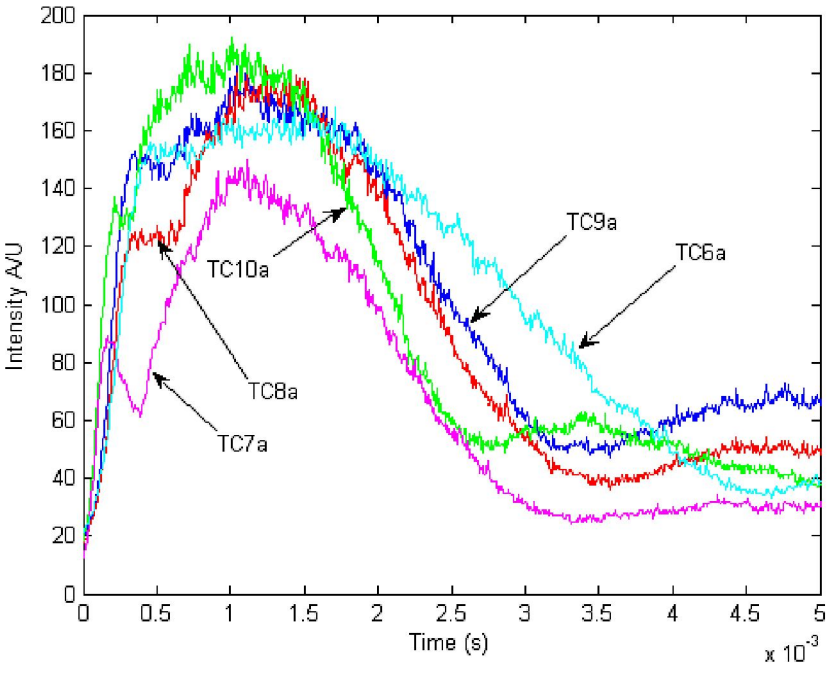

Fig. 6.9 AlO Intensity Profiles Versus Time

6.1.2.2 BO_2 Emission

The BO_2 molecule is a reactive intermediary gas-phase species formed throughout boron particle ignition and combustion[51]. According to Spalding[72], the BO_2 spectrum is readily observable during both the combustion and ignition stages of boron combustion. Figure 6.10 is a series of instantaneous BO_2 emission images. A camera shutter speed of 4 μs and a framing rate of 12 Hz was used to capture the images. A Narrow-band interference filter, centered at 546±2 nm was used to capture images of the BO_2 emission. Since the primary fuel was a hydrocarbon (Ethylene), the potential for hydrocarbon emission overlapping the BO_2 band existed. In particular, C_2 exhibits several bands in the vicinity of the filter. However, according to Gaydon[75], the C_2 bands near 546 nm are characterized as weak or very weak. In order to conclude without question that the emission detected was BO_2, several tests with ethylene only were conducted with the 546 nm filter in place. In each case any emission detected was negligible. An example of the testing for background hydrocarbon emission can be seen in figure 6.11, which shows that no emission was detected at the previously stated camera settings for tests that did not include boron.

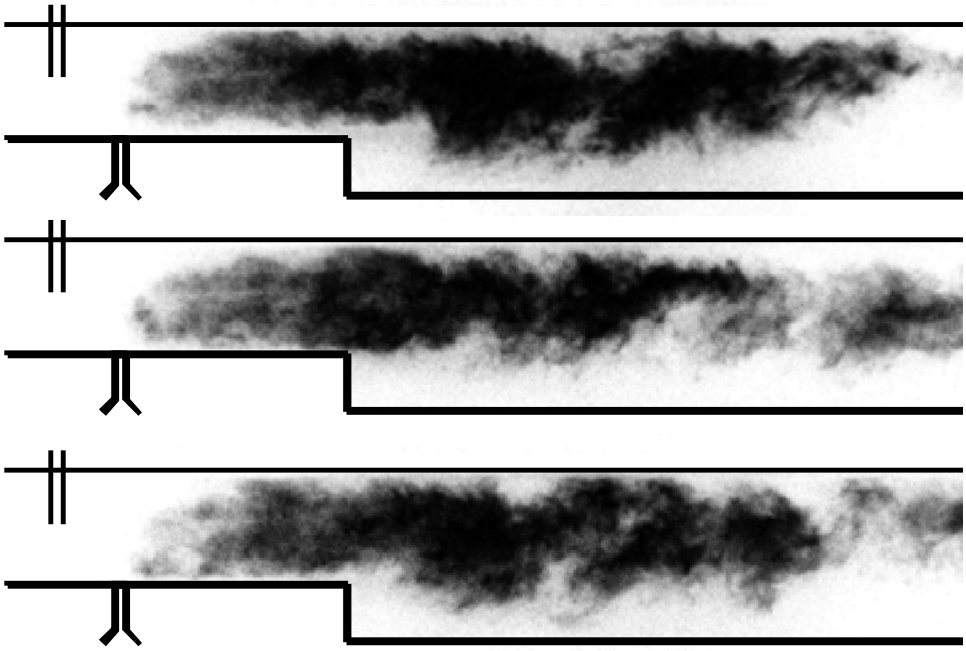

Fig. 6.10 Instantaneous Images of BO_2 Emission

Figure 6.11 provides a summary of intensity contours for all of the tests that contain boron particles. Just as in the ALEX experiments, the contours were created by averaging all of the images collected during an experiment except for the first second. In the case of the boron experiments, the typical test duration was 3 seconds. Therefore, 24 images were averaged to create the contours.

The top contour is the case in which no boron was injected to determine the extent of hydrocarbon emission interference. The second and third contours are for the slowest speed cases and show the largest intensities of all of the cases. The fourth and fifth contours are the middle speed cases, and the last contour is the highest speed case. The presence of BO_2 clearly indicates the ignition of the boron particles. It is interesting, but not surprising to note that all of the contours show that the highest intensity regions are significantly downstream of the pilot flame (X=0 cm) region suggesting a delay in the

ignition of the boron particles. Qualitatively, comparing the tests with similar velocities (1b and 2b, and, 3b and 4b), it is clear that the tests with higher adiabatic flame temperatures (1b and 4b) exhibited higher intensities of BO_2 emission and for longer spatial durations.

In order to make an estimate for the ignition delay, the intensity was plotted along the length of the combustor starting from the pilot flame (figure 6.12) at a combustor height of 3.75 cm and then converted to time (figure 6.13), by considering the combustor inlet velocity. Again, the ignition delay was estimated by taking the first instance when the intensity reaches half of its maximum value. The delay was virtually identical in all of the tests, ranging from 0.9 to 1.1 milliseconds. Typical uncertainty in this measurement is 0.1 millisecond.

Of interest, it should be noted that the tests corresponding to similar velocities had nearly identical profiles in both space and time during the first 15 to 20 cm of the combustor, regardless of boron concentration, equivalence ratio, or temperature. This implies that the pilot flame is once again the dominant source of ignition of the particles. The major difference in the tests having the same inlet velocity came further downstream in the combustor (or later in time). The higher temperature tests (TC1b and TC4b) exhibit BO_2 emission for longer durations than the tests of the same velocity but lower temperature (TC2b and TC3b). This suggests an increase in the oxidation of boron with increased temperature, which is not in itself a surprising result; it does however begin to provide boundaries for efficient combustor operation. In addition, the peak intensity values while consistent for a specific inlet velocity do not follow an increasing trend as might be expected with increasing temperature. This implies that inlet velocity, or more

specifically, residence time, may be as important, or perhaps more important than temperature alone.

In some test conditions (1b) the intensity level did not reach background levels even at the end of the combustor. Figures 6.12 and 6.13 imply that the boron may actually extinguish in some or all of the conditions. In Figure 6.12, the lower temperature cases reach the background intensity before the end of the combustor whereas the higher temperature cases still show significant intensity levels. Similarly, in the time analog (figure 6.13) the lower temperature conditions reach background levels in a shorter duration. This result indicates that the particles are potentially extinguishing, at least in the lower temperature conditions. In fact King[92] showed that temperature boundaries for boron particle extinguishment are a strong function of pressure and oxygen concentration. King[91] also showed that smaller particles required higher temperatures to prevent extinguishments. These tests were conducted at essentially at atmospheric pressure requiring higher temperatures to ensure that the particles do not extinguish.

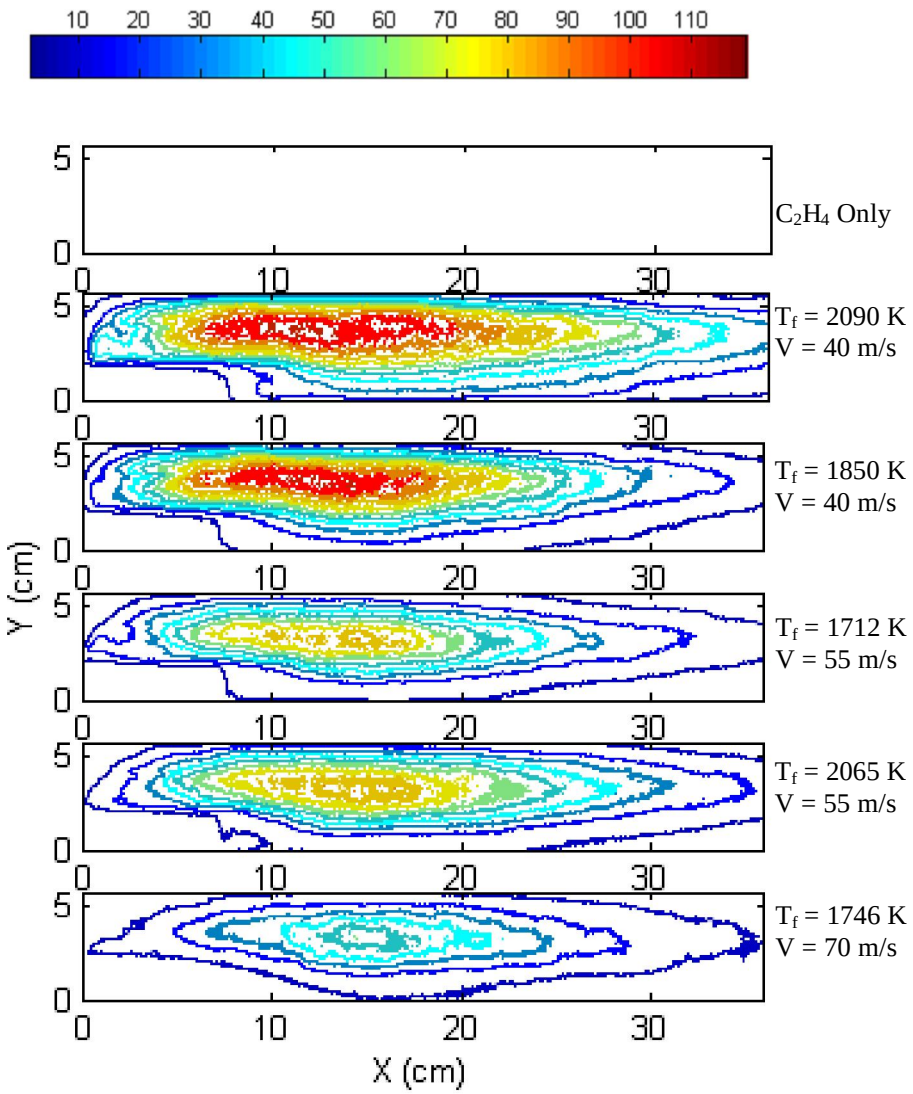

Fig. 6.11 BO_2 Chemiluminescence Contours (C_2H_4 only, 1b, 2b, 3b, 4b, 5b)

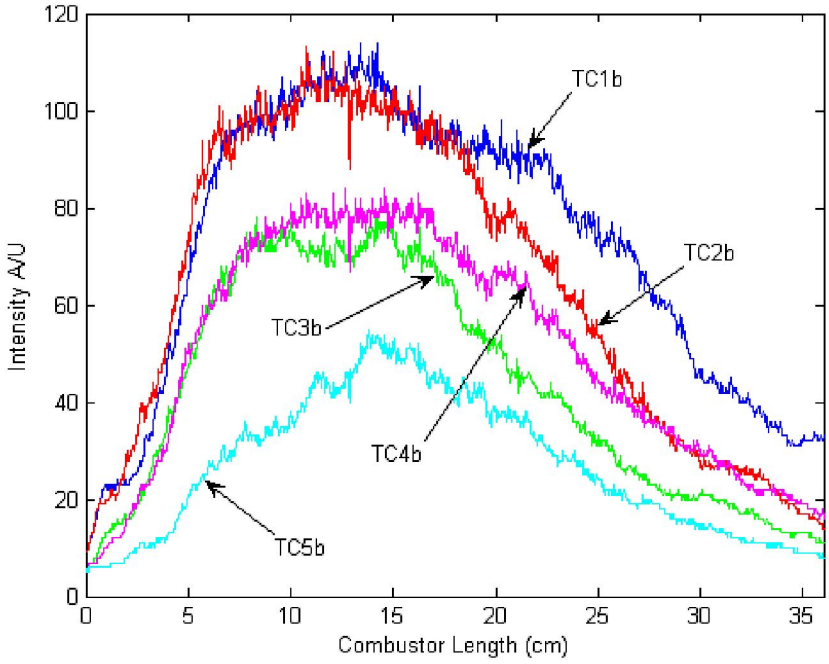

Fig. 6.12 BO_2 Intensity Profiles Versus Combustor Length

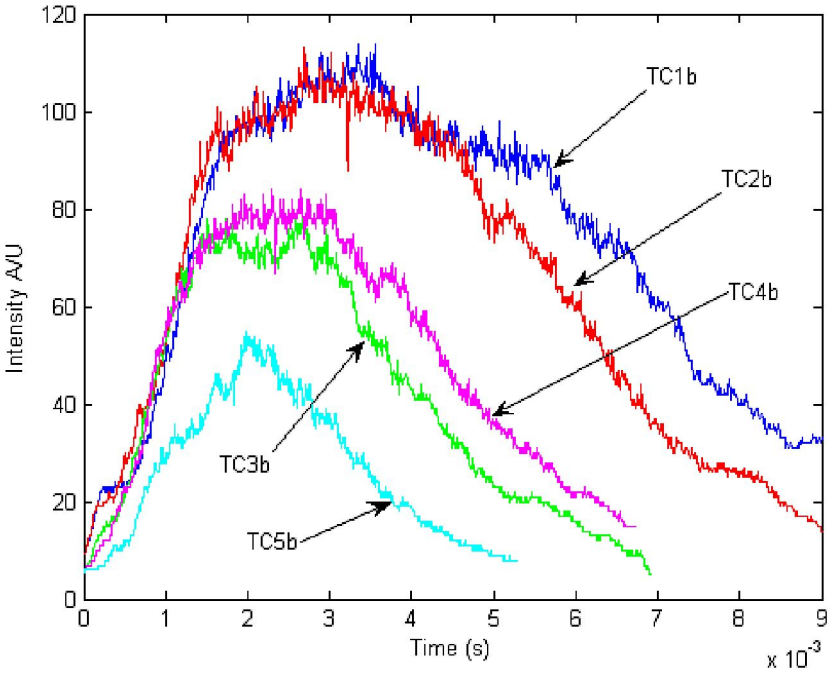

Fig. 6.13 BO_2 Intensity Profiles Versus Time

6.1.2.3 Chemiluminescence Summary

The presence of BO_2 and AlO clearly indicate that the particles were ignited and oxidation to some extent took place. Several observations can be made about the differences between the BO_2 and AlO contours. First, it is obvious that the majority of emission of BO_2 took place over a longer portion of the combustor than that of AlO under all conditions. Another observation is that the peak areas of AlO emission were clearly closer to the pilot flame ignition source (X=0) than the BO_2 emission, suggesting larger ignition delays for the boron particles.

The average intensity over the entire image of a given test condition is shown as a function of adiabatic flame temperature in figure 6.14, which shows all of the data for the test conditions summarized in Table 6.1. The aluminized data shows a clear trend for each aluminum mass flow rate of increasing average intensity with increasing flame temperature as would be expected, since the intensity is heavily dependent on flame temperature. However, the data collected in the boron loaded tests have no real trend to speak of, suggesting that temperature is not the lone influence on chemilumiscent intensity in these tests.

Figure 6.15 shows the product of average intensity and inlet velocity as a function of adiabatic flame temperature. Using this parameter, the boron-loaded tests now begin to show a smoother trend, suggesting that residence time as well as temperature is affecting the chemiluminescent intensity. The trend also shows that there is some temperature threshold that needs to be attained before significant amounts of boron combustion occurs. This threshold appears to be for experiments in which the adiabatic flame temperature exceeds 1800 K. The data obtained and presented in Chapter 5 shows

that there was a significant temperature dependence on burning time, particularly in the t_1, ignition stage, of boron combustion. The total burning times for X_{O2} = 0.15 at about 1700 K in the flat flame burning experiments was about 6 milliseconds, and was reduced to about 3.5 milliseconds at about 1800 K. For the two highest speed conditions, this would imply that a minimum temperature of about 1800 K would be required in order to possibly complete the boron particle combustion. At 1700 K, for X_{O2} = 0.1 t_2 combustion was not even achieved in the flat flame burner which has a typical residence time of about 12 milliseconds. As table 6.2 shows, the typical residence time in the airbreathing combustor testing was a maximum of 10 milliseconds, which implies that t_2 combustion would not be reached for test conditions at or below 1712 K and X_{O2} = 0.1.

The aluminized tests do not show an obvious trend with the product of velocity and intensity, implying that residence time is not affecting the chemiluminescent intensity. The resulting conclusion is that under these conditions the “same” amount of aluminum was being consumed in all of test conditions.

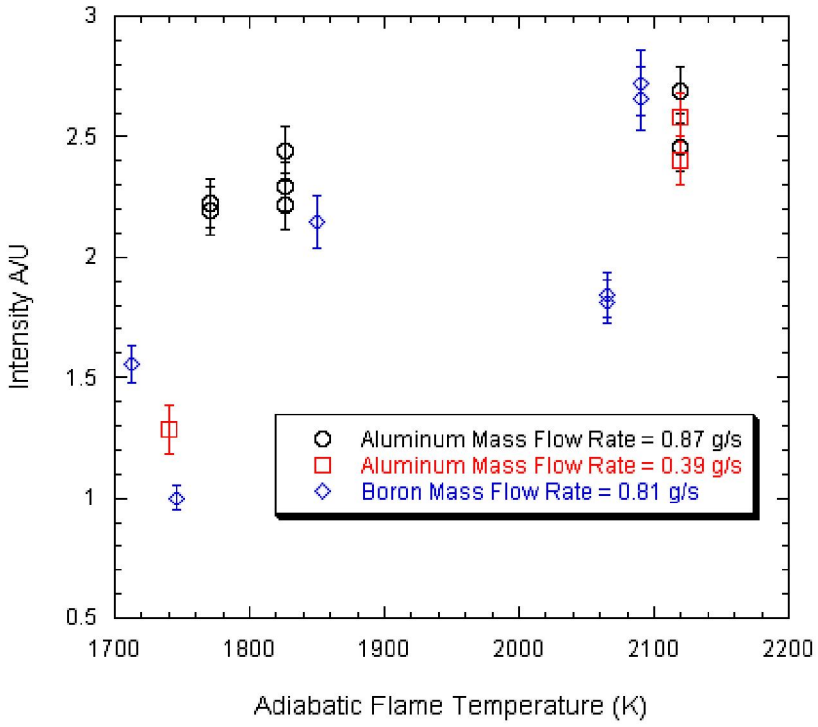

Fig. 6.14 Average Intensity as a Function of Adiabatic Flame Temperature

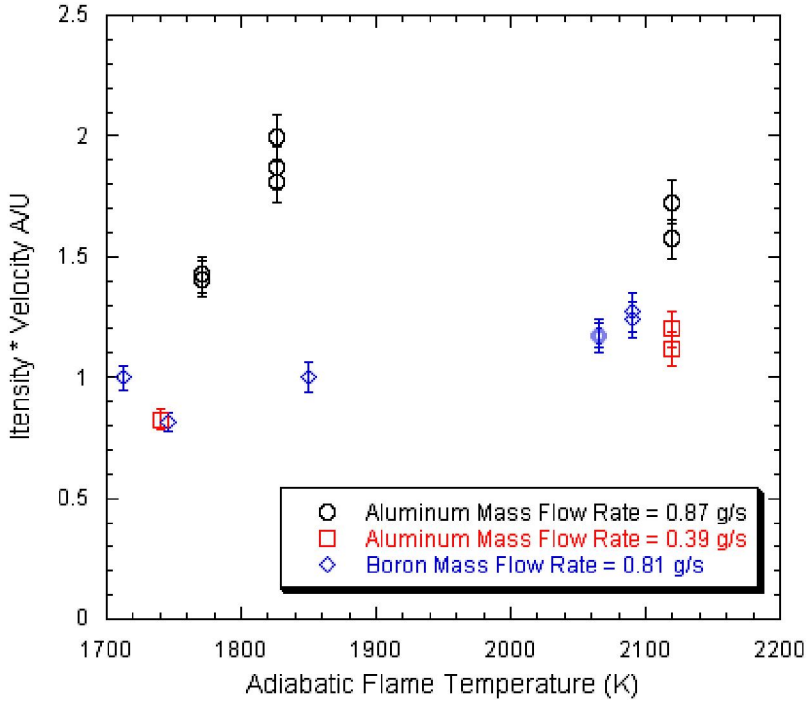

Fig. 6.15 Intensity-Velocity Coupling as a Function of Adiabatic Flame Temperature

6.1.3 Temperature Measurements

Combustion gas temperature measurements were made using thermocouples at approximately the exit plane of the combustor. In total, four thermocouples were placed at the exit plane of the combustor to form a "rake", which can provide temperature profiles for different test conditions. In general the two outermost thermocouples were K-types (Chromel-Alumel) with bead diameters of approximately 1000 μm, while the inner thermocouples were B-types (Pt-6%Rh/Pt-30%Ph) with bead diameters of approximately 200 μm.

Figure 6.16 shows a typical set of thermocouple traces prior to radiation correction. For analysis purposes, a period of 0.2 seconds near the end of the test was averaged and then corrected for radiation to provide temperature profiles for each condition. Figure 6.20 shows some typical profiles from aluminized tests. In general, the tests were very repeatable.

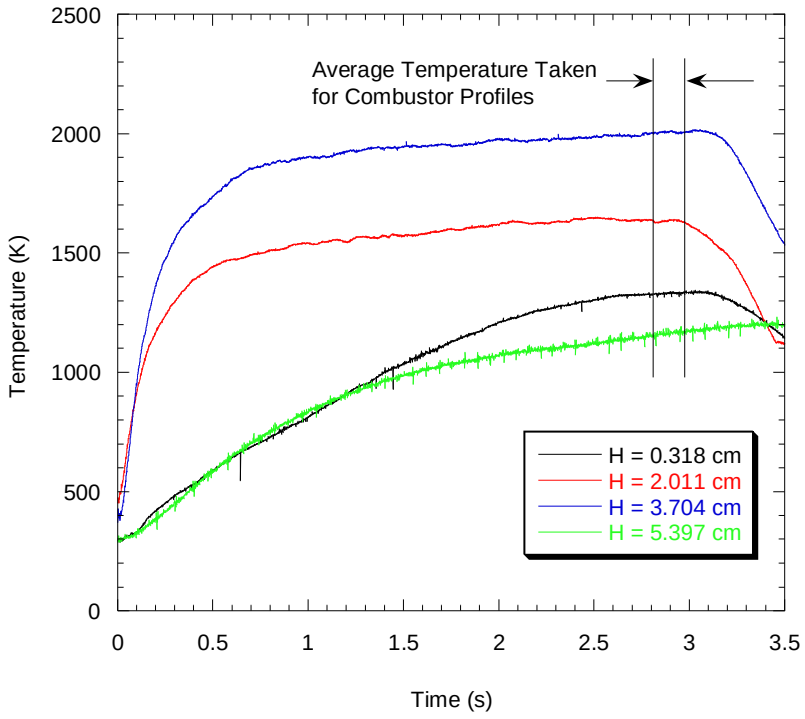

Fig. 6.16 Typical Thermocouple Trace (Uncorrected for Radiation) from Test Condition 1b (Inlet Velocity = 40 m/s, wt% B = 12.7, Φ = 0.69, T_{ad} = 2090 K)

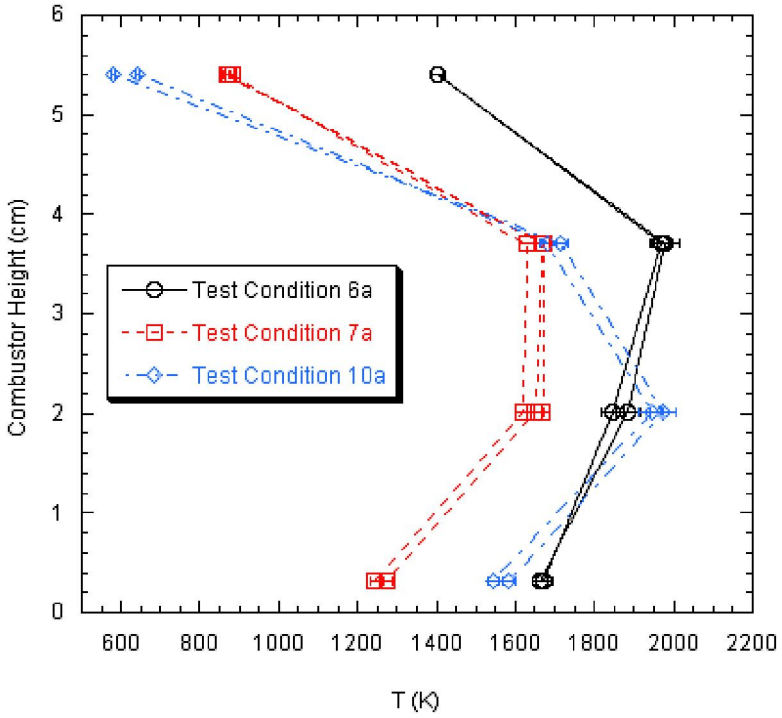

Fig. 6.17 Combustor Temperature Profiles for Selected Ethylene/ALEX Tests

Figures 6.18-6.20 show the results of the boron loaded experiments and their ethylene only analogs. Figure 6.18 shows the lowest speed tests (40 m/s inlet velocity), TC1b and TC2b, which had adiabatic flame temperatures of 2090 K and 1850 K respectively. For TC1b, the highest peak temperature measured was 2086 K, while for TC2b the highest peak temperature measured was 1820 K. For the most part, at each location, the boron loaded experiments had temperatures meeting or exceeding those of the ethylene only analogs.

Similarly figure 6.19 shows the intermediate speed cases (55 m/s inlet velocity), TC3b and TC4b, which had adiabatic flame temperatures of 1712 K and 2065 K respectively. The highest measured temperature for TC3b was 1592 K while the peak measured temperature for TC4b was 2069 K. Since the combustible mixture was not entirely uniform, it is possible that the highest measured temperature could exceed the adiabatic flame temperature. Interestingly for TC3b, the temperatures approximately meet or are significantly lower than its ethylene only analog. In particular, the top portion of the combustor had measured temperatures that are significantly lower than the ethylene only analog. Conversely, for TC4b, in most cases the temperatures approximately met or exceeded the ethylene only analog.

Finally, figure 6.20 shows the result of the highest speed (70 m/s inlet velocity), TC5b, experiment whose nominal adiabatic flame temperature was 1746 K. The highest measured temperature for this condition was 1688 K. Once again, in this experiment, the measured temperatures were at or below the ethylene analog.

In summary, experiments with nominal adiabatic flame temperatures of 1850 K or greater all showed increased combustor temperature than its ethylene analog. On the

other hand, experiments with adiabatic flame temperatures below 1850 K show either no temperature improvement, or in some cases a temperature reduction. This is not surprising in light of the results of the flat flame burning experiments described in Chapter 5, which showed that for X_{O2} = 0.1 second stage combustion was not even achieved until temperatures approaching 1800 K were reached for residence times of about 12 milliseconds.

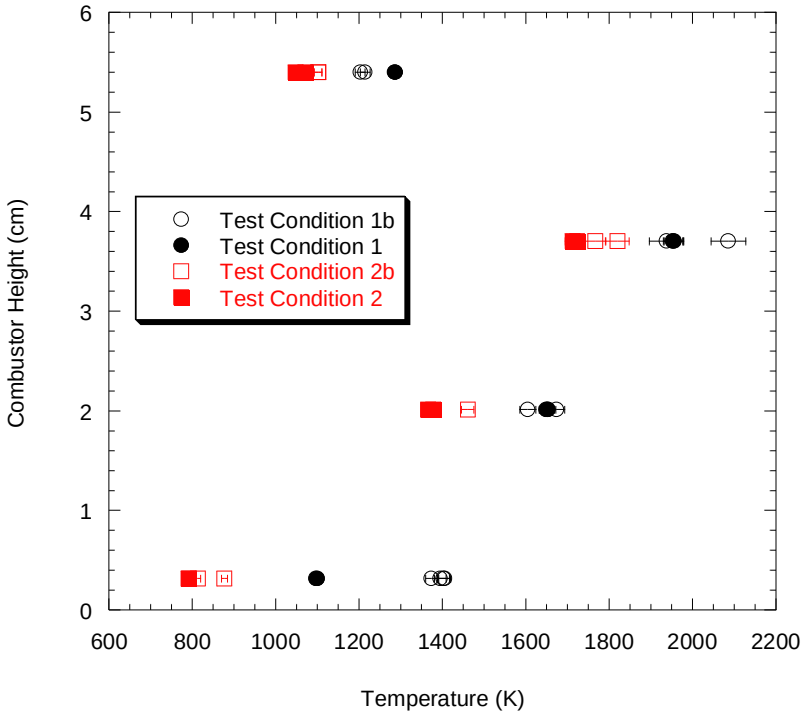

Fig. 6.18 Temperature Profiles for Test Conditions 1, 1b, 2, 2b (Inlet Velocity = 40 m/s)

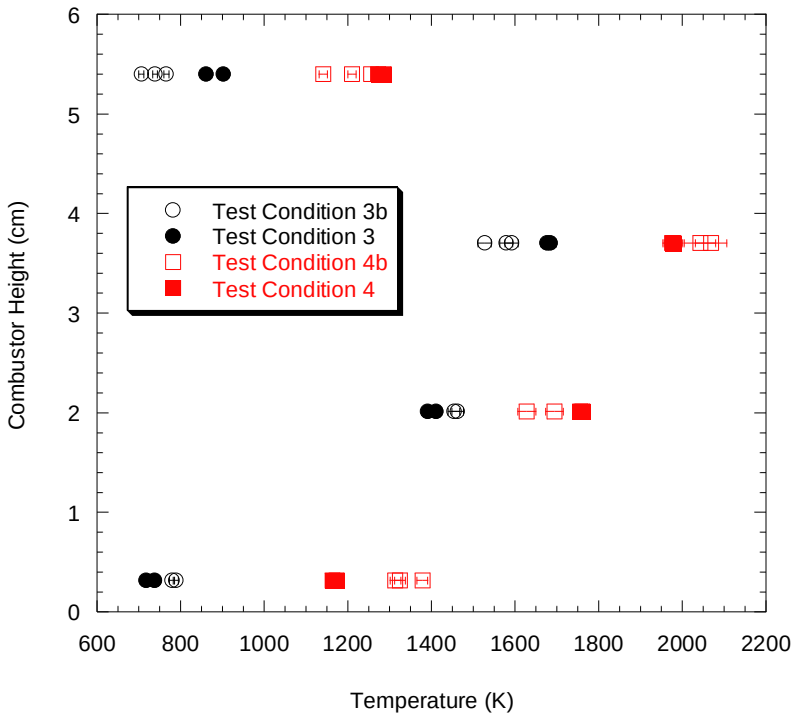

Fig. 6.19 Temperature Profiles for Test Conditions 3, 3b, 4, 4b (Inlet Velocity = 55 m/s)

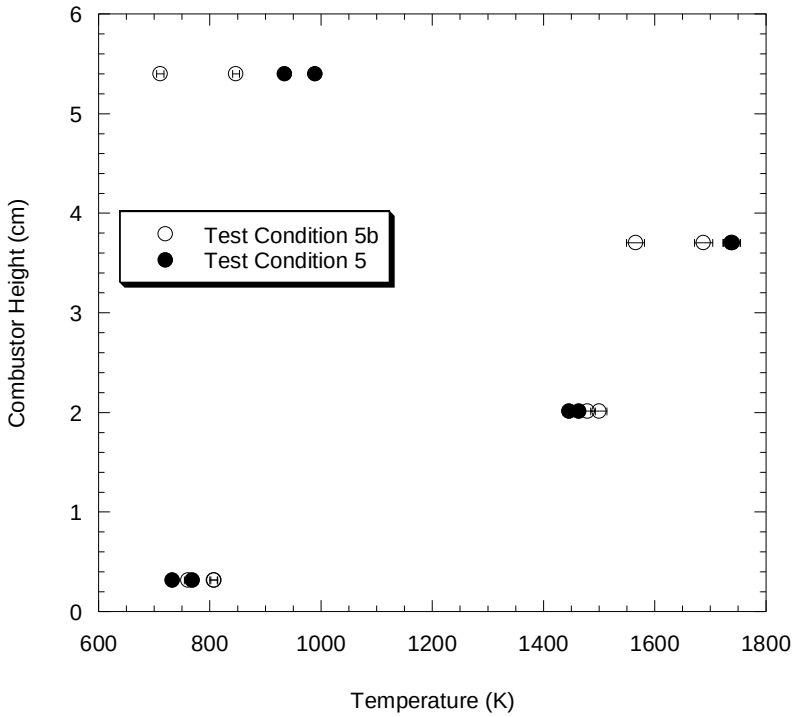

Fig. 6.20 Temperature Profiles for Test Conditions 5, 5b (Inlet Velocity = 70 m/s)

Figures 6.21-6.23 show the aluminized experiments and their ethylene only analogs. Figure 6.21 shows the results from the lowest speed case (40 m/s inlet velocity), which had an adiabatic flame temperature of 2120 K. The top three thermocouple locations show that the aluminized version provide similar or lower temperatures that the ethylene analog. However, the thermocouple located at the bottom of the combustor shows a dramatic increase in temperature ~350K. A similar result occurs for the intermediate (55 m/s inlet velocity) cases as seen in figure 6.22. For these cases the aluminized version has a temperature from 200 K to 400 K higher than the ethylene analog at the lowest thermocouple location. This result also occurs for the highest speed (70 m/s) case, TC10a as seen in figure 6.23.

This behavior can have several explanations, or a combination of explanations. First, the Mie scattering data provided in section 6.1.1 showed that although particle dispersion was fairly uniform, it did favor the bottom of the combustor. Further, the shape of the temperature profiles, namely the two innermost thermocouples, also indicates that the mixture is not entirely uniform. Otherwise, one would expect the two inner thermocouples to have approximately the same temperature measurements. If more aluminum were located in the bottom portion of the combustor than the top, then the equivalence ratio would be even more non-uniform than in the ethylene only analogs. In addition, the equivalence ratio would be higher in a relative sense than it would for the ethylene only analogs. This behavior is also seen in the boron-loaded tests, but not nearly as drastic. This is due to the fact that the nanoaluminum ignition temperature requirements are not nearly as high as the nano boron, therefore the boron along the “cool

wall area" does not necessarily achieve vigorous burning to the degree that the nanoaluminum would.

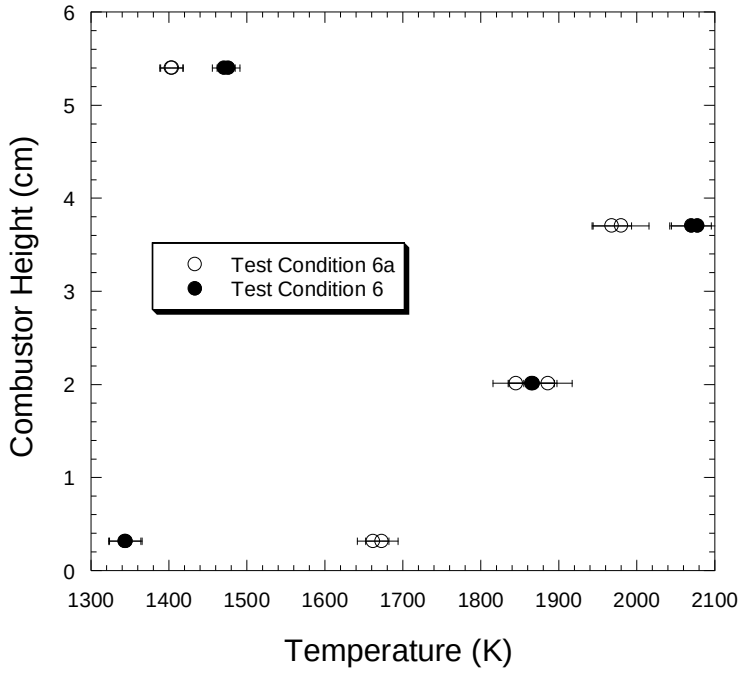

Fig. 6.21 Temperature Profiles for Test Conditions 6, 6a (Inlet Velocity = 40 m/s)

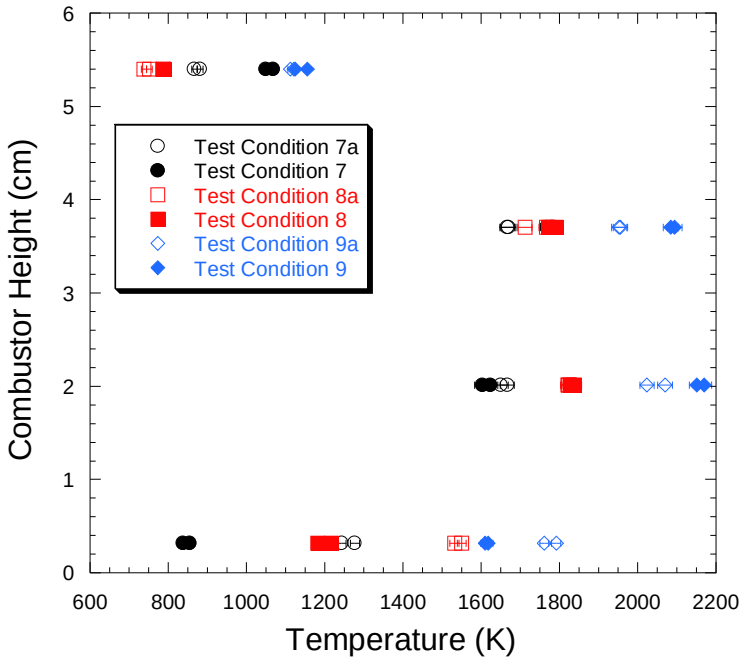

Fig. 6.22 Temperature Profiles for Test Conditions 7, 7a, 8, 8a, 9, 9a (Inlet Velocity = 55 m/s)

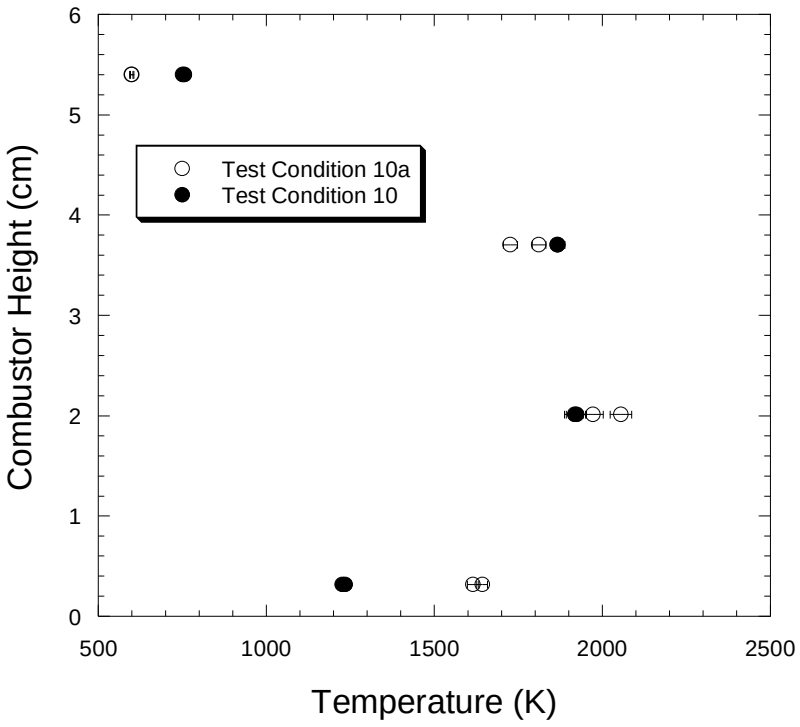

Fig. 6.23 Temperature Profile for Test Conditions 10, 10a (Inlet Velocity = 70 m/s)

When comparing the aluminized tests, it can be seen that the basic shape of the temperature profile was similar for tests 6a and 7a, but changes and was then the same for 8a – 10a. In test condition 6a and 7a the highest measured temperature comes from the second thermocouple from the top of the combustor, while in the other test conditions, the highest measured temperature shifts to the thermocouple located at the second from the bottom. This was a result of the increased mass flow rate of the seeder carrier gas and total seeder flow rate. For conditions 6a and 7a the carrier gas flow rate was 1 g/s and it was increased to 1.5 g/s for the other conditions. The increased flow rate of the carrier gas pushed more fuel toward the bottom of the combustor. This resulted in a shift in the peak of the local equivalence ratio.

In order to determine the effectiveness of the metal additives in the thermal output, the metallized cases were compared directly to hydrocarbon only cases. In this comparison, the ethylene mass flow rate was held approximately constant and the only difference in the test is the addition of the metal additive. The temperature at all four locations was averaged for a given test and normalized by their ethylene only analog. The ratio of adiabatic flame temperatures of metallized to ethylene only tests were also plotted against the adiabatic flame temperature of the metallized tests to give a boundary for the maximum attainable contribution from the metal addition. This can be seen in figures 6.24 and 6.25.

As the earlier inspection of the temperature profiles showed for the boron loaded experiments, the only experiments which showed positive contribution from boron addition were the three highest temperature cases, 1b, 2b and 4b. This can be seen more clearly in figure 6.24. Conditions 1b and 4b both have adiabatic flame temperatures calculated using the NASA CEA 2000[84] code, greater than 2000 K. These tests were the only ones conducted either on the upper end or well above the critical ignition temperature (1500-1950 K) given by other researchers[47,90,91]. Test 3b and 5b show that boron addition is not beneficial under those conditions. The BO_2 emission data does prove that boron ignition started, but it was possible that the temperatures were not high enough to promote sustained combustion or possibly start stage two combustion. So while ignition was achieved in all cases, it was possible that sustained or complete combustion of boron was never achieved in all of the conditions tested. Figure 6.24 provides further evidence of a critical temperature for sustained combustion of the boron particles. All the tests with measured peak temperatures below ~1700 K (adiabatic flame

temperature less than 1750 K) showed no positive contribution for boron addition, while all tests with measured peak temperatures above ~1770 K (adiabatic flame temperature greater than 1850 K) showed positive contributions from boron combustion.

In the case of aluminum addition (figure 6.25), all of the tests conducted showed a positive contribution from aluminum to the thermal output. This was primarily a result of the large temperature improvement on the lower portion of the combustor. The results indicate that efficient combustion even at very fuel lean conditions ($\Phi \sim 0.5$) was likely to be occurring, which is important in achieving maximum specific impulse.

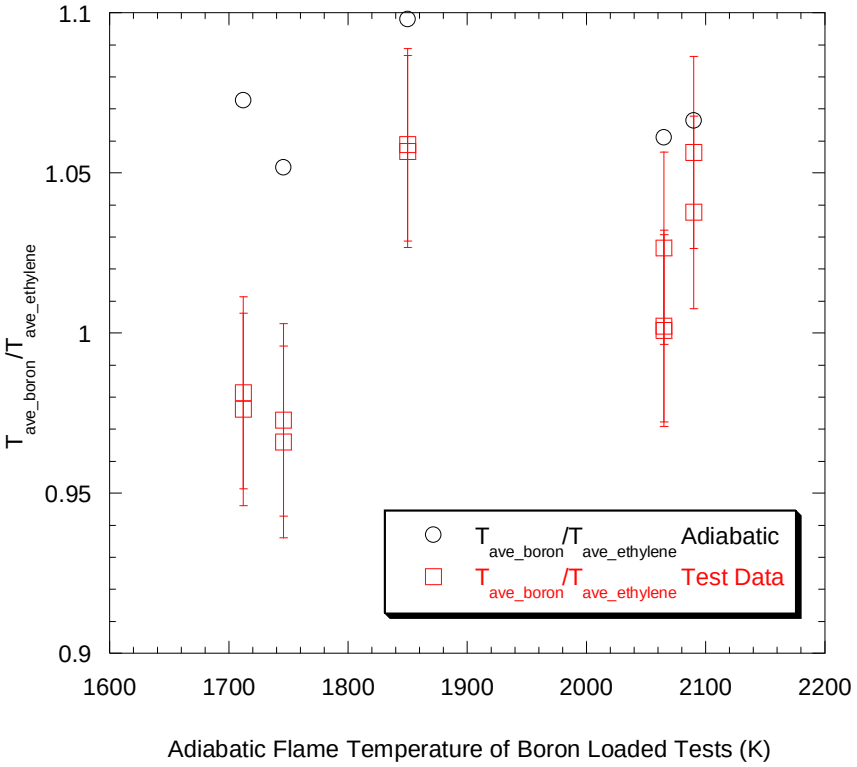

Fig. 6.24 Comparison of Ethylene and Boron Loaded Tests

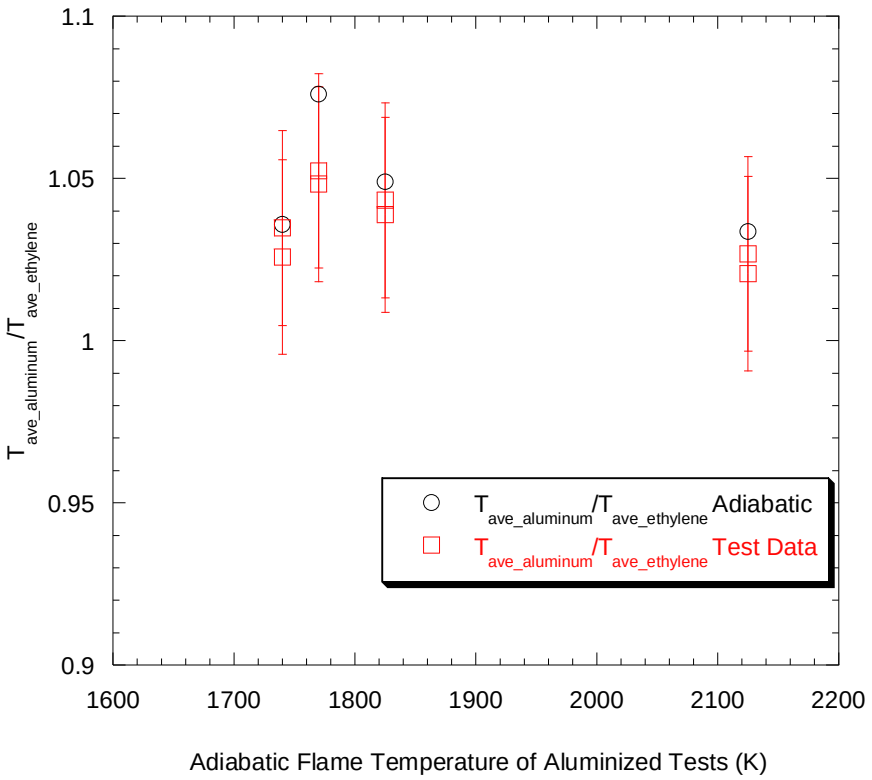

Fig. 6.25 Comparison of Ethylene and Aluminized Tests

In order to get a sense for how well the fuels were performing compared to their theoretical thermal output a thermal ratio was defined as:

$$\eta = \frac{\left[T_{ave\_metal} / T_{ave\_ethylene}\right]_{Test\_Data}}{T_{adiabatic\_metal} / T_{adiabatic\_ethylene}} \qquad \text{Eq. 6.2}$$

where the average temperatures have been normalized by the ratio of the adiabatic flame temperatures. The results are presented in figure 6.26, which shows that all of the aluminized tests come very close to theoretical performance limitations. Therefore at these conditions, temperature, time, and gas composition have no significant effect on the performance of the fuels loaded with aluminum nanoparticles.

Figure 6.26 shows that the boron performance improves as the temperature is increased, in particular there is a large jump in performance above 1800 K. However, and perhaps more telling is that the two conditions showing the highest thermal ratios, 1850 K and 2090 K, come from the two lowest speed conditions (40 m/s inlet velocity). At 2065 K (55 m/s inlet velocity) one data point is in the range of the lower speed cases, however, there are more data points that are several percent lower. On the other hand, the other data points for the 55 m/s inlet condition (1712 K) are significantly lower than the 2065 K condition.

The fact that the lower temperature, lower velocity data (1850 K and 40 m/s) was comparable or better than the higher temperature data and higher velocity data (2065 K and 55 m/s) indicates that time and oxygen mole fraction are the most important parameters in determining performance. At the same time the data points for the 55 m/s inlet condition (1712 K and 2065 K) show that even at lower oxygen concentration, the higher temperature condition had better performance, thus suggesting that time is the most dominant parameter when overall performance is considered for boron in this combustor.

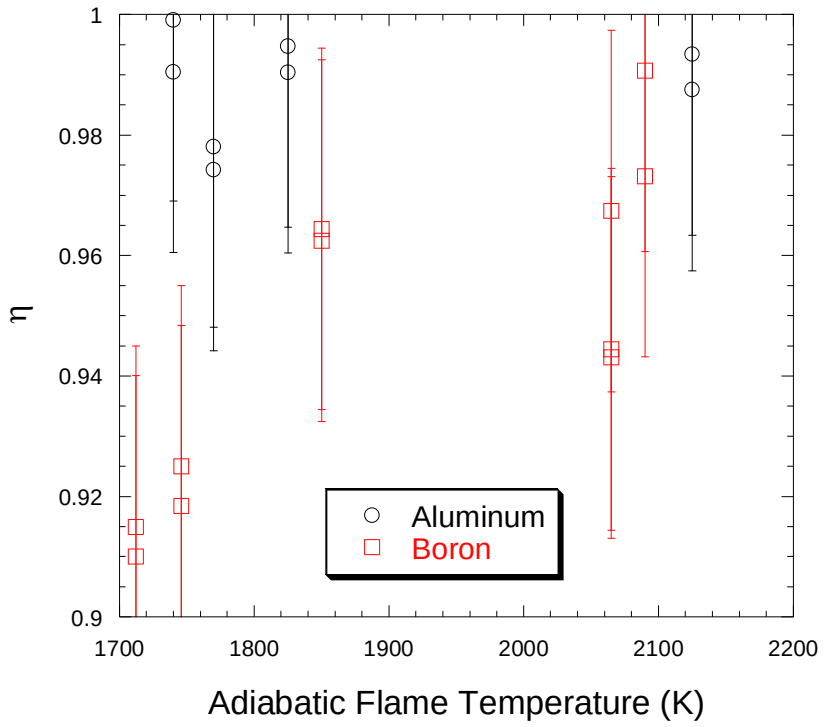

Fig. 6.26 Thermal Ratios

6.2 Data Interpretation

One possible interpretation of Figures 6.12 and 6.13 is that the boron may actually extinguish within the combustor for some of the test conditions. In figure 6.12, the lower temperature cases reach the background intensity before the end of the combustor whereas the higher temperature cases still show significant intensity levels. Similarly, in the time analog (figure 6.13) the lower temperature conditions reach background levels in a shorter duration. This is in direct contrast to what was expected, namely that at higher temperatures, the particles should combust quicker. This result would indicate that the particles are likely extinguishing, at least in the lower temperature conditions. In fact King[92] showed that temperature boundaries for boron particle extinguishment are a strong function of pressure and oxygen concentration. King[92] also showed that smaller particles

required higher temperatures to prevent extinguishments. Essentially once the particles become very small they may not be able to sustain their own temperature field as they begin to lose more heat to the surroundings than they can generate themselves. Li and Williams[87] performed an analysis to examine the extinction characteristics of boron particles in which they applied an energy balance between the rate of heat loss of the particle and the rate of heat generation by the particle. The rate of heat generation is balanced by the heat loss due to radiation and convection to the surrounding as described by Equation 6.2 (using Li and Williams'[87] notation).

$$Q_5\omega_5 = \frac{2\lambda\left(T_q - T_\infty\right)}{d_q} + \varepsilon\sigma\left(T_q^4 - T_\infty^4\right) \qquad \text{Eq. 6.2}$$

Here, Q_5, ω_5, λ, T_q, T_∞, d_q, ε, σ, are the heat released by the surface reaction given in equation 6.2, the kinetic rate constant, the thermal conductivity, the quenching temperature, the ambient temperature, the quenching diameter, the emissivity of boron, and the Boltzman constant respectively. The heat released is a result of the surface reaction described by equation 6.3.

$$2B(s) + O_2(g) \rightarrow B_2O_2 \qquad \text{Eq. 6.3}$$

With some manipulation and substitution of parameters provided in reference 87 including the selection of the melting temperature of pure boron as the particle surface quenching temperature, T_q, they arrived at an equation relating the particle-quenching diameter, d_q, to the surrounding temperature T_∞, and the oxygen partial pressure, p_{O2}.

$$d_q = \frac{2\lambda\left(T_q - T_\infty\right)}{Q_5\omega_5 - \varepsilon\sigma\left(T_q^4 - T_\infty^4\right)} \qquad \text{Eq. 6.5}$$

Where ω_5 is related to the partial pressure of oxygen by a constant:

$$\omega_5 = cp_{O_2} \qquad \text{Eq. 6.6}$$

Applying this result to the current set of test conditions (1 atm); assuming that the hydrocarbon is completely consumed before the boron, the oxygen mole fraction after complete combustion of the hydrocarbon is typically near 0.1 figure 6.27 shows that particles under the size of 11 μm on the lower temperature tests and 6 μm in the higher temperature tests would extinguish. Clearly the primary particle sizes used in this study are much smaller than the predicted quenching diameter. Even considering extreme amounts of agglomeration, this analysis would indicate that particle extinguishments is quite likely under the test conditions in this study. The other curves generated in figure 16 consider higher combustor pressures but still consider the mole fraction of oxygen to be 0.1. Although the figure shows that increasing pressure reduces the quenching diameter, the greatest reduction in quenching diameter occurs once the surrounding temperature exceeds 2000 K.

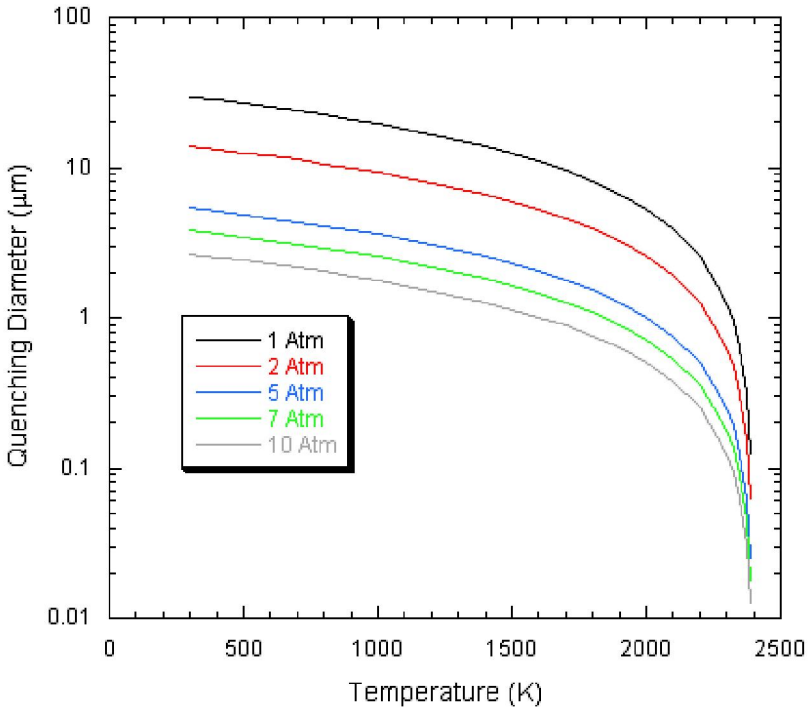

Fig. 6.27 Boron Particle Quenching

Under most practical situations, if boron were to be used as a fuel additive in an airbreathing combustor it would most likely be stored within a hydrocarbon, either gelled or as part of a solid fuel. At atmospheric pressure most hydrocarbons have maximum flame temperatures between 2200-2400 K near stoichiometric conditions. Since temperatures in this range are required by the analysis of Li and Williams[87] to sustain combustion of small boron particles, the mole fraction of oxygen available for consumption of boron would be quite low. However in a more realistic condition, the combustor pressure would be significantly higher than discussed here and the air temperature entering the combustor would be much higher. As an example Table 6.4 provides a brief summary of combustor conditions for a ramjet flying at an altitude of 8,000 m (~60,000 ft) if the airflow is decelerated isentropically to a Mach number of 0.3

as it enters the combustor. Ideally a ramjet follows a Brayton Cycle analysis, therefore the combustion process is considered isobaric. The adiabatic flame temperatures were calculated using the NASA CEA 2000 computer code[84], considering RP-1 as the hydrocarbon fuel, with combustor inlet conditions obtained from the isentropic flow calculations. Table 6.4 shows that even at higher flight Mach Number conditions, a majority of the fuel would still need to be a hydrocarbon in order to be certain that the temperature of the surroundings were high enough to sustain combustion of very small boron particles according to the analysis of Li and Williams[87]. At this point the mole fraction of oxygen remaining is quite small further complicating the problem.

Although the analysis by Li and Williams[87] suggests that particle extinction is possible, the results of Chapter 5 found no evidence of particle extinction. However, only one data point for $X_{O2} = 0.1$ was found to produce stage two combustion of the boron particles, and that data point corresponded to a burner temperature of 1791 K. For burner temperatures of 1614 K and 1712 K, stage two combustion was not achieved in the flat flame burner experiments. During the airbreathing combustor experiments the only boron loaded experiments to show a positive thermal contribution were the experiments with measured peak temperatures greater than approximately 1780 K.

Table 6.4: Flight Conditions

Flight Mach Number	Inlet Air Static Temperature (K)	Inlet Air Static Pressure (atm)	Φ for $T_f = 2200$ or T_{fmax} (K)	X_{O2} for Boron Consumption	Quenching Diameter (μm)
2	382	0.54	1.05, (2188 K)	0.0018	N/A
3	594	2.56	0.87	0.0244	4.25
4	891	10.57	0.72	0.0525	0.45

Therefore, another possible explanation of the results shown in figures 6.12 and 6.13 is that the particles never fully achieved stage two combustion under the lower temperature conditions. In fact Macek[47] found that even at very high temperatures and at low oxygen mole fraction, $X_{O2} = 0.08$, that it was impossible to distinguish between the ignition and full-fledged combustion stages for larger boron particles.

The presence of water vapor is known to inhibit boron combustion through the formation of HBO_2. In two of the test conditions, 1b and 4b, water vapor has the highest molar content of any of the main oxidizing species remaining after hydrocarbon combustion (see table 6.3). In the other cases water vapor is quite comparable to the oxygen mole fraction, which would serve to severely inhibit the performance of the boron loaded fuels should they actually achieve stage 2 combustion. The competition between the available oxygen and water vapor leads to a condition in which one would expect relatively poor performance for the boron loaded fuels when oxygen and water vapor are comparable.

The data collected for the aluminum nanoparticles shows great potential for the use of the particles as fuels or supplements. The chemiluminescence data showed that the aluminum completed combustion well within the combustor. The temperature data also showed that under all conditions, the aluminum provided additional thermal energy to the flow.

6.3 Additional Considerations

As was pointed out in Chapter 4, unless specially treated aluminum and boron nanoparticles suffer from the formation of an oxide layer that essentially removes a

substantial part of the available energy of a particle. For instance in the case of the SB99 particles, only about 72% was active boron, while for the ALEX particles only about 82% was active aluminum. The inactive content results in considerable performance loss from a theoretical standpoint. As an example, by calculating the lower heating values of a 50% metal/50% RP-1 mixture and comparing a pure metal to the real case of reduced active content one finds that the heating value of the aluminized mixture is reduced by about 8% and the boron loaded mixture is reduced about 17% on a mass basis. In this case the heating value is calculated in the following manner:

$$\Delta H_c = -\Delta H_R = H_{reac} - H_{prod} \qquad \text{Eq. 6.7}$$

where:

$$H_{reac} = \sum_{reac} N_i \bar{h}_i \quad \text{and} \quad H_{prod} = \sum_{prod} N_i \bar{h}_i \qquad \text{Eq. 6.8}$$

N refers to the number of moles of a reactant or product, h_i is the enthalpy of formation and the subscripts *reac* and *prod* refer to the reactants and products of the reaction. Applying these parameters to an ideal ramjet case under the following assumptions:

1) The compression and expansion of gases in the engine are both reversible and adiabatic
2) The combustion process is represented by a constant-pressure heat and mass addition process

the specific impulse and the density impulse were calculated by first specifying a flight Mach number. Once the Mach number was specified, the specific impulse, or I_{sp} was calculated by the following procedure:

$$U_\infty = M\sqrt{\gamma R T_\infty} \qquad \text{Eq. 6.9}$$

where M is the flight Mach number, U_∞ is the freestream velocity, γ is the ratio of specific heat of air, R is the gas constant for air, and T_∞ is the freestream static temperature. The freestream stagnation temperature $T_{o,\infty}$, was calculate from:

$$T_{o,\infty} = T_\infty\left(1+\frac{\gamma-1}{2}M^2\right) \qquad \text{Eq. 6.10}$$

With this information the gas velocity exiting the ramjet combustor, U_e, was calculated, where T_f was the adiabatic flame temperature of the combustion reactants in a constant pressure and enthalpy calculation, which was computed using the NASA CEA 2000 Chemical Equilibrium computer code.

$$U_e = U_\infty\sqrt{\frac{T_f}{T_{o,\infty}}} \qquad \text{Eq. 6.11}$$

The thrust per unit mass flow of air was calculated by:

$$\frac{F}{\dot{m}_o} = (1+f)U_e - U_\infty \qquad \text{Eq. 6.12}$$

where, f was the fuel to air ratio. In all of these calculations an equivalence ratio of one was assumed. Finally the specific impulse was calculated by equation 6.13, where g was the acceleration due to gravity.

$$I_{sp} = \frac{1}{gf}\left(\frac{F}{\dot{m}_o}\right) \qquad \text{Eq. 6.13}$$

The results of this analysis can be seen in figure 6.28-6.31. In the case of boron, the specific impulse (see figure 6.28) was typically about 12% lower for the fuels considering active content than for the theoretical values of the pure metal fuel. Similarly the density impulse (see figure 6.29) suffers about a 12% loss compared to the pure metal fuel. The

active content boron loaded fuel still however had density impulse about 20% greater than the hydrocarbon only fuel.

For the aluminized fuel, the specific impulse (figure 6.30) was about 5% lower than the pure metal fuel, while the density impulse was about 4% lower (figure 6.31) when active content was considered. Interestingly, in the aluminized version, the density impulse recovers some of the performance loss due to the relatively high density of alumina, which is about 47% higher than that of pure aluminum. While both metals still outperform the baseline hydrocarbon fuel, the analysis shows that the active content of the nanoparticles plays a large role in the final theoretical performance of the fuel and cannot be ignored. As seen by equation 6.14, the Breguet Range equation, a loss in I_{sp} results in a direct loss of vehicle range.

$$R = \frac{L}{D} \ln \frac{m_1}{m_2} I_{sp} U \qquad \text{Eq. 6.14}$$

where L, D, m_1, m_2 refer to the lift, drag, the initial mass of the vehicle, and the final mass of the vehicle.

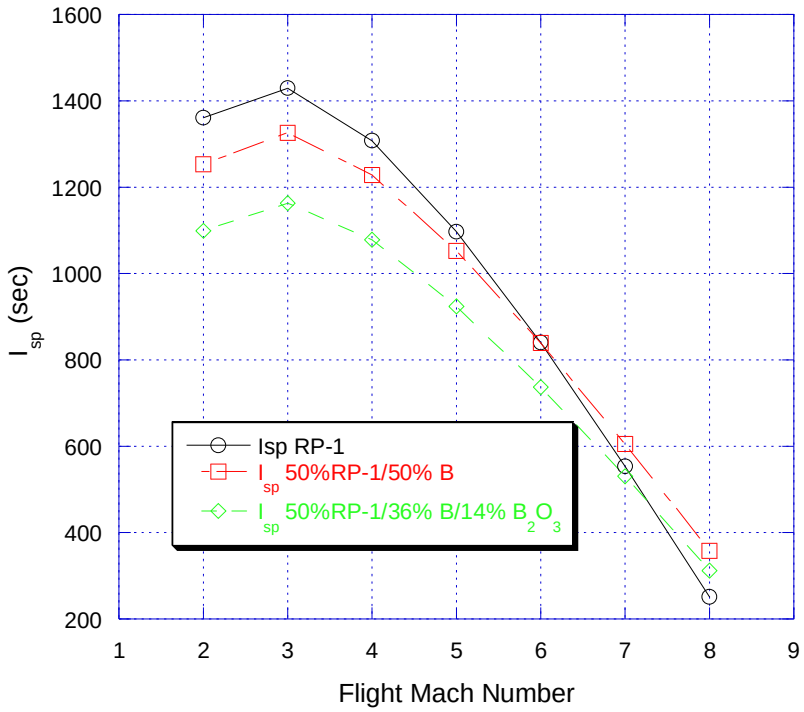

Fig. 6.28 Specific Impulse of Boron Loaded Fuels Considering Active Content

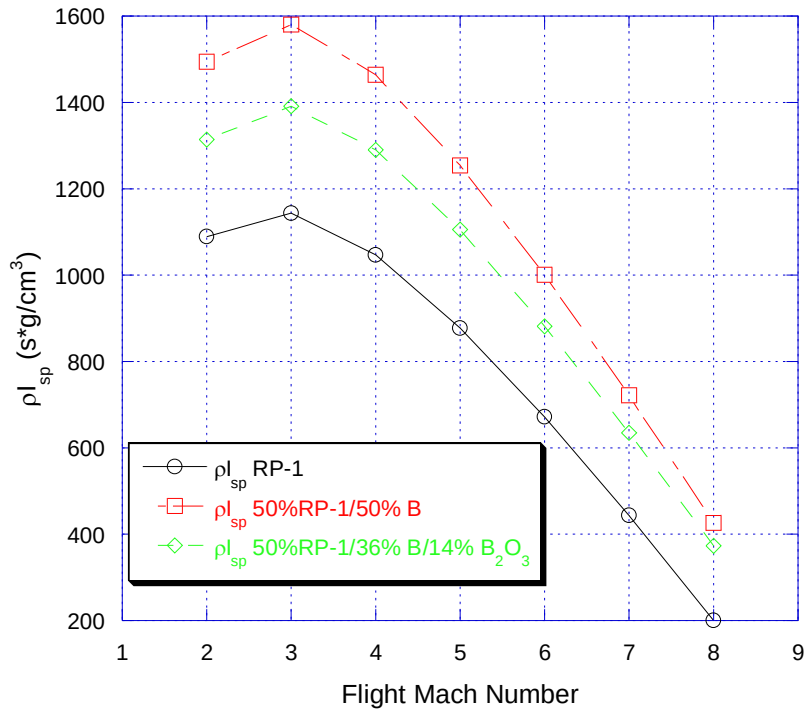

Fig. 6.29 Density Impulse of Boron Loaded Fuels Considering Active Content

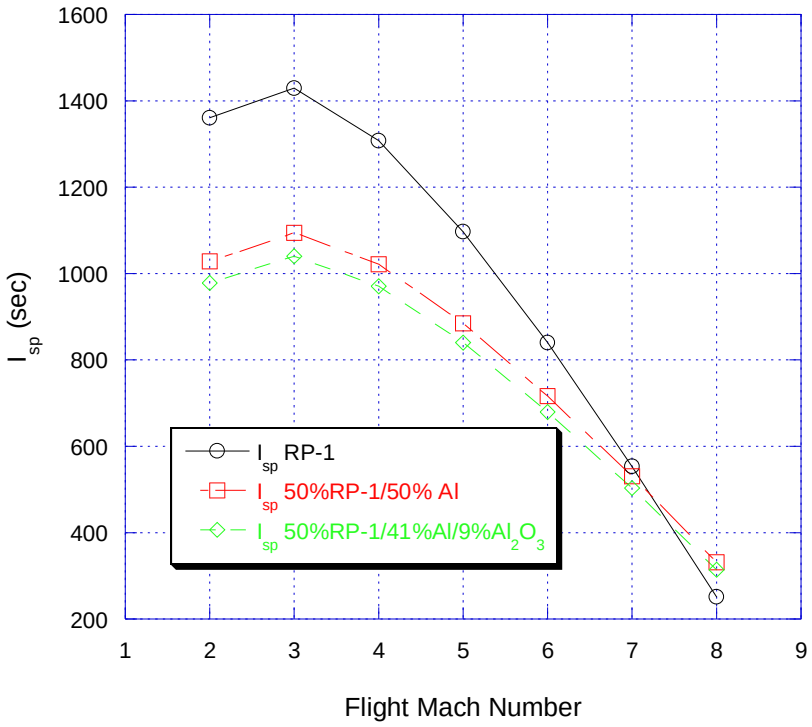

Fig. 6.30 Specific Impulse of Aluminized Fuels Considering Active Content

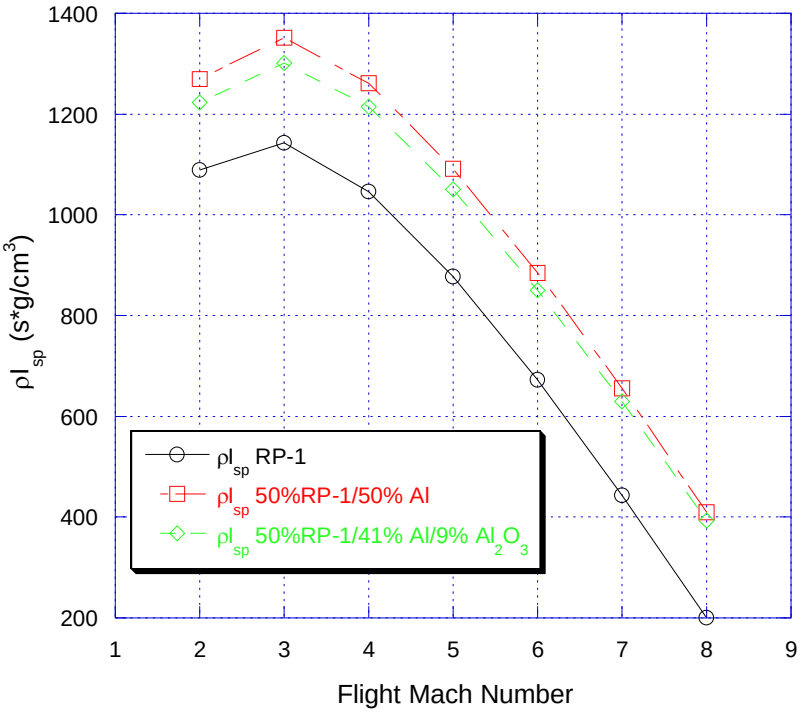

Fig. 6.31 Density Impulse of Aluminized Fuels Considering Active Content

CHAPTER 7

CONCLUSIONS AND FUTURE WORK

7. Conclusions and Future Work

Metals offer the potential of improving the performance of volume-limited airbreathing propulsion systems by increasing the energy density of the fuels utilized. Unfortunately due to small combustor residence times in high-speed applications, theoretical performance levels are difficult to achieve since burning times of metal particles are relatively long. However, with the development of metallic nanoparticles such as aluminum and boron, new hope has been raised for the performance potential of metals as fuels in high-speed airbreathing combustors.

This research effort was conducted in order to determine the viability of utilizing metallic nanoparticles as fuels or fuel supplements for high-speed airbreathing applications. The study was broken into two main parts; the first was a fundamental investigation into the combustion behavior of boron nanoparticles in a controlled setting, while the second was a demonstration of the performance potential of the nanoparticles in a realistic airbreathing combustor configuration. The following is a list of the major accomplishments achieved during this research effort.

- This study provided the first experimental data on boron nanoparticles burning times, which were obtained in the post-flame region of a flat flame burner.

- The study extended the range of control parameters from previous ignition time studies[87] involving nano-sized boron particles.
- The ignition and burning time data for the boron nanoparticles was obtained in a transverse flow configuration. Previous studies utilizing the post flame region of a premixed burner injected either micron or nano-sized particles axially.
- Examined the dependence of metallic nanoparticles' combustion behavior on surrounding temperature and oxygen concentration.
- Compared the experimental trend of boron nanoparticles combustion with respect to both kinetic and diffusion limited theoretical behavior.
- Provided nanoparticle combustion data in a controlled open flame environment, as well as in an enclosed combustor configuration that simulated the reacting flowfield in a high-speed airbreathing propulsion system.
- Demonstrated the potential of metallic nanoparticles for enhancing propulsion performance in volume-limited systems.

The subsequent sections provide a more detailed summary of the individual accomplishments achieved in each portion of the study, as well as direction for future studies.

7.1 Particle Characterization

- Two different types of nanoparticles were investigated during this study, SB99 boron nanoparticles, and 50 nm ALEX nanoaluminum. Scanning Electron Microscope (SEM) images revealed that the SB99 particles had primary particles

sizes of about 50 nm, but were highly agglomerated. SEM images of the ALEX particles showed a wide size distribution of spherical particles ranging from about 50 nm up to about 200 nm. The ALEX particles were also highly agglomerated.

- A Thermal Gravimetric Analysis (TGA) was performed on the particles to determine the active content of the particles. The SB99 particles had an active content of 72% by mass, while the ALEX particles had an active content of 82% by mass. In each case, the remaining content was assumed to be the particle oxides B_2O_3 and Al_2O_3 respectively.

7.2 Flat Flame Burning Experiment

- A new experiment was developed as a means of determining the ignition and burning times of boron nanoparticles. A standard McKenna flat flame burner was used for the study with a premixed mixture of CH_4/Air/O_2. This experiment differs from previous particle burning experiments[16,35,36,3744,46,47] in the post flame region of a flat flame burner, in that the particles were injected across the cross section of the flame rather than in the direction of the gas flow. This technique is advantages because the gas properties in the transverse direction are more uniform than in the axial direction. The results is that the particles are subjected to relatively constant gas properties.
- Since observation of a single nanoparticle is impossible at the moment, this technique allowed for the measurement of the ensemble average of the ignition and burning times of the particles.

- Temperature measurements were made for a variety of burner conditions and a range of product species compositions including oxygen mole fraction ranging from 0.1-0.3. Average measured temperatures ranged from 1578 ± 31 – 1872 ± 47 K. The burner temperature was relatively insensitive to equivalence ratio, but was influenced more by total flow rate due to heat losses to the burner hardware.
- Particle Image Velocimetry (PIV) experiments revealed that the centerline particle velocity follows laminar flow theory for a round jet very closely. For the PIV experiments, 5 μm water droplets from a sonicating atomizer were used as the seed particles. Three different injection flow rates were studied with twelve different crossflows and correlations for the centerline velocity were developed for all flow rates.
- The boron nanoparticles were injected into the post flame region of the flat flame burner via a sonicating atomizer. "As injected" particles were collected for Transimission Electron Microscopy (TEM) imaging and revealed that the particles were entering the post flame region as large non-spherical agglomerates of smaller primary particles.
- The "as injected" particles were passed through a Differential Mobility Analyzer (DMA), which revealed that the particles had a size distribution ranging from 50 nm to 400 nm in mobility diameter, with a mean mobility diameter of 200 nm.

7.2.1 Ignition and Burning Time Conclusions

- Under appropriate temperature and oxygen mole fraction, X_{O2}, conditions a two-staged combustion phenomenon was observed for the SB99 particles. Just after

injection there was no visible signature of combustion. After some delay, which was dependent on the test condition, a yellow/orange glow became visible and was attributed to the first stage, t_1, of boron combustion. The first stage of boron combustion was called the ignition stage, because according to reference 44 this stage is related the complete removal of the oxide (B_2O_3) layer. Following the first stage, a bright white glow zone was observed and attributed to the second stage, t_2, of boron combustion. The second stage combustion was considered full-fledged combustion of the "clean" pure boron particle.

7.2.1.1 Stage 1 Combustion of SB99

- The ignition stage time of nano boron combustion, t_1, was determined for a wide range of parameters, such as oxygen mole fraction X_{O2} ranging from 0.1-0.3, and temperatures ranging from 1580 K to 1810 K.
- Stage 1 combustion was found to be a strong function of temperature, but relatively insensitive to oxygen mole fraction in the ranges studied.
- Stage 1 burning times ranged from 1.5 milliseconds at the highest temperatures, to about 6 milliseconds at the lowest temperatures.
- When compared to available data from other researchers[46] employing micron-sized particles, the ignition stage of the boron nanoparticles was not substantially different from particles of approximately 2-3 μm in size.

7.2.1.2 Stage 2 Combustion of SB99

- Stage 2 combustion of boron nanoparticles was studied for $0.1 \leq X_{O2} \leq 0.3$, and temperatures ranging from 1580 K to 1870 K.
- At the lowest temperatures, the oxygen mole fraction played a large role in the t_2 burning time and affected the ability of the particles to achieve stage 2 combustion.
- For $X_{O2} \geq 0.2$ stage 2 combustion was achieved for temperatures as low as 1578 ± 31 K.
- At the lowest temperature condition, and $X_{O2} = 0.15$, stage two combustion was achieved but was not completed while the particles remained in the post flame region of the burner.
- For $X_{O2} = 0.1$, and the two lowest temperatures conditions, second stage combustion was not achieved while the particles were in the post flame region.
- t_2 burning times ranged from about 3 milliseconds to about 1.5 milliseconds over the test conditions.
    - As a comparison, Parr[16] measured burning times of 24 nm aluminum in water vapor that were between 2 and 3 times faster than the measured burning times of boron nanoparticles in this study.
        - A direct comparison is impossible because of the different oxidizing species.
        - Comparison of the available data for larger particles showed that aluminum burned about 4 times faster than boron under similar conditions.

- Comparison with other researchers data revealed that the t_2 burning times did not follow a diffusion limited D^2-*law* or a kinetic limited D^1-*law*. Instead the t_2 burning time was found to be far less dependent on particle size than observations for larger particles. In fact the dependence on sized was $t_2 \sim D^{0.2}$.
- An Arrhenius Burning Rate law was obtained which showed that the measured activation energy of the particles was consistent with other data[46] employing micron-sized particles. From the Arrhenius parameters, a burning time correlation based on a kinetically limited process was developed which resulted in showing a size dependence of $t_2 \sim D^{0.15}$. A similar result was found by other researchers[88] when correlating nanoaluminum burning time data.

7.3 Airbreathing Combustor Conclusions

An optically accessible airbreathing combustor was designed and fabricated to investigate the possibility of utilizing nanoparticles as fuel additives in a high-speed airbreathing propulsion system. The combustor is fully capable of utilizing a wide variety of diagnostics. In addition to the combustor a reverse cyclone particle seeder was also designed, fabricated, and characterized in order to provide a simple, reliable, and reusable means of delivering particles into the combustor.

Gaseous ethylene was selected as the baseline fuel for comparison with metallized fuels. The combustor was characterized to understand its behavior prior to utilization. The blowoff limits were obtained for combustor inlet velocities ranging from 25 m/s to 70 m/s. In addition, the pilot flame trajectory was analyzed as a function of inlet velocity, and a correlation was developed to describe its behavior.

Once combustor characterization was completed, testing commenced in which the performance of a hydrocarbon (ethylene) fuel with the addition of a metal nanoparticle, either aluminum or boron, was compared directly to an ethylene only analog. Testing proceeded under three different combustor inlet velocities, 40, 55, and 70 m/s and equivalence ratios of approximately 0.5 – 0.7. The active content of the metals made up from about 7% by weight to 15% by weight of the total fuel.

Planar Mie scattering was employed to study the particle dispersion patterns within the combustor. In general, the dispersion was fairly uniform with a slight bias towards the bottom of the combustor.

7.3.1 Boron Combustor Conclusions

- BO_2 emission was monitored with the use of an ICCD camera and a 546 nm bandpass filter and provided a measure of ignition delay for the particles. The emission data indicated that ignition of the particles was clearly achieved, with delays ranging from 0.9 to 1.1 milliseconds. Ignition delay was independent of combustor test condition, indicating that combustor flame temperature and chemical species played no role under the conditions tested. The BO_2 emission data also implied that a critical temperature existed for sustained combustion of boron. This was further verified by temperature measurements.
    - The BO_2 emission data showed that the product of the average intensity and the inlet velocity correlates well with flame temperature suggesting that residence time was as important of a parameter as temperature alone.

- Combustor temperature measurements indicated that the addition of boron only added to the combustor heat release in the highest temperature cases. In fact, in some cases measured temperatures were lower than the hydrocarbon analog tests. The experiments which achieved positive heat addition from the boron particles were the only tests where the flame temperatures were either on the upper end or well above the critical ignition temperatures (1500 – 1950 K) that were defined by other researchers[47,89,90]. The other tests were all well within the range of the defined ignition temperatures but the ethylene analog tests showed that the majority of the combustor temperature profile was either below the ignition temperatures or on the lower end.
- Although the BO_2 emission data clearly shows ignition of the boron particles, it is clear that the boron was not completely reacted. A critical peak combustor temperature for sustained boron combustion was identified. For all tests with measured peak temperatures below 1700 K (adiabatic flame temperature less than 1750 K) no positive contribution was achieved, while tests with peak temperatures above 1770 K (adiabatic flame temperature greater than 1850 K) all exhibited beneficial contributions from the addition of boron. In terms of the definition of a thermal ratio, only tests with flame temperatures above 1800 K achieved ratios above 96%, with some as high as 99%. Tests with flame temperatures below 1800 K had ratios near 0.91.
    - The highest thermal ratios for the boron testing were obtained for the two lowest inlet velocity conditions (40 m/s), with the higher temperature condition having the best thermal ratio.

- For similar test conditions, i.e. temperature and oxygen concentration, the flat flame burning experiments indicated that second stage combustion may not be achieved in the residence time for the two highest inlet velocity conditions of the combustor.
- At low oxygen mole fractions that would be prevalent in a hydrocarbon assisted airbreathing combustion, a critical temperature of about 1800 K exists for reasonably efficient boron combustion.
    - The airbreathing combustor experiments with X_{O2} ~ 0.1 showed no improvement in thermal output for temperatures with peak temperatures below about 1800 K
    - Similarly, the flat flame burner experiments showed that for X_{O2} = 0.1 second stage combustion was not even achieved until average burner temperatures reached almost 1800 K.

7.3.2 ALEX Combustor Conclusions

- Testing with "50 nm" ALEX nanoaluminum particles showed great promise for air-breathing applications.
- AlO emission detected with an ICCD camera and a bandpass filter centered at 488 nm indicated that the majority of the aluminum oxidation took place within the combustor under all conditions. The aluminum was consumed within the first 3 milliseconds of residence time in the combustor.
    - The average AlO intensity increased with increasing temperature alone, which would be expected for an event that is not dependent on time.

        - Indicates aluminum is being fully consumed.
- Ignition delays were about one third that of boron, typically being 0.3 milliseconds.
- Temperature measurements indicated that positive thermal output was achieved under all conditions with thermal ratios in the 99% range even at low equivalence ratios (~0.5). This is especially promising, since efficient operation at fuel lean conditions would improve specific impulse.

7.4 Overall Study Conclusions

- This study, as well as others[16,88] showed that nanoparticles burning times are indeed lower than micron-sized particles of similar materials as would be expected. However, the size dependence is not nearly as great as would be predicted by traditional diffusion or kinetic limited theories. The results of these studies show that $t_b \sim D^{0.2\text{-}0.3}$. This result combined with the effects of active content certainly call into question the benefit of using nanoparticles as fuel additives in high-speed airbreathing propulsion.
    - However, any burning time improvement is certainly beneficial for time-limited systems.
    - Active content may potentially be addressed through improved processing and coating of the materials in order to keep them from forming an oxide layer.
- The results of this study did not show any effect of increased reactivity of nano-sized boron compared to micron-sized boron. For example, ignition temperatures

were well within range of that demonstrated for larger particles. In addition, the measured activation energy was quite comparable to that of larger particles.

- Only a small window exists for efficient combustion of boron nanoparticles in high-speed airbreathing applications since both temperature and oxygen mole fraction are important parameters in the combustion behavior of boron nanoparticles.
- Thermochemical calculations showed that fuel performance improved with increasing boron content. However, boron requires significant thermal assistance in reaching its full-fledged combustion stage. Therefore, in a practical system utilizing a hydrocarbon as a matrix for loading boron, the hydrocarbon being utilized must supply enough heat to trigger full-fledged combustion of boron. This fact limits the amount of boron that can realistically be used as a fuel additive.
    - This limit however, is dependent on a number of variables including flight conditions.
    - This limit can also be improved through fuel formulation. For instance, coating the boron particles with an ignition accelerant such as magnesium can help supply much of the ignition requirements.
- The results of this study indicate that aluminum nanoparticles show great promise for use in high-speed airbreathing applications.

7.5 Benefits of this Study to the Scientific Community

- This study provided the first available data on burning times of boron nanoparticles. It also extended the range of control parameters for the ignition time data available for boron nanoparticles.
- This study was the first to examine the possibility of utilizing both aluminum and boron nanoparticles in a traditional ramjet and began to provide boundaries for efficient combustion of boron nanoparticles as fuel supplements in airbreathing propulsion systems.
- This study showed that aluminum nanoparticles have great promise for use in high-speed airbreathing engines and merits consideration for future studies and implementation in volume limited systems.

7.6 Recommendations for Future Work

- Study the effect of particle size on burning times of both boron and aluminum nanoparticles. As this study and another study[89] found, the size dependence on burning time cannot be explained by current diffusion limited (D^2-*law*) or kinetic limited (D^1-*law*) theories.
- Study the effect of pressure on the burning properties of boron nanoparticles. All testing under this study was conducted at atmospheric pressure. In a realistic propulsion system, combustion of the particles would take place under significant combustor pressure. Both diffusion limited and kinetic limited theories suggest that an increase in pressure could lead to significant reductions in burning times.

- Study the potential of boron nanoparticles in a ducted rocket environment. This study showed that the combustion behavior of boron nanoparticles is very sensitive to both temperature and oxygen mole fraction concentration. In a traditional ramjet, the available mole fraction of oxygen is limited by the amount of oxygen in the atmosphere as well as the amount of oxygen that remains after the hydrocarbon carrier completes combustion. In a ducted rocket environment, additional oxidizer is provided in the fuel. While some performance is lost, a greater chance for energy extraction exists.
- A study should be conducted in which mixtures of nano-sized aluminum and nano-sized boron are used as composite particles to create fuel additives. Since nanoaluminum has demonstrated lower ignition temperatures than traditional micron-sized aluminum, it can potentially be used as an additional ignition source for the boron particles.
- Conduct ramjet studies with nanoaluminum included in either a solid matrix such as hydroxyl-terminated polybutadiene (HTPB) or in a liquid such as RP-1 to create a gel or slurry. The initial screening this study provided suggests great promise for the use of aluminum nanoparticles in high-speed airbreathing applications. However, in a practical system, the nanoaluminum must be stored in a solid matrix, a gel, or slurry.

APPENDIX A – DESIGN DRAWINGS

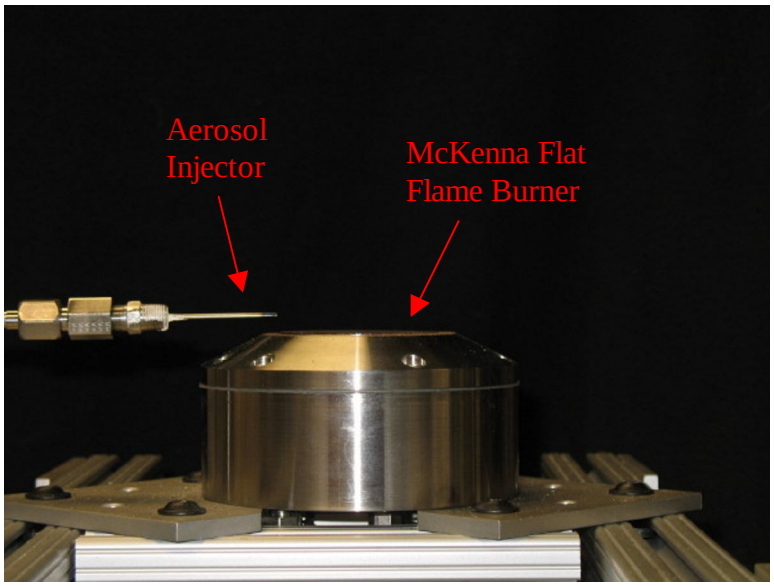

Fig. A.1 Photograph of Flat Flame Burner Experiment

Fig. A.2 Components of Sonicating Atomizer

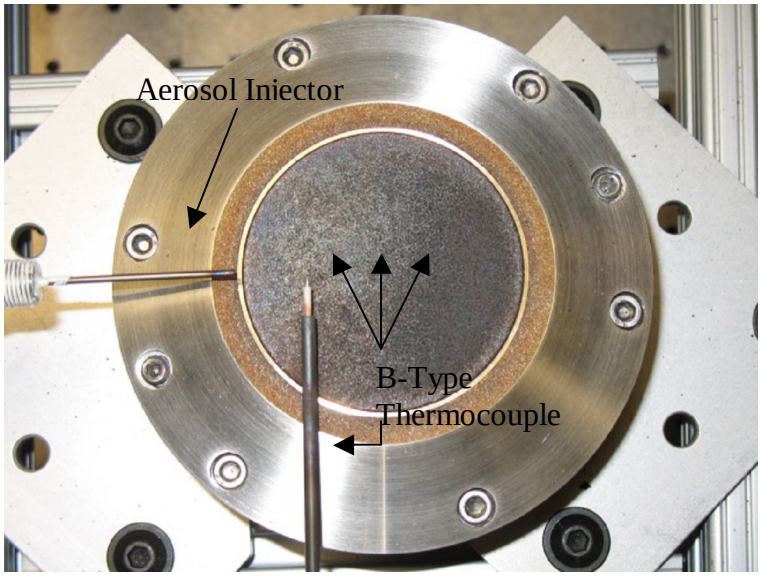

Fig. A.3 Photograph of Thermocouple Configuration

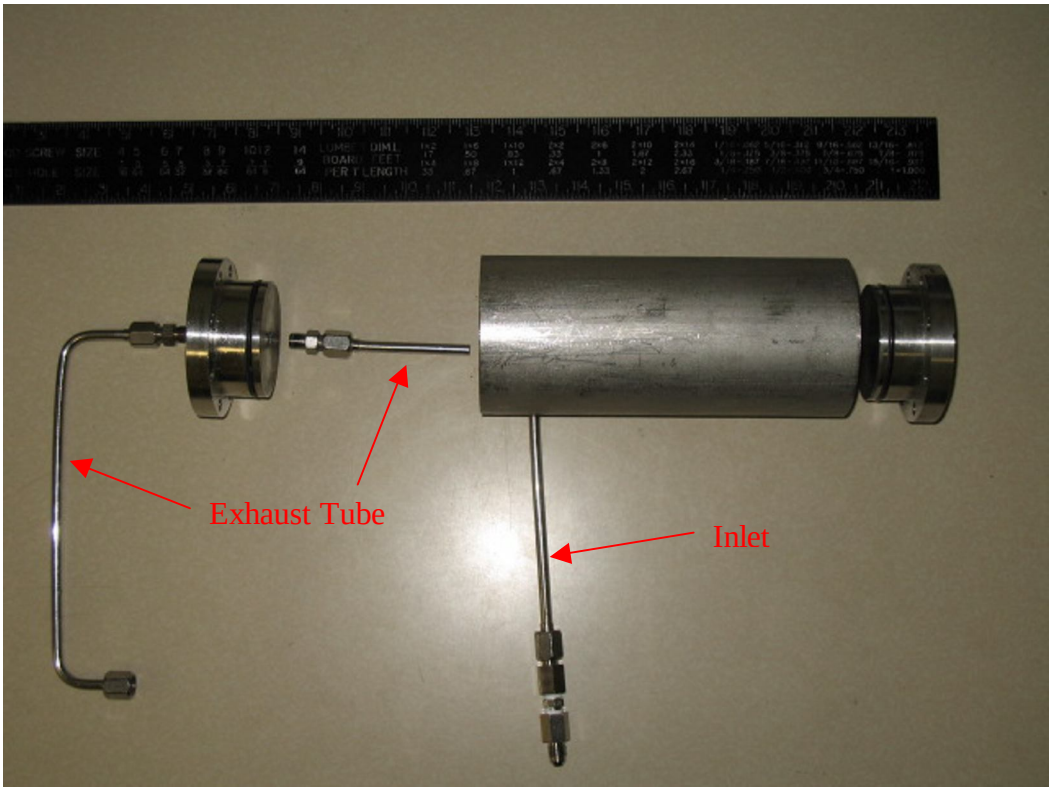

Fig. A.4 Photograph of Seeder Components

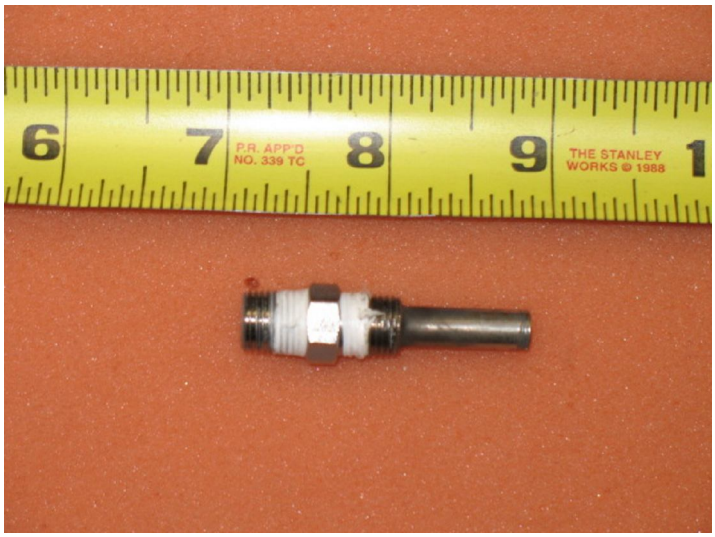

Fig. A.5 Modified Orifice Used For Particle Injection

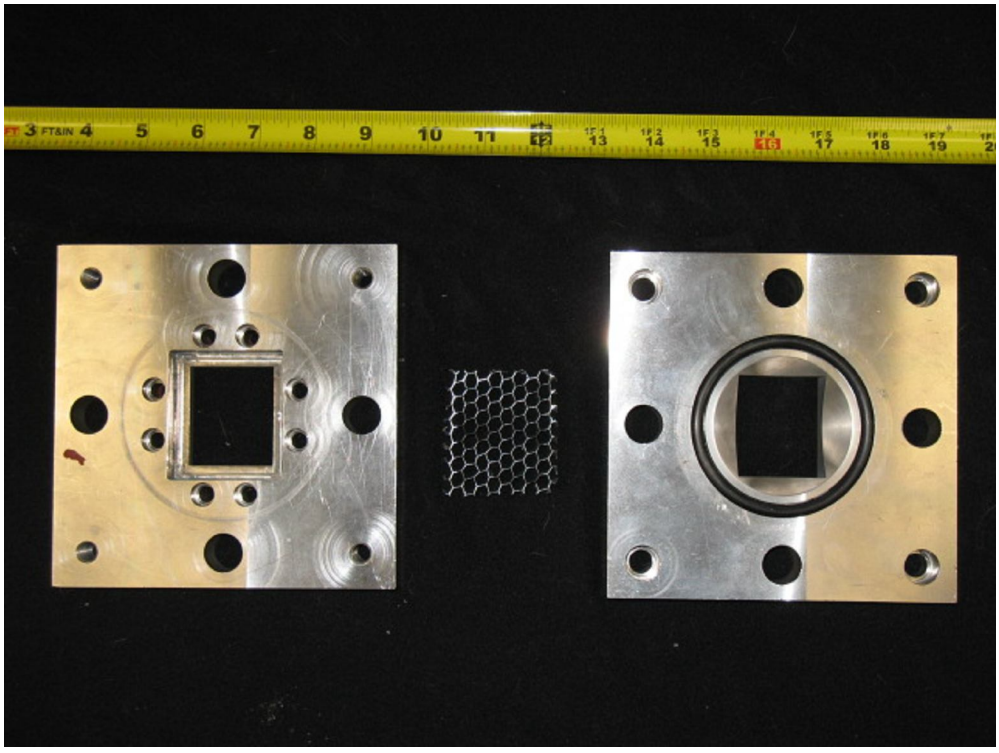

Fig. A.6 Specially Designed Adapter and Flow Straightener

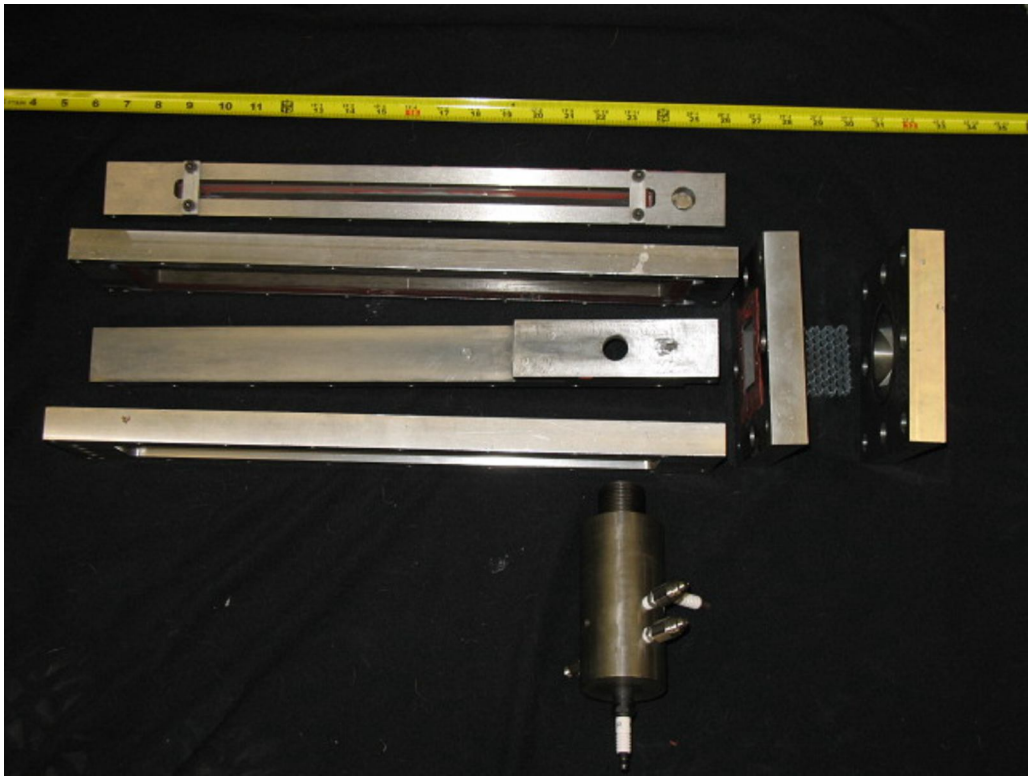

Fig. A.7 Combustor Components

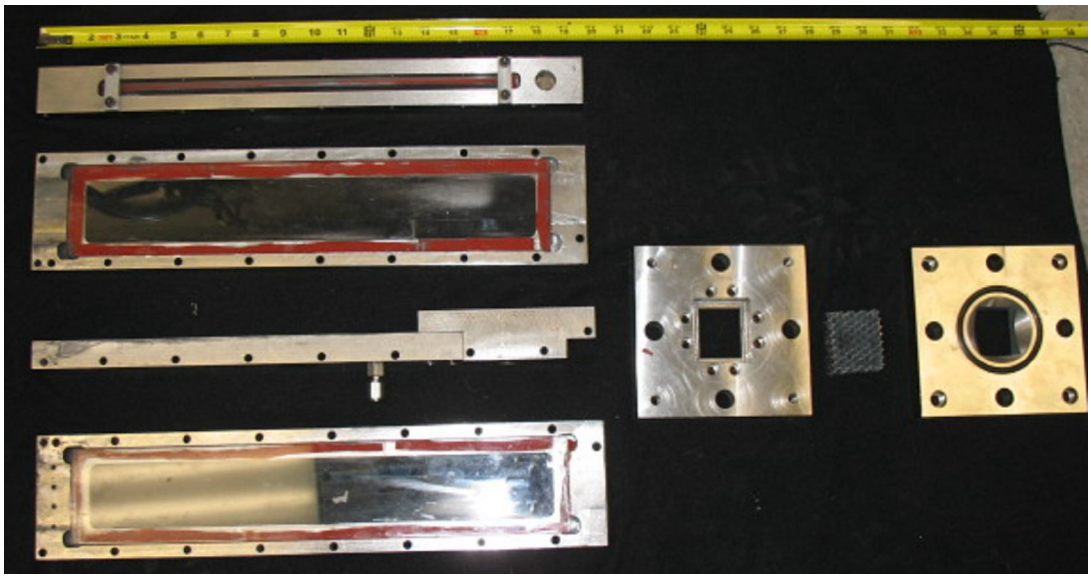

Fig. A.8 Exploded View of Combustor Components

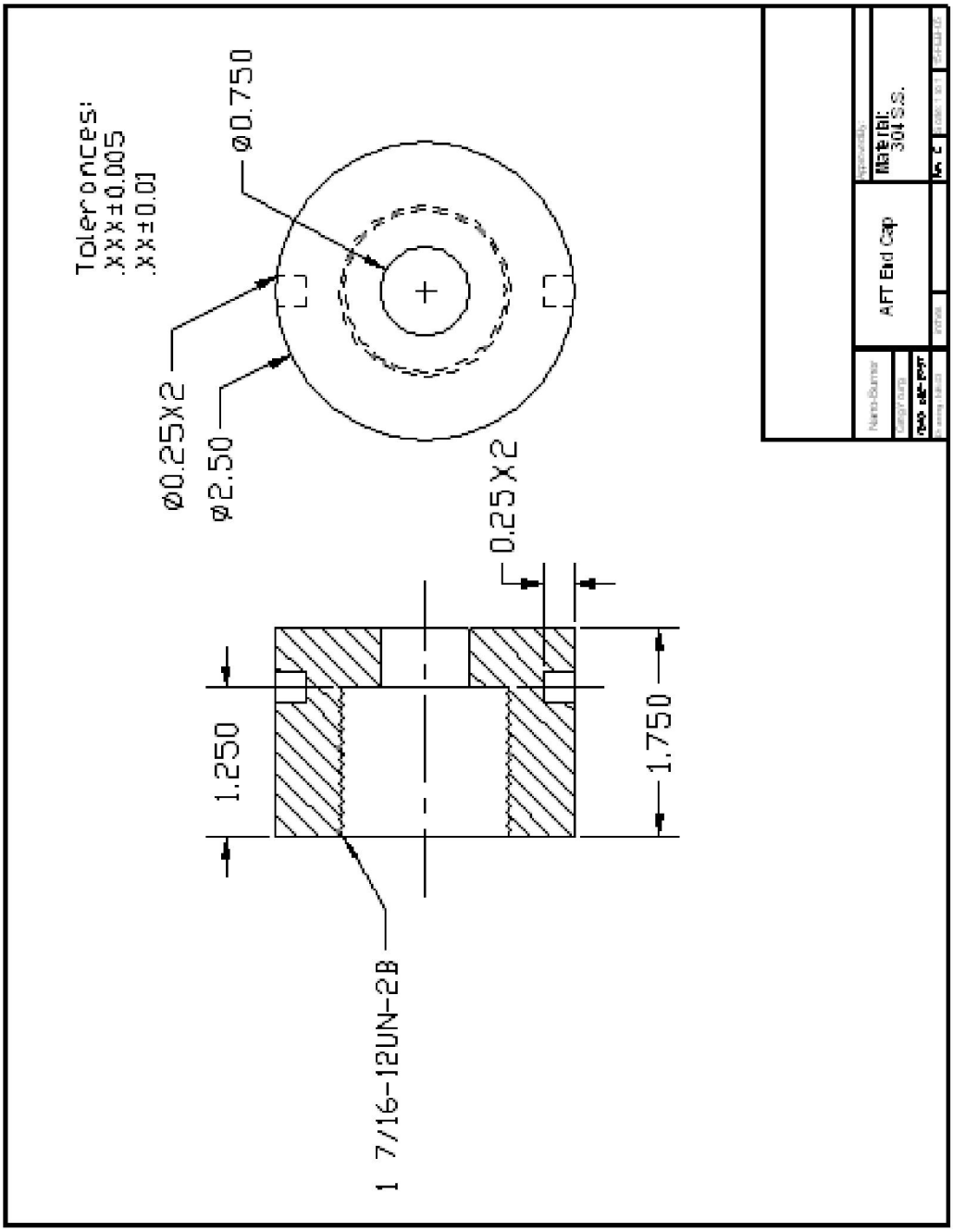

Fig. A.9 Pilot Flame Combustor Aft End Cap

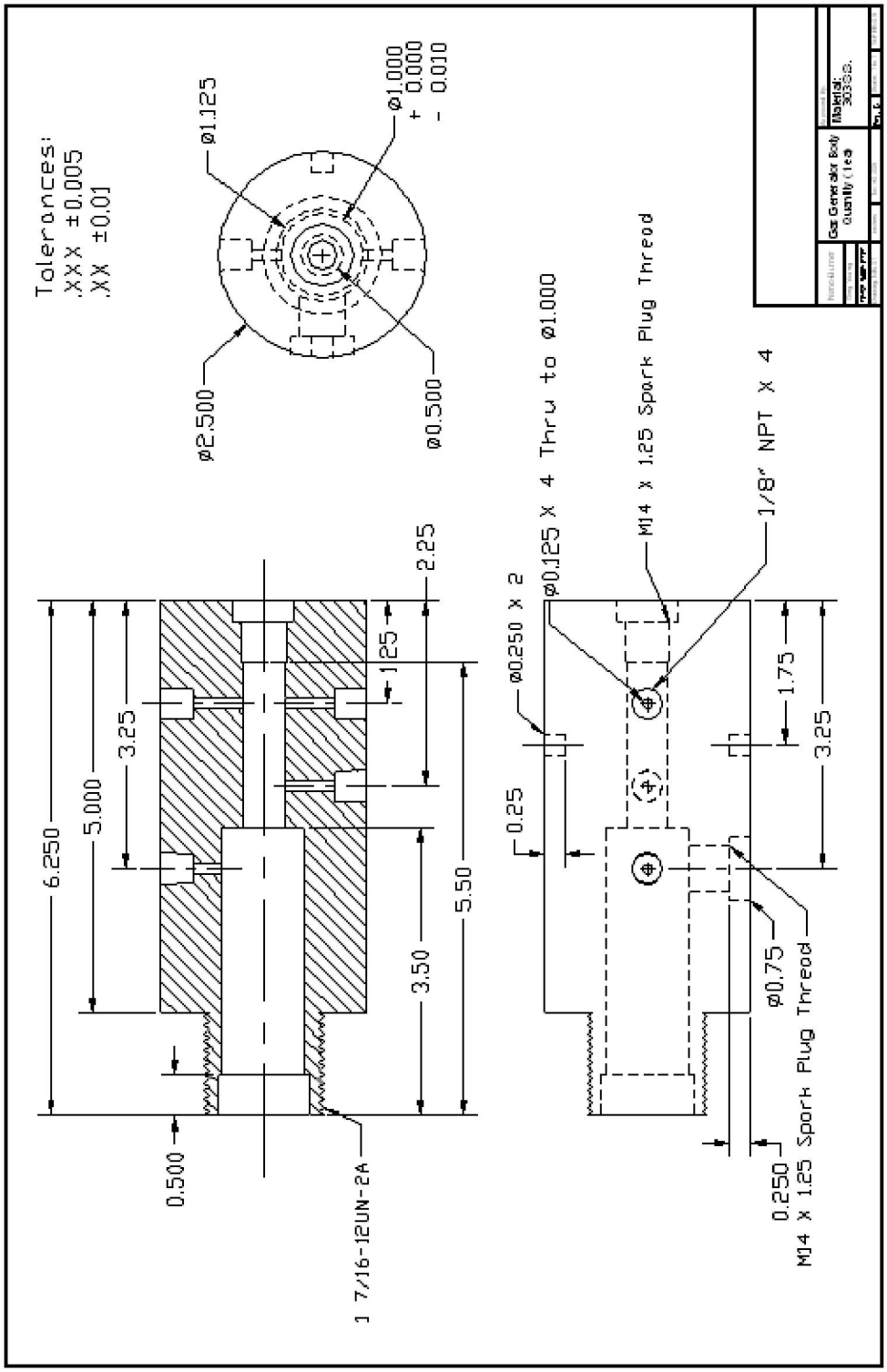

Fig. A.10 Pilot Flame Combustor Main Body

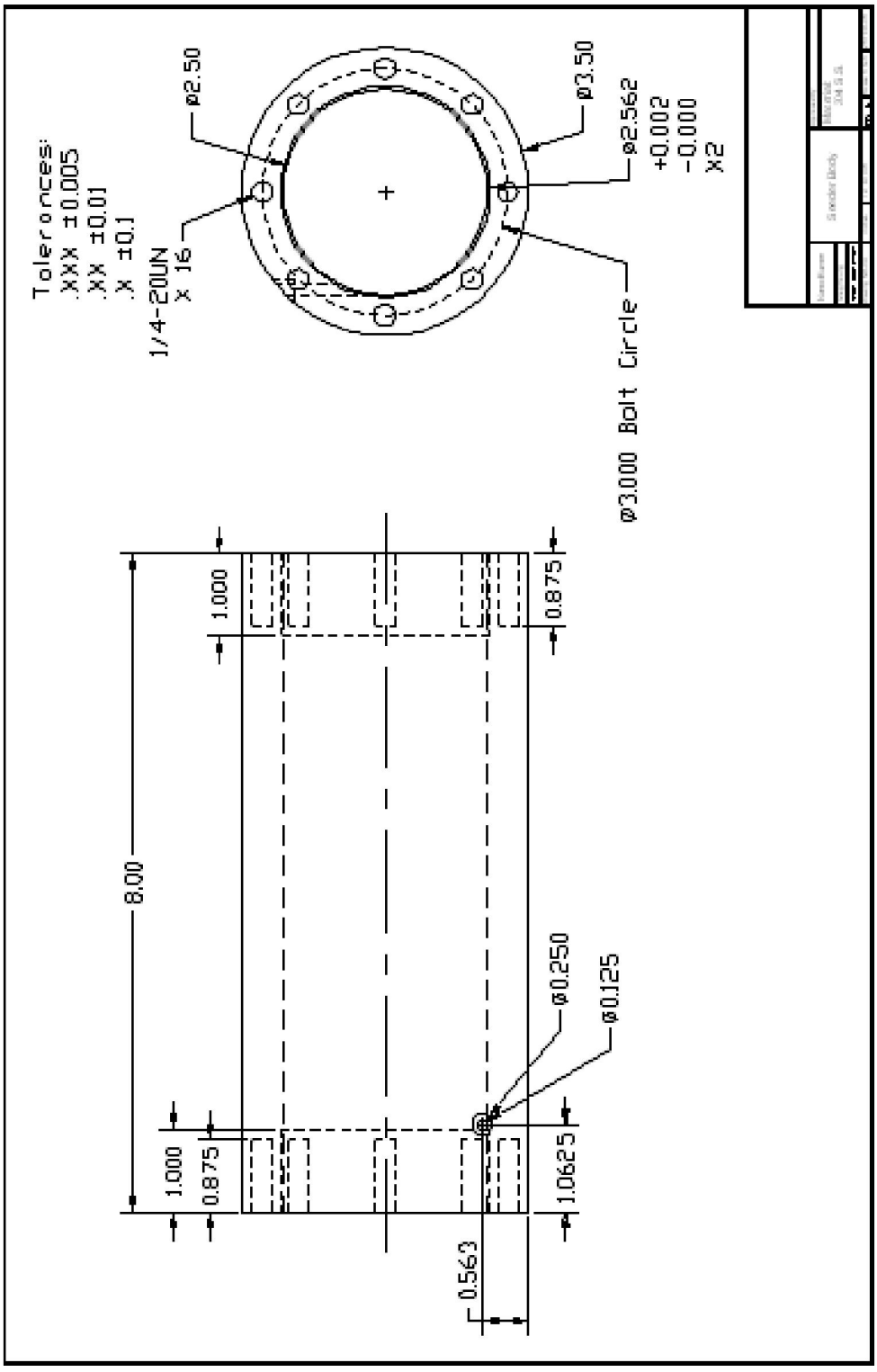

Fig. A.11 Seeder Body

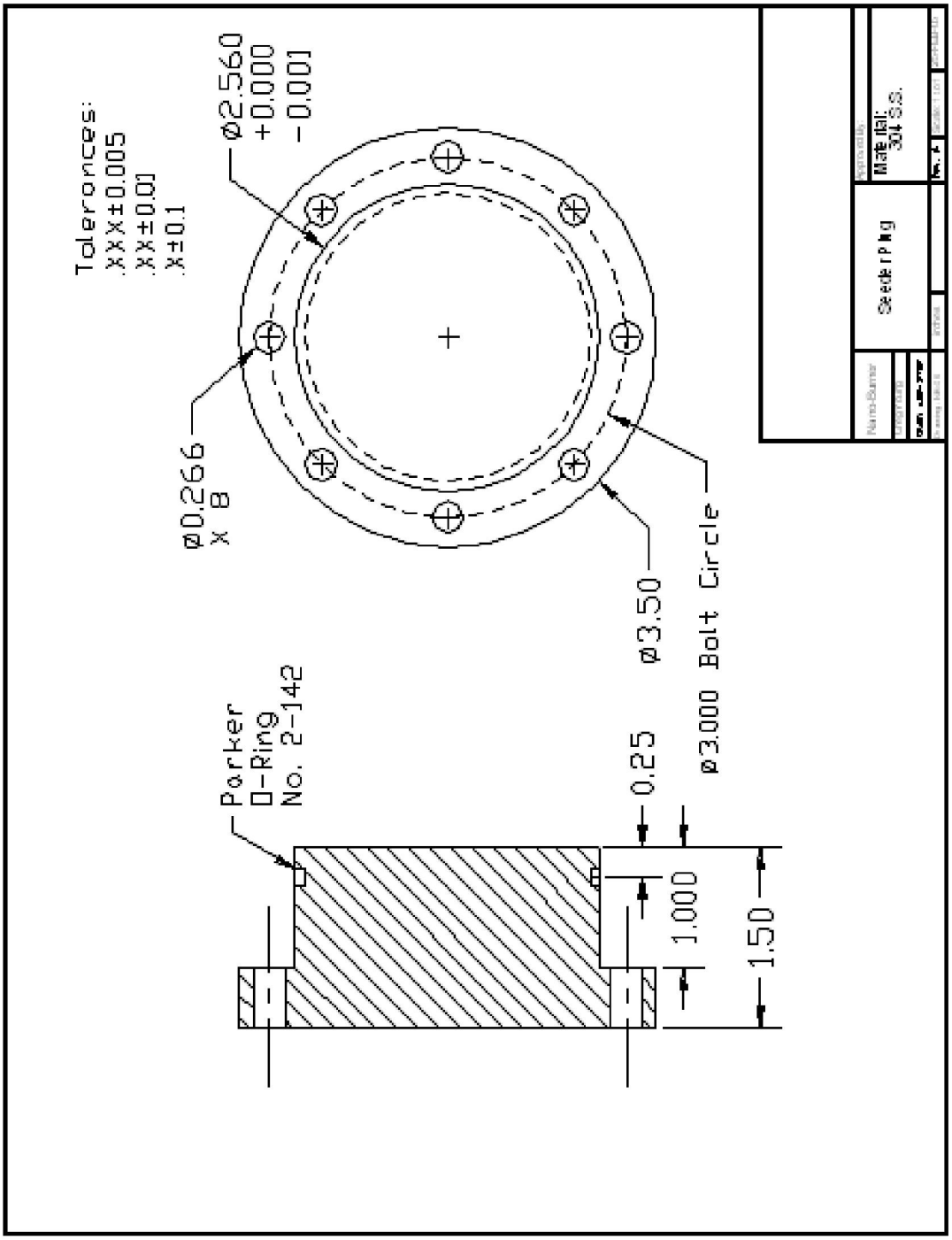

Fig. A.12 Seeder Plug

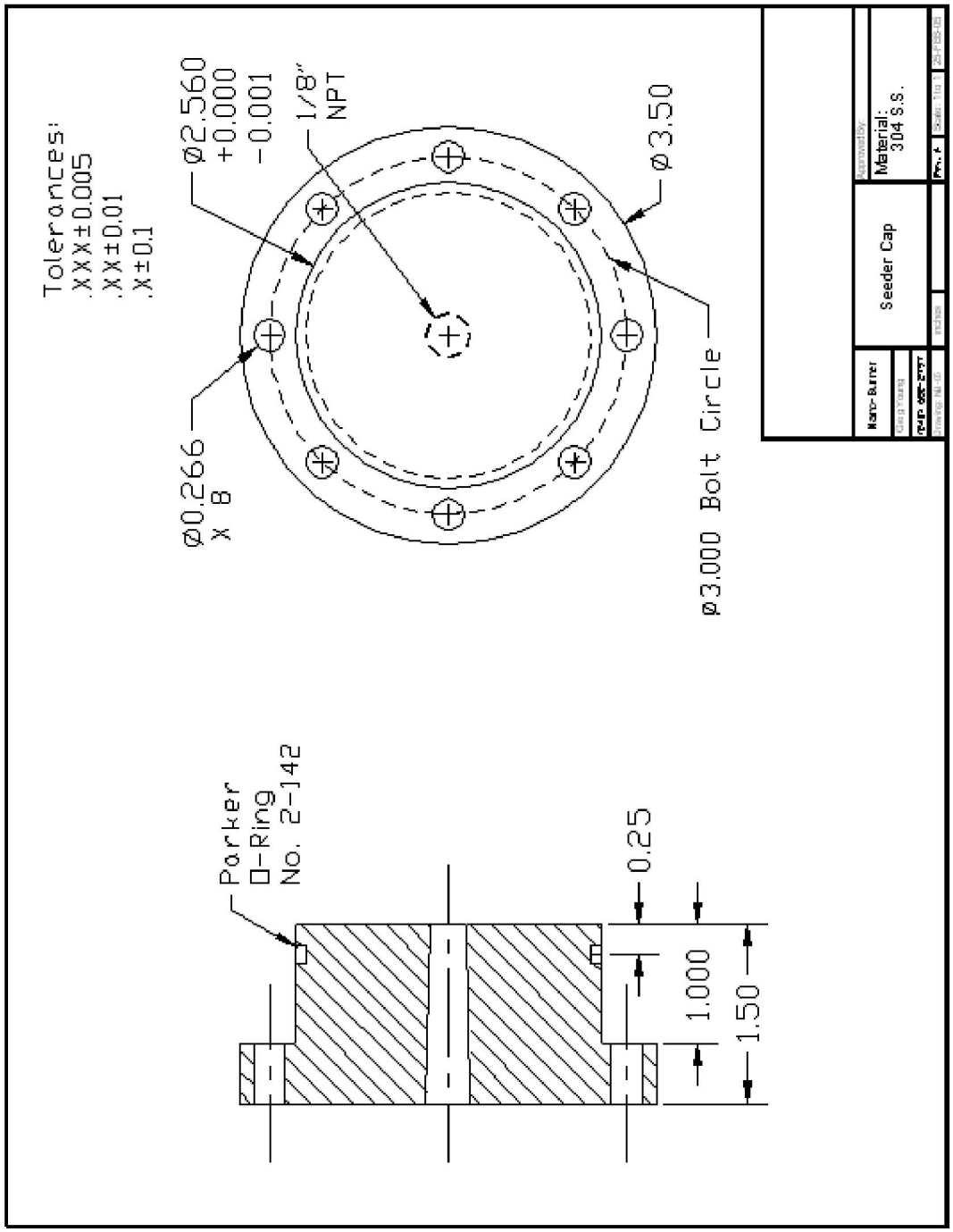

Fig. A.13 Seeder Cap

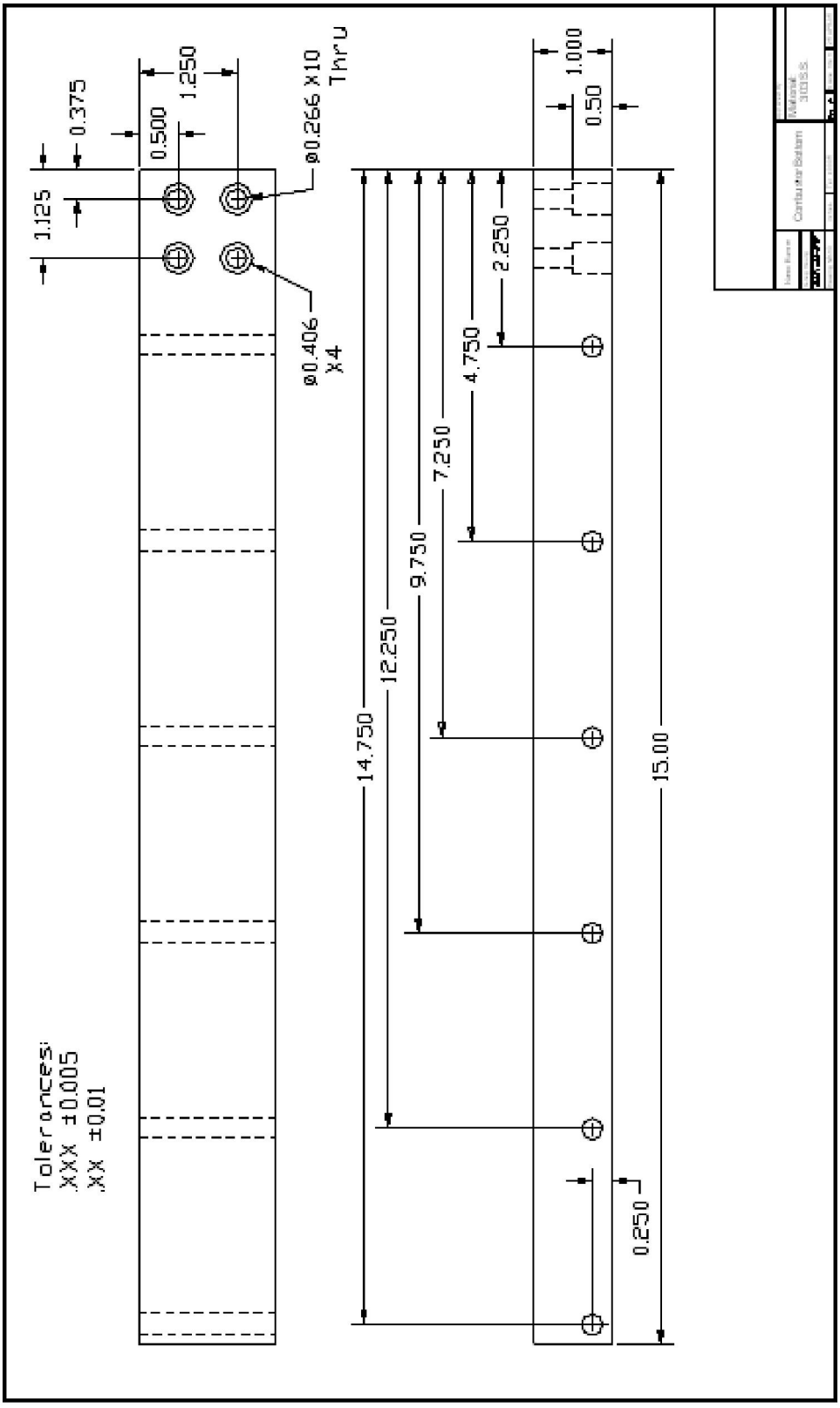

Fig. A.14 Combustor Bottom Plate

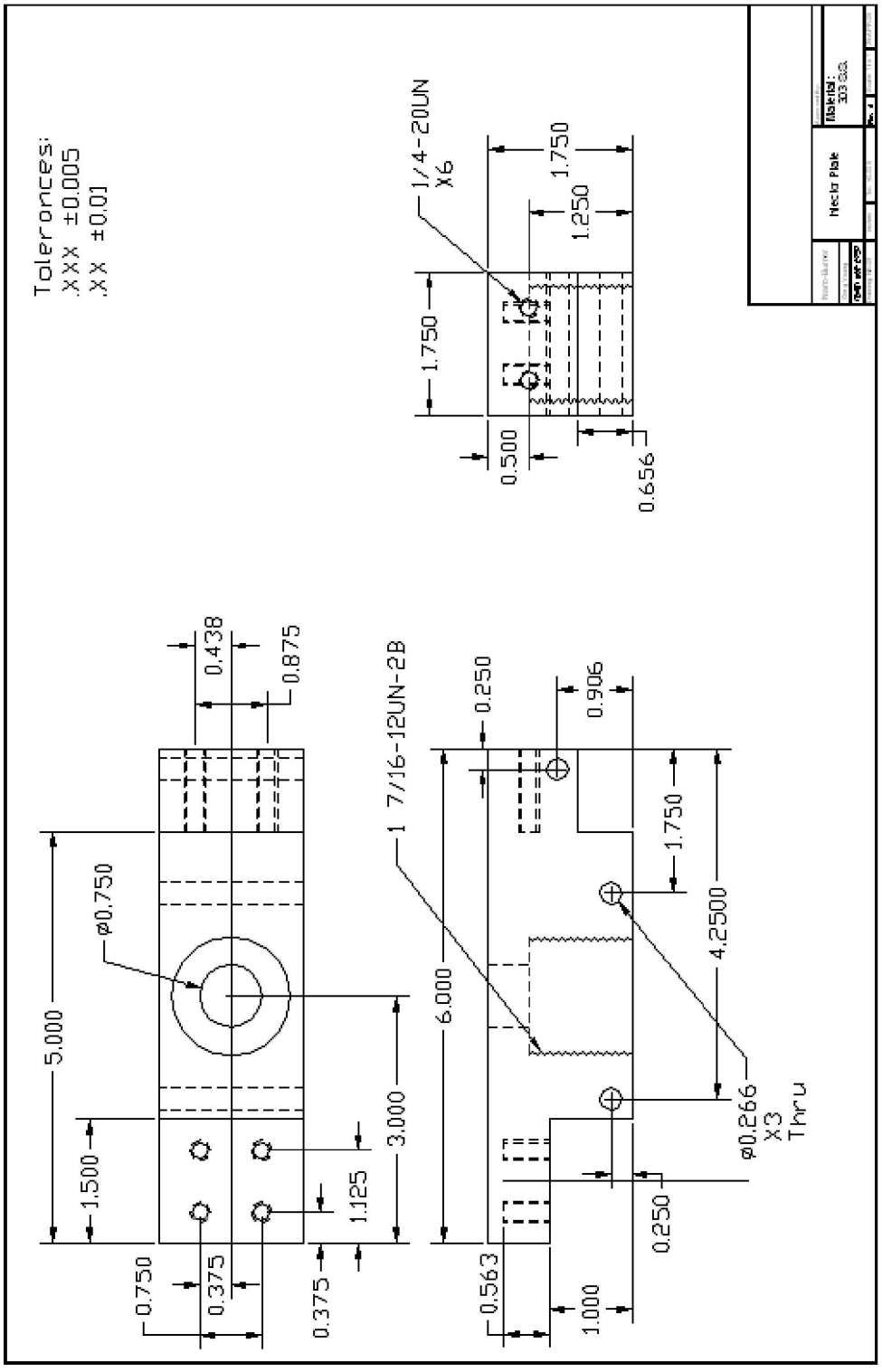

Fig. A.15 Combustor Injector Plate (Mates With Pilot Flame Combustor)

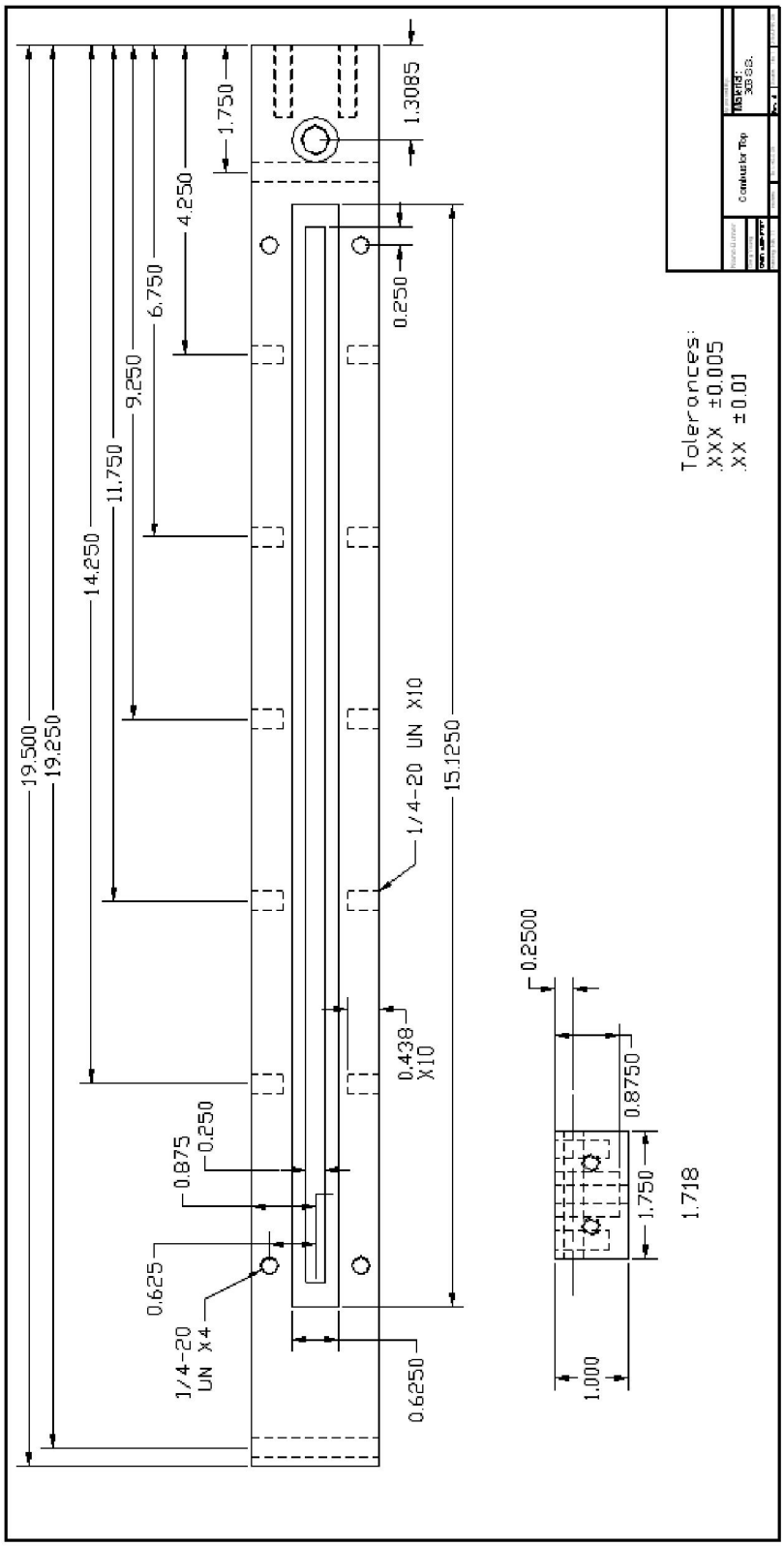

Fig. A.16 Combustor Top Plate

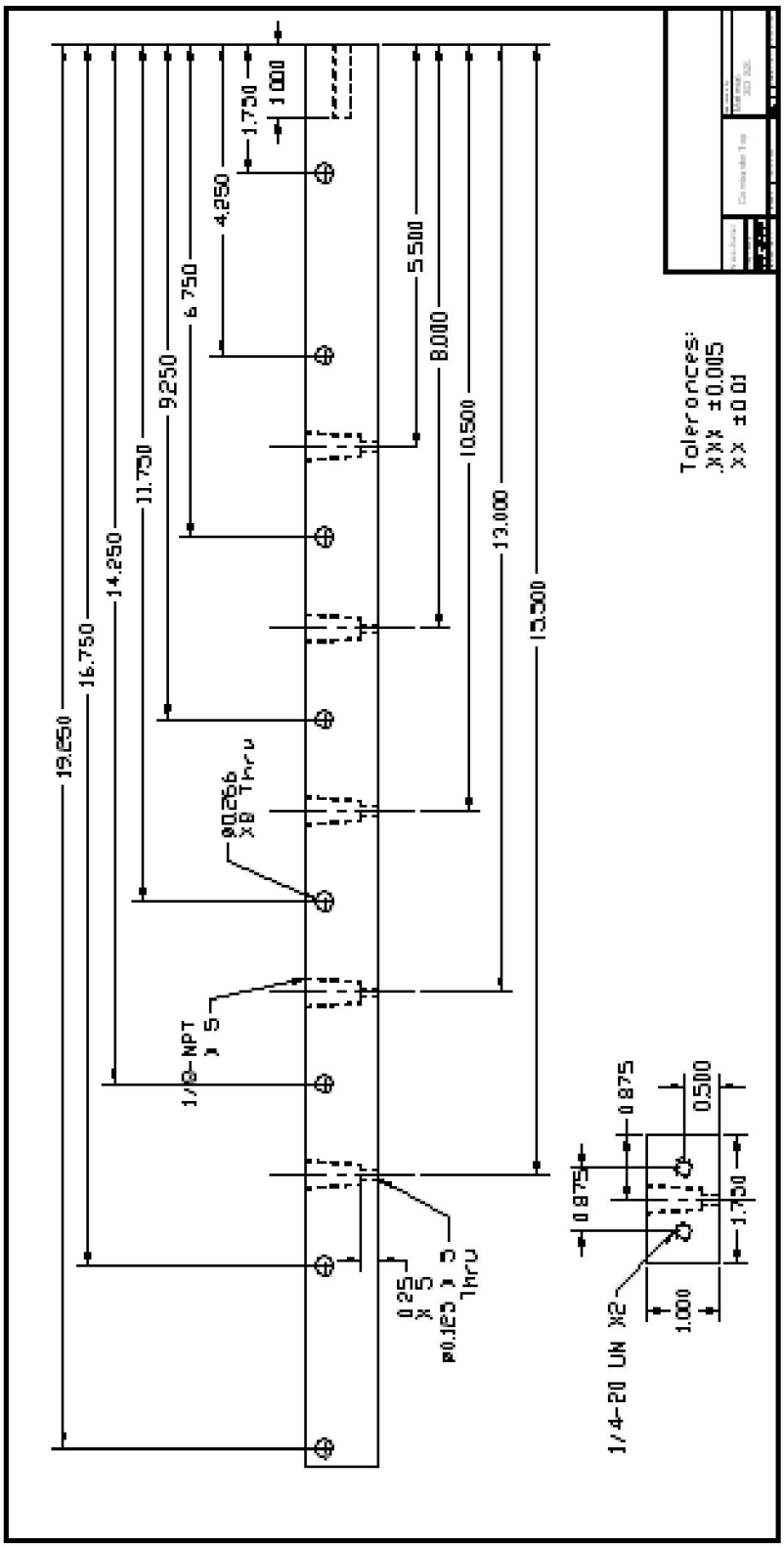

Fig. A.17 Alternate Top Plate

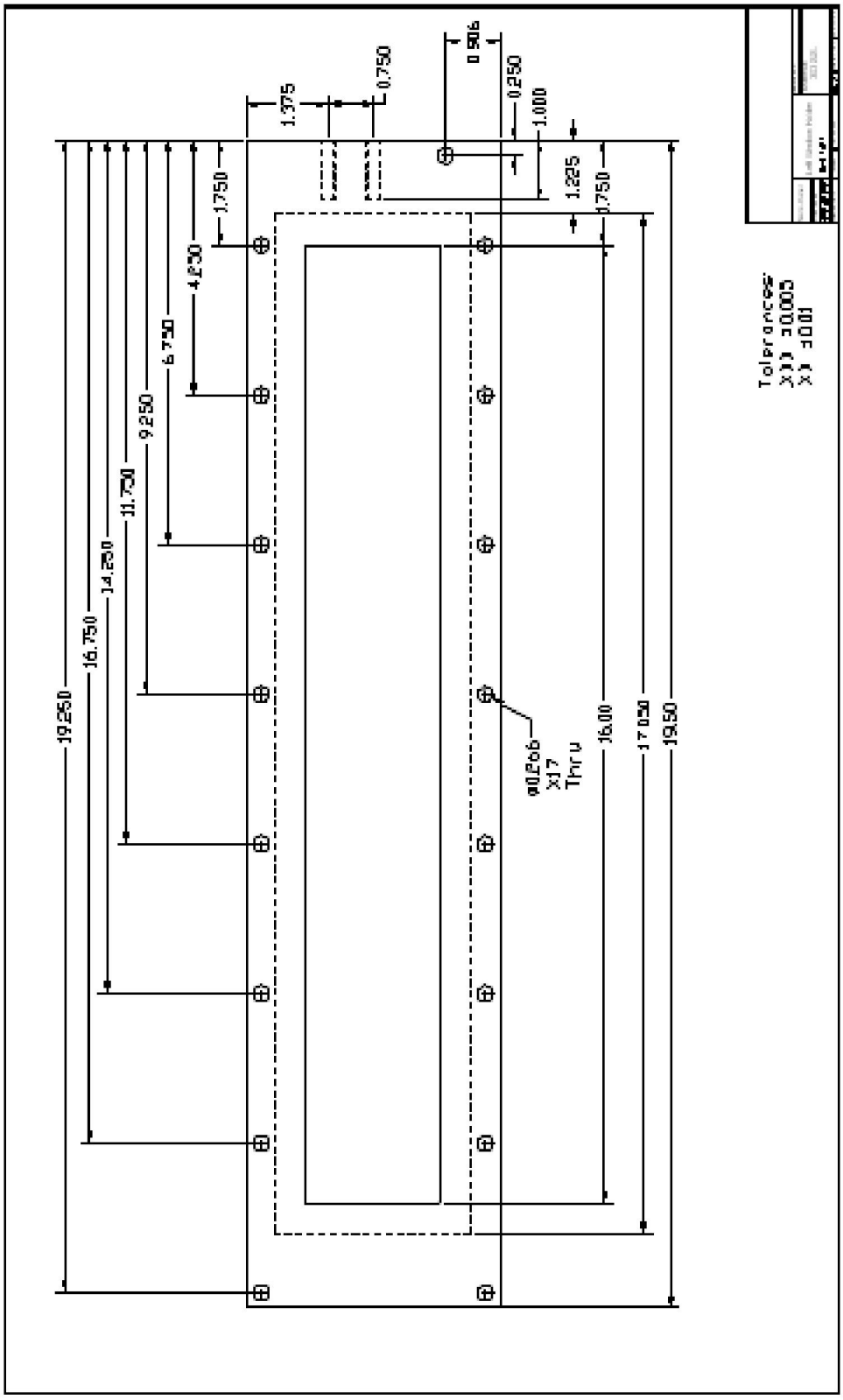

Fig. A.18 Left Window Holder Side View

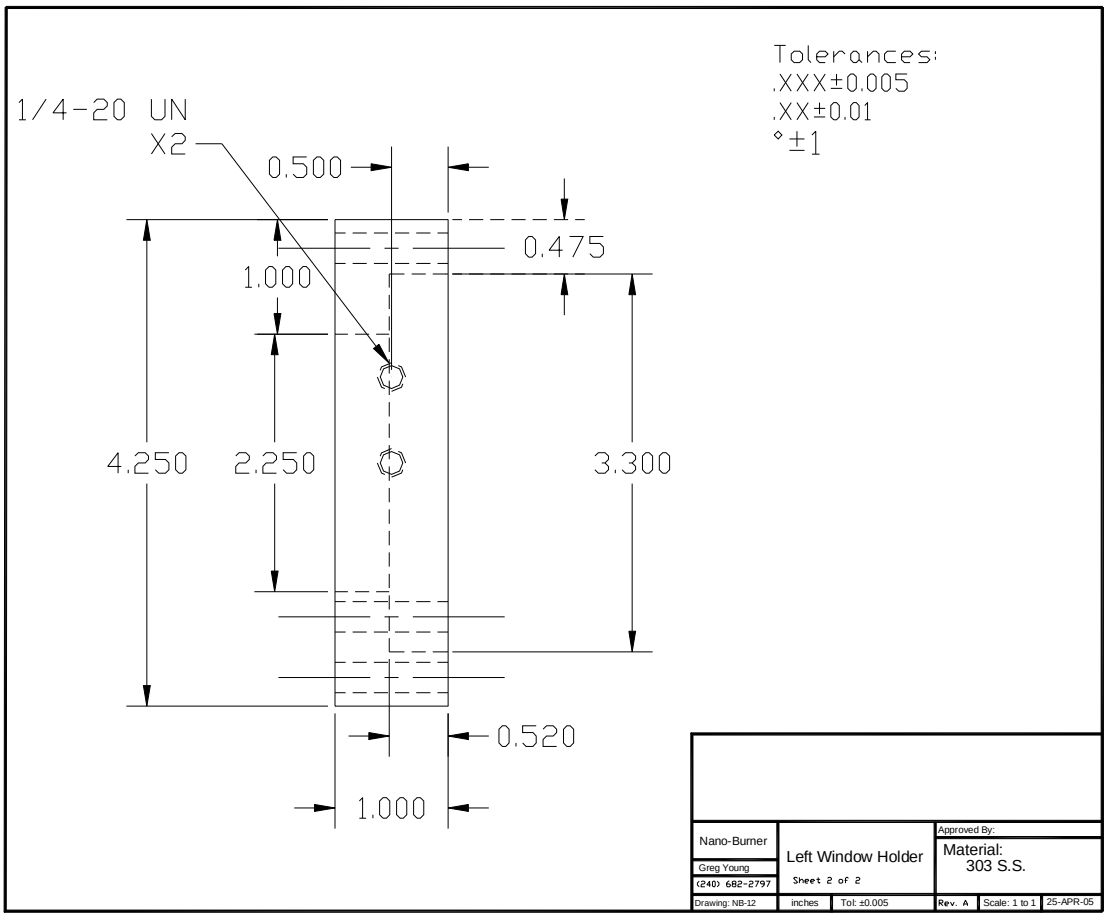

Fig. A.19 Left Window Holder End View

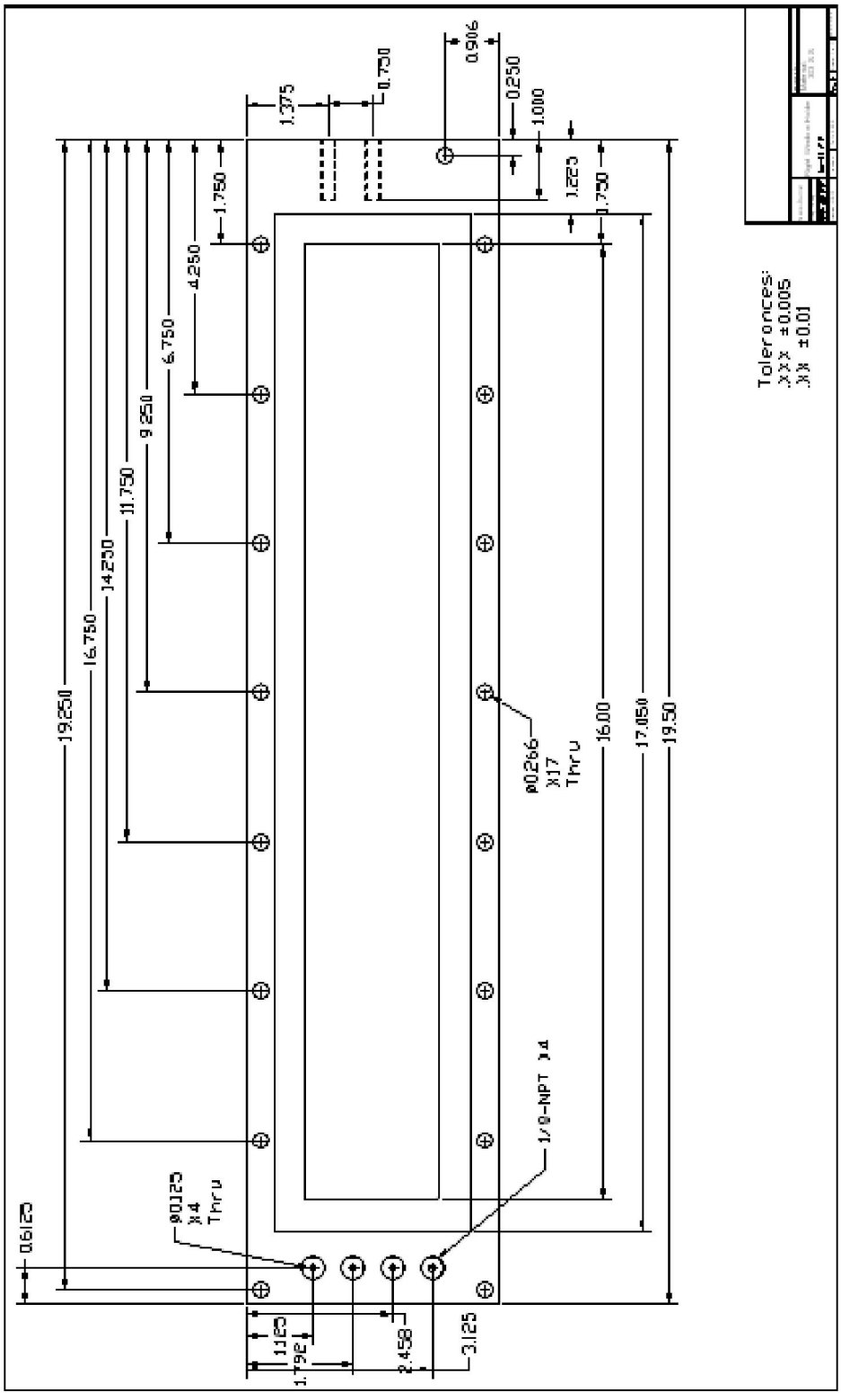

Fig. A.20 Right Window Holder Side View

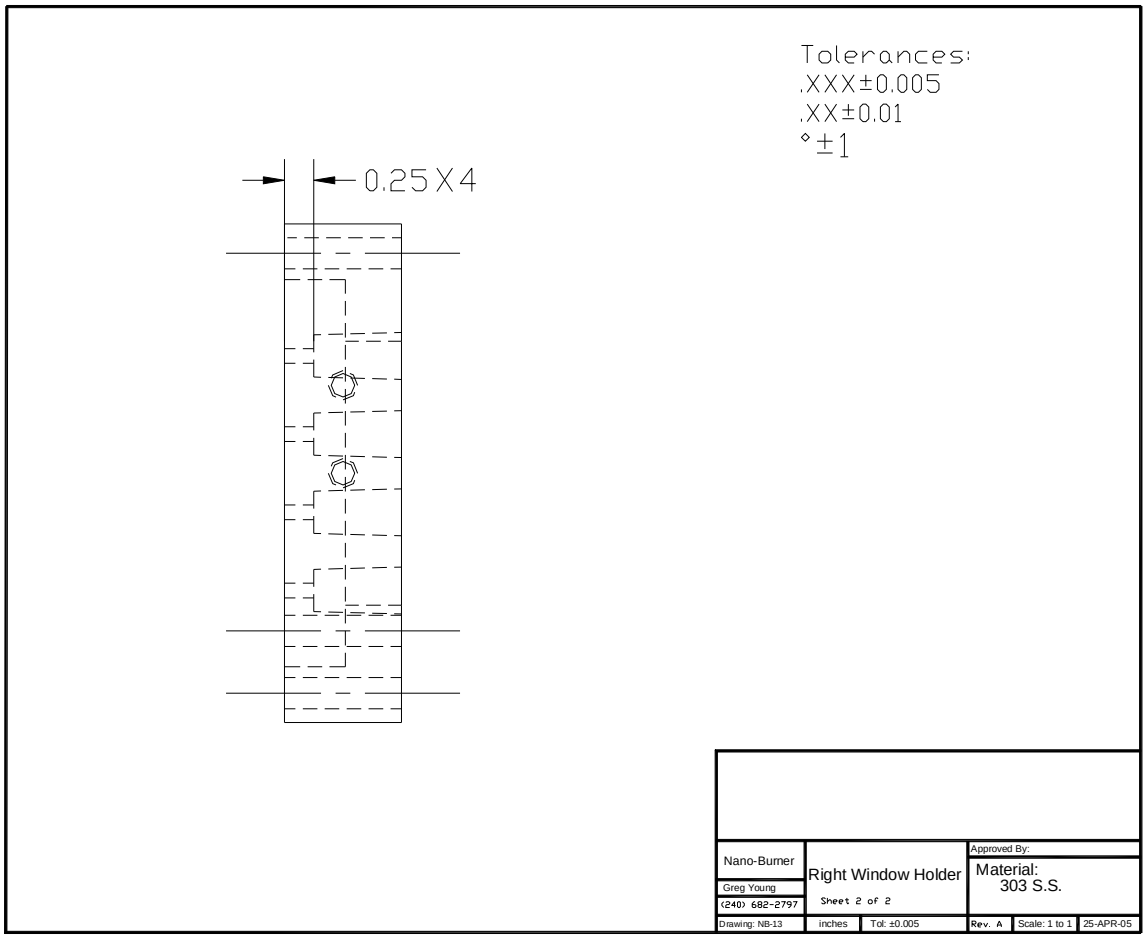

Fig. A.21 Right Window Holder End View

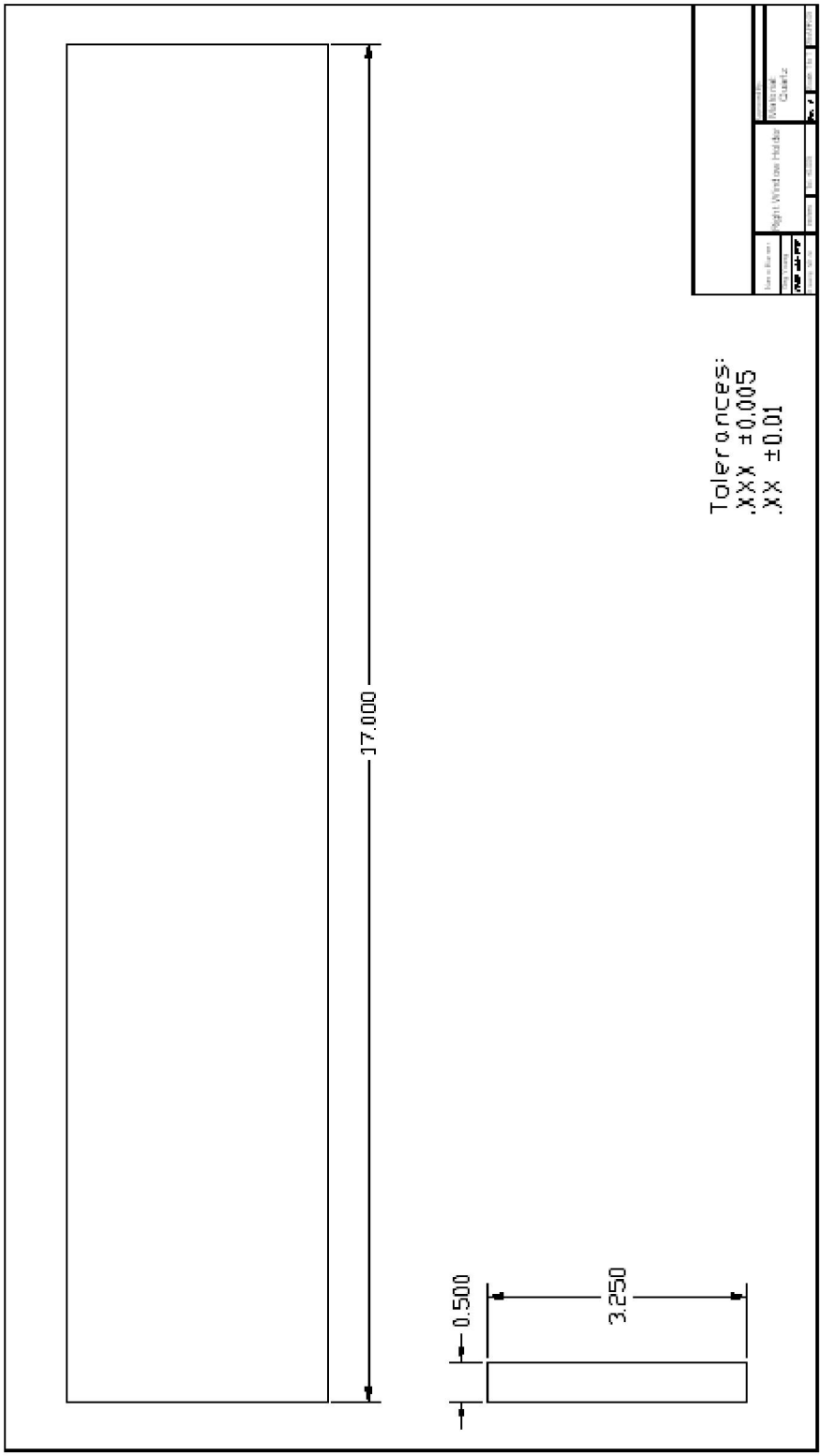

Fig. A.22 Quartz Window

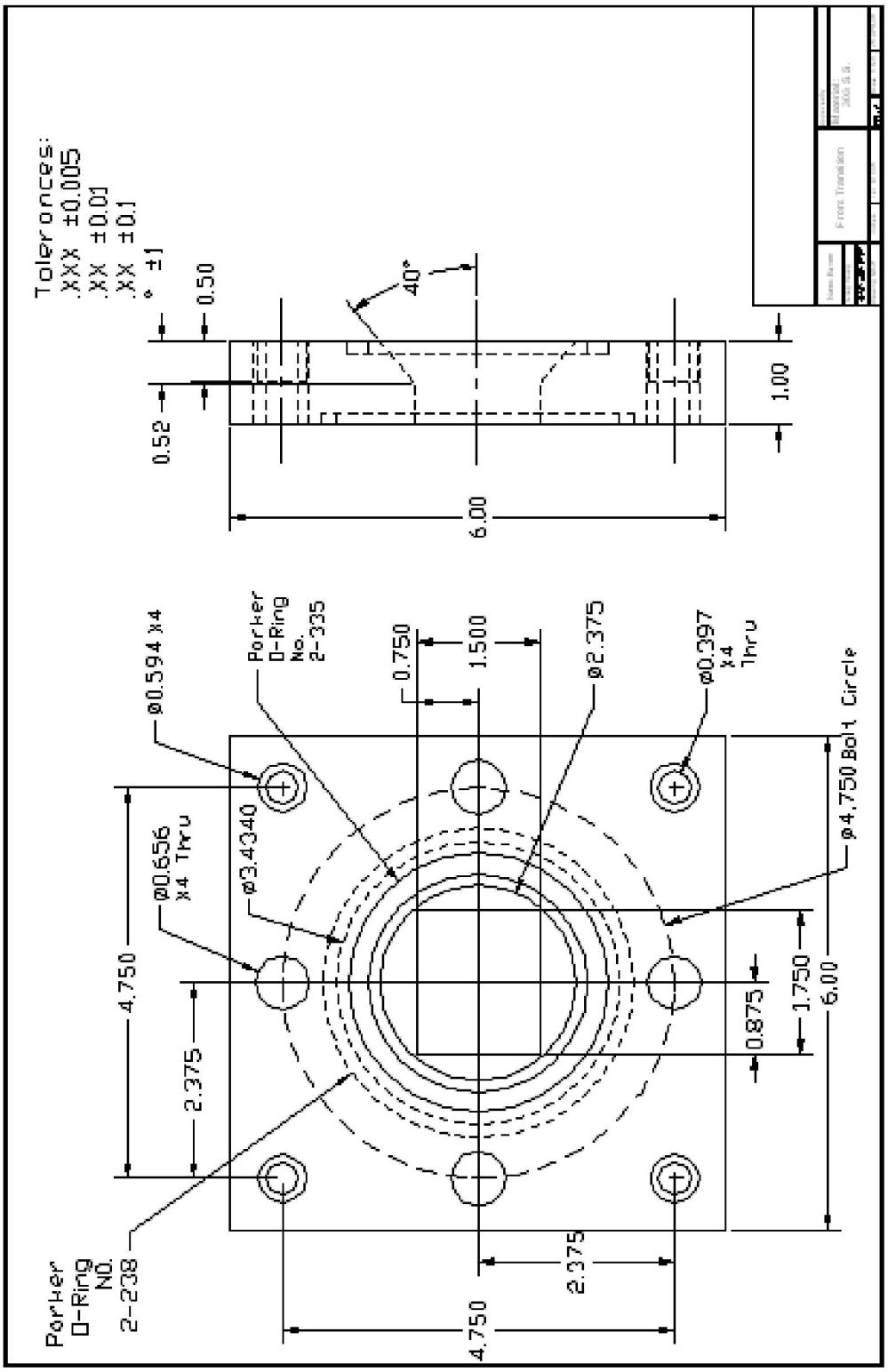

Fig. A.23 Front Transition

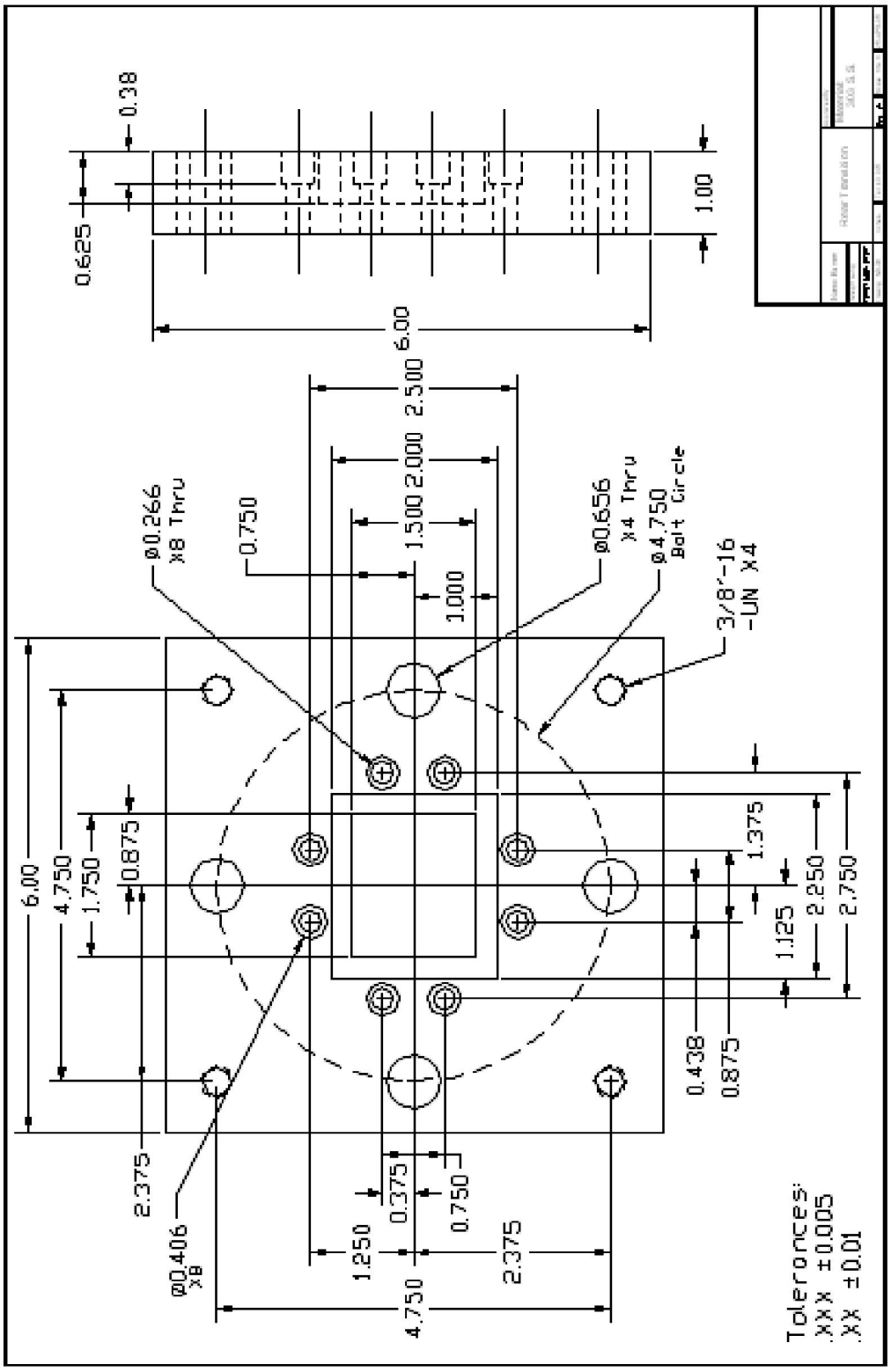

Fig. A.24 Rear Transition

APPENDIX B – UNCERTAINTY ANALYSIS

The uncertainty analysis in this study followed the procedures given by Kline and McKlintock[93]. The procedure dictates that for a given variable, *y* (see equation B.1), that the uncertainty, δy, in *y*, can be determined by equation B.2.

$$y = f\left(x_1, x_2, \ldots, x_n\right) \qquad \text{Eq. B.1}$$

$$\delta y = \sqrt{\left(\frac{\partial f}{\partial x_1}\delta x_1\right)^2 + \left(\frac{\partial f}{\partial x_2}\delta x_2\right)^2 + \ldots + \left(\frac{\partial f}{\partial x_n}\delta x_n\right)^2} \qquad \text{Eq. B.2}$$

As an example, the uncertainty in the radiation correction was examined. First, all of the variables and sub-variable involved were identified and can be seen in equations B.3-B.6.

$$\mathrm{Re}_d = \frac{Ud}{\nu} \qquad \text{Eq. B.3}$$

$$Nu = 0.42 * \mathrm{Pr}^{0.2} + 0.57 * \mathrm{Pr}^{1/3} * \mathrm{Re}_d^{1/2} \qquad \text{Eq. B.4}$$

$$h = \frac{Nu * k}{d} \qquad \text{Eq. B.5}$$

$$T_g = T_{tc} + \frac{\varepsilon_{tc}\sigma\left(T_{tc}^4 - T_\infty^4\right)}{h} \qquad \text{Eq. B.6}$$

Next, the uncertainty in each one of the variables was determined by the procedures outlined by Kline and McKlintock[93] as seen in equations B.7-B.9. The uncertainty in thermocouple diameter was taken to be a typical machining tolerance of 0.005 inches, while the uncertainty in all gas properties was taken as 10%. The emissivity values were taken from Shaddix[64] as 0.22 and 0.25 respectively for B-type and K-type thermocouples respectively.

$$\delta \mathrm{Re}_d = \sqrt{\left(\frac{d}{\nu}\delta U\right)^2 + \left(\frac{U}{\nu}\delta d\right)^2 + \left(\frac{Ud}{\nu^2}\delta \nu\right)^2} \qquad \text{Eq. B.7}$$

$$\delta Nu = \sqrt{\left(\left(0.2 * 0.42 * \mathrm{Pr}^{-0.8} + \frac{1}{3} * 0.57\,\mathrm{Pr}^{-2/3} * \mathrm{Re}_d^{1/2}\right) * \delta \mathrm{Pr}\right)^2 + \left(\frac{1}{2} * 0.57 * \mathrm{Pr}^{1/3} * \mathrm{Re}_d^{-1/2} * \delta \mathrm{Re}_d\right)^2}$$

Eq. B.8

$$\delta h = \sqrt{\left(\frac{k}{d}\delta Nu\right)^2 + \left(\frac{Nu * k}{d^2}\delta d\right)^2} \qquad \text{Eq. B.9}$$

and finally the uncertainty in the actual gas temperature is found by equation B.10.

$$\delta T_g = \sqrt{\left(\frac{\partial T_g}{\partial T_{tc}}\delta T_{tc}\right)^2 + \left(\frac{\partial T_g}{\partial \varepsilon}\delta \varepsilon\right)^2 + \left(\frac{\partial T_g}{\partial T_\infty}\delta T_\infty\right)^2 + \left(\frac{\partial T_g}{\partial h}\delta h\right)^2} \qquad \text{Eq. B.10}$$

where each term was evaluated in the following manner:

$$\frac{\partial T_g}{\partial T_{tc}} = 1 + \frac{4\varepsilon\sigma T_{tc}^3}{h} \qquad \text{Eq. B.11}$$

$$\frac{\partial T_g}{\partial \varepsilon} = \frac{\sigma\left(T_{tc}^4 - T_\infty^4\right)}{h} \qquad \text{Eq. B.12}$$

$$\frac{\partial T_g}{\partial T_\infty} = \frac{-4\varepsilon\sigma T_\infty^3}{h} \qquad \text{Eq. B.13}$$

$$\frac{\partial T_g}{\partial h} = \frac{-\varepsilon\sigma\left(T_{tc}^4 - T_\infty^4\right)}{h^2} \qquad \text{Eq. B.14}$$

The same procedure was used for determining the uncertainty for every measurement made in this study.

APPENDIX C – ROTAMETER CALIBRATIONS

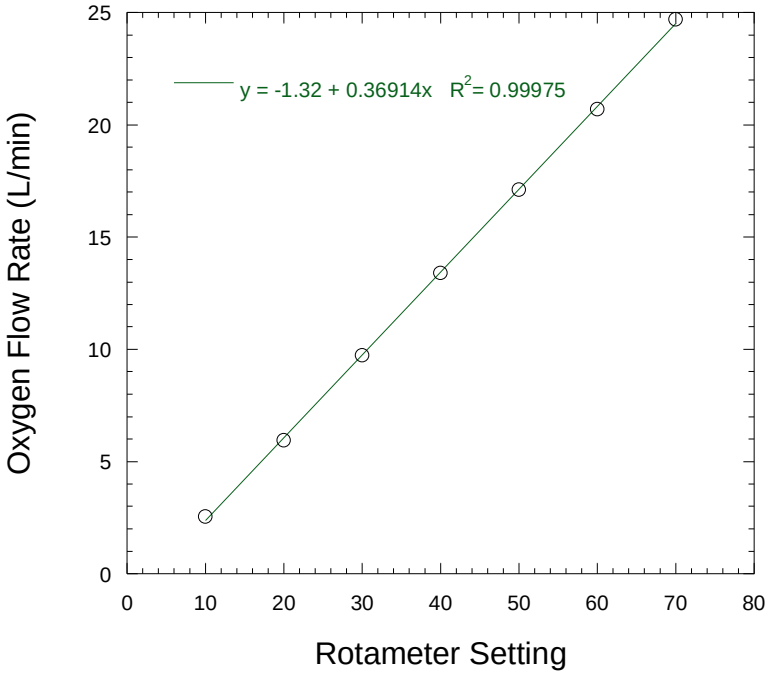

Fig. C.1 Calibration for Oxygen

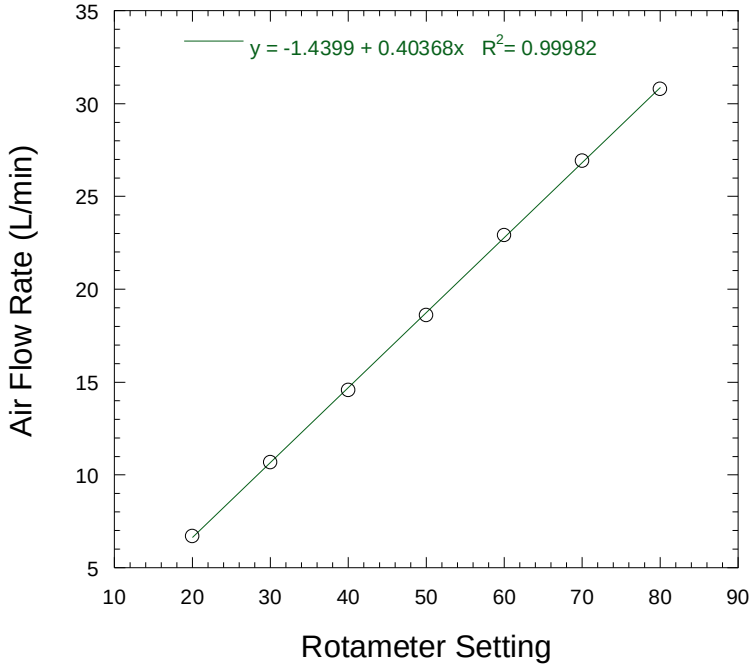

Fig. C.2 Calibration for Air

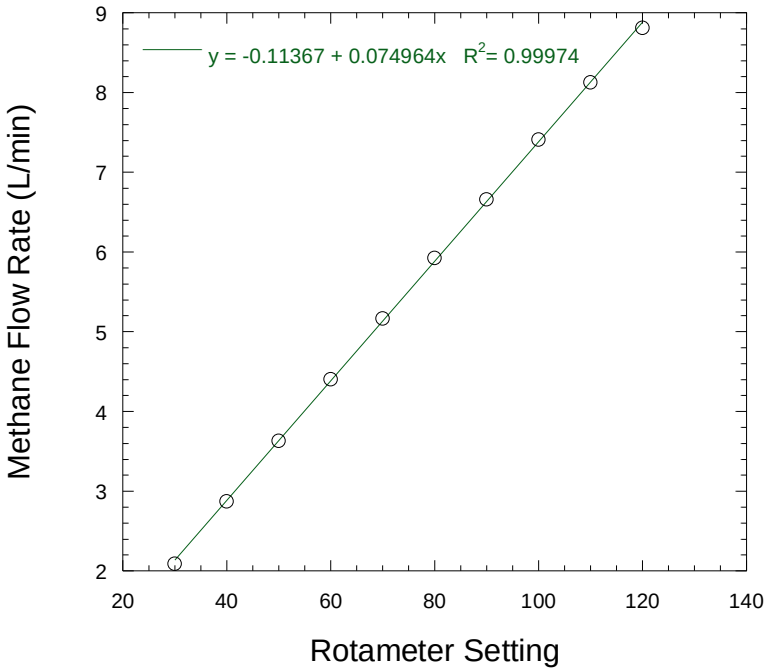

Fig. C.3 Calibration for Methane

References

1. Sutton, G.P., *Rocket Propulsion Elements: An Introduction to the Engineering of Rockets,* 6th Edition, John Wiley and Sons, Inc., 1992
2. Fry, R.S., "A Century of Ramjet Propulsion Technology Evolution", *Journal of Propulsion and Power,* Vol. 20, No. 1, January-February, pp. 27-58
3. Timnat, Y.M., *Advanced Airbreathing Propulsion*, Krieger Publishing Company, 1996
4. Harris, R.V., "On the Threshold – The Outlook for Supersonic and Hypersonic Aircraft", *Journal of Aircraft,* January-February 1992, pg. 10-19
5. Heiser, W.H., Pratt, D.T., *Hypersonic Airbreathing Propulsion,* American Institute of Aeronatics and Astronautics, 1994
6. Cazin, P., Laurent, J.M., "Liquid Fuel Ramjet Engine", *Tactical Missile Propulsion,* AIAA Volume 170, Gorden E. Jensen, David W. Netzer, Eds., pp. 423-446, Progress in Astronautics and Aeronautics, 1996
7. Leisch, S., Netzer, D., "Solid Fuel Ramjets", *Tactical Missile Propulsion,* AIAA Volume 170, Gorden E. Jensen, David W. Netzer, Eds., pp. 469-496, Progress in Astronautics and Aeronautics, 1996
8. Gany, A., Netzer, D.W., "Fuel Performance Evaluation of the Solid Fuel Ramjet", *International Journal of Turbo and Jet Engines,* 2, 1985, pp.157-168
9. Gany, A., "Combustion of Boron Containing Fuels in Solid Fuel Ramjets", *Combustion of Boron-Based Solid Propellants and Solid Fuels,* K. K. Kuo, R. Pein, Eds., pp. 91-112, CRC Press Begell House, Boca Raton, 1993

10. Ciezki, H.K., Sender, J., Claub, W., Feinauer, A., Thumann, A., "Combustion of Solid-Fuel Slabs Containing Boron Particles in Step Combustor", *Journal of Propulsion and Power,* Vol. 19, No. 6, November-December 2003
11. Wimmerstrom, P., Lundgren, R., "Studies of Fuel-Rich Magnesium Propellants in a Small Solid Fuel Ramjet Combustor", 22nd International Annual Conference of ICT, Karlsruhe, pp. 96-1 – 96-7, Germany, July 2-5, 1991
12. Leingang, J.L., Petters, D.P., "Ducted Rockets", *Tactical Missile Propulsion*, AIAA Volume 170, Gorden E. Jensen, David W. Netzer, Eds., pp. 447-468, Progress in Astronautics and Aeronautics, 1996
13. Hallion, R.P., "The History of Hypersonics: or, "Back to the Future – Again and Again"", AIAA 2005-0329, 43rd AIAA Aerospace Sciences Meeting and Exhibit, Reno, Nevada, January 10-13, 2005
14. Waltrup, P.J., White, M.E., Zarlingo, F., Gravlin, E.S., "History of U.S. Navy Ramjet, Scramjet, and Mixed-Cycle Propulsion Development", *Journal of Propulsion and Power,* Vol. 18, No. 1, January-February 2002, pp. 14-27
15. Olsen, S.E., Beckstead, M.W., "Burn Time Measurements of Single Aluminum Particles in Steam and CO_2 Mixtures", *Journal of Propulsion and Power*, Vol. 12, No. 4, pp. 662-671, 1996
16. Parr, T., Johnson, C., Hanson-Parr, D., Higa, Kelvin, and Wilson, K., "Evaluation of Advanced Fuels for Underwater Propulsion", 39th JANNAF Combustion Subcommittee Meeting, December, 2003

17. Bazyn, T., Krier, H., Glumac, N., "Shock Tube Measurements of Combustion of Nano-Aluminum", AIAA 2006-1157, 44th AIAA Aerospace Sciences Meeting and Exhibit, Reno, Nevada, January 9-12, 2006
18. Tepper, F. and Kaledin, L.A., "Combustion Characteristics of Kerosene Containing Alex Nano-Aluminum," 5th International Symposium on Special Topics in Chemical Propulsion, Stressa, Italy, June 18-22, 2000
19. Goroshin, S., Higgins, A.J., and Kamel, M., "Powdered Metals as Fuel for Hypersonic Ramjets", AIAA-2001-3919, 37th AIAA/ASME/SAE/ASEE Joint Propulsion Conference and Exhibit, Salt Lake City, Utah, July 8-11, 2001
20. Palaszewski, B., "Metallized Gelled Propellants: Oxygen/RP-1/Aluminum Rocket Engine Calorimeter Heat Transfer Measurements and Analysis", AIAA-97-2974, 33rd AIAA/ASME/SAE/ASEE Joint Propulsion Conference and Exhibit, Seattle, Washington, July 6-9, 1997
21. Mordosky, J.W., Zhang, B.Q., Kuo, K.K., Tepper, F., Kaledin, L.A., "Spray Combustion of Gelled RP-1 Propellants Containing Nano-sized Aluminum Particles in Rocket Engine Conditions", AIAA-2001-3274, 37th AIAA/ASME/SAE/ASEE Joint Propulsion Conference and Exhibit, Salt Lake City, Utah, July 8-11, 2001
22. Risha, G.A., Evans, B. J., Boyer, E., Wehrman, R. B., and Kuo, K. K., "Nano-Sized Aluminum- and Boron-Based Solid-Fuel Characterization in a Hybrid Rocket Engine," AIAA Paper No. 2003-4593, 39th AIAA/ASME/SAE/ASEE Joint Propulsion Conference and Exhibit, Huntsville, Alabama, July 2003

23. Palaszewski, B., Jurns, J., Breisacher, K., Kearns, K., "Metallized Gelled Propellants Combustion Experiments in a Pulse Detonation Engine", AIAA-2004-4191, 40th AIAA/ASME/SAE/ASEE Joint Propulsion Conference and Exhibit, Ft. Lauderdale, Florida, July 11-14, 2004
24. Park, K., Lee, D., Rai, A., Mukherjee, D., Zachariah, M.R., "Sized-Resolved Kinetic Measurements of Aluminum Nanoparticle Oxidation with Single Particle Mass Spectrometry", *Journal of Physical Chemistry B*, 109 (15), 2005, pp. 7290-7299
25. Kuo, K.K., Principles of Combustion, Wiley & Sons, New York, 1986
26. Price, E.W. and Sigman, R.K., "Combustion of Aluminized Solid Propellants," *Solid Propellant Chemistry, Combustion, and Motor Interior Ballistics,* AIAA Volume 185, Vigor Yang, Thomas B. Brill, and Wu-Zhen Ren, Eds., pp. 663-687, Progress in Astronautics and Aeronautics, 2000
27. Price, E.W., "Combustion of Metallized Propellants," *Fundamentals of Solid Propellant Combustion,* Editors Kuo, K.K., and Summerfield, M., AIAA Volume 90, pp. 479-513 Progress in Astronautics and Aeronautics, 1983
28. Melcher, J.C., Burton,R.L., Krier, H., "Combustion of Aluminum Particles in Solid Rocket Motor Flows," *Solid Propellant Chemistry, Combustion, and Motor Interior Ballistics,* AIAA Volume 185, Vigor Yang, Thomas B. Brill, and Wu-Zhen Ren, Eds., pp. 723-747, Progress in Astronautics and Aeronautics, 2000
29. Glassman, I., *Combustion,* 3rd Edition, Academic Press, San Diego, California, 1996

30. Branstetter, J.R., Lord, A.M., Gerstein, M., "Combustion Properties of Aluminum as a Ram-Jet Fuel," NACA Research Memorandum, NACA RM E51B02, March 28, 1951
31. Yetter, R.A., and Dryer, F.L., "Metal Particle Combustion and Classification", *Microgravity Combustion: Fire in Free Fall,* Academic Press, 2001
32. Beckstead, M.W., "Lectures on Metal Combustion", February 25, 1999, China Lake, CA
33. Liang, Y., Beckstead, M.W., "Numerical Simulation of Unsteady, Single Aluminum Particle Combustion in Air", AIAA Paper 98-3697, June 1998
34. Beckstead, M.W., Newbold, B.R., Waroquet, C., "A Summary of Aluminum Combustion", 39th JANNAF Combustion Subcommittee Meeting, December, 2003
35. Friedman, R., Macek, A., "Combustion Studies of Single Aluminum Particles", *Ninth Symposium (International) on Combustion*, 1963, pp. 703-709
36. Friedman, R., Macek, A., "Ignition and Combustion of Aluminum Particles in Hot Ambient Gases", *Combustion and Flame,* Vol. 6, 1962, pp. 9-19
37. Macek, A., " Fundamentals of Combustion of Single Aluminum and Beryllium Particles", *Eleventh Symposium (International) on Combustion*, 1967, pp. 203-217
38. Davis, A., "Solid Propellants: The Combustion of Particles of Metal Ingredients", *Combustion and Flame,* Vol. 7, 1963, pp. 359-367

39. Drew, C.M., Gordon, A.S., Knipe, R.H., "Study of Quenched Aluminum Particle Combustion", *Heterogeneous Combustion,* AIAA, Progress in Astronautics and Aeronautics Series, Vol. 15, Academic Press, New York, NY, 1964, pp. 17-39
40. Turns, S.R., Wong, S.C., Ryba, E., "Combustion of Aluminum-Based Slurry Agglomerates", *Combustion Science and Technology*, Vol. 54, 1987, pp. 299-318
41. Foelsche, R.O., Burton, R.L., Krier, H., "Ignition and Combustion of Aluminum Particles in H2/O2/N2 Combustion Products", *Journal of Propulsion and Power*, Vol. 14, No. 6, 1998, pp. 1001-1008
42. Bucher, P., Yetter, R.A., Dryer, F.L., Parr, T.P., Hanson-Parr, D.M., "PLIF Species and Ratiometric Temperature Measurements of Aluminum Particles in O_2, CO_2, and N_2O Oxidizers, and Comparison with Model Calculations", *Twenty-Seventh Symposium (International) on Combustion*, The Combustion Institute, Pittsburgh, PA, 1998, pp. 2421-2429
43. Bucher, P., Yetter, R.A., Dryer, F.L., Parr, T.P., Hanson-Parr, D.M., Vincenzi, E.P., "Flame Structure of Single, Isolated Aluminum Particles Burning in Air", *Twenty-Sixth Symposium (International) on Combustion,* The Combustion Institute, Pittsburgh, PA, 1996, pp. 1899-1908
44. Ulas, A., Kuo, K.K., "Ignition and Combustion of Boron Particles in Fluourine-Containing Environments", *Combustion and Flame*, Vol. 127, 2001, pp. 1935-1957
45. Beckstead, M., "Lectures on Comustion," Short Course on Metal Combustion, Applied Research Laboratory, The Pennsylvania State University, August 20, 2002

46. Yeh, C.L., Kuo, K.K., "Ignition and Combustion of Boron Particles", *Progress in Energy Combustion Science*, Vol. 22, pp. 511-541

47. Macek, A., Semple, J.M., "Combustion of Boron Particles at Atmospheric Pressure", *Combustion Science and Technology*, Vol. 1, 1969, pp. 181-191

48. Macek, A., Semple, J.M., "Combustion of Boron Particles at Elevated Pressures", *Thirteenth Symposium (International) on Combustion*, The Combustion Institute, Pittsburgh, PA, 1971, pp. 859-868

49. Macek, A., "Combustion of Boron Particles: Experiment and Theory", *Fourteenth Symposium (International) on Combustion*, The Combustion Institute, Pittsburgh, PA, 1972, pp. 1401-1411

50. King, M.K., "Boron Particle Ignition in Hot Gas Streams", *Combustion Science and Technology*, Vol. 8, 1974, pp. 255-273

51. Foelsche, R.O., Burton, R.L., and Krier, H., "Boron Particle Ignition and Combustion at 30-150 ATM," *Combustion and Flame*, No. 117, pp. 32-58, 1999

52. Yetter, R.A., Rabitz, H., Dryer, F.L., Brown, R.C., Kolb, C.E., "Kinetics of High-Temperature B/O/H/C Chemistry", *Combustion and Flame*, No. 83, pp. 43-63, 1991

53. Pearse, R.W.B., Gaydon, A.G., *The Identification of Molecular Spectra*, 4th edition, Chapman and Hall, London, 1976, p. 59

54. Wimmerstein, P., Lundgren, R., "Studies of Fuel-Rich Magnesium Propellants in a Small Solid Fuel Ramjet Combustor", *22nd International Annual Conference of ICT 1991*, Karlsruhe, Germany, July 2-5, 1991

55. Abbott, S.W., Smoot, L.D., Schadow, K., "Direct Mixing and Combustion Efficiency Measurements in Ducted, Particle-Laden Jets", *AIAA Journal*, Vol. 12, No.3, March 1974, pp. 275-282
56. Schadow, K., "Experimental Investigation of Boron Combustion in Air-Augmented Rockets", *AIAA Journal*, Vol. 7, No. 10, October 1969, pp. 1870-1876
57. Schadow, K.C., Wilson, K.J., Gutmark, E., Smith, R.A., "Effect of Gaseous Fuel Mixing on Boron Combustion in Ducted Rocket with Side Dump", *Combustion of Boron-Based Solid Propellants and Solid Fuels*, Editors Kuo, K.K., and Pein, R., CRC Press, Begell House, Boca Raton, 1993, pp. 402-411
58. Gany, A., "Combustion of Boron-Containing Fuels in Solid Fuel Ramjets", *Combustion of Boron-Based Solid Propellants and Solid Fuels*, Editors Kuo, K.K., and Pein, R., CRC Press, Begell House, Boca Raton, 1993, pp. 91-112
59. Natan, B., Gany, A., "Combustion Characteristics of a Boron-Fueled Solid Fuel Ramjet with Aft-Burner", *Journal of Propulsion and Power*, Vol. 9, No. 5, Sept.-Oct. 1993, pp. 694-701
60. Gany, A., "Comprehensive Consideration of Boron Combustion in Airbreathing Propulsion", AIAA-2006-4567, 42nd AIAA/ASME/SAE/ASEE Joint Propulsion Conference and Exhibit, Sacramento, California, July 9-12, 2006
61. Son, S.F., Dye, R.C., Busse, J.R., Sandstrom, M.M., Oschwald, D.M., Janicke, M.T., "Combustion of Nanoaluminum in Air", 39th JANNAF Combustion Subcommittee Meeting, December, 2003

62. Mench, M. M., Yeh, C.L., Kuo, K.K., "Propellant Burning Rate Enhancement and Thermal Behavior of Ultra-fine Aluminum Powders", Energetics Materials Production, Processing and Characterization, 29th International ICT Conference, June 30-July 3, 1998, pp. 3-01-3-05

63. Turns, S.R., An Introduction to Combustion, McGraw-Hill, Inc., New York, 1996,

64. Schlichting H., Boundary-Layer Theory, 6th Edition, McGraw-Hill, New York, 1968

65. Raffel, M., Willert, C., Kompenhans, J., Particle Image Velocimetry, Springer, New York, 1998

66. Shaddix, Christopher R., "Correcting Thermocouple Measurements for Radiation Loss: A Critical Review," NHTC99-282, Proceedings of the 33rd National Heat Transfer Conference, Albuquerque, New Mexico, August 15-17, 1999

67. Whitaker, S., (1972), AIChE J. 18:361

68. Incropera, F.P., Dewitt, D.P., Introduction to Heat Transfer, John Wiley & Sons, New York, 1996

69. Muruganandam, T.M., Kim, B., Olsen, R., Patel, M., Romig, B., and Seitzman, J.M., "Chemiluminescence Based Sensors for Turbine Engines," 39th *AIAA/ASME/SAE/ASEE Joint Propulsion Conference & Exhibit*, AIAA 2003-4490, 2003

70. Mayinger, F., "Optical Measurements: Techniques and Applications," *Springer-Verlag*, 1994, pp. 356

71. Gaydon, A.G., Wolfhard, H.G., Flames: Their Structure, Radiation, and Temperature, John Wiley & Sons, New York, 1979

72. Spalding, M.J., Krier, H., Burton, R.L., "Emission Spectroscopy During Ignition of Boron Particles at High Pressure," 35th AIAA Aerospace Sciences Meeting and Exhibit, January, 1997, AIAA 97-0119

73. Glass, M., Kennedy, I.M., "An Improved Seeding Method for High Temperature Laser Doppler Velocimetry," *Combustion andFlame*, No. 29, pp. 333-335, 1977

74. Yu, K.H., Parr, T.P., Schadow, K.C., "Planar Mie Scattering Visualization of Reacting and Nonreacting Supersonic Coaxial Jets," *Non-Intrusive Combustion Diagnostics*, Eds. K.K. Kuo and T.P. Parr, Begell House, Inc., New York, 1994, pp. 504-517

75. Gaydon, A.G., The Spectroscopy of Flames, John Wiley & Sons, New York, 1974

76. Katz, J., Tepper, F., Ivanov, G.V., Lerner, M.I., Davidovich, V., "Metastable Nanosize Aluminum Powder as a Reactant in Energetic Formulations," *JANNAF Propulsion Meeting, CPIA Publication 675*, Vol. 3, 1998, pp. 343-349

77. Impact Analytical Documentation for Thermal Analysis Website, http://www.impactanalytical.com, 2002

78. Verhoeven, J.D., "Scanning Electron Microscopy," ASM Handbook, Vol. 10, 4th Edition, January 1996, pp. 490-515

79. Hinds, W.C., Aerosol Technology, John Wiley & Sons, New York, 1999

80. Yang, Y., Wang, S., Sun, Z., Dlott, D., "Near Infra-red and Visible Absorption Spectroscopy of Nano-Energetic Materials Containing Aluminum and Boron," *Propellants, Explosives, and Pyrotechnics*, Vol. 30, 2005, No. 3, pp. 171-177

81. Mihalcea, R.M., Baer, D.S., Hanson, R.K., "Diode Laser Sensor for Measurements of CO, CO_2, and CH_4, in Combustion Flows," *Applied Optics*, Vol. 36, No. 33, November 1997

82. Mihalcea, R.M., Baer, D.S., Hanson, R.K., "A Diode-Laser Absorption Sensor System for Combustion Emission Measurements," *Measurement Science and Technology*, **9**, 1998, pp. 327-338

83. Friedlander, S.K., Smoke, Dust, and Haze, 2nd Edition, Oxford University Press, New York, 2000

84. B.J. McBride, S. Gordon, "*Computer Program for Calculation of Complex Chemical Equilibrium Compositions and Applications,"* NASA Reference Publication 1311, June 1996

85. Gruber, M.R., Nejad, A.S., Chen, T.H., Dutton, J.C., "Mixing and Penetration Studies of Sonic Jets in a Mach 2 Freestream," *Journal of Propulsion and Power*, Vol. 11, No. 2, March-April 1995

86. Keffer, J.F., and Baines, W.D., "The Round Turbulent Jet in a Cross-Wind," *Journal of Fluid Mechanics*, Vol. 15, 1963, pp 481-496

87. Li, S.C., Williams, F.A., "Ignition and Combustion of Boron Particles", *Combustion of Boron Based Solid Propellants and Fuels*, Kuo, K.K., and Pein, R., Eds., CRC Press, Boca Raton, 1993, pp 248-271

88. Bazyn, T., Krier, H., Glumac, N., "Oxidizer and Pressure Effects on the Combustion of 10-μm Aluminum Particles," *Journal of Propulsion and Power*, Vol. 21, No. 4, July-August 2005, pp. 577-582

89. Huang, Y., Risha, G.A., Yang, V., Yetter, R.A., "Combustion of Bimodal Nano/Micron-sized Aluminum Particle Dust in Air," *Proceedings of the Combustion Institute 31*, 2007

90. Yuasa, S., Isoda, H., "Ignition and Combustion of Small Boron Lumps in an Oxygen Stream," *Combustion and Flame*, Vol. 86, 1991, pp. 216-222

91. Pen'kov, S.N., "Investigation of Boron Ignition and Combustion by Means of Fast Cinespectrography", *Combustion of Boron Based Solid Propellants and Fuels*, Kuo, K.K., and Pein, R., Eds., CRC Press, Boca Raton, 1993, pp 218-231

92. King, M.K., "A Review of Studies of Boron Ignition and Combustion Phenomena at Atlantic Research Corporation Over the Past Decade", *Combustion of Boron Based Solid Propellants and Fuels*, Kuo, K.K., and Pein, R., Eds., CRC Press, Boca Raton, 1993, pp 1-80

93. Kline, S.J., and McClintock, F.A., "Describing Uncertainties in Single Sample Experiments," Published by the American Society of Mechanical Engineers, 1953